ADDITIVE MANUFACTURING OF FUNCTIONAL MATERIALS FOR POLYMER MICRO REACTORS

THESIS SUBMITTED IN ACCORDANCE WITH THE REQUIREMENT OF

THE UNIVERSITY OF LIVERPOOL FOR THE DEGREE OF DOCTOR IN PHILOSOPHY

By

Jetinder Singh

March 2012

ABSTRACT

This work investigates the development of functional materials by using additive manufacturing techniques; specifically digital light processing (DLP) based Stereolithography to manufacture micro reactors containing functional materials for sensing and actuating devices in a single build. The envisionTEC Perfactory is a DLP based Stereolithography machine (addressed as the DLP system) and has the ability to manufacture feature size in the micron range with high precision. This ability to manufacture small features with high precision is used for the manufacture of polymer micro reactors.

Using the DLP system for processing functional composites is a novel approach. The DLP system offers high resolution and accurate manufacture of parts. This ability to process functional materials will be used for developing devices for sensing and actuating applications.

In order to identify the feasibility of manufacturing composite of the DLP system, barium titanate ($BaTiO_3$) ceramic was added to the photopolymer. The composites containing up to 19 vol% $BaTiO_3$ as functional material were manufactured by the DLP system. Poling these specimens showed a maximum piezoelectric coefficient of 5 pC/N, measured at 30 MV/m and 90 °C. Measuring ferroelectric properties of these composite specimens showed a maximum remnant and saturation polarisation of ±0.041 $\mu C/cm^2$ and ±0.359 $\mu C/cm^2$, measured at electric field of 249.97 kV/cm at room temperature.

As the parts were manufactured in layers; an investigation was undertaken to identify the effect of build layer orientation on the mechanical properties. The polymer specimens for the XY (horizontal) and the Z (vertical) build direction showed strength of 39 MPa and 29 MPa, being achieved in the respective specimen.

The DLP system was also employed for developing micro fluidic devices, specifically focusing on the development of micro reactors. The polymer based micro reactor with 500 μm channels was successfully used as a bioreactor.

This work also investigates the feasibility of the DLP system for developing micro reactors and integrating them with functionally active sensing and transducing devices, manufactured in a single build. In conclusion, it was verified that it could be possible to manufacture micro reactors integrated with functional devices manufactured in a single build but the further manufacture will require more research. Based on the discussion presented in this work, few proposals are made for further continuation of this research.

ACKNOWLEDGEMENTS

I would like to express gratitude to my supervisors Dr. Chris Sutcliffe and Prof. Paul Chalker for their guidance, suggestions, encouragement and support. I am thankful to them for giving me an opportunity to pursue my degree and showing their faith and belief in me.

I acknowledge the EPSRC for supporting the project and for providing all the funding needed for this work. My appreciation also extends to all the members of this project, particularly those from the University of Bath.

I am also immensely grateful to Mr. Lawrence Bailey, Mr. Alan Tidbury, Mr. Derek Neary, Mr. Dave Atkinson, Ms. Denise Bain and Dr. Bob Murray for their support during my degree. I would like to convey my special gratefulness to all my colleagues, especially Dr. Dan Jones, Mr. Xiadong Song, and Mr. Joseph Robinson for the help provided during my write up without any hesitation. I am also indebted to Dr. Ashwin Roa for his support while writing my thesis and Dr. Xinming Wan, for his help to me with analytical measurements on my test specimens.

I would like to thank all my family members specifically my parents for their support and encouragement in good and bad times while pursuing this degree. I would like to thank all my friends for being with me when they were most needed and being a family whilst away from home.

CONTENTS

NOMENCLATURE

Symbols	Description	Units
A	Cross-section area of the duct	mm^2
C	Capacitance	F
C_d	Curing depth	µm
D	Dielectric displacement	C/m^2
D	Diameter of the duct	mm
D_h	Hydraulic diameter,	m
D_p	Penetration depth	mm
E	Electric field	V
E_c	Critical exposure	ms
$E_{c'}$	Coercive field strength	
E_i	Internal field	
E_{max}	Maximum exposure	ms
E_o	Exposure at resin surface	ms
E(t)	Time dependent electric field	
E^o	Amplitude of the electric field	
E(z)	Exposure at a depth z	µm
F	Uni-axial force	N
I	Moment of inertia	mm^4
Kn	Knudsen numbers	
L	Length of channel	mm
N_{Re}	Reynolds number	
P	Wetted perimeter	mm
P	Pressure	MPa
P	Polarisation	C/m^2
P(T)	Time dependent polarisation	ms
P_{sat}	Saturation polarisation	C/m^2
P_s	Spontaneous polarisation	C/m^2
P_r	Remnant polarisation	C/m^2
Q	Volume flow rate	m^3/s
Q	Electric charge	C
R_a	Average Roughness	µm
S(*v*)	Compliance of composite material	m^3/N
S^p_{11}	Compliance of ceramic particles	m^3/N
Tan δ	Dielectric loss	
V	Fluid velocity	m/s
Y	Modulus of elasticity	MPa

d	Spacing between the atomic planes in a crystal	µm
d	Piezoelectric constant	pC/N
d_{min}	Minimum characteristics dimension of the channels	pC/N
d_{33}	Piezoelectric coefficient	pC/N
f	Fanning's friction factor	
f'	Volume fraction of reinforcing material	
k	Stiffness	N/m
ℓ	Length of the beam	mm
n	Number of poles	
v	Density of elastic dipoles	
N	Poisson's ratio	
z	Depth of resin	µm
δ	Phase difference of the sinusoidal electric field	rad
ε	Surface roughness	µm
ε	Permittivity	F/m
ε_0	Permittivity in vacuum	F/m
ε_r	Relative permittivity	
ε'	Real part of frequency dependent dielectric constant	F/m
ε''	Imaginary part of frequency dependent dielectric constant	F/m
ε	Strain	
δ_{max}	Maximum deflection in a beam	mm
λ	Wavelength of the monochromatic rays	nm
λ	Molecular free path of the fluid	µm
θ	Angle formed by the incident ray with the diffraction	rad
µ	Dynamic viscosity	Pa.s
ω	Angular frequency of the electric field	
χ	Dielectric susceptibility	
σ	Density of fluid	kg/m^3
σ_A	Average external stress applied on composite material	MPa
σ_M	Volume averaged external stress on matrix	MPa
σ_f	Volume averaged external stress on reinforcement	MPa
σ	Stress on a crystal	MPa
σ_M	Average tensile strength	MPa

CHAPTER 1

1.0 Introduction

Current work considers manufacturing of micro reactors integrated with functionally active materials by a novel approach of using additive manufacturing (AM) techniques. The capability of AM techniques can be used to manufacture novel piezoelectric ceramics and composites for sensor and actuator applications and at the same time, integrating it with the fabrication of microfluidic devices in a single build will be a big step forward.

Scientists and engineers have been attracted to the outstanding properties of dielectric materials; these materials are extensively used in semiconducting devices, specifically for the fabrication of embedded capacitors for integrated electronic devices. Earlier dielectric materials were bonded with polymers, in the form of thin films as it was easy to process polymers.

With the emergence of high permittivity dielectric materials, the development of devices suitable for high frequency applications were made possible. However, materials with high dielectric properties are brittle and require high processing temperatures. The properties possessed by these materials have raised great interest in functional composites and for fabricating mechanically robust components possessing high piezoelectric and ferroelectric properties. Polymers were the most preferred choice for the development of functional composites.

The production of chemical reactors often requires a multitude of manufacturing operations. Typically, the reactors are large and may operate with hazardous materials. Designers therefore use traditional formative manufacturing routes such as rolling, forming and extrusion combined with subtractive processes such as cutting, grinding, machining, milling etc. to produce a working reactor. Micro reactors however are smaller in size and operate at small volume. They are therefore for hazardous chemical reactions. In case of failure, the loss of chemical

is relatively insignificant resulting in a decrease in risk. Compared to conventional reactors, high heat and mass transfer rates can also be achieved with close control of process variables, delivering higher efficiency and improved yield, particularly if these devices are arranged in parallel. This means that they can be effectively used for studying new chemical reactions with highly reactive and hazardous reagents. For the large-scale production of chemicals, micro reactors can be concatenated to form a continuous production unit; enabling scale-up to full production is simple and safe.

Additive manufacturing (AM) has revolutionised some aspects of manufacturing, particularly prototyping and very low production runs of non-critical components. AM is a collection of techniques, following common methodology for manufacturing of shaped components. A Computer Aided Design (CAD) model representing the physical component is converted into a standard Stereolithography (STL) file format that is utilised by manufacturer of all rapid prototyping (RP) / rapid manufacturing (RM) machines. This file is analysed and sliced into sections. Each slice represents a layer, which is repeatedly deposited to obtain finished product by an automatic machine. This is represented schematically in Figure 1:

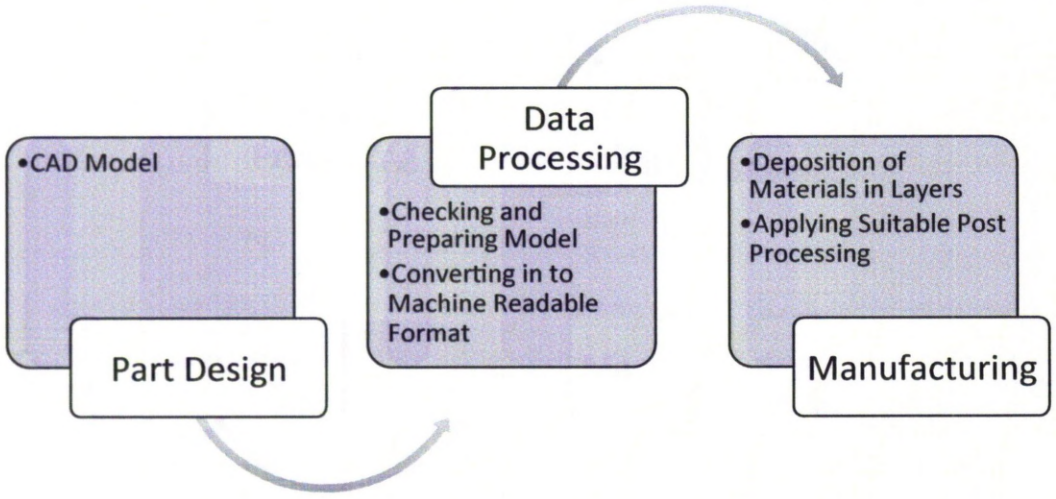

Figure 1: The Basic Sequence for Additive Manufacturing.

AM has been extensively used in a number of fields including highly complex tooling, advanced casting, reverse engineering using digital scanning and to improve the part quality. Components manufactured from wax, metals, polymers, or a combination of these materials is made possible using AM techniques [1].

There are now a few sectors that utilise AM techniques to contribute to the development of new and more sophisticated and customisable products. Examples of these include Medical (e.g. surgical or dental implants & prostheses)[2], Jewellery [3], Consumer Goods (e.g. personalised footwear, especially for athletes)[4], Automotive [5] and Aeronautical [6]. In addition, contribution by AM techniques for humanitarian efforts performing reconstructive surgeries is well documented [7].

AM of chemical micro reactors may be an alternative process capable of delivering high product quality, consistency and repeatability of highly complex designs. Manufacturing using functional materials may be used for sensing and actuation applications. Integration of these sensors and actuators with a micro reactor will result in a smart micro reactor. However, exploring the literature suggests AM techniques can result in tangible micro reactors containing functional devices, although this has not yet been achieved.

The capability of AM techniques to manufacture 3D components building the part in a layer-wise manner without using molds, dies, or hard tooling can be used to manufacture novel piezoelectric ceramics and composites for sensor and actuator applications and at the same time, offering high resolution and high precision by AM techniques for fabrication of microfluidic devices.

This work, aims therefore to identify the suitability of AM techniques, specifically digital light Processing (DLP) based Stereolithography for the fabrication of micro reactors. The research further continues to explore a novel approach to identify the feasibility of AM for the development of functional composites.

In the current work, various aspects of manufacturing of functional composites along with characterising their piezoelectric and ferroelectric properties has been explored to develop sensing and actuating devices. It continues further to identify the suitability of AM techniques for fabrication of polymer micro reactors.

Chapter two contains a literature review for the current research work presenting the theory of dielectric, piezoelectricity and ferroelectricity along with discussion of the various manufacturing routes. It further continues to review the mechanical and electric behaviour of the composite materials. An overview of micro fluidic devices and micro electromechanical systems followed by AM techniques are also presented.

Chapter three considers the material aspects of polymers and ceramic material used here. AM techniques used for the specimen fabrication is discussed in detail. The properties of barium titanate and poly methyl methacrylate (PMMA) along with all the apparatus and techniques used in the investigation are also presented.

Chapter four presents the various reactor designs and the methods adopted to improve surface finish of micro reactors. The experimental setup for cell culture applications is discussed. In order to reduce the effect of surface roughness that may cause change in fluid behaviour, specimens varying layer thicknesses were manufactured and examined. An adaptive slicing algorithm was developed with the purpose of reducing the surface roughness and improving quality of the built components. Results from the application of this algorithm are also described.

Chapter five discusses the development of functional composites by DLP. Here, a conventional route was initially used to manufacture the composites identifying the challenges that may occur during the development of active material by DLP. Subsequently, the ceramic – polymer composites with various loads were developed on the DLP system by identifying build parameters as adding piezoelectric ceramics to standard R5 polymer was found to influence standard parameters. The material developed by DLP was examined for the influence of the build layer orientation on the mechanical properties and the build resolution for

the polymer alone and ceramic – polymer composite specimens. These composites developed by DLP were also examined for functional activation. The composite material was poled and piezoelectric coefficient d_{33} was measured for different values of temperature and electric fields. Ferroelectric properties and change in capacitance of composites as a function of frequency is also reported.

Finally, Chapter six details the outcome of this effort and proposes future work.

CHAPTER 2

2.0 Background

The current research aims to manufacture of micro reactor containing functional materials by using novel route of additive manufacturing. In order to fulfil this aim, a literature survey was undertaken and presented in various sections outlining various disciplines such as the theory of dielectrics, methods of polarisation, processing routes, mechanical and electrical properties of the functional composites, specifically focusing on the barium titanate ceramic. It further continues to discuss the micro fluidic device and micro electromechanical systems (MEMS), followed by a background on AM techniques.

2.1 Dielectrics

Dielectrically active materials are extensively used in the production of non-volatile memory and micro electromechanical systems (MEMS). They are poor conductors of electricity, but posses an efficient electrostatic field. The dielectric material is usually described in terms of dielectric strength, which is measured by an uncontrolled current flowing through the material, when a field is applied. Earlier design of capacitor was using thin films of low permittivity dielectric material impregnated with papers and polymers. Although performance of dielectric materials has improved, there are still many challenges associated with them typically polarisation fatigue, ageing, electrical and frequency dependent properties.

2.1.1 Properties of Dielectrics

The capacitance of parallel plate capacitors, consisting of two parallel plates separated by a fixed distance is given by:

$$C = {}^{\varepsilon A}/_{d} \tag{2.1}$$

Where A is the area of the plates, d is the distance between the plates and ε is the permittivity of the material between the plates. The permittivity ε is the product of relative permittivity ε_r (or dielectric constant K) and absolute permittivity ε_0. Hence, the permittivity of a material can be expressed as [11]:

$$\varepsilon = \varepsilon_r \varepsilon_0 \qquad (2.2)$$

The permittivity of a vacuum, usually denoted as ε_0 is given as:

$$\varepsilon_0 = 8.85\times10^{-12} \text{ farads / metre} \quad \text{or} \quad \varepsilon_0 = \frac{1}{36\pi}\times10^{-9} \text{ m.k.s. units} \qquad (2.3)$$

The charge is stored in the capacitor or a dielectric and has a real (in phase) component ε′ and an imaginary (out of phase) component ε″ caused by resistive leakage or dielectric absorption. The dielectric constant is expressed as:

$$\varepsilon_r = \varepsilon' + j\varepsilon'' \qquad (2.4)$$

The charge stored in the capacitor is converted to heat and is generally expressed as D, the dissipation factor or dielectric loss tan δ, expressed as the ratio of imaginary phase ε″ to the real phase components ε′.

The permittivity or dielectric constant is an important material property. It is independent of field strength, but strongly dependent on the frequency of the alternating electric field, temperature, density, pressure and the chemical composition of the material.

The dielectric loss is generally considered to be a factor indicating the quality of capacitance devices. Although the acceptable dielectric factor is based on a particular dielectric material and its application, high dielectric loss is usually undesirable in most applications due to generation of heat. The high dissipation however can be used as a suppression mechanism for absorption of high frequency energy in combination with high resistivity [12].

2.1.2 Piezoelectricity

Pierre and Jacques Curie discovered piezoelectricity in 1880 [13]. "Piezo" from the Greek word meaning pressure and as the name suggests, piezoelectricity is the ability of certain crystalline materials to develop electric polarisation in proportion to an applied mechanical stress. Piezoelectric materials can be ceramics, liquid crystals or polymers. The external mechanical stress applied to these materials causes the development of internal dielectric displacement. The internal dielectric displacement manifests itself either as surface electric charge of opposite sign or an internal electric polarisation. Lipmann's theory later predicted the converse effect of piezoelectricity by the application of thermodynamics [14].

The Piezoelectric effect is derived from the symmetry of the crystal. Crystals can be categorised into 32 classes based on their geometric nature [13]. If the class of crystals is symmetric with respect to a point, it is centrosymmetrical. 11 crystal classes are centrosymmetrical and cannot be polarised. The remaining are non-centrosymmetric, but only 20 exhibit piezoelectric behaviour. 10 of this non-centrosymmetrical class have polar axes even if unstrained; hence, they exhibit a spontaneous dipole or polarity. Since these are already piezoelectric, they do not need poling, [13]. The presence of a spontaneous electrical moment in a specific crystalline direction can be altered by the application of an external alternating current (AC) electric field. These materials are known as ferroelectric materials.

Applying mechanical stress to a piezoelectric crystal, shifts negative and positive charges within the unit cell of the crystal. This shift in positive and negative charges forms an internal dipole giving the crystal polarity. The polarity can be either permanently or temporarily imparted by applying an external direct current (DC) electric field in a process known as "poling" [15].

The dipolar arrangement in the piezoelectric material may be oriented in such a way that they collectively compensate the net dipole moment. The application of pressure along one of the directions results the formation of aligned dipole. The

net dipole will however remain unchanged or zero if uniform pressure is applied on all the surfaces of the crystal.

Polycrystalline materials may have electrical dipoles arranged in random orientations so that the net dipole of the material is zero. The application of an external stress σ to the material aligns the dipoles so that they are parallel to the strain, shown in Figure 2. If *"n"* is the number of poles per unit volume of dipoles, the equivalent strain S and polarisation P can be given as [16]:

$$S = nv \tag{2.5}$$

$$P = np \tag{2.6}$$

Where p is the density of electric dipoles and v is the density of elastic dipoles.

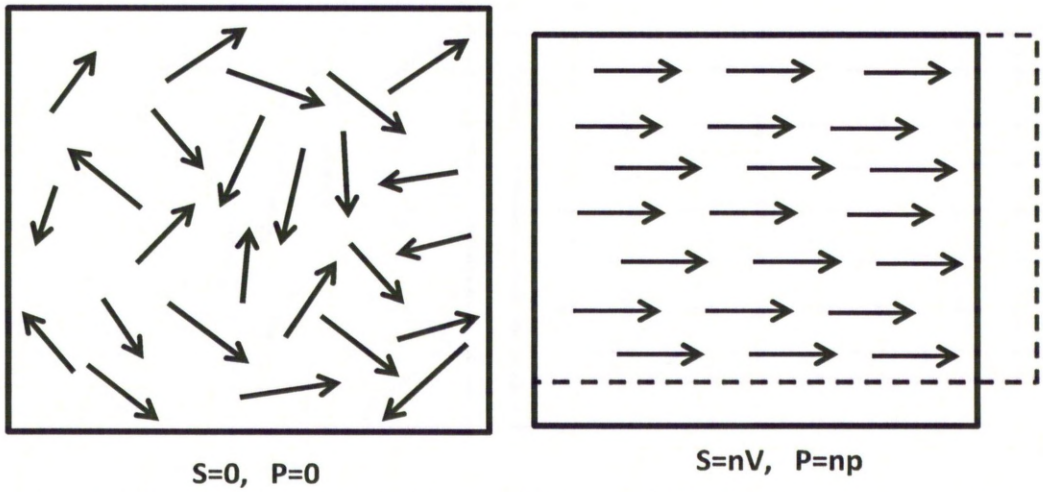

Figure 2: Orientation of Electrical Dipoles (a) Pre and (b) Post-Poling or Deformation

If the positively and negatively charged particles in a material are symmetric to the central axis, the net charge will be zero. However, an exposure to an external electric field E, an internal field E_i is induced in every particle and is proportional to the external electrical field. In the case of conductors, the net dipoles remain at equilibrium due to displacement of particles where as for insulators; small displacement of electrons relative to the nuclei induces a shift in positively and negatively charged particles. This displacement is proportional to the external

electrical field. However, the electrons in insulators remains bound to the nuclei hence limiting their displacement.

2.1.3 Polarisation

Applying an electric field on the piezoelectric material leads to a dielectric displacement of positive and negative charges in an atom, ion or molecule, resulting in polarisation. The dielectric displacement can therefore be expressed in terms of polarisation as [16]:

$$D = \varepsilon_0 \boldsymbol{E} + P \qquad (2.7)$$

or in terms of dielectric material as, $D = \varepsilon' \varepsilon_0 \mathbf{E} + P$. Rearranging Equation 2.7 in terms of P gives:

$$P = \varepsilon_0(\varepsilon' - 1)\boldsymbol{E} \qquad (2.8)$$

Polarisation is therefore linearly proportional to the applied DC electrical field [15]

$$P = \chi \varepsilon_0 \boldsymbol{E} \qquad (2.9)$$

where χ is called dielectric susceptibility, which is dependent on the temperature, pressure and composition of dielectric material, which can derive [17]:

$$D = E + 4\pi P \qquad (2.10.a)$$

and therefore, $$D = (1 + 4\pi\chi)E \qquad (2.10.b)$$

giving $$D = \varepsilon E \qquad (2.10.c)$$

At high field intensities, the above proportionality dependence is not valid [17]. However, this can be corrected by the addition of E^3 to Equation 2.9.

$$\mathrm{P} = \chi \mathrm{E} + \xi \mathrm{E}^3 \qquad \text{Or} \qquad (2.11.a)$$

$$\mathrm{P} = \chi \mathrm{E} + \xi \mathrm{E}\mathrm{E}^2 \qquad (2.11.b)$$

Where ξ is the fourth order tensor. The additional terms can be generated under intense optical irradiation and gives rise to non-linear optics.

In practice, the existence of perfect isotropy is not possible. Hence, the above expressions are valid only under ideal circumstances. For anisotropic materials, the scalar susceptibility χ in Equation 2.9 along with the permittivity ε is replaced with a tensor as [18]

$$D_x = \varepsilon_{11}E_x + \varepsilon_{12}E_y + \varepsilon_{13}E_z \quad (2.12.a)$$

$$D_y = \varepsilon_{21}E_x + \varepsilon_{22}E_y + \varepsilon_{23}E_z \quad (2.12.b)$$

$$D_z = \varepsilon_{31}E_x + \varepsilon_{32}E_y + \varepsilon_{33}E_z \quad (2.12.c)$$

Or, in terms of vectors

$$E = \begin{Bmatrix} E_1 \\ E_2 \\ E_3 \end{Bmatrix} \quad (2.13)$$

$$D = \begin{Bmatrix} D_1 \\ D_2 \\ D_3 \end{Bmatrix} \quad (2.14)$$

Figure 3 shows the coordinate axes used in Equation 2.12. Equation 2.12 can be further generalised as:

$$D_m = \varepsilon_{mn}E_n \quad (2.15)$$

Where m and n are the size of the matrix.

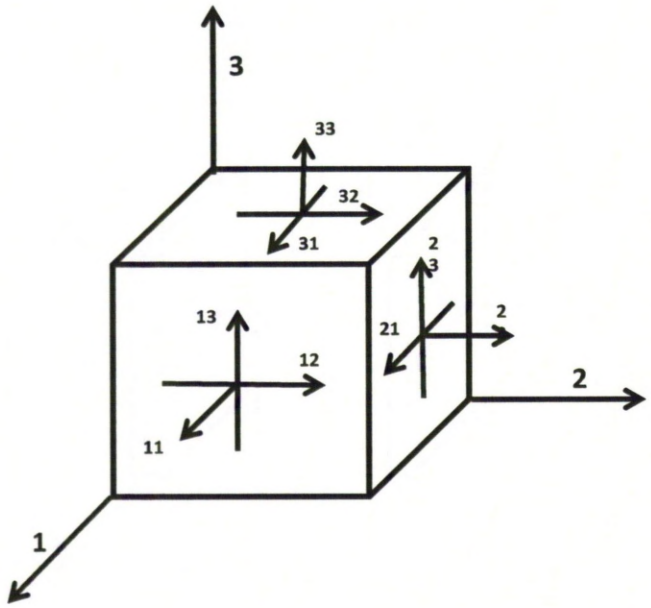

Figure 3: Piezoelectric Cube Indicating The Coordinate Axes.

Stress "σ" applied on a crystal causes proportional strain "S". The modulus of elasticity Y (Y considered in derivation to differentiate from electric Field E) can then be related as [18]:

$$S = \frac{1}{Y}\sigma \qquad (2.16.a)$$

$$S = c\sigma \qquad (2.16.b)$$

Where c is the compliance. For piezoelectric materials, in additional to this mechanical behaviour, an electric charge is created by the applied stress σ. This is known as the direct piezoelectric effect. The dielectric displacement D (Coulombs/square meter, C/m^2) produced by the applied stress σ can be written as [18]:

$$D = Q/A = \sigma d \qquad (2.17)$$

Where Q is the charge, A is the area and d is piezoelectric constant expressed in Coulombs/Newton (C/N). However, the application of an electric field E to the crystalline material produces a strain ε of proportionate magnitude. This converse piezoelectric effect is expressed as [18]:

$$D = dE \tag{2.18}$$

The strain experienced by the crystal surface can be tensile or compressive, depending on the direction of applied electric field. For a piezoelectric material, a mechanical stress σ and an electrical field E will both contribute to the charge displacement D introduced in the crystal structure. Combining Equation 2.16 and 2.18 can be combined:

$$S = \frac{\sigma}{Y} + dE \tag{2.19}$$

Equation 2.19 can be expressed in terms of compliance "c" as:

$$S = c\sigma + dE \tag{2.20}$$

Strain from Equation 2.16.b expressed, as vectors will be

$$\begin{Bmatrix} S_1 \\ S_2 \\ S_3 \\ S_4 \\ S_5 \\ S_6 \end{Bmatrix} = \begin{Bmatrix} c_{11} & c_{12} & c_{13} & c_{14} & c_{15} & c_{16} \\ c_{21} & c_{22} & c_{23} & c_{24} & c_{25} & c_{26} \\ c_{31} & c_{32} & c_{33} & c_{34} & c_{35} & c_{36} \\ c_{41} & c_{42} & c_{43} & c_{44} & c_{45} & c_{46} \\ c_{51} & c_{52} & c_{53} & c_{54} & c_{55} & c_{56} \\ c_{61} & c_{62} & c_{63} & c_{64} & c_{65} & c_{66} \end{Bmatrix} \begin{Bmatrix} \sigma_1 \\ \sigma_2 \\ \sigma_3 \\ \sigma_4 \\ \sigma_5 \\ \sigma_6 \end{Bmatrix} \tag{2.21}$$

Or $$S_{ij} = c_{ijkl}\sigma_{kl} \tag{2.22}$$

Coupling between the electrical and mechanical variables can be expressed in above expression for three-dimensional constitutive relationships. Typically, nine states of strain are related to three applied electric fields as:

$$S_{ij} = D_{ijn}E_n \tag{2.23}$$

Similarly, three terms for the electrical displacement are related to a mechanical stress through:

$$D_m = D_{mkl}\sigma_{kl} \tag{2.24}$$

Combining Equation 2.15, 2.22, 2.23 and 2.24, an equation comprising all components of a linear piezoelectric material can be written as:

$$S_{ij} = c_{ijkl}\sigma_{kl} + D_{ijn}E_n \qquad (2.25)$$

$$D_m = D_{mkl}\sigma_{kl} + \varepsilon_{mn}E_n \qquad (2.26)$$

In practice, the piezoelectric effect is obtained by inducing polarisation. Hence, the dipoles in a piezoelectric material are aligned through the application of a strong external electric field (Figure 4). The piezoelectric sample is either placed in a vacuum, submerged in an insulating fluid or in open air to ensure that the contact does not reach the edge of the sample and avoids arcing or an electrical breakdown as arcing across the specimens may permanently damage it [19]. The electrodes can be formed by evaporation, sputter coating or the application of conducting paint.

Variable surface contact at the sample may lead to local discharges, a dielectric breakdown or an inhomogeneity in the poling field and hence care must be taken while forming electrodes [20]. The probability of dielectric breakdown also increases when a high voltage is applied for a prolonged period of time or in a damp atmosphere.

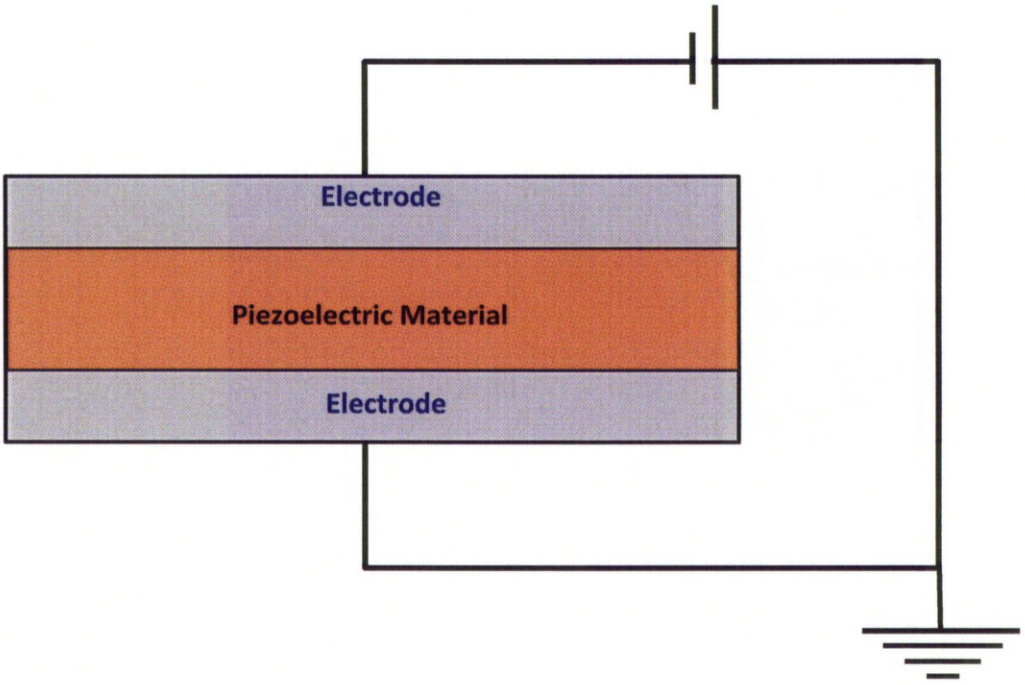

Figure 4: Schematic of Direct Electrode Poling System [20].

Figure 5 is a schematic outline of an alternative technique to direct electrode poling known as corona poling that can be used for polarisation. Here, a surface is placed on a heated plate with its lower surface connected to earth [21]. A needle or blade corona tip is suspended above the sample and 8 – 10 kV voltage is applied. The dry air at the tip is ionised due to the electric fields and ionised particles are accelerated towards the ground in a corona discharge. The ionised particles are deposited on the surface to an extent dependant on the magnitude of the field at the surface. A metallic grid is placed between corona source and the piezoelectric material. The grid is usually placed 3 - 4 mm from the material surface with voltage varying from 0.2 – 3 kV.

Corona poling is mostly used for thin films or poling large samples. However, it has a considerably more complex process for setup and is more difficult to optimise than the direct electrode method [21].

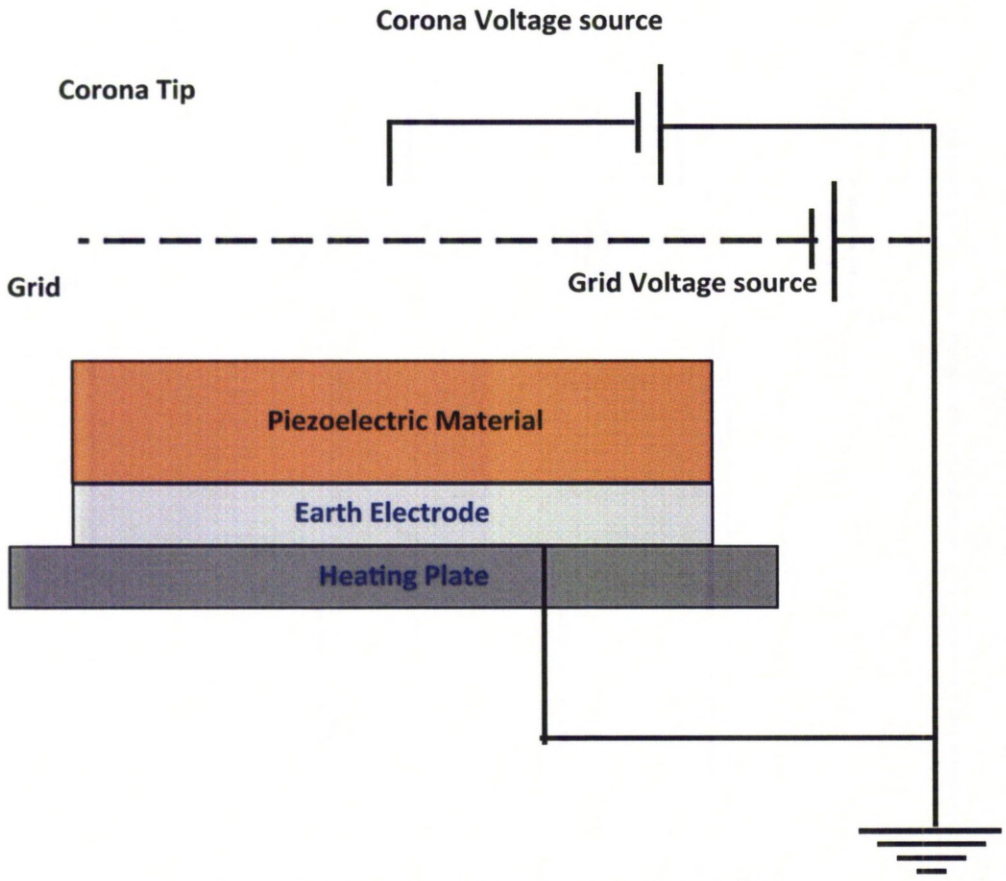

Figure 5: Schematic of Corona Poling System [21].

2.1.4 Ferroelectricity

Ten non-centrosymmetric crystals possesses spontaneous polarisation without transition to a separate phase [13]. These materials, known as ferroelectric materials are polar in nature, possessing at least two equilibrium orientations of the spontaneous polarisation vector. The spontaneous polarisation possessed by the ferroelectric material is not always aligned along the same direction. The directions of the permanent polarisation in these materials can be altered by an external electric field of sufficient intensity. This phenomenon is known as ferroelectricity.

Most ferroelectric materials undergo structural phase transition from a high temperature nonferroelectric (or paraelectric) phase to low temperature ferroelectric phase. Most of the crystals used for ferroelectric characterisation have perovskite crystal structure, such as barium titanate, lead titanate, potassium

niobates and so on [22]. In the case of barium titanate, transitions are observed from the paraelectric cubic structure to tetragonal structure. These transitions occur at Curie point, T_c. The dielectric permittivity falls above Curie point, following Curie- Weiss law. Although barium titanate undergoes a number of transitions from high temperature to low temperature, only the first transition from paraelectric to ferroelectric phase is called the Curie point. During the phase change, the crystal structure undergoes strain resulting in transition. This strain is associated with spontaneous polarisation resulting from phase transition.

During the transition at the Curie point, the crystal has equal probability of spontaneous polarisation in any direction. The direction of polarisation in a ferroelectric will be governed by the mechanical and electrical boundary conditions. Crystals with uniformly oriented polarisation are called domains. The onset of spontaneous polarisation may lead to the formation of charge at the surface. This surface charge produces an electric field, know as the depolarisation field E_d, which is oriented in the opposite direction to the spontaneous polarisation. The depolarisation field may result in a non-uniform distribution of spontaneous polarisation [23].

The dipole moment in a spontaneously polarised material is also a function of temperature [24]. On change in temperature, charges flow to and from the surface to adjust to the new value of the dielectric polarisation. This temperature dependent spontaneous polarisation of a dielectric is called the *pyro*-electric effect. The direction of the spontaneous polarisation can only be reversed by the application of a strong electrical field. In ferroelectric materials, a sub-group of pyroelectric materials, this leads to the reorientation of the domains in the direction of the field [25]. If the material is ferroelectric, a field can reverse the direction of the polarisation in the domain. This ability to switch the domain results in the occurrence of a hysteresis loop in ferroelectric materials [23].

A typical ferroelectric curve (Figure 6) follows the hysteresis loop, starting from the origin for un-poled materials. The domains align in the positive direction with increasing electric field E, leading to gradual increases in polarisation following the

path OAB on the graph. Increasing the electric field beyond point B shows a stagnant polarisation, leading to an almost flat response curve from B to C. The ferroelectric material therefore reaches saturation polarisation P_{sat} (C). The saturation polarisation does not completely collapse on removal of the electric field. If the electric field is reduced across the ceramic material, the polarisation gradually reduces following the path represented by CBD. Spontaneous polarisation P_s (OE) for ferroelectric ceramics is obtained by extrapolating the polarisation at high fields P_{sat} (CB) back to zero field along the tangent. The material possess some polarisation, even when the electric field is completely removed, this is known as remnant polarisation P_r, indicated as point D on the curve [26].

The remnant polarisation can be nullified by an application of a reverse electric field. This reversed electric field is known as the coercive field strength $E_{c'}$ and its magnitude is equivalent to the distance OF on the hysteresis curve. Increasing the reverse (-ve) electric field results in the reverse saturation to G on the curve. The direction of polarisation flips if the field is increased further to a high negative value; hence, a hysteresis loop is obtained. An increase in P_s is also observed when the temperature is decreased, crossing the Curie point and reaching saturation at low temperature. The coercive field $E_{c'}$ (OF) on the hysteresis loop is influenced by temperature, applied frequency and the waveform of the applied voltage [27].

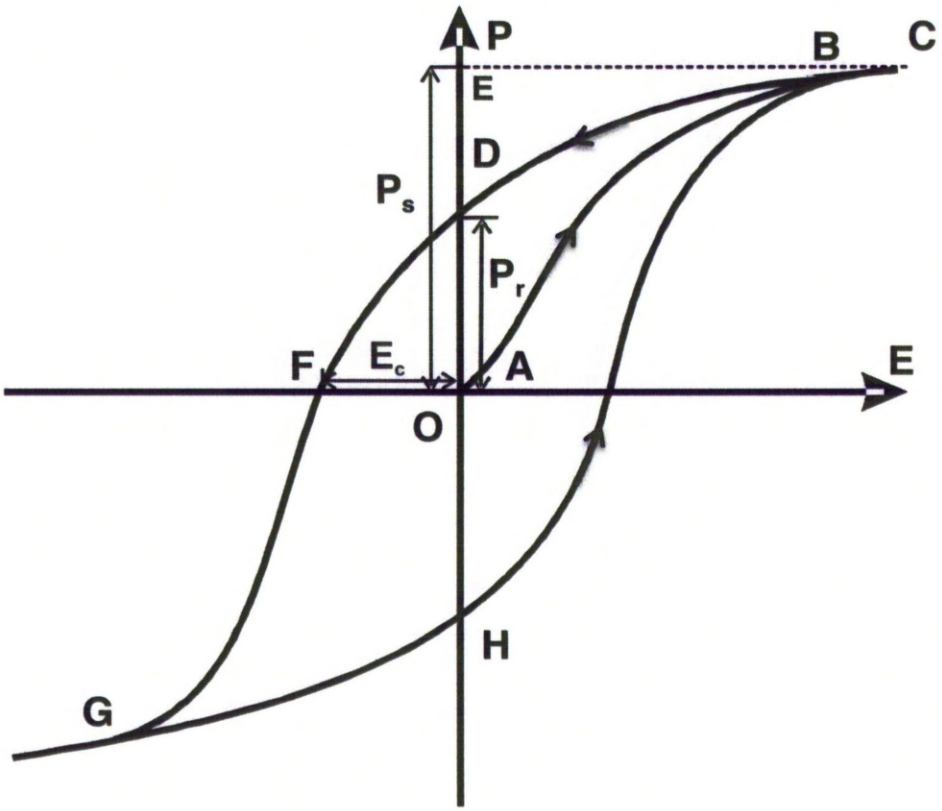

Figure 6: Typical Hysteresis Loop for Ferroelectric Materials [26].

Unlike polarisation caused by a time – independent electric field where equilibrium with an external electric field may be reached, polarisation by a periodic electric field may never reach equilibrium. If E(t) is the time dependent electric field and P(T) is the polarisation: a linear, isotropic dielectric material follows Equation 2.9, rewritten for the time dependent variable [17]:

$$\mathrm{P}(\mathrm{t}) = \chi \mathbf{E}(\mathrm{t}) \tag{2.27}$$

Similarly, Equation 2.10.c can be restated as:

$$\mathrm{D}(\mathrm{t}) = \varepsilon \mathbf{E}(\mathrm{t}) \tag{2.28}$$

If the time dependent electric field varies sinusoidally:

$$\mathbf{E}(\mathrm{t}) = \mathbf{E}^0 \cos(\omega \mathrm{t}) \tag{2.29}$$

Where E^0 is the amplitude and ω is the angular frequency of the sinusoidal variation [17]. The dielectric displacement for linear, isotropic systems lags behind the electric field by a phase difference δ, expressed as [17]:

$$D(t) = D^0 \cos(\omega t - \delta) \qquad (2.30)$$

Where D^0 is the amplitude of the sinusoidal vibration. Change in the frequency of the applied field simultaneously changes to phase difference δ, with δ becoming zero as ω approaches 0. Splitting the dielectric displacement into two sinusoidal varying parts having a phase difference of $\pi/2$:

$$D(t) = D^0 \cos\delta \cos\omega t + D^0 \sin\delta \sin\omega t \qquad (2.31) \quad \text{or}$$

$$D(t) = \varepsilon' \mathbf{E}^0 \cos\omega t + \varepsilon'' \mathbf{E}^0 \sin\omega t \qquad (2.32)$$

Where $\text{Cos}\,\delta(\omega) = \varepsilon'(\omega)\, E^0/D^0$, and $\text{Sin}\,\delta(\omega) = \varepsilon''(\omega)\, E^0/D^0$.

The above Equation 2.32 replaces the amplitude of the dielectric displacement D^0 with ε' and ε'' and phase difference δ. The magnitude and direction of the amplitude of sinusoidal vibration can be computed from Equation 2.48 as:

$$D^0 = \mathbf{E}^0 \sqrt{\varepsilon'^2 + \varepsilon''^2} \qquad \text{and} \qquad (2.33)$$

$$\tan\delta = \frac{\varepsilon''}{\varepsilon'} \qquad (2.34)$$

For a time-independent or static electric field with zero frequency, Equation 2.32 reduces to:

$$D(t) = \varepsilon'(0) E^0 \qquad (2.35)$$

ε' is termed the frequency dependent dielectric constant; $\varepsilon''(\omega)$ determines the displacement D(t) with a phase difference of $\pi/2$ with respect to E(t), and is known as the loss factor. At low frequency, $\varepsilon'(\omega)$ is equal to the static dielectric constant ε and $\varepsilon''(\omega)$ is almost zero. Increasing frequency slowly reduces $\varepsilon'(\omega)$ initially

followed by sharp decrease in $\varepsilon'(\omega)$ at higher frequency. $\varepsilon''(\omega)$ shows a peak where $\varepsilon'(\omega)$ changes (Figure 7).

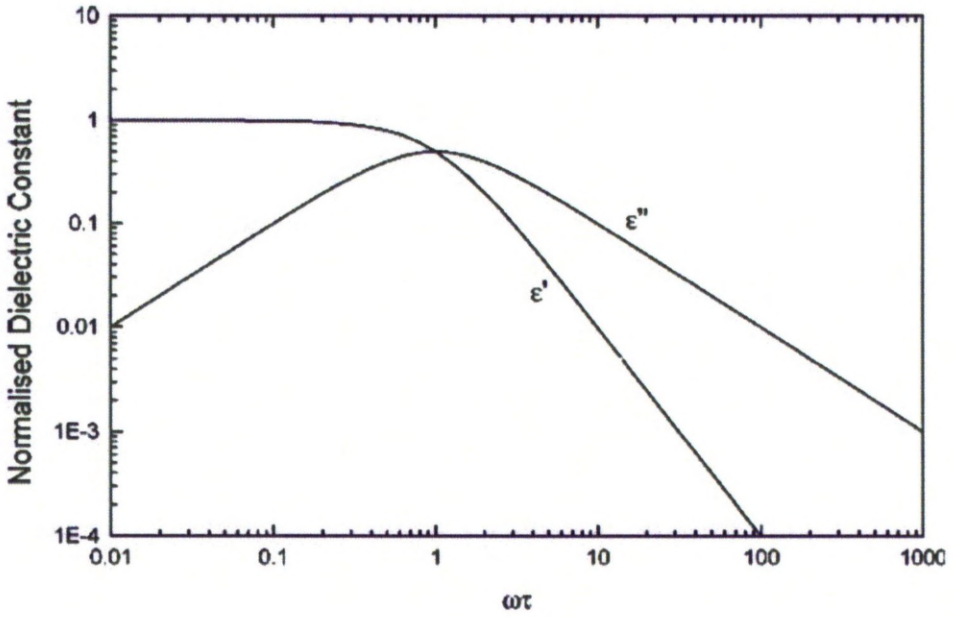

Figure 7: Typical Frequency Response Curve for Real and Complex Part of Dielectric Loss Function.

2.1.5 Mechanisms of Polarisation

Various mechanisms of polarisation are described in the literature [11]. The net polarisation in a dielectric material will be resultant of each of these mechanisms. When a frequency of the visible light falling on the dielectric material is equal to or higher than the natural frequency of the electrons, a dipole moment is formed by the displacement of the electrons in an atom. This mechanism of polarisation is known as an optical or electronic polarisation.

In case of diatomic molecules, dipole moment is formed between interacting atoms leading to a distribution of electrons between the interacting atoms. The distribution of electrons for large non-identical molecule has large dipole moment causing polarity. Under the influence of an applied field, a polar material may alter the distance between the electron distribution resulting in atomic polarisation. However, if the molecule rotates itself to align with the applied field, the polarisation is caused by orientational polarisation.

Sometimes defects in the crystals create localised accumulation of charges, when the external field is applied. The polarisation caused by this method is called interfacial polarisation.

2.1.6 Properties of Barium Titanate

Wul and Goldman discovered barium titanate ($BaTiO_3$) in 1945 [28]. It has a classic ABO_3 centrosymmetric cubic perovskite structure above 120 °C. $BaTiO_3$ can be viewed as a cube with Ba ion located in the corners of the cube, the Ti ion is located at the body centre and the oxygen at the face centre forming an octahedral around each Ti ion as shown in Figure 8a [29]. Alternately, Figure 8b shows the structure as a three-dimensional network of TiO_6 sharing the corner of an octahedron, arranged in a simple cubic pattern. In each octahedron, the oxygen ions at the apices are shared with the neighbouring octahedron and the Ti ion is located at the centre of each octahedron. The Ba ion occupies the space formed between the eight neighbouring octahedron.

The most common method to prepare $BaTiO_3$ is by the reaction of $BaCO_3$ and TiO_2, carried out at 1350 °C [30]. Barium titanate is initially formed in the air, at the grain boundary of $BaCO_3$ – TiO_2 with further reaction progressing due to diffusion. The reaction of $BaCO_3$ with TiO_2 initially forms Ba_2TiO_4 until all $BaCO_3$ is utilised. However, an incomplete mixing of $BaCO_3$ and TiO_2 results in the formation of Ba_2TiO_4 and $BaTi_3O_7$. For the reaction temperature below 1100 °C, the reaction is inhibited by formation of CO_2. It can also be prepared by other non-conventional methods like sol – gel [31], citrates and polymeric precursor methods [32].

The phase diagram of $BaTiO_3$ shows a hexagonal structure above 1460 °C, whereas at lower temperature it shows a stable cubic or equivalent structure [24][33]. The occurrence of a hexagonal phase in a ceramic crystal could be due to impurity or disequilibrium in the system at room temperature.

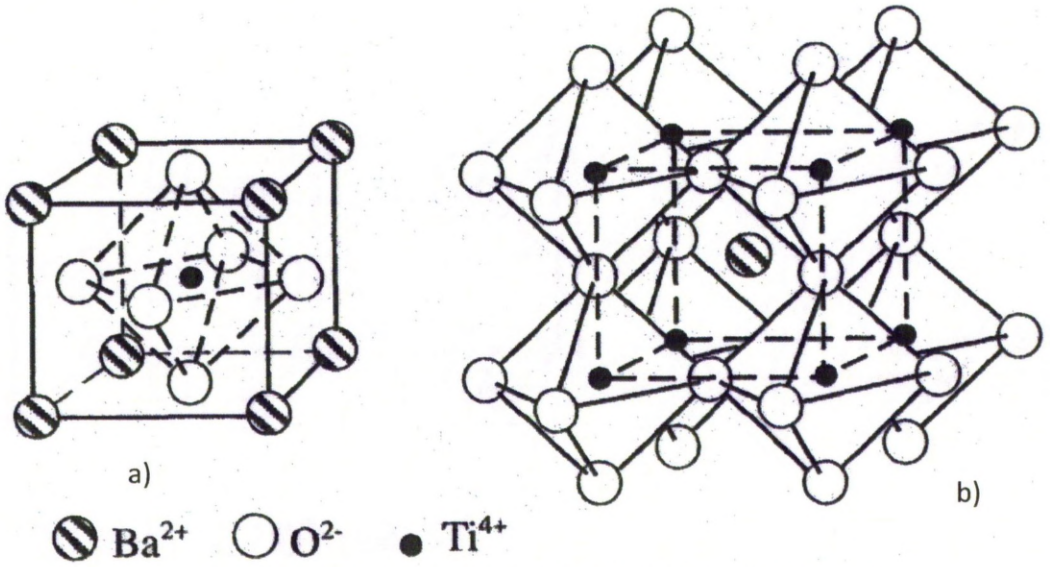

Figure 8: Simple Cubic Perovskite Structure of Barium Titanate.

Merz [34] carried out extensive investigations on the single crystal of $BaTiO_3$ showing that the dielectric constant measured along the a-axis and c-axis are similar above Curie point of 120 °C. Below the Curie temperature, the cubic structure becomes tetragonal with a similar shifts being observed at 0 °C and -80 °C where the crystal structure changes from tetragonal to orthorhombic and further to rhombohedral structure, respectively (Figure 9) [35]. During these transition temperatures, the structural distortion of the atoms in $BaTiO_3$ is highly correlated in neighbouring cells [36]. The formation of multi domains is also reported at lower transformation points, although domain size is reported to be smaller than observed for the tetragonal phase [37].

Spontaneous polarisation by applying a modified Sawyer and Tower method showed an immediate rise in polarisation at a temperature just below 120 °C which remains constant to almost 0 °C [34]. A sudden fall in polarisation was observed at 0 °C and -80 °C due to formation of multiple domains. The piezoelectric coefficient of the $BaTiO_3$ ceramic increases along with temperature until the Curie temperature degrades the piezoelectric property and destroys the poling effect. Alternately, the piezoelectric effect for amorphous (crystallinity < 0.1%) $BaTiO_3$ layer deposited at a rate of 2 – 5 mm/h through the temperature gradient has been reported to originate due to spatial distribution of the non – centrosymmetric ion [38].

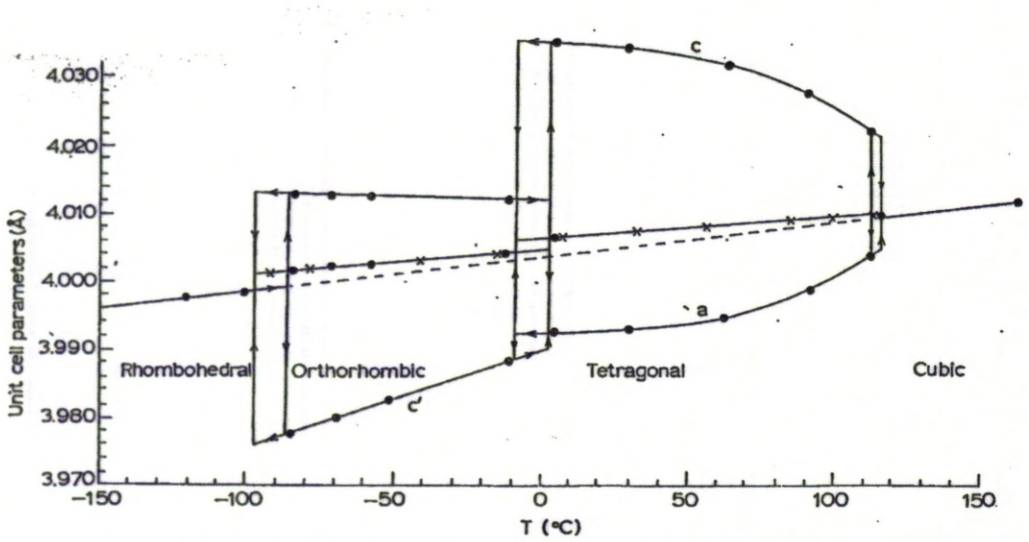

Figure 9: Temperature Dependent Cell Parameters of $BaTiO_3$ Crystals [27].

The thermal expansion coefficient for an un-poled single $BaTiO_3$ crystal is dependent on the lattice constant of each phase varying with the temperature, as given below for each phase [39]:

Lattice Structure	Thermal Expansion Coefficient
Rhombohedral	5.2×10^{-6} / °C
Orthorhombic	4.6×10^{-6} / °C
Tetragonal	6.5×10^{-6} / °C
Cubic	9.8×10^{-6} / °C

Thermal expansion coefficient and hydrostatic pressure data available in the literature verifies larger volume of orthorhombic phase than tetragonal phase [37]. As the thermal expansion coefficient is expected to increase at elevated temperatures, piezoelectric ceramics are prone to thermal shock damage while cooling.

Although a Curie temperature of 120 °C has been widely reported, changes in the Curie temperature with changing pressure applied to a piezoelectric crystal has also been reported in the literature [40]. For $BaTiO_3$ single crystals, a hydrostatic pressure of up to 2.4×10^8 N/m^2 causes a linear decrease in the curie point with a slope -5.71×10^8 °C/(N/m^2). However, application of two-dimensional pressure in

the plane perpendicular to the polar axis of the crystal results in increase of Curie point with a slope of 3×10^8 °C/(N/m^2).

The behaviour of dielectric constant and dielectric loss of unpoled $BaTiO_3$ in Figure 10 shows reducing dielectric constant with increasing frequency, whereas the dielectric loss is higher at high frequency. Both, the dielectric constant and dielectric loss increases sharply at the Curie point reducing again at temperature in excess of the Curie point, although this behaviour was not visible in a dielectric loss at low frequency [24].

$BaTiO_3$ ceramic powder with a particle size below 10 μm was studied for dielectric properties. Pressed and unsintered powder shows non-linearity in the dielectric constant due to water vapour adsorbed on the surface of the particles [37]. This non-linearity was observed for a temperature range of 30 - 170 °C. The dielectric constant linearly increases from 30 – 90 °C and fall rapidly until 120 °C. Fall in dielectric constant continues until 170 °C, rather gradually. However, the linear behaviour was observed on removal of an adsorbed surface layer. The ferroelectric effect was observed to be absent in small particles and appearing only in the larger sized particles.

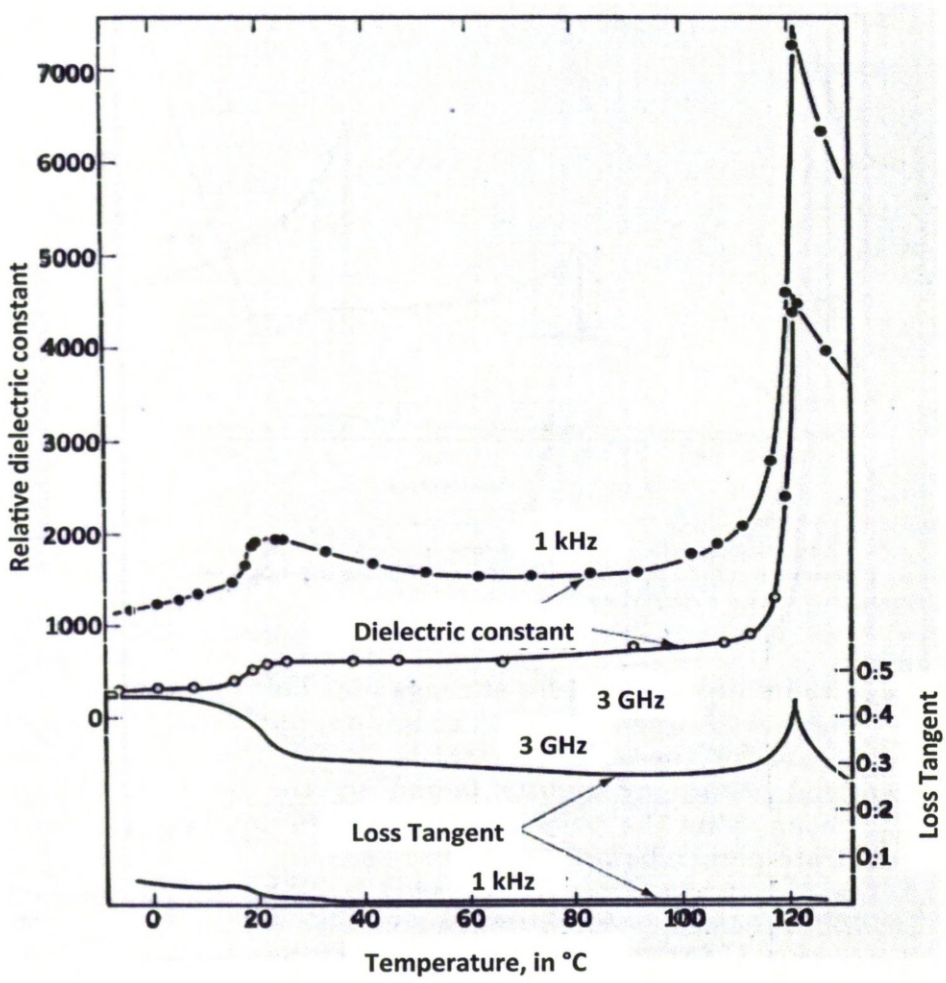

Figure 10: Relative Dielectric Constant and Loss Tangent for Unpoled Barium Titanate [24].

Figure 11 shows the tertagonility of $BaTiO_3$ for different particles sizes, measured at 25 °C. For particle sizes smaller than 5 μm, a gradual reduction in the tetragonal deformation in fine grain $BaTiO_3$ was observed. The tetragonal phase of $BaTiO_3$ may continue to exist at temperatures in excess of 500 °C [24][41-43]. A dielectric constant of 5000 measured for 0.7 μm to 1.0 μm particles of $BaTiO_3$ ceramics below the Curie point has been reported [44]. However, this dielectric constant reduces significantly due to phase transformation to tetragonal to pseudo cubic the particle sizes below 0.7 μm [45]. This transformation of cubic to nonferroelectric structure in nano-polycrystalline $BaTiO_3$ is caused by structural defects, absence of long-range cooperative interactions, possibility of depolarisation effect and elastic constrains [46].

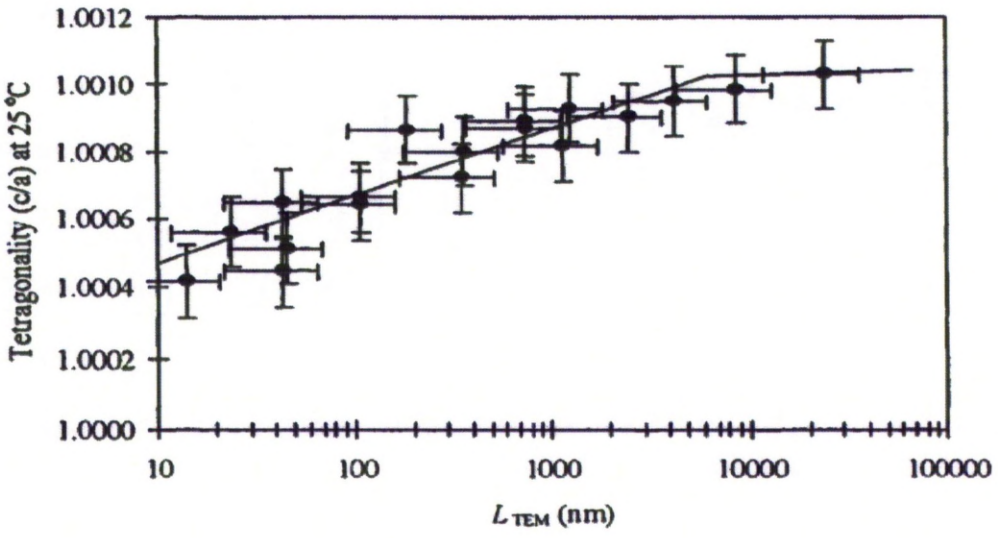

Figure 11: Plot Showing Restricted Tetragonility of $BaTiO_3$ for Different Particle Size Measured at 25 °C [41].

The dielectric constant of $BaTiO_3$ is strongly influenced by the grain size [47]. If the grain size is smaller than 2 μm, the dielectric constant was found to be greatly decreased. The thin films of $BaTiO_3$ have a cubic symmetry at room temperature and show low values of dielectric permittivity (ε = 60 - 200). This grain size effect could be a result of 90° domain walls and small size domains are formed due to internal stresses. In similar work, high temperature sintering usually forms the large grain size in $BaTiO_3$ ceramic [48]. Sintering temperature of 1050 °C and 1250 °C for the specimen preparation shows a grain size of 1.8 μm and 4.6 μm, respectively [47]. Higher piezoelectric coefficient and lower dielectric loss was observed for the higher grain size specimens, when compared to lower grain size specimens [49].

2.1.7 Processing of Functional Materials

Processing of dielectric materials depends on the nature of material. The processing techniques vary for solid such as perovskite – structured ceramics powder or liquid polymers such as vinyl difluoride (VDF) and its copolymer. Most of the work for characterisation of dielectric composites confirms the typical manufacturing route for the ceramic powder and the liquid polymer by uniform

mixing, followed by high pressure and high temperature sintering [50]. This process route is similar to that for the manufacturing of ordinary particulate composites where high-density and increased connectivity in the composites are achieved by the application of pressure in the mould.

A completely different processing route is required for the fabrication of thin film functional materials, hence vapour deposition, physical and chemical vapour deposition; and solution deposition methods are used [51]. The vapour deposition methods offer uniform deposition of the material but do not have stoichiometric control. The solution deposition allows improved stoichiometric control but is not appropriate for uniform deposition.

Sol gel methods [52-54] can also be used for the manufacture of functional composites allowing for improved control of the stoichiometry at low crystallisation temperature. This results in the controlled powder morphology and sub-micron range ceramic grains allowing the production of nano-composites.

The dielectric materials in the composite are usually combined with other material by bonding. They can be viewed as intermediate combination between two extreme materials, one giving flexibility, formability, mechanical strength and the other piezoelectric and ferroelectric properties. The properties of these composites will be based on the processing method used while manufacturing and the properties of each of the individual components.

Electronic devices working at high frequency require high mechanical properties combined with high dielectric properties and ease of processing. Use of polymers, as a binder becomes an obvious choice due to their easy processing for the formation of a high dielectric constant material. It is difficult however to achieve the unique combination of mechanical and dielectric properties as polymers exhibit low dielectric constant and electro active ceramics are brittle and require high temperature processing. This reduces the compatibility of the ceramic polymer combination for electronic applications. Processing high dielectric constant

polymer having robust mechanical properties can be used in combination with ceramics for achieving an ideal composite.

$BaTiO_3$ has excellent dielectric properties but have poor mechanical properties. They are often therefore combined with other materials to improve their mechanical properties. $BaTiO_3$ is hard and undergoes brittle failure where as polyvinyl difluoride (PVDF) and its copolymer, possess high ductility. Most of these materials are utilised in combination with other materials in the form of a functional composite by a either physical method, chemical method or a combination of both [55].

Composites including ferroelectric material such as $BaTiO_3$ in a polymer matrix form electrical stress controlled materials for alternating current (AC) applications. These composites exhibit electric field dependent permittivity characteristics. Spontaneous alignment of domains due to the application of an electrical field achieves enhanced polarisation.

In practice, ceramic – polymer composites are fabricated by mixing molten polymer with a ceramic, followed by cooling [56]. In this case, the particles are randomly arranged, but in contact with other particles, a maximum density of 0.6 is reached depending on the particle shape. There is a limit to the amount if particle that can be introduced into the polymer. An attempt to increase ceramic content in the composite will increase the porosity resulting in decreasing electric field distribution, lowering of the dielectric constant and an early dielectric breakdown.

As discussed earlier, the mechanical and electrical behaviour of functional composites are based on the physical properties and compatibility of the materials involved [57]. This, however, may not be true for electrical or magnetic properties. Composites are designed to achieve a specific desired property requiring the correct connectivity pattern and an appropriate manufacturing process capable of achieving it. These patterns are ultimately reflected in the behaviour of the composite. A two-phase (diphasic) system is used to define the connectivity in composites exhibiting multi-interfacial connectivity [58-59]. The continuity of each

phase could be in either zero, one, two or three dimensions. Composites can be described as (0-0), (0-1), (0-2), (0-3), (1-1), (1-2), (2-2) and so on. The first digit refers to the degree of freedom the active phase possess, while the second digit represents the inactive phase. Figure 12 below explains a few examples of this identification system.

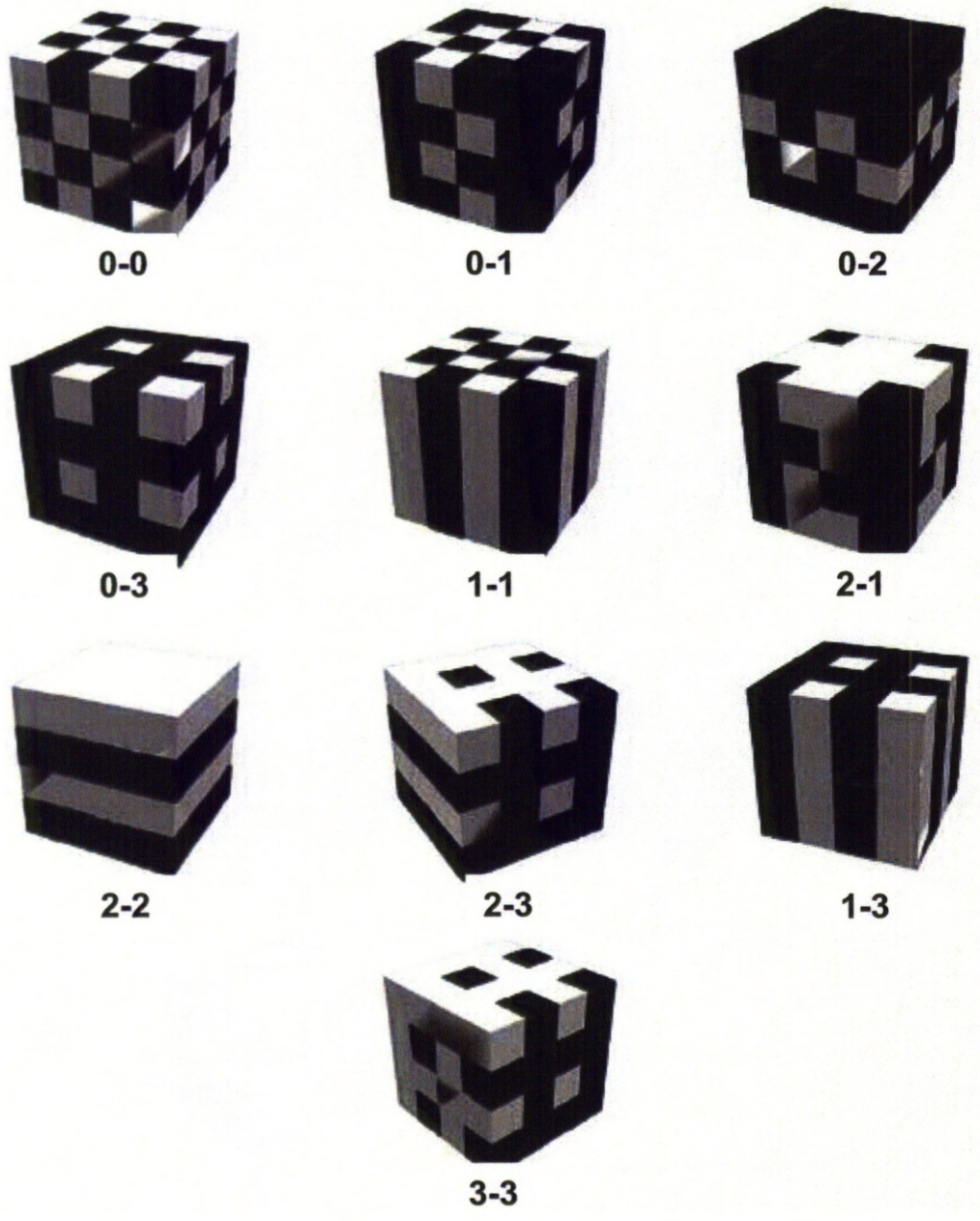

Figure 12: Classification System Explaining Connectivity Pattern for Composites [58].

Fabrication of composites containing filler particles embedded in the matrix requires a simple procedure of mixing followed by pressing and drying at the softening temperatures. These composites usually have 0-3 connectivity and often suffer from poor particle distribution in the polymer, poor adhesion of components phases and entrapped air.

2.1.8 Dielectric Behaviour of Functional Materials

Dielectric properties of composites are influenced by the connectivity of the materials used to produce them [60]. Manufacture of ceramic polymer composites requires selection of correct materials and processing methods, enabling the best possible combination of mechanical and electrical properties. Connectivity in a functional material is crucial in determining the electrical behaviour, such as the effect of frequency on resonance, the interfacial effect between the filler and the matrix, and effect of porosity [61]. Matching electrical and mechanical properties in particulate composites requires proper consideration, as it is difficult to orient a randomly distributed ceramic grain during polarisation in high resistivity, low permittivity of polymer matrix without triggering electrical breakdown.

Connectivity in a composite material mostly containing two components is represented by the two digits system [58]. The connectivity system however becomes confusing for high-density composites as the volume of the filler exceeds the volume of the matrix, therefore contradicting the definition of the filler and the matrix based on the classification system.

Based on the properties of the constituent materials, the interference volume fraction and the type of connectivity, various mathematical models are proposed for predicting the dielectric properties of composites. The models proposed for calculation of piezoelectric properties are based on parallel and series connectivity. Composites having a parallel connectivity show superior properties compared to series connectivity [62]. The ceramic particles in a composite are typically a combination of series and parallel connectivity. The analytical models for the prediction of macroscopic properties have established the connectivity in the

components is crucial for the correct functional behaviour [63-65]. The reliability of the predicted behaviour requires knowledge of structural complexities and shape of the filler material.

The complex relative permittivity, both real (ε') and imaginary (ε") parts of the dielectric constant, is an outcome of the combination of two different materials, along with internal geometry and strength of the electric field [66]. Increase in both the real and imaginary dielectric permittivity is apparent with increasing ceramic volume fraction. However, packing efficiencies in the composite limit the ultimate performance attained. Colloidal processing of ceramic particles followed by drying may improve the filling function and hence the dielectric constant.

The dielectric properties of a ceramic-epoxy composite were studied with varying loads of $BaTiO_3$ in an epoxy matrix [67]. It was showed that the level of $BaTiO_3$ in the epoxy resin influences the permittivity of the resultant functional composite. Processing high viscosity polymers to manufacture composites is difficult and usually diluted epoxy is used to increase the $BaTiO_3$ content resulting in increased permittivity. The increase in permittivity was also confirmed by Vrejoiu [68]. Here a direct deposition of 0 – 3 connectivity material was achieved by direct deposition by spin-coating $BaTiO_3$ particles dispersed in the diluted polymer on different substrates.

The dielectric properties of the $BaTiO_3$ crystal are influenced by the presence of impurities. The impurities are sometimes intentionally induced in the material, aiming to increase the dielectric properties of functional composites. Park [69] studied the dielectric properties of nickel (Ni) coated $BaTiO_3$ - polymer composite for 40 % and 50% volume loading. $BaTiO_3$ powder of about 500 nm particle size was mixed in a nickel ion-containing solution and dried on a heating plate followed by heat treatment at 900 °C. The doped $BaTiO_3$ particles were then mixed with a epoxy resin and pressure sintered to form a disk. Although the process failed to completely dope the particles, the dielectric constant measured at a frequency of 1 MHz increased significantly up to 40% volume fraction. The dielectric constant at 50% volume fraction was lower due to irregular connectivity in the polymer and the

presence of voids. Dielectric loss reduced with an increase in particle content in the composite by almost 40% when measured at a frequency of 1.0 MHz [70].

Increasing the ceramic load in the composite increases the dielectric permittivity, particularly for a composite containing larger particle sizes [50]. $BaTiO_3$ – polymer manufactured by mixing, followed by compression moulding at 130 °C were measured at 25 °C and 10^4 Hz frequency shows higher values in large particle size containing composite specimens than small particle size composites. The relative permittivity also increases with increasing the ceramic particle content. However, clear relaxation was observed for large size (1.33 μm) ceramic composites [71]. For the small size (0.19 μm) ceramic composites, a shift in the relaxation frequency was observed, attributing to the modulated domain structure.

The distribution of particles cannot be perfectly uniform in the matrix. Although isotropic particles are embedded in an isotropic matrix, the behaviour of the composites can be anisotropic. An investigation by En-Bo [72] shows that the anisotropic dielectric properties observed in the composites were dependent on the shape and orientation of the principle axes of the particle. The anisotropy can however be controlled by rotating anisotropic crystal particles in the matrix. In work carried out by Dulieu-Barton and Fulton [73] confirms that manufacturing in a controlled environment can reduce the anisotropy and can reproduce mechanical properties of the material.

Popielarz [74] studied the frequency dependence of $BaTiO_3$ composites manufactured from different polymers for a wide range of frequencies. The highest volume fraction of 45 vol% $BaTiO_3$ – polymer composites manufactured by mixing $BaTiO_3$ ceramic (avg. size - 1 μm) and polymer, followed by curing under UV light. The composites (30 vol%) containing $BaTiO_3$ - polar polymers shows a higher dielectric constant (ε') of 41 as compared to 24 for $BaTiO_3$ – non-polar polymer composite, measured up to 1 kHz frequency.

Multi-doped $BaTiO_3$ powder composites were prepared by Kuo [75] by ball milling for different time spans. The particle size was dependent on the processing time in

the ball mill, at any given process temperatures. The temperature in the ball mill ensures uniform properties for the complete batch. As expected, the piezoelectric coefficient of the composite increases with $BaTiO_3$ content. However, the processing temperature does not influence the piezoelectric constant.

According to the dielectric theory, the dielectric constant of most of the polymers measured at high frequencies reduces to the square of the polymer refractive index as a limiting value. The dielectric constant therefore measured by increasing the frequency up to 10 GHz exhibits similar values irrespective of the type of polymer in the composite [74]. It can also be interpreted that the dielectric constant of the ceramic is dominated by higher frequencies. The dielectric loss (Tan δ) for the composite with polar polymer was higher than non-polar polymer composite, showing better stability in non-polar polymer composites, for the entire range of frequencies.

Increasing frequency and volume fraction of ceramic particles increases the dielectric loss in the ceramic - polymer composites. The addition of metal particles along with the ferroelectric ceramic has been shown to yield extraordinarily high dielectric constant [76]. Measuring ferroelectric curves shows a higher remnant polarisation due to the addition of metal particles [77]. The capacitance of the composites was however independent of frequency and increased slightly with temperature. The dielectric loss decreases for high metal content for unannealed specimens.

2.1.9 Theory of Dielectric Relaxation

Under the influence of an external electric field, the dielectric properties have to overcome the mechanical resistance induced by the surrounding polymer. The difficulty of surfacing domain charges may result in reduced dielectric measurement. This is particularly evident for 0-3 composites.

Electrode deposition is generally required for measuring the dielectric behaviour of specimens. These are either physically deposited using a conductive paint or by

metal deposition techniques like nickel – chromium. Theoretically, it is assumed that the edges of the electrode lie perpendicular to the surface of the specimen and the flux generated by these electrodes is negligible and does not influence the measurements. However, in practice, absence of high permittivity medium across the specimen or the dimensions of the electrodes compared to the specimen may form a fringing field. It is therefore, desirable to have a high dielectric material, also known as High-K material for the capacitance application. Most of the electrodes form barrier layers and blocking contacts in which Schottky barriers may be significant [78-79].

The electrodes may contribute to parasitic capacitances if a good connection is not formed with the dielectric material. The effect of the metal electrodes may result in the formation of dielectric absorption. This occurs when the small current continues to flow and takes a long time to reach the constant level corresponding to the resistivity of the dielectric. A small current also flows during discharge leading to the formation of a small potential, in open circuit capacitance. The dielectric is an extension mechanism of dielectric loss occurring at low frequencies, due to low mobility of ions. The dielectric absorption may also arise from the depletion of carrier from Schottky barriers formed at the dielectric-electrode barrier [78]. The measurement of absorption is difficult in practice as it involves a very small amount of current passing through the specimen for a considerable time.

Dielectric relaxation is commonly observed in piezoelectric and ferroelectric materials. It is a lag in the dielectric constant of the material causing delay in molecular polarisation. It was observed that presence of defects within the specimen or occurring due to electrode deposition experiencing Debye relaxation in all the piezoelectric materials and occurrence of orientation polarisation forming 90° domain walls in ferroelectric materials [16]. Debye relaxation is the dielectric relaxation experience by the dipoles due to external electric field. Debye relaxation is expressed in terms of complex permittivity as a function of frequency [80].

A relaxation spectrum similar to Debye relaxation is observed in the heterogeneous systems in which the dielectrics have a difference in conductivity. This is referred

to as Maxwell – Wegner relaxation, where an external current passes through the interfaces between two different dielectric media [81-82]. The difference in conductivity leads to surface charge piles up at the interface of different media and gives rise to Debye relaxation under external alternating electric field. Unlike Debye relaxation, the Maxwell – Wegner relaxation is not an outcome of dipole relaxation but an externally caused relaxation.

In practice, the real and imaginary part of the permittivity varies with the frequency. The permittivity will be relatively stable at a frequency lower than the resonant frequency. The permittivity will also be the function by which the polarisation lags. However, it will gradually increase as the frequency approaches the resonant frequency. At a frequency greater than the natural frequency, the dipole oscillation will drop due to an exponential decay factor. At the natural frequency, the dipole experiences the harmonic oscillation, characterised by power absorption at the characteristic resonant frequency. The ferroelectric materials will experience resonant relaxation [11].

A higher dielectric constant of the composites can be achieved by either increasing the permittivity of the ceramic filler or of the polymer matrix itself. Different approaches have been examined for maximising the dielectric constant. One of the methods uses polyvinyl difluoride (PVDF) and its copolymer as matrix for the formation of composites. Apaydin [83] has successfully exploited the idea for manufacturing multilayer GPS antenna from ceramic – polymer composite [86]. Higher dielectric constants along with higher capacitance were achieved by mixing metal – ceramic – polymer materials [84].

High – energy particle irradiation of PVDF and its copolymers significantly increases the dielectric constant, due to a ferroelectric to paraelectric transformation [85]. Klein [83] studied similar transformations, however the transformation in polyvinyl difluoride – trifluoroethylene (PVDF-TrFE) was introduced by a defect formation due to copolymerisation of chlorofluoroethylene (CFE) with PVDF-TrFE [81-82].

$BaTiO_3$ having 2 μm particle size were mixed with acrylic resin to obtain ceramic – polymer composites in the range of 0 – 35 vol% and were used for the study of ferroelectric behaviour [86]. Composites were manufactured by the conventional route of mixing and degassing at a pressure of 0.0025 MPa followed by casting. The Hysteresis curves showing typical dynamic relationship of the polarisation against an electrical field strength (P-E) was obtained for varying composites. The hysteresis curves for all the specimens were symmetrical. However, the saturation polarisation and remnant polarisation increases in high loading composites. The remnant polarisation of 0.0016 C/m^2 and 0.0002 C/m^2 was observed at an electric field of 7 kV for 35 vol% and 15 vol% composites, respectively.

$BaTiO_3$ – PVDF composites with 70 wt % of $BaTiO_3$ shows saturated polarisation measured at 30 °C was close to 0.1 x 10^{-6} C/m^2. The remnant and saturation polarisation also increases with the increasing temperature, even beyond the Curie temperature of $BaTiO_3$ [55]. The saturation polarisation was not influences by the temperature and any peak in saturation polarisation due to Curie point was absent.

2.1.10 Application of Functional Materials

A piezoelectric thick film fabricated using sol-gel process combined with micromachining techniques have been successfully employed for a low temperature, ultrasonic transducer application [87-88].

Functional composites find a wide range of uses in electrical applications, namely: capacitors chiefly utilised for power filtering and power conversion [89]; reactive load compensation [90]; radio frequency systems [91] and so on. Utilisation of ceramic – polymer composites offer improved characteristics in a single physical system with higher dielectric constant, high flexibility for diverse manufacturing methods and nonetheless, at a low cost of manufacture.

The ability to fabricate dielectric material is utilised for applications such as ultrasonic transducing [92]; biomedical imaging for piezoelectric materials [93]; development of non-volatile memory devices [94] and high frequency based

electronic devices [95] for ferroelectric materials. Dielectric material with low acoustic impedance, lower electromechanical coupling factor, higher dielectric and mechanical losses may not be suitable for piezoelectric and ferroelectric based applications but can be advantageous for pyroelectric detectors [96].

An application of piezoelectric composites used for enhanced healing of bone fracture in the presence of electric field is relatively new [97]. Composite of $BaTiO_3$ and PVDF-TrFE developed with 3-0 and 3-1 connectivity were employed to generate fields for healing the bone fractures. The combination of piezoelectric ceramic and polymer was a meritorious choice as it has excellent dielectric properties, its lightweight and mechanical strength, but still highly flexible [98].

2.2 Composite Materials

This section gives an overview of the theory and classification of composites. It further discusses various mathematical models from the literature for a theoretical prediction of mechanical properties focusing on particulate composites.

2.2.1 Classification of Composite Materials

Composite materials are composed of two or more materials, combined together on a macroscopic scale. Formulation of the desired composite material is based on properties exhibited by the composite components. For example, a "reinforcement" component is added to a "matrix" component present in abundance, to achieve desired properties like enhanced strength or stiffness, density, higher or lower thermal expansion coefficient and low cost. Although, the addition of one component to another may be beneficial to some properties, it can equally impede others. To obtain a composite material with desired properties, a degree of experimentation and optimisation is usually required.

Natural materials are often excellent examples of composite structures. These materials show unique properties by recurrent use of constituent molecules at different level of hierarchy [99]. For example, bones, tendons, wood, cell membranes and soft tissue all show structural hierarchy.

Tendons should be highly elastic, yet stiff to absorb a large amount of energy without fracturing. Collagen fibrils are packed parallel into large fibres and are aligned together longitudinally between the bones and the muscle. This unique hierarchical structure of tendons is reflected in the stress-strain behaviour, which is non-linear below 1 MPa and at high stress it gradually becomes linear due to progressive strengthening of crimp [100].

In the case of wood, a high specific strength and stiffness is demonstrated along the direction parallel to the trunk. Wood is composed of a crystalline polysaccharide, cellulose in an amorphous matrix of hemicelluloses, lignin and other compounds. This remarkable mix and arrangement shows per unit weight stiffness comparable to steel [99].

Articular cartilage exhibits strength and stiffness along with an outstanding frictional, lubricating and wear resistant properties. Cartilage is a porous-permeable, fibre-reinforced composite collagen filled with fluid matrix of aggregating proteoglycans. Collagen content and collagen fibre orientation vary with the depth from the articular surface with the surface layers oriented parallel to the surface and inner layers perpendicular to the bone surface. The centre zone has orientation at nearly 45° to the surface. Such hierarchical structure of collagen – proteoglycan matrix is responsible for the fibre – reinforced properties of this tissue.

The combination of materials found in the nature have been carefully studied by engineers and often emulated in the manufacture of synthetic composites. Composite materials are usually classified by the matrix, as shown in Figure 13.

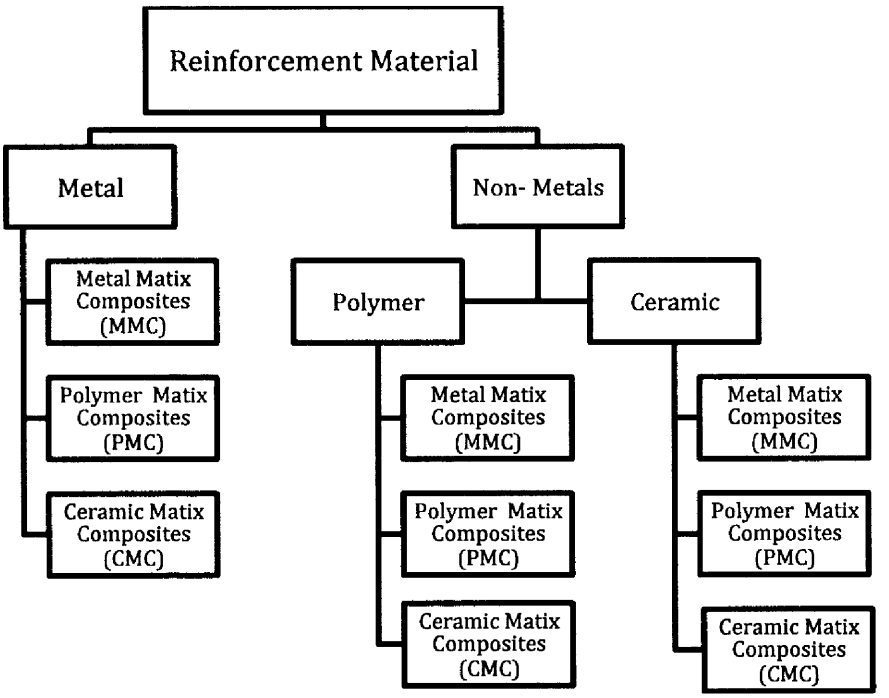

Figure 13: Classification of Composites for Matrix and Reinforcement Materials.

Man-made material composites such as Glass Reinforced Plastic (GRP) are made from glass strands in a polymeric matrix. Similarly, materials manufactured containing metal matrix and ceramic matrix are known as Metal Matrix Composites (MMC) and Ceramic Matrix Composites (CMC) respectively [100]. This suspension of one material in another and perhaps even a third component confers a number of unique properties to these complex materials. A typical 3D woven carbon fibre containing 0.15 – 0.17 volume fraction in an epoxy matrix shows a high stiffness to weight ratio [101]. Similarly, an impact resistance of 139 J/m was observed in 40 wt% glass fibre-Nylon-66 composite [102]. Biodegradable fibres (20 wt%) with thermoplastics exhibit Young's modulus of up to 140 MPa [103].

Generally, the matrix material is used as the medium for the bond formation between the reinforcing elements. Flexibility in choosing reinforcement materials with a suitable matrix offers a wide range of options.

2.2.2 *Mechanics of Composite Materials*

Designing a composite material is based on a concept of load sharing amongst its constituent components. It is assumed that the load at the surface is uniformly distributed and the stress is experienced by each component of the composite. It can be estimated by distributing the load in proportion to the volume fraction of each component. It follows that [100]:

$$\sigma_A = (1 - f')(\sigma_M) + (f')(\sigma_f) \qquad (2.36)$$

Where σ_A, σ_M and $\sigma_{f'}$ are average external stress applied on the composite material, volume averaged matrix and filler stresses, respectively, f′ is the volume fraction of reinforcing material in the composite on a plane normal to the direction of load. As long as the applied stresses are within the elastic limit of the components and that a strong bonding exists between the matrix and the reinforcement, the proportion of load borne by each component will be a function of its volume fraction.

Constituent materials for the fabrication of a composite should be compatible for strong interfacial bonding. Materials such as aramid fibre, natural fibres or modern synthetic fibres are combined with polymers, metals and ceramics [104]. Both material and its physical form play a critical role in deciding mechanical properties and the fracture behaviour of the final material.

Composites usually have ideally arranged regular or random packing. A regular pattern is usually either a square pattern or a hexagonal pattern observed in the cross section. The volume fraction of the filler, f′ is give as [100]:

- For a square pattern:

$$f' = \frac{\pi}{4}\left(\frac{r}{R}\right)^2 \qquad (2.37)$$

- For a hexagonal pattern:

$$f' = \frac{\pi}{2\sqrt{3}}\left(\frac{r}{R}\right)^2 \qquad (2.38)$$

Figure 14 shows a schematic arrangement for hexagonal and square packing where 2R is the centre – to – centre distance between fillers. The volume fraction of the composite will maximise if 2R is equal to the sum of radius of two fibres i.e. 2R = 2r. Maximum volume fraction f' of 0.785 and 0.907 can be theoretically achieved for a square and hexagonal arrangement, respectively [100].

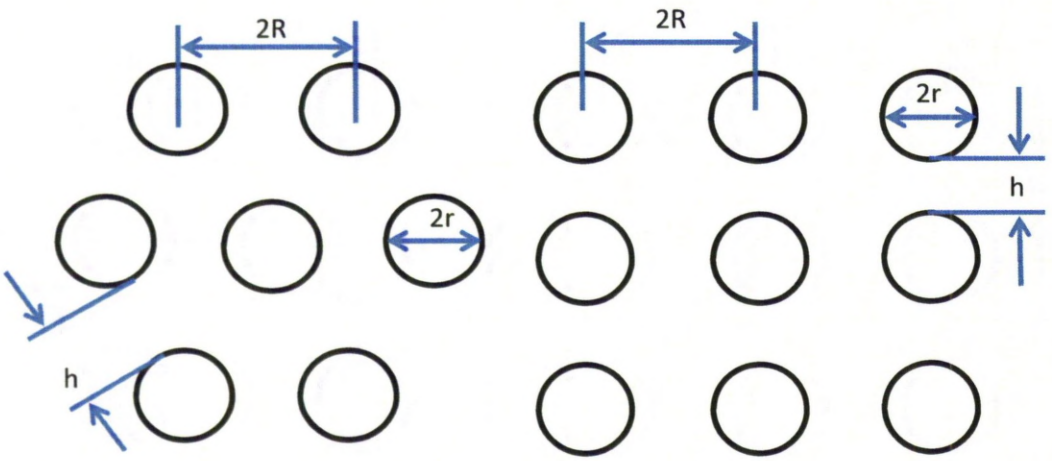

Figure 14: Schematic Arrangement of Hexagonal and Square Packing of Fibres in Matrix.

Applying a uni-directionally tensile load to each component of the composite will experience similar strain, provided the interfacial bonding is strong enough to avoid localised sliding. For the equal strain condition [105]:

$$\varepsilon_1 = \varepsilon_{f'} = \frac{\sigma_{f'}}{Y_{f'}} = \varepsilon_m = \frac{\sigma_m}{Y_m} \qquad (2.39)$$

Where ε_1, $\varepsilon_{f'}$ and ε_m is overall strain in the composite, strain in the filler and strain in the matrix components, respectively. As the load is redistributed, the stress experienced by the composite material is given by:

$$\sigma = (1 - f')\sigma_m + f'\sigma_{f'} \qquad (2.40)$$

Equation 2.40 is based on "the rule of mixtures". Since all the components in a composite material are equally strained, Equation 2.40 can be rearranged to equate the modulus of elasticity of a composite, Y [105]:

$$Y = (1 - f')Y_m + f'Y_{f'} \quad (2.41)$$

Where Y_m and $Y_{f'}$ are the modulus of elasticity for the matrix and reinforcement material, respectively. The equations above are valid for a fibre composite subject to unidirectional alignment of all the fibres.

In the transverse direction (as shown in Figure 15), the stress is applied to both – the filler and the matrix. The strain in the filler and matrix is highly complex and non-uniform. Generally, the strain in the matrix is relatively high and reduces towards the interfacial region. The strain in the filler and the matrix can be found from stresses [105]:

$$\epsilon_{f'} = \frac{\sigma_t}{Y_{f'}} \quad (2.42)$$

$$\epsilon_m = \frac{\sigma_t}{Y_m} \quad (2.43)$$

Where σ_t is transverse stress. The resultant deformation along the transverse direction will be a cumulative deformation for each component. In terms of volume fraction of fibre f', modulus of elasticity Y_t for the component can be expressed as [105]:

$$Y_t = \frac{Y_{f'}Y_m}{V_m Y_{f'} + V_{f'} E_m} \quad (2.44)$$

This behaviour is more specific to particulate composites.

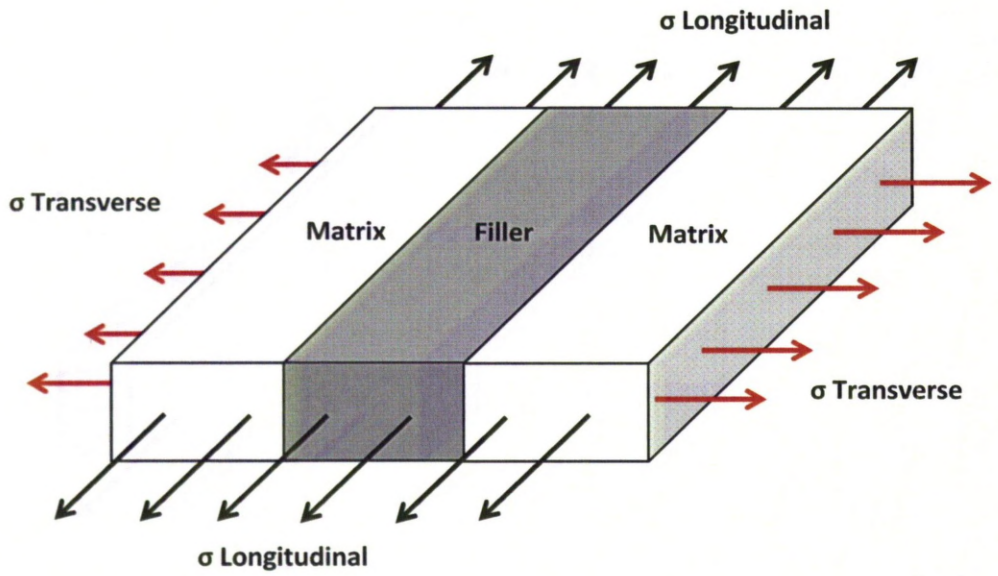

Figure 15: Representation of Composite Volumes with Longitudinal and Transversal Stress.

2.2.3 Theoretical Models for Composite Behaviour

In the case of particulate composites, an inclusion of one material is suspended randomly in the other. The particles and / or the matrix can be either metallic or non-metallic. Based on wettability, particle loading, particle size interfacial bonding, etc.; the behaviour of particulate composites varies [106-107]. The interfacial bonding between constituent materials reduces interfacial shear, resulting in the transfer of stress across the complete cross section of the composite.

Size and shape of the filler material and compatibility with the matrix material determines the physical and mechanical behaviour of the composite. In theory, two approaches explain the tensile strength of the material filled with varying solid particle loads. According to one approach, stress concentration around the particles in the composite material leads to the failure as the composite strength decreases with increased loading of the particles [108]. The other approach explains the occurrence of failure in the composite due to a decreased cross sectional area in the load bearing polymeric matrix.

Eshelby proposed a theoretical model for predicting the behaviour of a composite [109]. The model considers a long fibre with an ellipsoidal cross section, aligned uniformly in an infinite matrix experiencing uniform stress. The intensity of the stress is uniform across the cross section if the stiffness of both materials is similar. Hence, the composite material will strain uniformly. However, if the stiffness of the components differs significantly, the stress in the components will be different resulting in a non-uniform strain.

A model proposed by Mori and Tanaka includes interaction between the filler and matrix by including the volume fraction of each component [110]. The model assumes a uniform distribution of the filler in the matrix and suggested the average strain will represent overall strain experienced by the composite. They further explained that the stress is uniformly distributed in the matrix, where the stress in the filler material locally fluctuates leading to an anisotropic behaviour [111].

Hill [112] developed several theories including elastic behaviour, inelastic behaviour, and the "self consistent" methods for predicting overall modulus of the composite based on filler materials of circular cross section and the volume fraction of the constituent components. The model uses the bounding approach proposed by Voigt and Reuss for upper and lower bounding limits [113-114]. However these are influenced by an individual component behaviour. Eshelby's method for composite materials was additionally modified producing a "self consistent" model for fibre and particulate composites [115]. For materials having a large variation in stiffness, the model fails to provide accurate prediction of the behaviour of the composites, particularly at high volume fractions of the filler material.

Hashin and Shtrikman [116] developed an alternative principle for heterogeneous composites, verifying the work done by Brown [117] stating that the properties of composites are not completely defined by the statistics of the constituent components. Similar to models discussed earlier, the Hashin and Shtrikman [118] method assumes isotropic behaviour with varying volume fractions of filler material. The filler particles are considered to be concentric spherical shells with filler uniformly surrounded by a matrix. Hashin and Shtrikman implemented upper

and lower bounds for effective poly-crystal moduli using variational principles. They also attempted generalisation of variational principles for an anisotropic and non-homogeneous elastic composites. Although the model considers transformation from an isotropic, homogeneous composite materials to anisotropic and non-homogeneous composites, it failed to be verify by experimental validation.

The mechanical and volumetric behaviour of these particulate composites are influenced by the interfacial bonding of the filler and matrix [119]. Vratsanos [120] considered an alternative approach, for developing a mathematical method for predicting de-bonding of a particle by use of an energy balance. Behaviour predicted by the model was valid for higher volume fractions. The behavioural change occurring in the composite material under stress shows a non-linear strain caused by de-bonding. The model assumed homogeneous and uniform properties, along with no loss of energy to dissipation [119, 121-122].

The Equivalent Box Model (EBM) [115] considered for prediction of the modulus and the strength of polymer blends uses a homogeneous material properties. By considering weak adhesion and strong adhesion between the constituents, the model obtains lower and upper bounds, respectively. Three perpendicular plate (3PP) Cubic Orthogonal Skeleton and Cross Orthogonal Skeleton models were proposed by Kolarik [123]. They ignored adhesion between two materials forming a composite and it presumes the adhesion is sufficient to transmit stress across the interfacial area in the linear stress-strain region. The method is relatively simple and composite behaviour is related to only the same phase structure and considers the modulus or yield strength along with the volume fraction of components. It considers the calculation of upper bound limit for binary components using rule of mix, mentioned in Equation 2.36. For lower bound, however, the model considers a binary system of two immiscible materials where the volume fraction of each constituent material is regarded in parallel or in series relative to the acting force. This can be mathematically presented as:

$$Y_b = \left(Y_1 f_{1p} + Y_2 f_{2p}\right) + \left(f_s^2 / \left[\frac{f_{1s}}{Y_1} + \frac{f_{2s}}{Y_2}\right]\right) \qquad (2.45)$$

where Y is the modulus of elasticity, f is the volume fraction of constituent materials described by subscripts 1 and 2. The volume fraction of the material in series or in parallel with the acting force is described as subscript s and p, respectively.

The models discussed above represents a few from the plethora of research work available on modelling composites, they represent a fair view of available methods for predicting composite behaviour. None of these models are precise and only offer an approximation of the experimental performance.

2.2.4 Behaviour of Composite Materials

Addition of rigid particles to the polymer reduces the thermal expansion coefficient but increases the stiffness of the material, creep resistance and the fracture toughness [124-125]. It might be expected that increasing the total filler loading in a composite will exhibit higher tensile strength values. It has been shown however that the total filler content in a high-density composite does not correlate to the theoretical behaviour [126].

Penn [127] also confirmed that the mechanical properties of particulate composites are influenced by the size; shape and the particle size distribution, rather than the loading of particles. The reduction in Young's modulus reported for bigger particles composite, for any given volume fraction is attributed to the "skin" effect where surface skin is depleted from the particle.

The properties of particulate composites, determined in various investigations shows that the mechanical strength of the composites increases by increasing the particle content up to a critical limit after which it deteriorates. Work by Landon [126] confirms that the tensile strength measured for composites containing different particle diameters reduces with increasing volume fraction. The tensile strength observed for composites containing 21 μm solid spheres decreases linearly with volume fraction of solid, whereas the tensile strength for the composites fabricated from 216 μm solid spherical particles showed a non-linear relation to

particle volume fraction. The tensile strength for the small spheres was closer to the upper bound limit of the theoretical prediction, where as the lower bound limit was approached with the larger particles.

The polymer matrix particulate composites were typically observed for brittle fracture occurring at the polymer – particle interfaces [105]. The fracture energy of the particulate composite material increased with increasing the particle size, for any given volume fraction [127]. However, the characteristics behaviour for any particle size observed could not be generalised with varying volume fraction of particles.

Fabrication of alumina ceramic by Laser Engineered Net Shaping (LENS) is a laser based AM technique. This technique was used for the fabrication of fully dense alumina structures [128]. It was observed that the compressive strength of 123 MPa for as – fabricated specimens marginally increase to 159 MPa when heat-treated at 1600 °C. The mechanical strength of these specimens was influenced by the build orientation. The compressive strength of as – fabricated specimens observed for build directions perpendicular to test direct was 86% higher than that parallel to test direction. The strength was higher for heat-treated specimens, resulting in a marginal influence of build orientation on mechanical strength. Heat-treating specimens of 10 – 25 mm in size also showed increased grain size from 6 – 200 μm and hardness from 1550 – 1700 Hv.

2.3 Micro Fluidic Devices and Micro Electromechanical Systems (MEMS)

Nearly three decades ago, a miniature gas chromatographic analyser was fabricated on silicon [129]. It was a 'first' for both, miniaturisation of devices on silicon chips and the integration of functional devices. The concept of a miniaturised total-analysis system, known as micro Total-Analysis Systems (μTAS) [130-131] or Lab-On Chip (LOC) [132] followed. Although, this pioneering development failed to get attention, it was seen later as a sea-change for the future of micro devices.

The concept of μTAS embodies multiple processes aiming at the separation and detection of chemicals [133]. It consists of several discrete steps, starting with the specification of the μTAS, considering the reagents involved, chemical reaction kinetics, reaction temperature, single or multiple uses, etc. It also requires the design and development of a suitable manufacturing procedure that integrates all analysis and sensing processes. This requires input from chemical reaction engineering, fluid dynamics, thermodynamics and manufacturing to ensure an efficient performance of the whole μTAS. Computer simulation of micro fluidic devices can significantly shorten the design, manufacturing and testing process and is now common in the design and development of μTAS systems [134].

The design of a μTAS integrates micro channels with sensors and actuators controlled by a computer. Fabrication techniques developed for LOC applications must be capable of producing feature size between 1 μm and 1 mm [135]. The micro reactor is an extension of micro electromechanical systems (MEMS) aimed at performing chemical reactions involving mixing, heat and mass transfer along with monitoring reaction progress. The MEMs are essentially transducers that convert energy between the electrical and mechanical domains or vice versa and often integrated with micro fluidic devices. The techniques to manufacture micro fluidic devices and MEMS also widely overlaps.

Due to smaller operational volume of micro reactors, they are advantageous for hazardous chemical reactions. In case of failure, the loss of chemical is relatively insignificant resulting in a decrease in risk. Compared to conventional reactors, high heat and mass transfer rates can also be achieved with close control of process variables, delivering higher efficiency and improved yield, particularly if these devices are arranged in parallel. This means that they can be effectively used for studying new chemical reactions with highly reactive and hazardous reagents. For the large-scale production of chemicals, micro reactors can be concatenated to form a continuous production unit; enabling scale-up to full production is simple and safe.

2.3.1 Micro Manufacturing Techniques

The raw material chosen for these devices should be non-reactive with the chemical system used. Silicon [136-137], glass [138] and polymer materials [139] are commonly used for the production of μTAS and a plethora of on-chip manufacturing methods suitable for these materials have been developed over the years. Techniques available for micro fabrication are broadly categorised as shown in Figure 16. Silicon based manufacturing routes are currently preferred for micro fluidic devices and MEMS due to excellent semiconductor properties, high mechanical strength, chemical resistance and excellent resolution [140].

Substrate fabrication takes silicon wafer of 200 to 650 μm in thickness and 75 – 300 mm diameter with (100), (110) or (111) Miller planes [141]. The basic procedure for on-silicon manufacturing follows the processes shown in Figure 16. Each of these processes has a complex operational procedure and requires a high degree of skill. Photolithography is the most common processing method for the production of devices from silicon [142]. Coating can be produced by deposition of thin film materials. Here material of a few microns or less can be easily deposited by using techniques such as chemical vapour deposition (CVD), low pressure chemical vapour deposition (LPCVD), sputter coating and resistive heating deposition [143-144].

Another widely used micro manufacturing method is LIGA, which is a German acronym for lithographie, galvanoformung, abformung (lithography, electroplating, and moulding) [145]. As the name indicates, it is a sequence of micro fabrication steps combined with deep X-ray lithography followed by the additive process of plating through a mask and mould. The technology is used for both silicon and other substrates, and offers ultra precise fabrication of components.

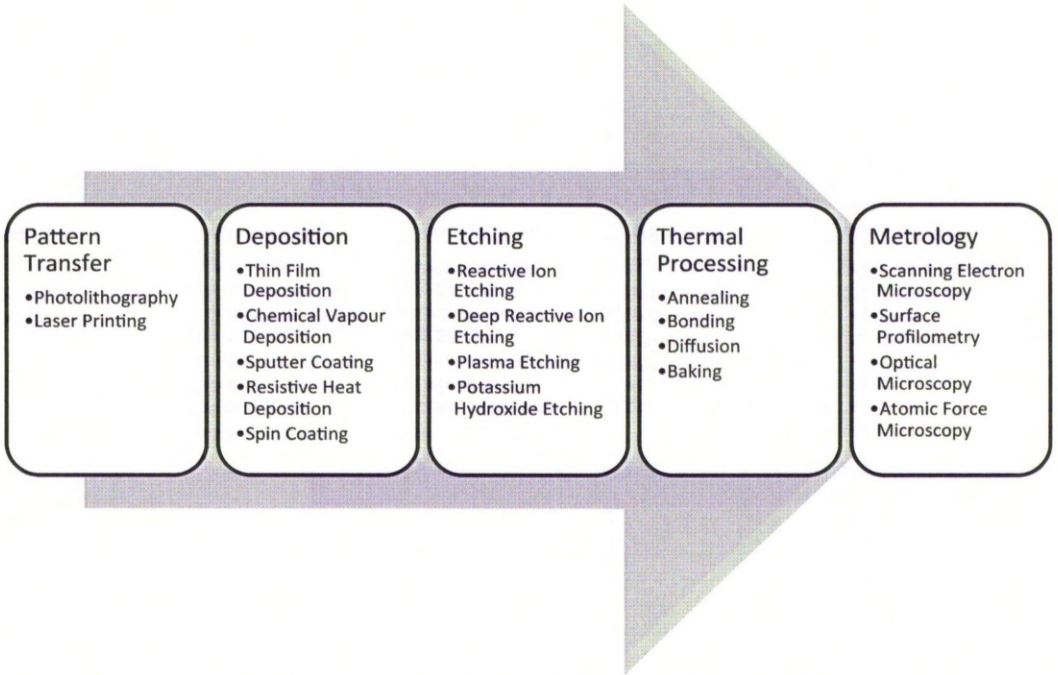

Figure 16: Basic Process Silicon Micro Fabrication [146].

Glass and quartz are also used for the manufacture of micro fluidic devices [147]. These materials have demonstrated potential in chemical applications such as capillary electrophoresis and electro-osmosis of liquids for analysis [148] and medical application, where human physiological fluids were transported in the form of droplets using electro-wetting analysis [149].

The use of the polymer can offer a range of material properties and has a surface chemistry required to optimise performance. Their low cost, high volume and relatively simple processing are distinct advantages in comparison to the other material. Manufacturing of polymer micro fluidic device by hot embossing has been successfully demonstrated using PMMA and polycarbonate (PC) [150]. Low cost, flexible manufacturing of micro fluidic systems by injection moulding, lithography and laser photo – ablation for various applications was successfully achieved by Becker [151].

Standard processes like photolithography, wet and dry etching, low-pressure chemical vapour deposition (LPCVD), sputter coating and various other micro manufacturing methods are employed for manufacturing MEMS [152]. Most of

these methods are highly complex and a combination of these methods is needed for MEMS manufacture. Some of these methods need post-manufacturing processing to achieve smooth finished surfaces as they leave burred edges [153].

Flawless working of a micro electro-hydrodynamic (EDH) injection pump was achieved by staking two silicon parts and bonded together [154]. Both the silicon parts were KOH etched to make a grid of holes while the other side was gold coated to form pump electrodes. Applying an electric field injects charged particles in the fluid, resulting in pumping of fluid. Similarly, a micro-pump system using piezoelectric actuation has been developed where a single Stereolithography process where ultraviolet – photocurable polymer material was used to manufactured pump body. The piezoelectric disk was glued to the pump body for piezoelectric actuation [155]. Investigations were also carried out by Cohen [156], who used an electrochemical fabrication technique for on-silicon manufacturing of MEMS and a well-presented comparison with LIGA.

Photolithography technique discussed earlier has been used as a standard process for fabricating polymer microstructures by sacrificial layer micro moulding and patterned substrate micro moulding. Fabrication of 5 μm features was successfully achieved, however with some non-uniformity [157]. Micro machining of polymers is an alternative cost-effective approach for the development of MEMS [158].

2.3.2 Hydrodynamics of Micro Fluidic Channels

When designing microfluidic process equipment, the prediction of pressure drop across the devices is crucial. As pressure at the exit will be the input pressure for next component connected in the series. It is therefore a prerequisite to keep the pressure drop as small as possible between devices. This concept is equally applicable for micro- and macro – fluidic devices. Significant experimental and theoretical work has been done to predict the flow behaviour of the fluids in the micro channels. Based on flow classification by Knudsen number, channels sizes are generally referred as [159]:

Conventional channel (macro channels) -	$D_h > 3mm$
Mini channels -	$3mm \geq D_h > 200\ \mu m$
Micro channels -	$200\ \mu m \geq D_h > 10\ \mu m$
Transitional Channels -	$10\ \mu m \geq D_h > 0.1\ \mu m$
Transitional micro channels -	$10\ \mu m \geq D_h > 1\ \mu m$
Transitional nano channels -	$1\ \mu m \geq D_h > 0.1\ \mu m$
Molecular nano channels -	$0.1 \geq D_h$

In micro fluidic devices, the dimensional analysis of a fluid flowing through the channel is characterised by the Reynolds Number N_{Re} and Fanning's friction factor f [160]. Pressure drop due to frictional losses, is related to the length of the channel, the surface roughness, inlet and exit conditions, viscosity and flow velocity. For $N_{Re}<2100$ flow of fluid through the duct is laminar, whereas at $N_{Re} > 4000$ turbulence is dominant [161]. The condition $2100 < N_{Re} < 4000$ is a known as transition where the flow is neither fully laminar nor turbulent. Fanning's frictional factor for these conditions can be expressed as [162]:

$$f = \frac{16}{N_{Re}}, \quad \text{for } N_{Re} \leq 2100 \tag{2.46}$$

$$f = \frac{0.079}{N_{Re}^{0.25}}, \quad \text{for } 4000 \leq N_{Re} \leq 10^5 \tag{2.47}$$

The fluid behaviour in the transition flow regime is irregular and unpredictable. For smooth surface channels, the friction factor is a function of Reynolds number and is independent of surface roughness [162]. Friction predominates for channels with rough surfaces i.e., high ratio of surface roughness (ε) to diameter of the duct (D).

Reynolds number N_{Re} is a ratio of inertial forces ($V\rho$) and viscous forces (μ/L), is given by [162]:

$$N_{Re} = \frac{V\rho L}{\mu} \tag{2.48}$$

Where V is fluid velocity (m/s), ρ is density of fluid (kg/m^3), L in case of circular ducts is the diameter (D) and μ is the dynamic viscosity (Pa.s). For non-circular

ducts, D is replaced by an equivalent hydraulic diameter, D_h. The hydraulic diameter D_h is a method to describes the non-circular ducts as equivalent to the circular ducts, expressed as [163]:

$$D_h = \frac{4A}{P} \qquad (2.49)$$

where A is the cross section area of the duct and P is the wetted perimeter of the channel cross section.

2.3.3 Fluid Flow behaviour of Micro Channels

Like conventional reactors, the design of a micro reactor depends on control parameters such as mass flow rate, viscosity, density, heat transfer coefficient, solubility and Reynolds number. Design calculations for reactors revolve around high heat and mass transfer being achieved at a minimum pressure drop [164-165].

The Knudsen number is the ratio of molecular free path of the fluid λ and the minimum characteristics dimension of the channels d_{min}, indicating the degree of flow rarefaction. The fluid is considered as a continuum for low Knudsen numbers (Kn ≤ 0.01), whereas for higher Knudsen numbers, rarefaction effects such as "slip-flow" on the walls appear [166].

The effect of surface roughness on the fluid flow was analysed by Satish [167] on a test specimen made of two individual flat surfaces forming the top and the bottom of a flow channel. Each surface was machined to roughness, R_a of 0.21 μm and saw tooth surface with aligned and offset saw tooth (R_a = 17 μm). The effect of roughness was measured for D_h ranging from 325 μm to 1819 μm with the relative roughness between 0.01 and 0.14, N_{Re} ranging from 200 to 7200 for air and 200 to 5700 for water. The variation in friction factor for both, air and water flow, observed for D_h of 953 μm (relative roughness of 0.0735 μm) shows no agreement with the theoretical laminar or turbulent flow. The frictional factor for both the cases lies significantly above the theoretical frictional factor following the equation for Fanning's factor. It was also observed that the transition to turbulent flow begins at Reynolds number in the range of 1800 – 2100 for smooth channels.

However, an early transition to turbulent flow was reported for saw tooth surfaces with relative roughness of 0.06 – 0.14.

Steinke [168] have made a review of more than 150 experimental sets of data involving flow in micro channels. It reveals that the most common range of hydraulic diameter of micro channels varies from 100 – 200 μm. The experimental data gathered confirms that the Reynolds number decreases with decrease in hydraulic diameter and increasing pressure drop. Experimental data reviewed for the fluid flow behaviour of micro channels shows an agreement with the conventional theory. However, the experimental uncertainty observed in the micro channels was dominated by the aspect ratio of the micro channels.

Channel geometry has been reported to have a significant effect on the pressure drop [169-170]. Optimising the aspect ratio of the micro channels can optimise the flow in the channels. For example, increasing the channel length increases the pressure drop, whilst increasing the width of the channel reduced the pressure drop. Increasing the flow rate in the channels results in increasing turbulence. The effect of flow behaviour for varying aspect ratio of micro channel shows increasing friction factor for a given Reynolds number, when the channel cross section was changed from the square (aspect ratio of 1) to parallel plates (aspect ratio 0). In terms of a pressure drop, the transformation from the square to the rectangular cross section gradually increases the pressure drop due to increase in friction factor, shown in Figure 17.

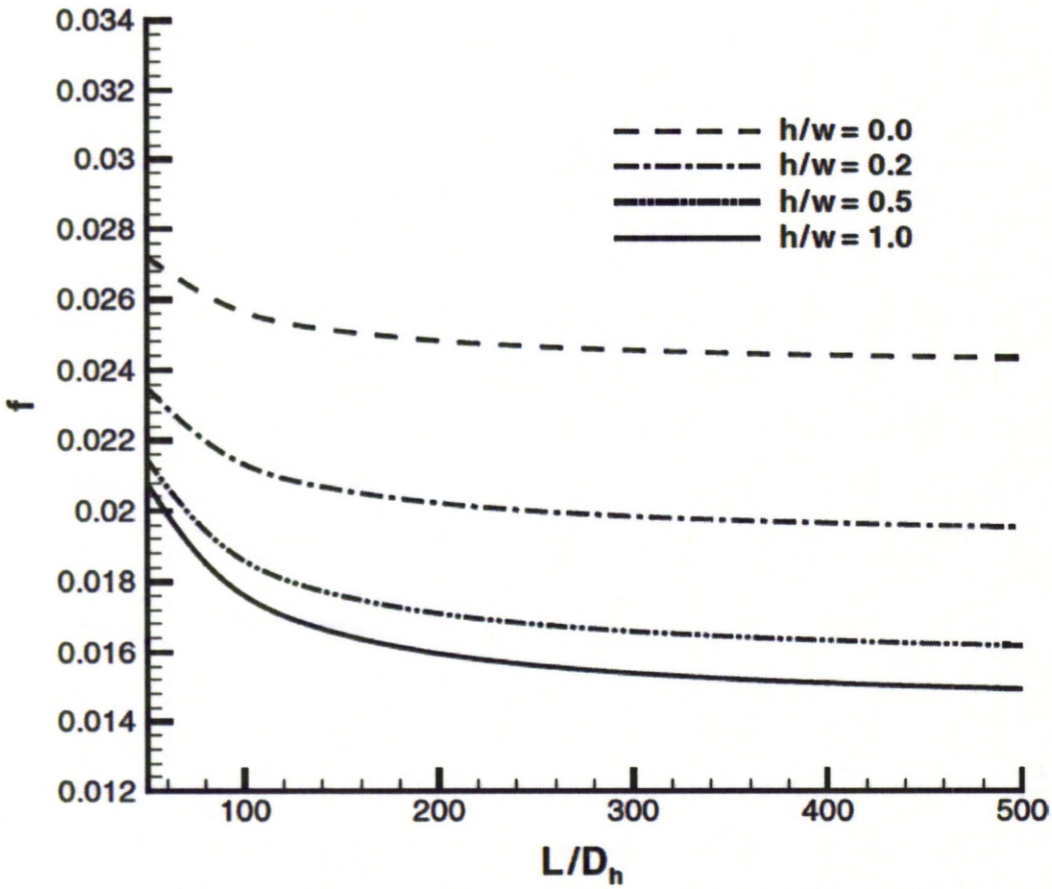

Figure 17: Effect of Height-to-Width Ratio on Friction Factor for N_{Re} = 1000 [167].

The flow characteristics in the micro channels were observed to be different from those predicted for macro channels. Stainless steel and fused silica micro tubes with diameters ranging from 50 - 254 μm were tested at Reynolds number up to 2500 [163]. The flow rate was kept constant for all the tests and the pressure drop was measured. Conventionally, the pressure gradient (ΔP/ΔL) required to force liquid through a straight pipe in a uniform cross section generally follows the relationship with the volume flow rate Q,

$$\frac{\Delta P}{\Delta L} = Q^n \qquad (2.50)$$

For the laminar region, n=1; in the laminar to turbulent region 1<n<2 and in the turbulent region n ≥ 2. However, experimental observation for conventional laminar region (N_{Re} < 2300) shows a non-linear relationship between (ΔP/ΔL) and Q.

For stainless steel micro channels of 130 μm diameter, theoretical prediction was given as

$$\frac{\Delta P}{\Delta L} = 118.91\ N_{Re} \qquad (2.51)$$

However, for the range of N_{Re} < 650, experimental data is found to correlate with the equation:

$$\frac{\Delta P}{\Delta L} = 121.77\ N_{Re}^{1.072} \qquad (2.52)$$

Comparing Equation 2.51 and 2.52 clearly shows deviation from the theoretical prediction of fluid flow in the micro channels [171-172].

A separate study conducted by Brackbill [173] investigates behaviour of rectangular channels in the turbulent flow condition (N_{Re} = 1000 – 15000). The pressure drop at the surface was measured for a capillary with relative roughness of 0.17. It was observed that the channels from 200 – 1000 μm (D_h = 394 – 1849 μm) with smooth surfaces have verified the theoretical behaviour, however, more uncertainty in the data was observed for 1000 μm channels. Channel sizes of 405 μm with relative roughness of 0.0397 showed poor correlations with the predictions made by Kandlikar [159].

Work conducted by Shau-Shing [174] presents the fluid flow behaviour in the rectangular channels. The pressure drop at the inlet and outlet of the duct along with friction factor was analysed for different mass flow rates yielding N_{Re} up to 1000. The device used for the analysis consists of micro channels with the dimension 200 μm x 115 μm x 24000 μm and have a hydraulic diameter of 146 μm. It was observed that for N_{Re} < 200 shows a linear behaviour of ΔP/ΔL, which was in agreement with the conventional theory. However, the relation changes to non-linear with increasing N_{Re}.

Comparison of experimental results for the flow behaviour of various micro channels usually shows no deviation in the behaviour predicted for the flow in the laminar region for hydraulic diameters down to 50 μm [175-176]. But it has also

been shown that micro channels manufactured on a highly polished silicon wafer showed good correlation with the predicted behaviour, even at diameters of 6 μm [177].

Computer simulation tools for analysis of the fluid behaviour can be employed for the design optimisation and process performance evaluation [178-179]. The computer simulation for the fluid behaviour successfully verified the experimental work by Mies [180]. Although some non-uniform flow behaviour due to low-pressure distribution was observed during the experiment, this was not thought to have influenced the performance, as the deviation was in the acceptable range.

2.3.4 Applications of Micro Fluidic Devices

Micro fluidic devices are found in inkjet printers, biological and chemical analysis, forensic analysis, molecular diagnostics, and medical diagnostics. They are integrated with a digital system for micro control and sensing of system parameters such as the temperature, pressure fluid flow and so on [181]. An in-depth review by Erickson and Li [182] presents the "state-of-the art" integrated micro fluidic devices for DNA analysis.

Micro reactors manufactured by photolithography were successfully deployed for various gas and liquid phase catalytic reactions in the channel size range 200 μm x 200 μm x 30 μm. They were successfully used in multi step, complex and hazardous chemical reactions, confirming the commercial versatility of these systems [183].

Micro fluidic devices fabricated by lithography have been used for chemical studies in biological sciences for the development of cell-based assays, single-cell assays, gene-expression profiling, high-throughput and combinatorial methods. The development of micro fluidic devices was presented as cost effective and efficient for health care devices for bio-analytical detection [184]. These micro fluidic channels use small volume for transportation that can be as small as droplets of 10 – 500 μm in radius. Mixing in such a small volume can use surface acoustic waves generated by using functional materials [185].

Micro fluidic devices were utilised for the study of reaction kinetics [186]. High heat transfer, mass transfer and mixing obtained in micro reactors opens up new pathways for advances in the reaction engineering. This is combined with a low operational risk that arises from the miniaturisation of the chemical volumes employed [186]. Micro reactors have to be specifically designed for each task. They can be integrated with the chemical and optical sensors for process control with rapid feedback. Ikuta [162] successfully tested an opto-sense micro reactor for cell free protein synthesis.

2.3.5 Micro Electro-Mechanical Systems (MEMS)

There are various definitions of MEMS available in the literature. They can be viewed as a special class of semiconducting device. MEMS are the devices that can range from 0.1 μm to 1 mm. MEMS are transducers that convert energy between the electrical and mechanical domains or vice versa [187]. The scope of MEMS is not limited to increasing number of transistors on an IC, but a conscious effort for integrating multiple technologies / functions in a single package. The functioning of micro fluidic devices and MEMS widely overlaps and hence, has similar approaches for development and fabrication.

MEMS are often utilised as sensors or transducers. Although, both these terms are often used as synonyms, they reflect the functional objective of the MEMS. Sensor is derived from the word "*Sentire*" meaning "to perceive", where as transducer is originated from "*Transducere*" means, "to lead". Sensors supply a measure of a parameter, whereas transducers will sense the input parameter to translate it into a useful signal to a controlled mechanism.

The development of smaller, faster, more efficient and reliable devices continue to challenge many engineering disciplines. Developments in micro electro mechanical system (MEMS) have lead by transformation of analogue to digital systems. MEMS are a perfect combination for efficient and well coordinated performance in various engineering disciplines enabling many functions to be embedded in a single

package and made possible only by understanding the material science and fabrication techniques.

Manufacturing of MEMS by Stereolithography is a novel method of manufacturing 3D devices and structures ranging from micron to millimetre range. Sometimes referred to as the poor man's LIGA process, it starts with defining a CAD model following the procedure of layer based manufacturing, discussed in Section 2.4. Although, development of polymers using parylene, polyimide, acrylics (PMMA), photo patternable epoxy, and polydimethylsiloxane (PDMS) elastomer has been reported [188], there are, however, significant challenges associated with polymer bases MEMS such as usability, stability at high temperatures and performance shift over time. In similar work by Sameoto [189], the SU-8 based MEMS were developed and successfully verified their applicability and functionality.

2.3.6 Application of MEMS

Microfluidic devices are one of the successful commercialisation of MEMS. Their use in applications such as inkjet printing [190], micro pumps [191] and valves [192] are well documented. The fabrication of these devices conventionally follows silicon manufacturing, discussed in Section 2.3.1.

The smallest functional MEMS device has been designed as thermal, optical and mechanical sensors. They also extend to semiconducting chemical sensors and micro fluidic systems for biological systems, as well as micro actuators. Although they are used as generic terms, each MEM is highly specifically designed for a particular functional performance.

Since the mid 1950's, MEMS have been an area of investigation [193]. Comparing with the earlier designs, the current state of MEMS is highly sophisticated. It employs highly complex manufacturing processes for generation of 3-D microstructural components for miniaturisation of these devices.

MEMS based on physical sensing have been successfully manufactured as accelerometers, strain gauges, microphones, pressure sensors and many more.

Micro cantilever beams have been employed to convert a variety of chemical and physical phenomena into mechanical movement. A work by Tabard-Cossa [194] used a differential micro – cantilever beam for measuring surface stress occurring during the electrochemical reaction. The change in surface stress induced by the ionic adsorption on the coated metal surface and by electromechanical transformations was measured by opting beam technique.

Advantages offered by beam structure have been equally explored for many applications [195-199]. Due to simple construction and behaviour, cantilever beams are relatively popular. They can be easily manufactured by utilising a range of manufacturing processes, including AM techniques. Radio frequency, piezoelectric, capacitance, vibrational methods form the basis of cantilever beams based MEMS.

Surface acoustic waves (SAW) based pressure sensor was designed, where the force exerted by the deflecting plate under pressure is transferred to an acoustoelectric sensitive X-cut quartz substrate [200]. The resonant frequency is generated by the transmitted forces and was calibrated for the applied pressure on the plate. In another design, the SAW resonators was integrated with quartz diaphragm. Deflection in the diaphragm causes generation of frequency, which was measured as a function of applied pressure. Micro manufacturing techniques of materials for silicon wafer, polymer and ceramic composites has also been suitably utilised for wireless sensing [201-203].

Vacuum-sealed silicon diaphragm based capacitive pressure sensors have been utilised over a large dynamic pressure range, with low temperature sensitivity [204]. Although, they perform with consistent repeatability, the capacitance measured was less than theoretical prediction due to higher residual stresses developed during manufacturing. Such capacitance-based pressure sensors offer high sensitivity low noise, large dynamic range combined with minimum power utilisation. These pressure sensors are commonly manufactured on silicon due to its high mechanical strength, high consistency, electrical properties and the precisely controllable thickness of silicon membranes [205].

2.4 Additive Manufacturing

Additive manufacturing (AM) is the commonly used term to encompass AM techniques; layer based manufacturing techniques (LBMT); solid freeform fabrication (SFF); rapid prototyping (RP); and rapid manufacturing (RM). The term refers to group of technologies used for building tangible objects by joining together materials in liquid, powder or sheet form. Parts that have a complex structural design, which are difficult to fabricate by other fabrication techniques can be manufactured using AM.

2.4.1 History of Additive Manufacturing

AM emerged from two areas: topography and photosculpture. In 1890, Blanther suggested stacking layers of wax plates to manufacture a 3D contour map [206]. The wax plates were cut to the contours of 2D map and pressed together. Perera (1940) used a similar approach with cardboard, whereas Zang (1964) achieved further refinement using transparent plates with topographic details inscribed on each transparent plate. Matsubara (1974) propose a topographical process where refractory particles like sand or graphite powder coated with photopolymer resin was spread into a layer. The layer was selectively heated by a mercury vapour lamp to form a coherent sheet. Solvents were than used to dissolve the unhardened area resulting in a casting mould [207].

Baese (1904) described a technique where photosensitive gelatine is exposed using graduated light [208]. The annular rings of gelatine were fixed on a stack to make a replica of an object to obtain 3D photography. Munz (1956) proposed a process similar to current Stereolithography where layers of transparent photo emulsion were cured in a layer-wise manner [208]. Although, the layers were created from a scanned object, the manufactured structure was either manually carved or photochemical etched out to create a 3D object. In 1968, Swainson proposed a process for direct manufacturing of plastic patterns by selective, three dimensional polymerisation [209]. This was achieved by the intersection of two UV laser beams. At around the same time, Ciraud described a process for making objects with a

partially meltable material, which was subsequently fused together. Similar process was designed at Battelle laboratories (Schwerzel, 1984) for building 3D parts by photochemical machining [210].

In 1979, Housholder presented the earliest description of a laser sintering powder method in a patent. He discussed sequential deposition of powders in layers and the solidification of each layer of powder by selective masking and heating [210].

2.4.2 Basic Principle of Additive Manufacturing

Most of the conventional manufacturing methods like turning, milling, drilling and so on remove materials to form a component of desired shape. They are collectively known as subtractive manufacturing. AM techniques, on the contrary forms a component by joining material. The material is deposited by stacking layers up on top of each other. Each layer has a 2D contour in the XY plane and constant thickness. Figure 18 shows the generic manufacturing process of AM. The model formed by the AM techniques is directly transferred from the CAD model prepared on a computer. Hence the dimensional and aesthetic detail remains unaltered. The CAD model prepared on the computer is sliced using mathematical methods to obtain the contour information for each layer. The information for each layer is transferred to the AM machine where a single layer is deposited on top of the previous layer. Deposition of all layers collectively forms the final product.

A 3D data set is required for the generation of 2D data points to manufactured individual layer. Since CAD models are developed on various CAD software, a neutral data transfer is required. The neutral format usually an STL file of the model is then processed by software that is supplied with a particular AM machine to establish the geometrical information along with manufacturing parameters for deposition of layers.

The slicing of a CAD model is achieved by first defining the model surface by a series of tessellated triangles forming an STL file, the de facto industrial standard [211]. The advantage of an STL file is its simplicity but this simplicity results in some

significant disadvantage including file size, resolution and tolerance. A CAD model converted into an STL file has advantages as triangles provide good quality of geometric information that is reasonable error free. The tessellated STL models permit rescaling without manipulation of the original CAD file.

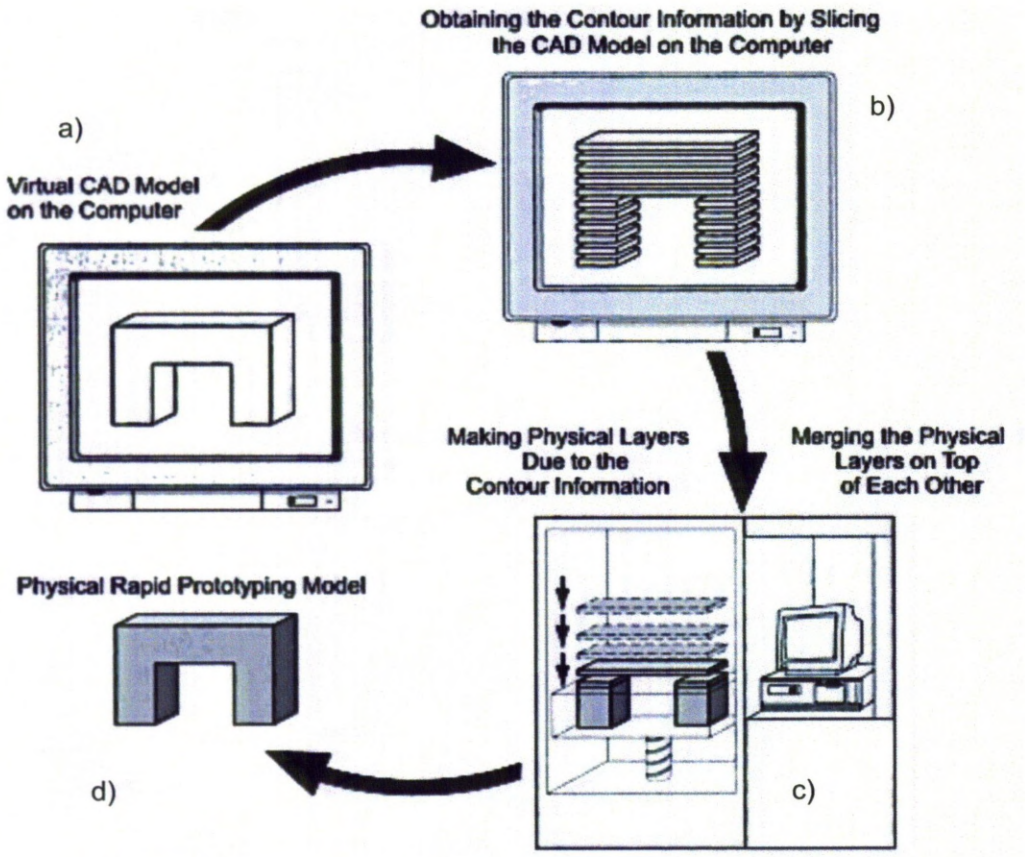

Figure 18: The Principle of Model Generation by Additive Manufacturing: a) Preparation of CAD Model on the Computer, b) Slicing for Obtaining Contour Information, c) Deposition of Layers, d) Finished Physical Model (Gebhardt 2003) [211].

2.4.3 Additive Manufacturing Techniques

AM has progressed in parallel with improvement in computer architectures, CAD techniques and process control mechanisms. A series of commercially available AM techniques encompassing different materials have developed over three decades. The classification of AM techniques based on nature of feed material is shown in Figure 19. Typical AM techniques are Stereolithography (SL), Selective Laser Sintering (SLS), Fused Deposition Modelling (FDM) and 3D Printing.

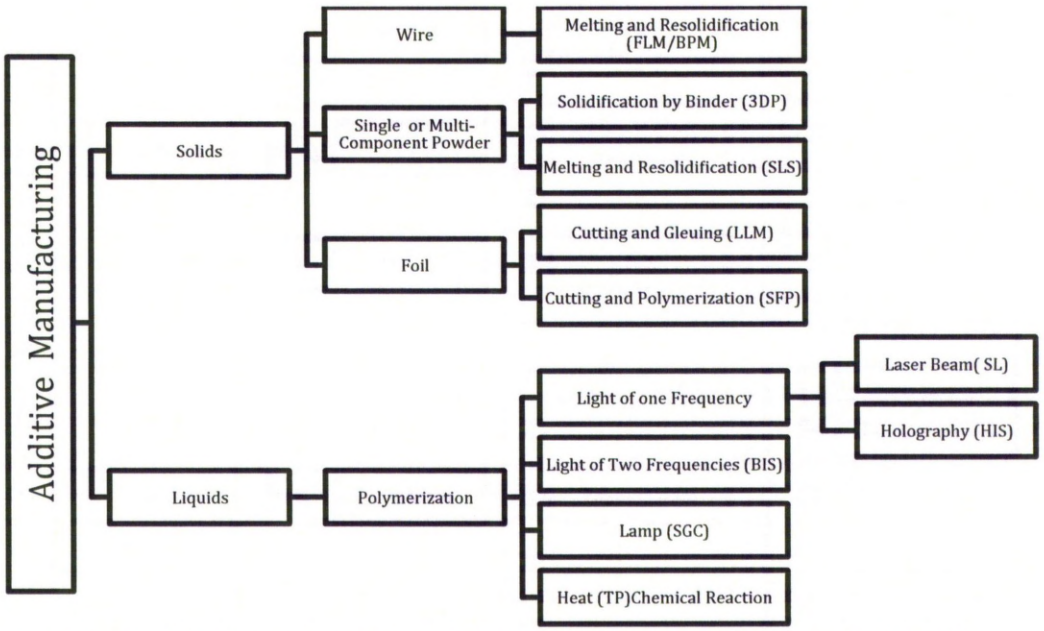

Figure 19: Classification of Generative AM Processes (Adapted: Gebhardt, 2003) [212].

The first commercially AM process was 3D System's Stereolithography (SL) process based on liquid photopolymer [212-213]. Typically a Stereolithography apparatus (SLA) consists of a container that stores the liquid polymer and acts as a building chamber. A vertically movable build platform located in the polymer container; where the layers of polymer are deposited by a wiper blade and subsequently solidified using scanning laser beam. After the layer is deposited and the part solidified on the build platform is lowered by one layer thickness. A new layer is prepared by a recoating and the laser scanning system again exposes the next layer (Figure 20).

The laser beam has a Gaussian energy distribution indicating parabolic penetration characteristics of the resin [213]. The beam penetrates the previous layer while depositing new layer to achieve inter – layer cross – linking. This is known as depth of penetration. It ensures cross – linking between the layers and over curing the previous layer.

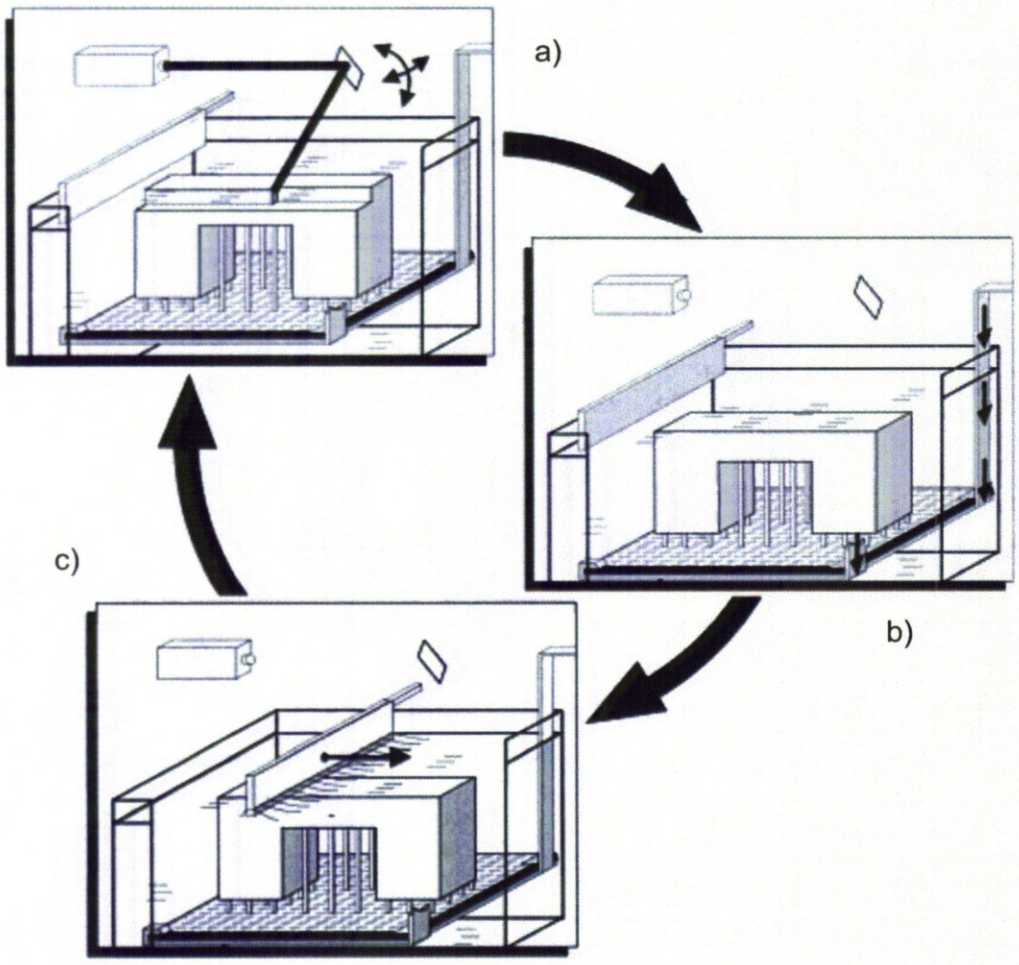

Figure 20: Typical Layer Deposition in SLA: a) Layer Deposition by Laser Scanning, b) Lowering of Build Platform, c) Preparation of New Layer by Recoating [212].

Some AM techniques require the solidification of powder or granules for the formation of layers. Selective Laser Sintering (SLS) was the first to be developed. In the SLS process, particles are deposited on a build substrate to form a powder bed of 50 – 100 µm in layer thickness [9][206]. During this process, the chamber is gradually heated up to 80% of the melting temperature of the material. The laser beam only needs to add the amount of energy for sintering; hence keeping the process temperature in a small tolerance window is important. The process chamber is also filled with inert gas, usually nitrogen (typically up to 0.1 % to 3.5 % residual oxygen) [212] to reduce oxidation of the powder. The powder bed is generally closely packed and then melted by the laser beam solidifying due to fusing of particle in a layer [214]. The build substrate is lowered once the layer

solidifies and is subsequently recoated with powder. Melting and solidification of second layer joins it to first layer. The process is shown in Figure 21.

Electron Beam Meting (EBM) can also be used for melting solid powder [215]. EBM uses a high-energy electron beam to selectively melt solid metal particles. EBM is similar technique to SLS; however, the manufacturing process is operated under vacuum and at high temperature and can be used only for metals. The EBM based system has faster scanning speeds but poor surface finish and resolution in comparison to SLS.

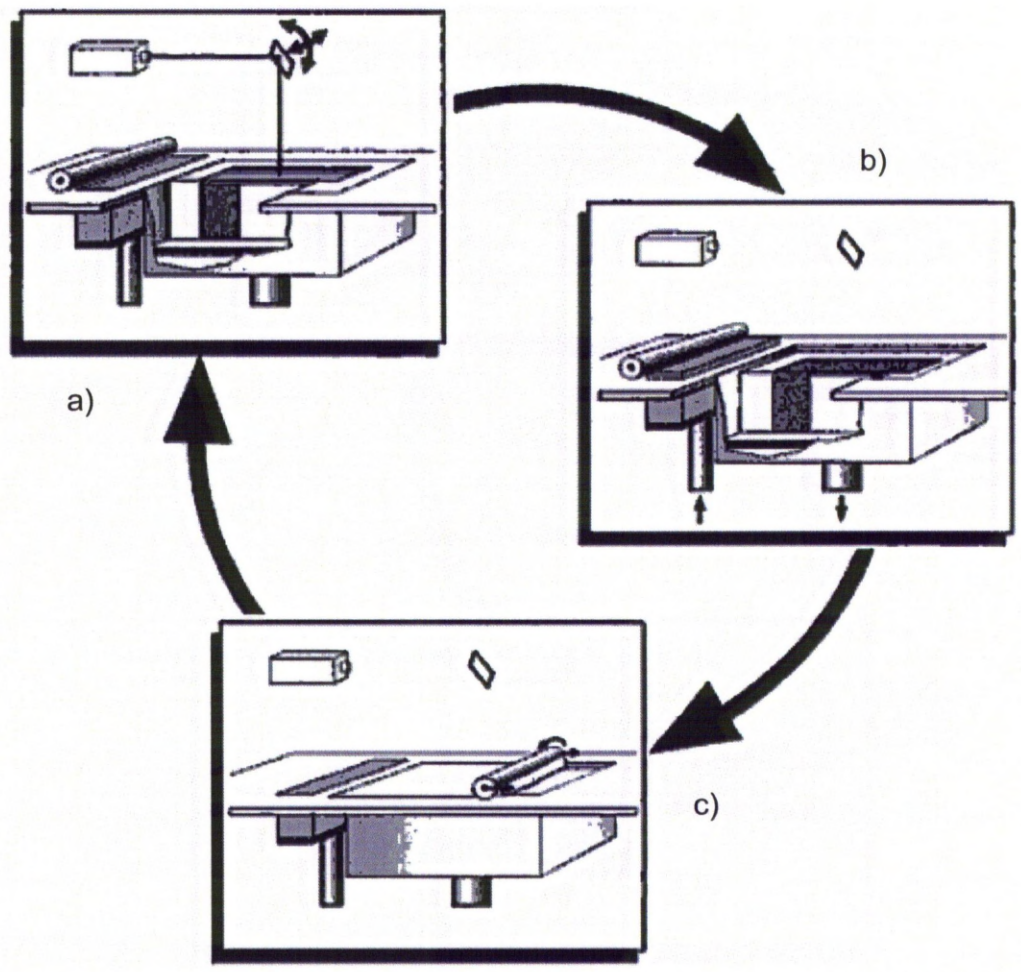

Figure 21: Typical SLS Process: a) Layer Deposition by Laser Scanning, b) Lowering of Build Platform, c) Deposition of Powder Bed by Recoater [212].

In another AM technique, the solid material is extruded in the form of molten material by continuously feeding in material as filament to a heated nozzle. This technique is known as Fused Deposition Modelling (FDM) [216]. The solid material is either fed to the extrusion chamber under gravity or using a screw. The materials that are fed to the system under gravity require a plunger or a compressed gas to force the molten material through the nozzle. If the system is screw fed, it pushes the material though the base and simultaneously generates sufficient pressure needed to push material though the nozzle, resulting in a uniform feed rate and constant cross-sectional diameter of the depositing material. The nozzle, controlled to move in the XY plane. After the layer is deposited, the base plate is lowered by one layer thickness [70]. Figure 22 shows schematic representation of FDM technique.

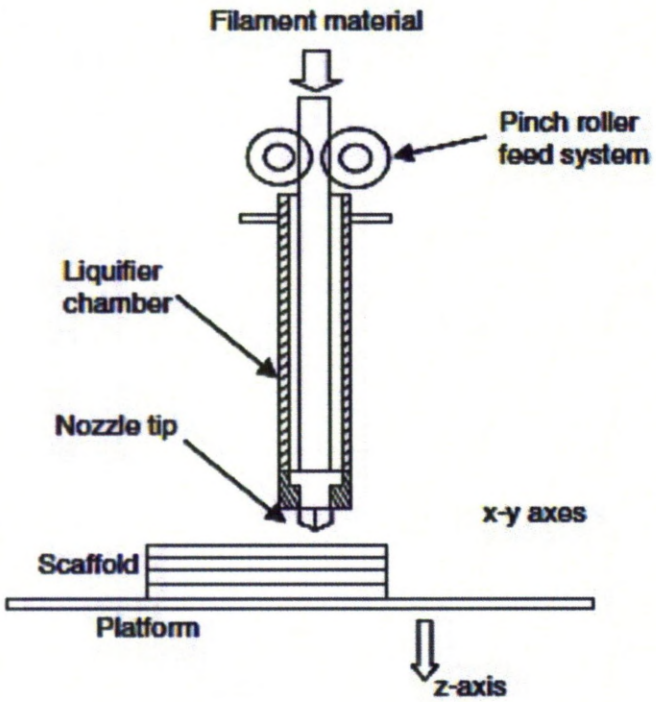

Figure 22: Schematic Representation of FDM Process [209].

A three dimensional printing process, commonly known as 3D printing was commercialised as Zcorp's in 1997 [216]. It works on a binder printing method

where a binder or other additive is printed onto a powder bed, as shown in Figure 23.

Although, the development of materials for printing is a challenge, many examples have been commercialised such as Solidscape, 3D Systems and Object Geometries have all successfully launched AM machines based on inkjet technology. The machines developed by Solidscape contain two single jets – one to deposit thermoplastic material and other to deposit wax supports [216]. These machines are slow but accurate and are used extensively in the fabrication of investment casting patterns for the jewellery and dentistry industries.

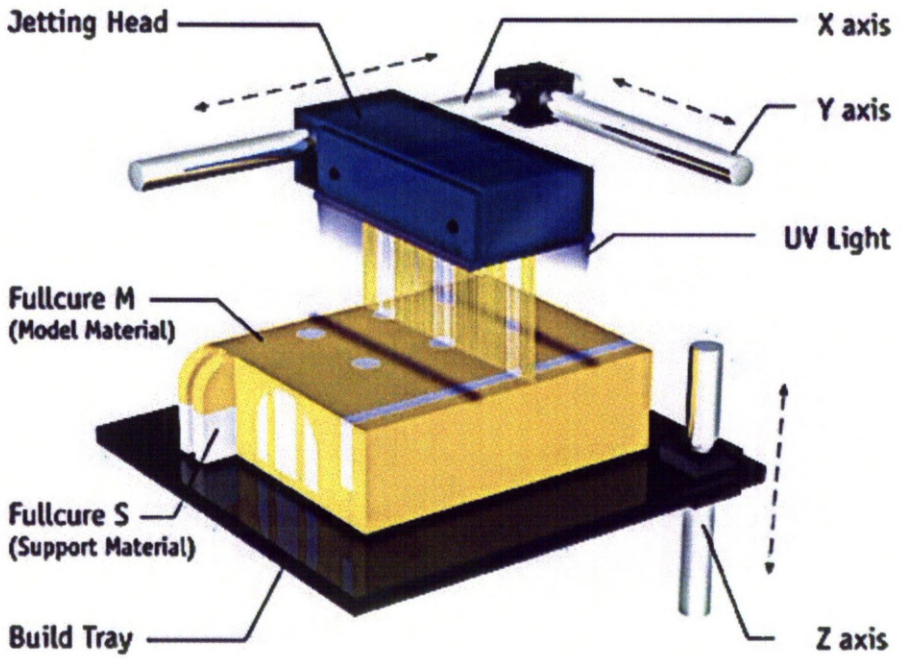

Figure 23: Schematic Representation 3D Printing Using Polyjet Technology [217].

The 3D Systems and Object Geometries machines offer printing and curing of acrylic photopolymers using inkjet heads. These machines print a number of acrylic based materials, at a layer thickness of 0.015 mm. In the Object polyjet system materials are deposited from the print head containing 1536 individual nozzles [216]. Following deposition, the layers are subsequently flashed with UV light, which activates photoinitiated polymerisation.

2.4.4 *Photopolymer Curing*

Liquid polymers can be selectively cured using gamma rays, X rays, electron beams, UV rays and visible light. The SLA technique commonly uses UV rays, laser and visible light for curing. A typical example of SLA machine uses an Nd:YVO_4 laser system (iPro 9000XL SLA Center / 1450 mW) to cure liquid monomer layer [218]. The liquid monomer containing photo catalysts are exposed to radiation of wavelength λ 354.7 nm, chosen for its ability to cross link monomer units into polymer [219]. During the SL process, the laser irradiation penetrates slightly more than the layer thickness resulting in the partial curing of the liquid polymer and the further curing the surface of the previously scanned layer. In the case of a laser, the exposure E will decrease exponentially with the depth z and follows:

$$E(z) = E_o \, e^{\left(-z/D_p\right)} \qquad (2.53)$$

The above equation is known as the Beer-Lambert law of absorption [213]. E(z) is the exposure at a depth z, E_o is the exposure at resin surface, z=0, D_p is the resin penetration depth. Practically, polymerisation is not effective beyond a limited depth, at which the exposure is below a certain threshold value. The exposure level at which the polymer transforms in to a solid is termed as its gel point. This threshold exposure for gel formation is known as the critical exposure E_c. Exposure is a measure of radiation energy per unit area. It is proportional to the radiation power density and inversely proportional to the product of radiation bandwidth at the liquid surface and the scan speed [207]. The maximum depth of the polymer cured by a single pass is given as:

$$C_d = D_p \ln\left(\frac{E_{max}}{Ec}\right) \qquad (2.54)$$

The equation above is the fundamental equation of SLA, where C_d is the curing depth of the polymer. For a photopolymer, threshold exposure E_c is constant and the curing depth C_d is a function of depth of penetration D_p and maximum exposure $E_{max.}$ at the surface [207].

The gel point is reached when the photopolymer is exposed to radiation at E_c, however, at the gel point, the material does not possess significant strength. It is therefore necessary to expose the photopolymer at E_x, in excess over E_c to obtain useful strength. Strength of the photopolymer achieved after exposure to E_x is termed as green strength [213]. The green strength should be sufficiently large to ensure the part does not deform while being manufactured or handled.

During manufacturing, support structures may be needed particularly for layers with overhanging or undercut features. Supports for such overhanging or undercut features may be avoided by reorienting the CAD model. Supports are generated in such a way that the part is held in place to avoid distortion. The design of support structures vary from simple cantilever beams to a complex mesh extending and supporting part features.

2.4.5 Characteristics of Polymer Components

The components manufactured by SLA technique using laser curing permit high precision. The mechanical property of the photopolymer improves with curing of the polymer [220]. They are however, time dependent and tend to degrade with aging. They are also influenced by humidity and temperature.

The stress strain behaviour of the test specimens manufactured using SLA show the average Young's modulus of 1050 MPa for the green parts increase up to 1320 MPa for the specimens maintained in the conventional oven under uniformly maintained temperature by Salmoria [221]. The average strain in the green part was highest of all the test specimens.

An investigation undertaken by K. Chockalingam [222] identifies influence of layer thickness on mechanical properties of test specimens manufactured in epoxy resin by SLA. These tensile test specimens were manufactured with 100 μm, 125 μm and 150 μm layer thickness. The analysis shows that increasing the layer thickness leads to decrease in yield stress, ultimate tensile strength and impact strength of the

material. SEM analysis of thick-layered tensile test sample shows formation of large voids, reducing the density and mechanical strength of the material [223].

Separate work by K. Chockalingam [224] shows that build orientation (33%) followed by post curing time (29%) are majorly contribution to part strength in SLA. Segal [225] presented a comparison of mechanical properties of polystyrene parts manufactured by SL moulding and steel moulded parts. It shows that parts manufactured by steel moulding possess better tensile strength and elongation were higher by 12% and 16% respectively, when compared to SL moulded parts. The flexural strength however for the SL moulded was 21% higher than steel moulded parts. The ability of the polymer materials to absorb moisture from the surrounding atmosphere has been reported to alter the mechanical properties [226].

The specimens manufactured by polymer for SLA process shows surface roughness due to layers, surface roughness due to shrinking of polymers and inaccuracy due to poor thermal conductivity for SLA moulding [227].

The specimen manufactured using SLA may often show inhomogeneity in chemical and physical properties in the cured part due to the limitation of curing depth of the radiation [228]. The process of curing the photopolymer therefore, fails to provide isotropic material properties.

The ability of 3D printing was used to pattern three-dimensional ceramic parts through the deposition of colloidal and polymer- based ink for biomedical, structural and functional applications [229]. However, challenge associated to micro mixing and controlling parameters such as viscosity of ink, rate of deposition and accuracy were presented.

The advantage of flexible manufacturing offered by AM was utilised for manufacturing of composite transducers [230]. A Fused Deposition of Ceramic (FDC) was specifically developed for fabrication of 2-2 and 3-3 connectivity ceramic

composites for transducer applications. FDC was used for fabrication of complex transducer shape such as spirals, curves, dome, multi-layered tubes and bellows.

A frontal photopolymerisation based AM technique was used for fabrication of micro fluidic devices [231]. They were fabricated by photo masking of multifunctional thiolene-based optical adhesives. The micro fluidic device having a combination of 190 μm and 340 μm micro channels was fabricated using UV radiation (365 nm).

Manufacturing of ceramic-polymer composites using μSLA technique by addition of ceramic in the polymer greatly increases the turbidity of the ceramic suspension, leading to a decrease in absorption [232]. Addition of ceramic particles greatly modifies the behaviour of the resin under photopolymerisation. The particles were dispersed in the liquid polymer forming a colloidal solution. This however resulted in increased turbidity of the polymer and the penetration depth (D_p) of the mixture was significantly reduced.

Further, a direct writing technique has been used to successfully fabricate embedded micro channels on silicon by using SU-8 photo resist [233]. A proton beam of 1 μm^2 spot size with energies of 0.6 and 2.0 MeV was used for layer deposition. The micro channels of 125 μm x 20 μm x 25 μm were successfully manufactured.

2.5 Summary

The current section summarises the discussion presented in the literature for the research undertaken here, aiming to manufacture a micro reactor in a single build by AM route using functional material forming sensing and transducing parts.

An overview on the theory of dielectric, piezoelectricity and ferroelectricity was discussed along with different methods used for polarisation. The degree of polarisation for the dielectric material is depended on the structural arrangement. Various phases of perovskite structured $BaTiO_3$ ceramic powder along with their piezoelectric and ferroelectric behaviour was discussed. Excellent piezoelectric and

ferroelectric properties of $BaTiO_3$ have been used for various applications such as power filters, radio frequency systems, transducer applications, bio-imaging, medical applications and non-volatile memory.

As discussed, the dielectric relaxation occurring in the dielectric materials reduces functional activation. Various dielectric relaxation mechanisms resulting in dielectric loss occurring either internally or due to external field were reviewed. Various other factors such as particle size, shape, volume fraction, density, connectivity, frequency, pressure and temperature also influences the piezoelectric and ferroelectric behaviour were also discussed in detail.

Natural materials exhibit excellent multi- functional properties. A unique combination of a strength, stiffness and flexibility observed in natural materials is due to exceptional arrangement of constituent molecules. This molecular arrangement and diversity in functional behaviour continue to appeal to engineers. In order to bring multi-functional materials, two or more materials are combined together to form a composite material. The classification is based on combination of materials and mechanics of these composites and is discussed in-depth. Various mathematical models are available in the literature to prediction the mechanical behaviour of composite materials were also presented. The mechanical behaviour of the composite materials, specifically particulate composite along with factors influencing their mechanical performance such as particle size, shape, density and interfacial bonding was also assessed in the literature review.

The typical manufacture route used for the fabrication of particulate composites involves uniform mixing of two or more materials followed by high pressure sintering. Applying high pressure and high temperature increases the density and connectivity of the composite materials. A similar manufacture route is used for fabrication of functional composites at high temperature, increases the grain size and therefore increasing the piezoelectric coefficient. Other manufacturing routes such as sol gel methods or different vapour deposition techniques forming thin films are highly complex process performed under extremely controlled atmosphere. They further require transforming in a designed shape by moulding,

pressing or similar other processes. These processes typically suffer from poor dimensional tolerances, porosity and other similar defects.

A micro fluidic device such as μTAS is a typical example where multiple processes such as separation and detection of various chemicals are preformed. The micro channels in the μTAS usually contains sensing and transducing device. Basic manufacturing route typically used for the development of functional micro fluidic device consists of series of processes discussed in Section 2.3.1. These processes are well established for micro fabrication on silicon wafers.

The AM techniques can manufacture high resolution and precision 3D components. These 3D components are typically manufactured in a layer-wise manner without using molds, dies or hard tooling. These techniques have been successfully employed in various sectors. Various manufacturing techniques were discussed in literature survey. Although, most of the commercially available AM machines are typically designed to fabricate single material components, they have been utilised for fabrication of functional composites and multi - materials. This can be further used for the development of complex designs for chemical reactors integrated with micro sensing devices, fabricated in a single build.

The discussions presented in the literature clearly highlight the mechanical and electrical behavior of the functional material composites along with usability of these materials for various applications. It was understood that the polymer material has always been a meritorious choice for the development of composites as offer ease of processing. However, development of these composites was considered by use of AM techniques instead of conventional routes discussed in the literature, followed by a brief review on the basic principle of AM techniques.

In order to demonstrate the application of development of functional material by AM, the manufacture of micro reactors were considered, as they require multitude of various disciplines and widely employed for various applications. Exploring the literature therefore suggests that the fabrication of part having functional materials using AM techniques in a single build can result in tangible micro reactors

containing functional devices, which has not yet been achieved yet.

2.6 Aims and Objective of the Research

The aim of this research is to investigate the feasibility of using AM techniques for the development of functionally active composites for sensing and actuating MEMS / micro reactors.

This aim can be reached by fulfilling following technical objectives:

1. To identify the feasibility of using the envisionTEC AM technique for the development of micro fluidic devices
2. To design micro reactors and employ them in real systems
3. To identify improvement areas for the performance of micro reactors
4. To development functionally active materials for use on the DMD based SLA
5. To identify the electrical and mechanical properties of the functional material build by DLP
6. To characterise the performance of polymer based devices
7. Develop methods to integrate functional materials into the sensing or actuating parts of micro reactor systems

CHAPTER 3

3.0 Materials and Methods

This chapter gives an overview of various materials considered for the experiments, along with a detailed description of the equipment and manufacturing parameters used for fabrication of the test specimens. The design, manufacturing and operational principal of apparatus used for analytical measurement are also discussed.

3.1 Manufacturing Equipment

The equipment used for the current investigation is described below:

3.1.1 envisionTEC Perfactory

The apparatus used for the current work was a digital light processing (DLP) based AM machine (envisionTEC Perfactory, SXGA, W/ERM, envisionTEC, Germany) with mini multi-lens. The envisionTEC Perfactory based SLA process uses DLP rather than a laser to cure the material. DLP is a projection technology containing a digital micromirror device chip (DMD) was invented by Texas Instruments in 1987 [234]. DMD is an optical device, which has hundreds of thousands of micro mirrors, arranged in an array. Each micromirror or a pixel on a DMD chip, may be independently rotated about its fixed axis. Non-rotating mirrors reflect light outside the work piece space resulting in a dark pixel in the resin. Rotating mirrors results in a exposed voxel (or volume pixel) of the material on the build plane.

The envisionTEC Perfactory is aimed at providing a cost-effective AM machine for the SLA process. Unlike most SLA machines, the system works with visible light [235]. The machine is simple to use and does not need any expert skill for installation. It is easily connected to a user's desktop computer for transfer of part data. It contains an embedded PC for data processing to enable it to function independently of the user computer.

Each slice is represented by a black and white bitmap as shown in Figure 24c, where black region represents void and white represents exposed material. These images are projected by the DLP chip onto the photopolymer resin, where the white region of the bitmap is illuminated, selectively curing the photopolymer resin.

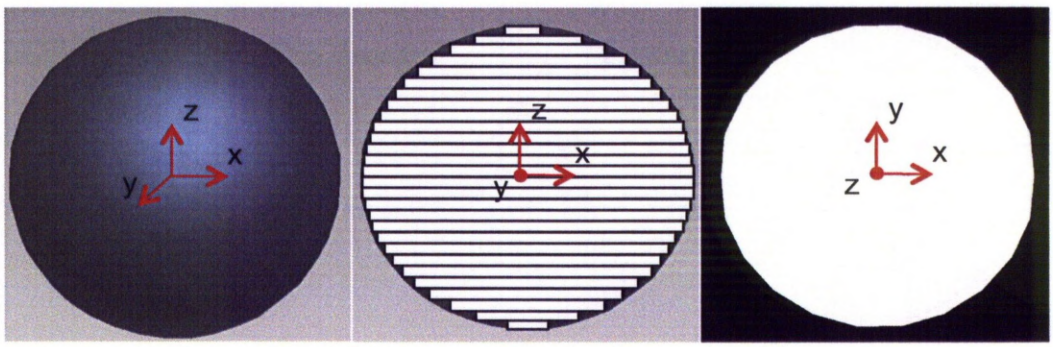

Figure 24: a) Front View of CAD Part, b) Slicing of Vertical Dimension of Sphere into Layers, c) Image Data Processed for Each Layer.

The schematic arrangement of the machine is shown in Figure 25. The build platform comprises of a thick glass slide held horizontally and a stepper motor that is capable of moving vertically to a tolerance of ± 6 μm. An independent embedded PC monitors the complete operation and controls the process during the transfer of the manufacturing data for each layer. An option for automatic and manual transfer of the CAD model provides operational flexibility to both, new and expert users.

The mask of each layer is projected from below into the resin by the DLP chip through the lens. Based on the image projected by the DLP chip, each active voxel is illuminated and cured [236]. Once the resin is cured, the stepper motor raises the platform by one layer thickness maintaining one layer thickness gap between the part and the glass. While the platform moves upward, it slowly peels the cured layer away from the bottom surface of the glass, allowing the liquid photopolymer to flow in to the gap between the part and the glass by the capillary action. The next layer is built following the same methodology and the process is repeated until the entire part is manufactured.

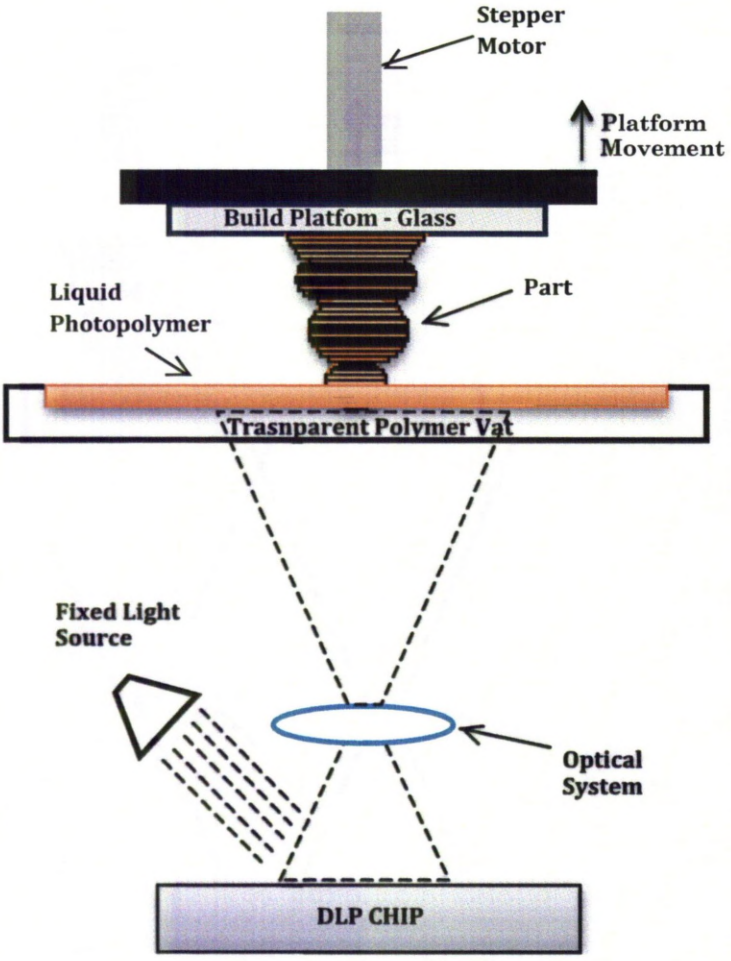

Figure 25: Schematic Representations of DLP Chip in envisionTEC Perfactory.

The final properties of the components are influenced by various parameters including beam intensity, exposure time, peeling velocity, waiting time, levelling, photo initiator concentration and layer thickness. Optimum selection of these parameters is needed to achieve the best mechanical and aesthetic properties of the part.

The building time of the DLP system is about 1 hr/50 mm of build height, irrespective of the complexities in the XY plane. The build envelope of the machine is dependent on the resolution and the number of pixels on the DMD chip and the zoom factor of the projection system. The system allows a choice of lens described in Table 1. The availability of enhanced resolution mode (ERM) offers manufacturing of components with fine detail.

Table 1: Build Envelope Project by Lenses with Various Focal Lengths.

Focal Length, (mm)	Length of Build Envelope Along X Axis, (mm)	Length of Build Envelope Along Y Axis, (mm)	Projection Voxel Resolution for DLP Structure, (μm)
60	84	63	60
75	45	34	32
85	27.7	20.8	20

The build envelope is the matrix of pixels projected through the optical lens. A lens with smaller focal length gives large builds envelope and lower projected resolution, and *vice versa*. There is therefore a trade-off between the build envelope and projection mask resolution.

The system used in this research (Figure 26) consists of a super extended graphics array (SXGA) DLP chip and 85 mm optical system resulting in resolution of 1400 x 1050 pixels on a build envelope of 27.77 mm x 20.8 mm on XY plane. This results in a pixel size at the specimen of 20 μm in the X and Y direction at a minimum layer thickness of 25 μm [235]. The system was chosen as it enables the highest-resolution available for the manufacture of micro scale structures. The procedure to manufacture a build on the DLP system is simple [237]. A CAD file is prepared using 3D modelling software and converted to a STL file. The manipulation of the STL file such as placing, reorienting, scaling, etc. needed to position the file within the manufacturing envelope of the machine and levelled with the build platform is performed in Magics™ X software (Magics™ Materialise, Belgium). Any supports required for the CAD model are generated and exported as *filename*_s.STL. Once the changes are made, the STL file is saved and recalled in the envisionTEC Perfactory RP software (version 2 is currently installed). Prior to manufacture, the build file is verified by the software for sliced layer thickness; placement; quantity of the parts; and build parameters defined in Table 2.

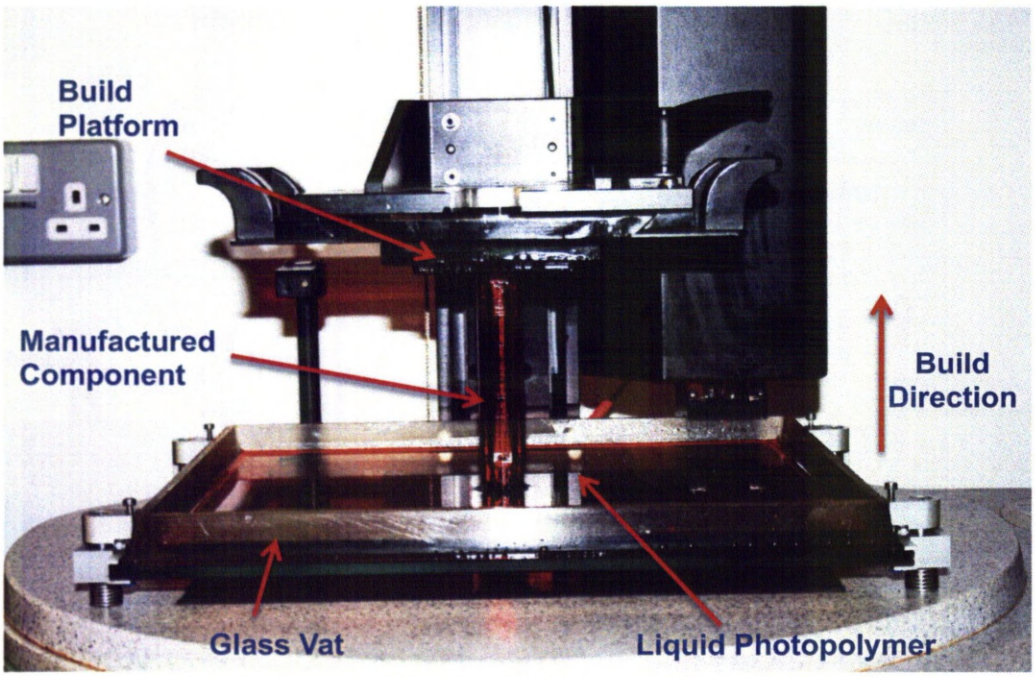

Figure 26: envisionTEC Perfactory mini multi lenses

Table 2: Default Build Parameters for 25 µm Layer Deposition for envisionTEC.

Build Parameters	Burn-in Range Default Values		Units	Standard Range Default Values	
	Minimum	Maximum		Minimum	Maximum
Separation Distance	2000	7500	µm	2000	7500
Exposure Time	500	20000	ms	500	20000
Velocity					
Peeling	300	2000	µm/s	300	2000
Levelling	300	2000	µm/s	300	60000
Waiting Time					
After Peeling	0	60000	ms	0	60000
After Levelling	15000	60000	ms	500	60000

Support generation is specific to the component geometry and is dependent on the operator. The Magics™ X software has a considerable number of features that makes it the ideal software for this application.

Perfactory StartCenter (addressed here as PF Slicer) is proprietary software developed by envisionTEC to transfer manufacturing data to the machine. Parameters for the burn-in range and standard range are assigned with this software. The burn-in range parameter defines the parameters of the initial 2 mm deposition on the base plate along allowing higher exposure during manufacture to form stronger supports for holding the build components.

The inverted nature of manufacturing in the DLP system means that the excess resin drains away due to gravity during the build. Once the manufacturing of the part has finished, the stepper motor moves upwards to the home position and the part is removed from the build platform by peeling.

The finished parts require cleaning in the ultrasonic bath (VWR International, Malaysia) with clean isopropanol for a minimum of 10 minutes. For the current investigation, the green parts were cleaned in the ultrasonic bath for 30 minutes and dried in open air, for a minimum of 60 hours, to avoid damage to the delicate structures. Functional materials manufactured using the DLP system were dried similarly.

3.1.2 Sputter Coating

Where parts require, gold coating (Gold coating disk – 99.9%, B7355A, Agar Scientific Limited, England) was completed by evaporation using a coating system (Edwards S150, Edwards High Vacuum International, United Kingdom). During the process, the parts were placed in the chamber with the surface to be coated facing upwards in the evaporation chamber and a vacuum of between 6×10^{-6} to 8×10^{-6} MPa was applied. The discharge current was typically 60 - 80 mA across the chamber. The parts were left in the chamber for between 15 - 20 minutes to ensure a consistent deposition of 2 – 4 μm of gold on the parts.

3.1.3 UV Exposure

For the current work, polymer specimens were also exposed to a UV radiation for curing using Lawtronics EPROM eraser ME5E (Astrosyn International Technology

Ltd, England). The UV source operates from 230 V at 50 Hz, emitting an exposure intensity of 4000 $\mu W/cm^2$ at a wavelength of 253.7 nm. Exposure time for different specimens vary based on the requirement.

3.2 Measuring Apparatus

The current investigation used various analytical techniques. The apparatus required for the analysis are discussed below.

3.2.1 X-Ray Diffraction

X-ray diffraction (XRD) patterns for the material specimens investigated were acquired using an X-ray diffractometer (Rigaku Miniflex, Rigaku Corporation, Japan). It consists of a source of X-ray, generated by accelerating electrons into a copper target. The emerging Cu Kα X-rays have a wavelength of 1.540 Å and energy of 8.04 keV; an absorber foil filters out unwanted wavelengths generated such as the $K\alpha_2$, $K\beta_1$, forming a monochromatic beam. Monochromatic X-rays interact with the crystalline material in a manner proposed by W. L. Bragg, following Bragg's law as [238]:

$$n\lambda = 2d \sin\theta \tag{3.1}$$

Where n is the order of diffraction, λ is the wavelength of the monochromatic rays, d is the spacing between the atomic planes and θ is the angle formed by the incident ray with the diffraction plane. θ is the angle recorded and knowing λ, d_{hkl} may be calculated.

The proprietary software for the Rigaku miniflex diffractometer is used to measure and recorde the X-ray diffraction pattern. The software allows post - processing options such as background radiation correction and the calculation of integrated peak intensities. A reference card index system is used to assign the crystal structure, indicating the size and perfection of their constituent crystallites and monitoring material phase. The X-ray diffraction pattern for $BaTiO_3$ was recorded

at 30 kV, 15 mA for Cu Kα (1.540 Å) with a scanning speed of 0.3°/min with a step size of 0.01° in 15 – 70° 2θ at room temperature.

3.2.2 Scanning Electron Microscopy (SEM)

The specimens for the current work were observed using various SEM apparatus used as listed in Table 3. All the test specimens were manufactured from polymer, and gold coated to achieve a conductive surface as mentioned in Section 3.1.2. Most of the test samples were observed at 25 kV accelerating voltage for the optimum resolution.

Table 3: SEM apparatus used for observation of test specimens

Instrument	Manufacturer	Type	Operating Pressure (MPa)	Accelerating Voltage (KV)
Hitachi S-2460N	Hitachi Ltd. Japan	Standard	$2.7x10^{-4}$	0 - 30
JOEL JSM-6610	Joel (U.K.) Ltd., England	Field Emission with EBSD	$2x10^{-4} – 3x10^{-4}$	0.3 – 30
JEOL JSM 7001f	Joel (U.K.) Ltd., England	Field Emission with EBSD	$5x10^{-5}$	0 - 40

3.2.3 Surface Profilometry

A white light interferometer (Wyko NT3310, Veeco, United States of America) was used for the examination of surface topography. The system contains an interferometer that splits a coherent beam of light from an existing source into two beams and recombines them after passing over the specimen as shown in Figure 27. The fringed pattern generated by the interference of the beams is similar to a contour line on a map, indicating topography of a surface.

This system was used to measure the surface roughness of the specimens. The machine can run phase shift interferometry (PSI), vertical scanning interferometry (VSI) and a combination of both PSI and VSI in an approach known as enhanced vertical scanning interferometry (EVSI). For the current work, VSI mode was used at 50x magnification.

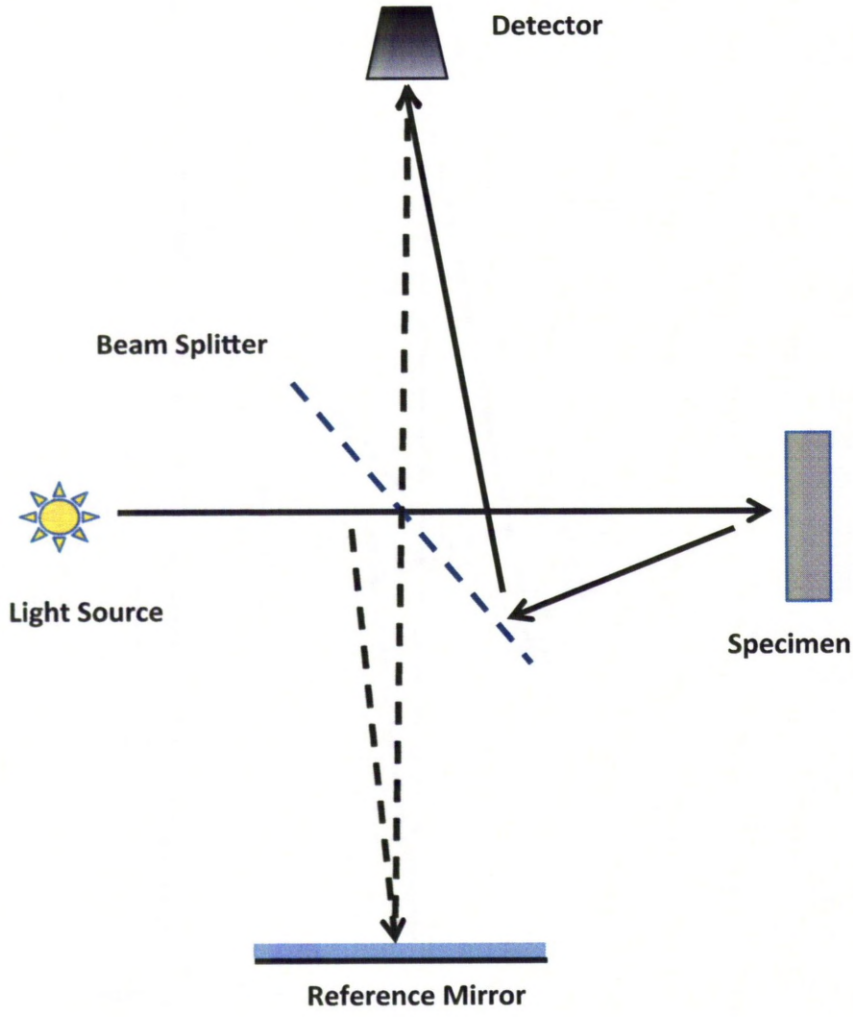

Figure 27: Simplified arrangement of Wyko NT3310 interferometer

3.2.4 Piezoelectric Measurement

The piezoelectric coefficient d_{33} was measured using a piezometer (Piezometer PM300, Piezotest, United Kingdom), consists of a force head connected to an electronics unit with a display panel showing the piezoelectric property under observation. The specimen is inserted between force heads and clamped by winding the armature, closing the gap between the specimen and the curved force head. The piezometer offers a wide range of operational flexibility, and has a measuring range of 10 pC/N to 1000 pC/N. The test frequency of 110 Hz was chosen for measurement with a force of 0.25 N. The frequency of the apparatus

can be varied from 30 Hz to 300 Hz. Since d_{33} is temperature dependent, the force heads contain a reference sample, which compensates for the effect of temperature linearising response. The measurements of piezoelectric materials were carried out at standard temperature and pressure.

The system has four operational modes d_{33}, capacitance, loss (Tan δ) and their combination can all be measured and displayed. The force heads are connected to positive and negative input terminals that were connected to the differential amplifier circuit. This circuit prevents mains borne interference from being amplified and reduces the effect of any stray fields.

3.2.5 Tensile Testing

Mechanical properties of the photopolymer specimens built on the envisionTEC were assessed using a uniaxial testing machine (Instron 3342, Instron, United States of America). The tensile test specimen was held between two wedge grips. The dimensional details of the test specimens were fed into the software. A computer controls the strain rate of the test specimen, while it undergoes testing and the computer software simultaneously records the test data.

A standard operating procedure was defined in the software controlling the machine. All the dimensional details of test specimen such as gauge length and cross sectional area in the gauge length were input and the crosshead speed was set to 1 mm/min. Once the specimen was clamped into the machine, the location of the clamps was set to 0 and the tensile test was started. The data from the measurement was saved in the computer and exported as CSV file for further analysis.

3.2.6 Particle Size Analysis

Particle size analysis of the powder was completed using a laser diffraction based particle sizing machine (Mastersizer 2000, Malvern instruments Ltd., United Kingdom). The analysis of the particles is driven by standard operating procedure

(SOP) for laser diffraction particle sizing [232]. The parameters defined in the operating procedure for measuring $BaTiO_3$ powder are shown in Table 4 below.

Table 4: Parameters Defined Measuring Barium Titanate Powder.

Parameters Defined in the SOP	Value	Units
Powder Density	5850	kg/m^3
Refractive Index	-	2.42
Pump Speed	rpm	3500
Ultrasonic Displacement	µm	0
Number of Observations	-	10

In laser diffraction, the particles diffract the laser beam and the diffraction angle of the beam is inversely proportional to the particle size. Photo detectors, positioned to achieve maximum resolution across the broad range of particle sizes, detect these diffracted beams measuring the diffraction angle of the beam. The system can measure particle size ranging from 0.02 µm to 2000 µm, based on Mie scattering model for the calculation of particle size for wide range of scattering angles. Mie scattering theory considers light scattered by an isotropic sphere surrounded by the homogeneous medium. Although this theory consider only perfect spherical particles, it is has been used to measure scattering and absorption properties of non – spherical particles.

3.3 Poling Apparatus

In order to generate a piezoelectric effect, the piezoelectric composites must be poled under a high electric field at constant temperature. For smaller size composites, geometric field amplification leads to frequent voltage discharges making the poling of small composite components challenging. A poling station was designed and manufactured based on the poling methodology described in Chapter 2 and shown in Figure 4. The approach was suitable for holding a high

voltage (typically 30 kV) across the small size composites at elevated temperatures. Poling of these composites whilst completely submerged in silicone oil reduces the probability of a voltage discharge through the air as silicone oil has a higher permittivity than air.

Silicone oil (CAS 63148-62-9) (Sigma Aldrich, United States of America) 100 wt%, was used as the poling medium up to 200 °C in the poling apparatus. It is a clear, colourless, odourless liquid that is insoluble in water and has a flash point of 300 °C.

The construction of the poling apparatus is show in Figure 28. The composite is submerged in the beaker with the voltage terminals in contact with the composite. The electric field was generated by a power supply (Alpha Series, Brandenburg Ltd., England) and is applied across the composites while they are submerged. The beaker is lowered in to the oil bath (SEBA, United Kingdom) until the temperature in the beaker reaches the poling temperature. The beaker is then removed from the oil bath and cooled to room temperature without removing the electric field from the specimen.

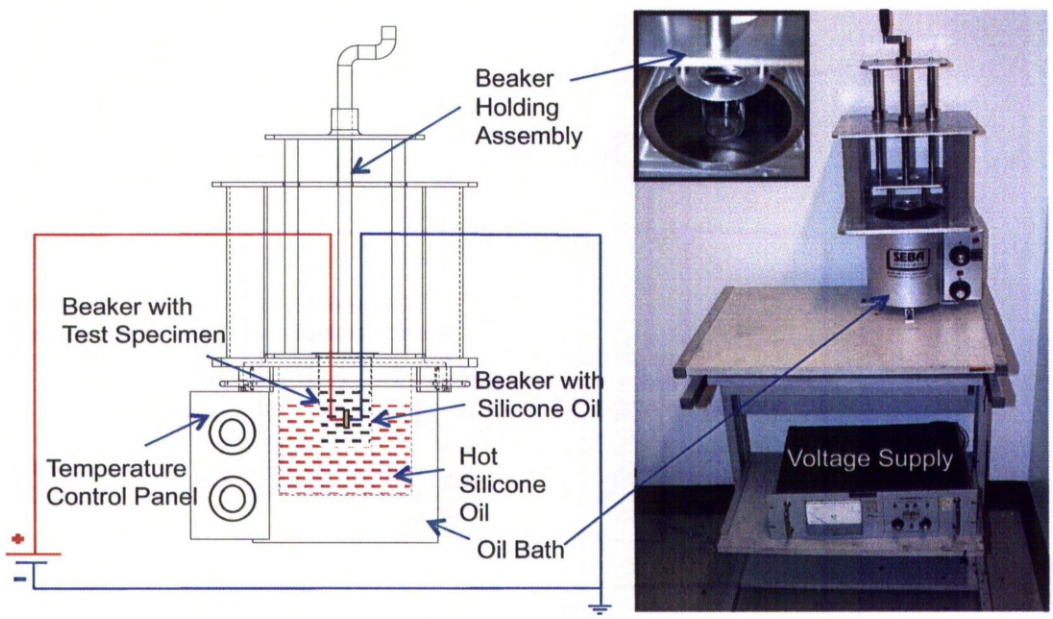

Figure 28: View of CAD Model of Poling Apparatus (Left) and Fabricated Assembly of Poling Apparatus (Right).

The $BaTiO_3$ composites were poled as descried below:

- The specimen is held between the voltage terminals
- The specimen is submerged in the beaker filled with silicone oil
- The voltage is applied across the specimen with the poling voltage kept constant for each run
- The oil bath is switched on and the silicone oil is heated in the oil bath to a predetermined poling temperature
- The beaker is lowered in to the oil bath
- Once the silicone oil in the beaker reaches the test temperature, the beaker is lifted upward out of the oil
- The silicone oil in the beaker is cooled to room temperature without removing the voltage field across the piezoelectric specimen
- Once the temperature of silicone oil reaches room temperature, the voltage field is switched off and the composite material is removed
- Each run is conducted at a constant voltage field and a specific poling temperature

3.4 Materials Manufacturing

The following section describes the materials used in this study.

3.4.1 Barium Titanate

Barium titanate (99%) powder - $BaTiO_3$ (99.9%-Ba) (CAS – [12047-27-7] FW: 233.21) (Strem Chemicals Inc., United States of America) was used in the current work. The powder is opaque white in appearance and has Curie temperature of 120 °C ± 4 °C. Figure 29 below shows the particle size analysis for the $BaTiO_3$, shows that the majority of the particles are in the range 0.3 μm - 6 μm, with a mean of 1.75 μm. Small percentage of the particles of the order 10 μm is apparent in the sample analysed.

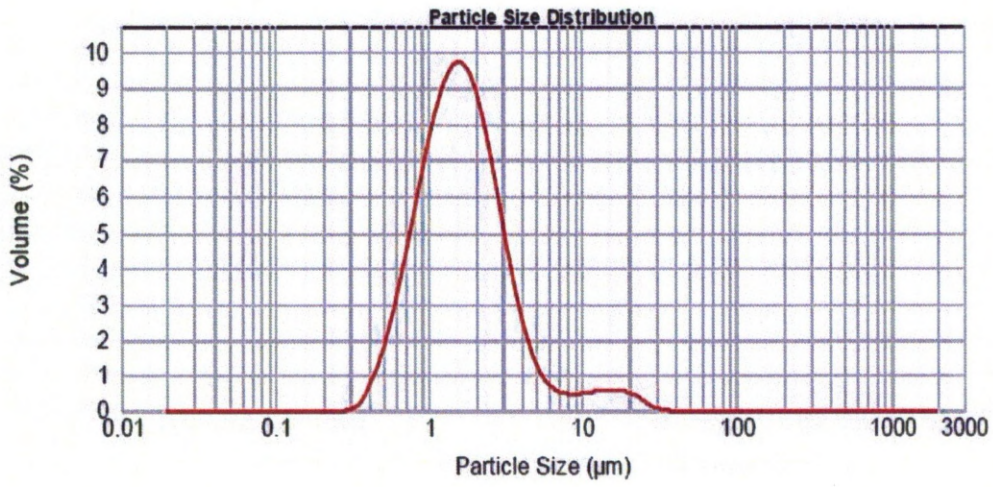

Figure 29: Particle Size Analysis for $BaTiO_3$ Ceramic Powder

The $BaTiO_3$ ceramic is mixed with photopolymer resin to produce composite specimens. Since, this work concentrates on manufacturing of devices with features on the micron-scale, the particle size of $BaTiO_3$ is crucial as it affects the minimum feature size possible with the manufacturing equipment.

X-ray diffraction was used to confirm the phase of the $BaTiO_3$. The diffraction pattern is shown in Figure 30 confirms the tetragonal phase of piezoelectric $BaTiO_3$, (reference card no 5-626, STOE WinXPOW, version 1, Germany). Hence the powder is piezoelectric.

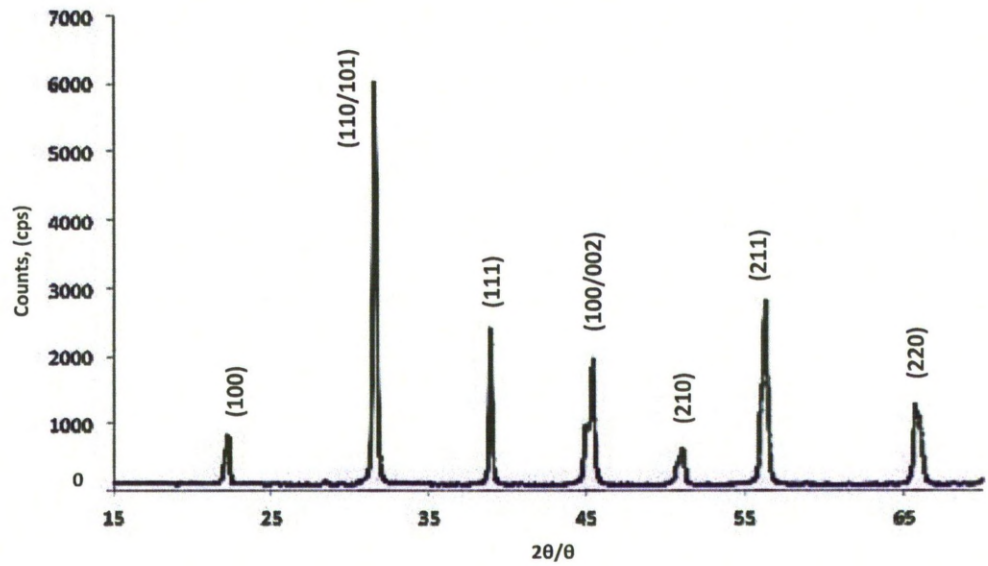

Figure 30: XRD Analysis of $BaTiO_3$ Ceramic.

3.4.2 Photopolymer

The photopolymer used in the DLP system is suitable for 50 - 150 µm voxel fabrication on the envisionTEC system. It is an acrylic resin having a material composition of Pentaerythritoltri / tetra-acrylate (CAS 4986-89-4) + 1,1,1 Trihydroxymethylpropyl - triacrylate (CAS 15625-89-5, 3524-68-3). It is otherwise known as polymethylmethacrylate (PMMA) and is supplied by envisionTEC using the pseudonym R5 – a general purpose building material for production of RP models.

Perfactory R5 is a dark orange in colour with a density of 1215 kg/m^3 and a glass transition temperature of 120 – 150°C (DIN53765). It is viscous liquid with a viscosity of 643.1 mPa.s (DIN 1342-2).

3.5 Slicing Software

Software tools used for slicing of CAD files and loading job files and the proprietary software Perfactory StartCenter along with a bespoken software tool for adaptive slicing are discussed below.

3.5.1 Perfactory StartCenter

Perfactory StartCenter was used in the current investigation. It is the proprietary software that is used for uploading component job files onto the envisionTEC machine. The CAD file is processed as discussed in Section 3.1.1.

3.5.2 Customised Slicing

The adaptive slicing algorithm (ASA) was based on the standard machining algorithm for CAM-style slicing. It was originally written on the Spiral Growth Manufacturing (SGM) project for rotational printing in C++ and Python [233]. It is based on conventional computer aided manufacturing (CAM) and requires the specification of a tool geometry to produce the slice data. The algorithm considers a contour data at a height "Z" by forming a grid slightly larger than the cross section

of the component. The contour or tool path is then calculated from the tip centre by passing the tool along grid lines as shown in Figure 31. Contour points are identified when the tool shape intersects the surface of the STL file.

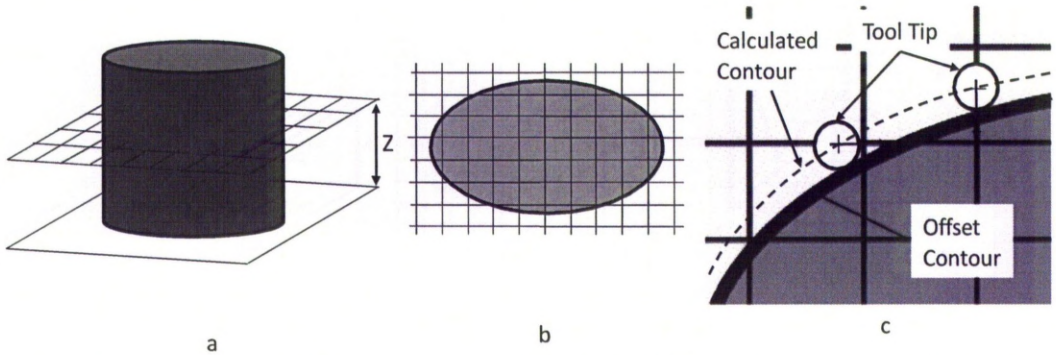

Figure 31: (a) Location of Slice Height in Z Direction, (b) Slice Contour and Grid, (c) Calculation of Contour Data With Tool Tip.

The resolution of the contour data is governed principally by the resolution of the grid, which is user specified. The size of the tool tip determines how efficiently the tool can navigate small features and internal corners. For the current work, the grid resolution was set to 0.01 mm and the selected tool was described as a flat disk with a radius of 0.05 mm. These parameters were chosen as a trade-off between slice calculation and contour resolution. The observed processing time of 8 minutes to generate data was comparable to the standard PF slicer.

Build accuracy, resolution and build time were improved by adopting additional features such as detection of Z height position of all horizontal surfaces as shown in Figure 32a. The layers considered for ASA can be either defined manually, or can be automatically modified by reducing the stepping effect with the geometric profile of the STL file (Figure 32b). This is achieved by calculating the largest step value between the current layer z_{hi} and the layer below z_{lo} (Figure 32c). If the step change is greater than a user defined threshold value then a second slice is taken half way between z_{hi} and z_{lo} and the calculation repeats. The iterations continue until the maximum step change equals or falls below the assigned maximum value. All contour data for the layers is stored within a single directory where keys (Z height and contour type) point to the data point arrays.

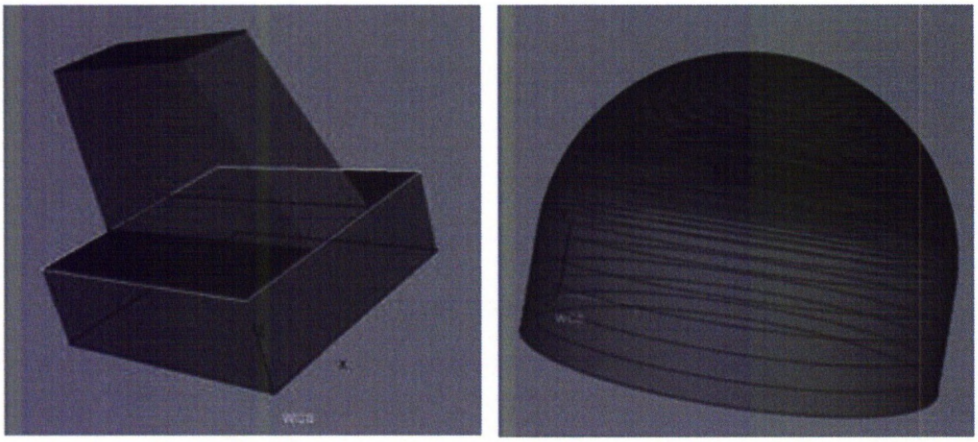

a) b)

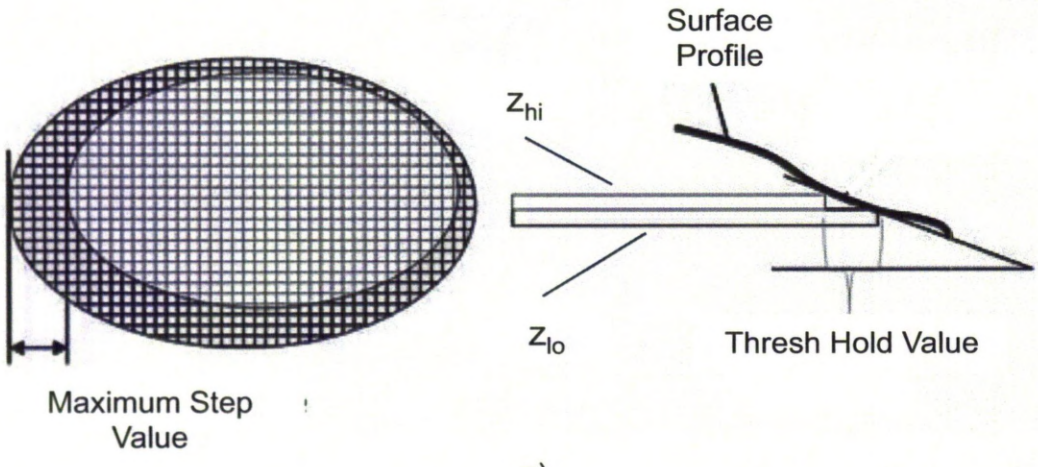

c)

Figure 32: (a) Detection of Flat Planes, (b) Adaptive Slicing and (c) Calculation of Slice Height in Adaptive Slicer.

The adaptive slicing methodology requires new process parameters because of its ability to vary the layer thickness. Different parameters are used for the various layer thicknesses. In order to define a set of new parameters for these layer thicknesses, the standard Perfactory settings were adopted. The parameters recommended for the material were used for manufacture of test specimens with the time of exposure (T-Exp) interpolated from standard Perfactory, settings for 25, 50 and 100 µm layers. The curve shown in Figure 33 was fitted to the data from Table 5.

Table 5: Default Exposure Time and Projector Brightness Used for Calculation

Parameter	25 µm Layer	50 µm Layer	100 µm Layer
Burn-in Range Exposure Time (ms)	7000	10000	12500
StandardRrange Exposure Time (ms)	3000	4500	6500
Projector Brightness (mW/dm^2)	530 - 580	530 - 580	530-580

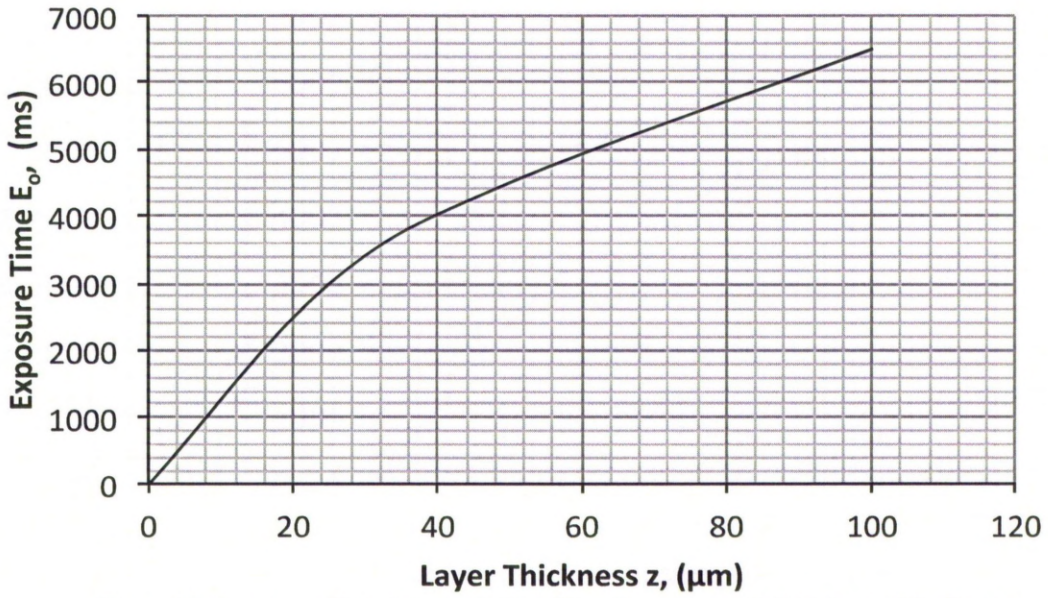

Figure 33: Exposure Time Interpolation From Recommended Values of Perfactory.

Like Perfactory StartCenter, the ASA code is simple to use. The protocol below was followed when preparing ASA files:

- Open the STL file in the ASA software tool
- Choose the format for the job file option (*.zip file or *.job)
- Specify radius and offset of the slicing disk
- Define the slice resolution, slice difference and layer thickness
- Define build parameters using data shown in Figure 33
- Generate the job file
- Transfer the job file using Perfactory Direct

The bit map image generated from the slice data of the part by applying an imaging function to the contour and creating image masks for each layer. Once all of the image masks are generated, they were saved along with an XML file that contains all machine and layer parameter settings that creates the job file. Images were first scaled according to the resolution of the DMD processing chip and the size of the projected area of 1400 x 1050 pixels. An image in PNG format, suitable for the resolution of the DMD chip, is then created with all pixels initialised from the origin. Filled polygons are created in each black & white image representing the layer to be manufactured. White represents the cured material that is hardened and black is uncured material. Since each sliced layer was formed from a centralised PNG image, the potential to build multiple parts in a single build operation is currently not supported.

There is one noticeable difference between the ASA software and standard software. In comparison to the typical Perfactory bitmap, the images generated on the ASA software, have different edges (Figure 34). Image masks created using the ASA program were comparable with image masks created using the PF slicer in terms of density. However the Perfactory system had a lower intensity grey scale border that was absent in the ASA system.

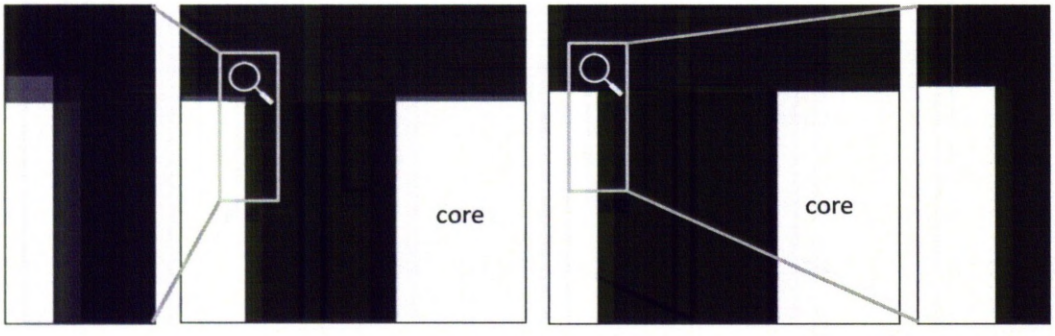

Figure 34: (a) Perfactory Image Mask Showing Grey Scale Border and (b) ASA Slicer Image Masks Showing No Border.

This grey or blurred edge was thought to be due to the standard software working in enhanced resolution mode (ERM). The ERM implemented by the PF slicer is intended to improve part resolution and surface roughness. When the ERM is

active, the Perfactory software suite processes each layer twice. Each repeated layer is digitally offset from the first by shifting the projection the image by one pixel in both x and y directions, having higher intensity in the second image mask. Unfortunately, no information was available for ERM mode in the present study.

CHAPTER 4.

4.0 Additive Manufacturing of Micro Fluidic Reactors

Micro reactor engineering has been gathering increasing attention from chemists and engineers across the world [148][241]. Experimental development of micro reactors has enabled new methods to control chemical reactions, exploring the possibility of achieving high yield with low chemical volume and high-energy efficiency [242]. This has been particularly evident for systems involving hazardous chemicals where micro reactors offer an alternative to their large-scale counterparts. This chapter considers the suitability of the digital light processing (DLP) system for manufacturing micro reactors. The results obtained from various analytical techniques are discussed further.

4.1 Preliminary Micro Fluidic Devices

Preliminary work involving the manufacture of micro fluidic devices by DLP has been undertaken to assess factors such as the build rate and feature size [237]. Here micro fluidic devices were manufactured from standard R5 polymer with an optical lens of 60 mm focal length, as described in Section 3.1.1.

4.1.1 Design of Preliminary Microfluidic Devices

The preliminary reactor consists of a main channel connected to intermediate side channels. The main channels were 100 μm wide connected to 25 μm wide small channel and side channels of 20 μm width. The nomenclature used for these channels is shown in Figure 35 and Figure 36. In order to assess the effect of the build direction, the reactors were manufactured in four orientations namely, horizontal (sample 1), vertical (sample 2), 10° (sample 3) and 20° (sample 4) as shown in Figure 36.

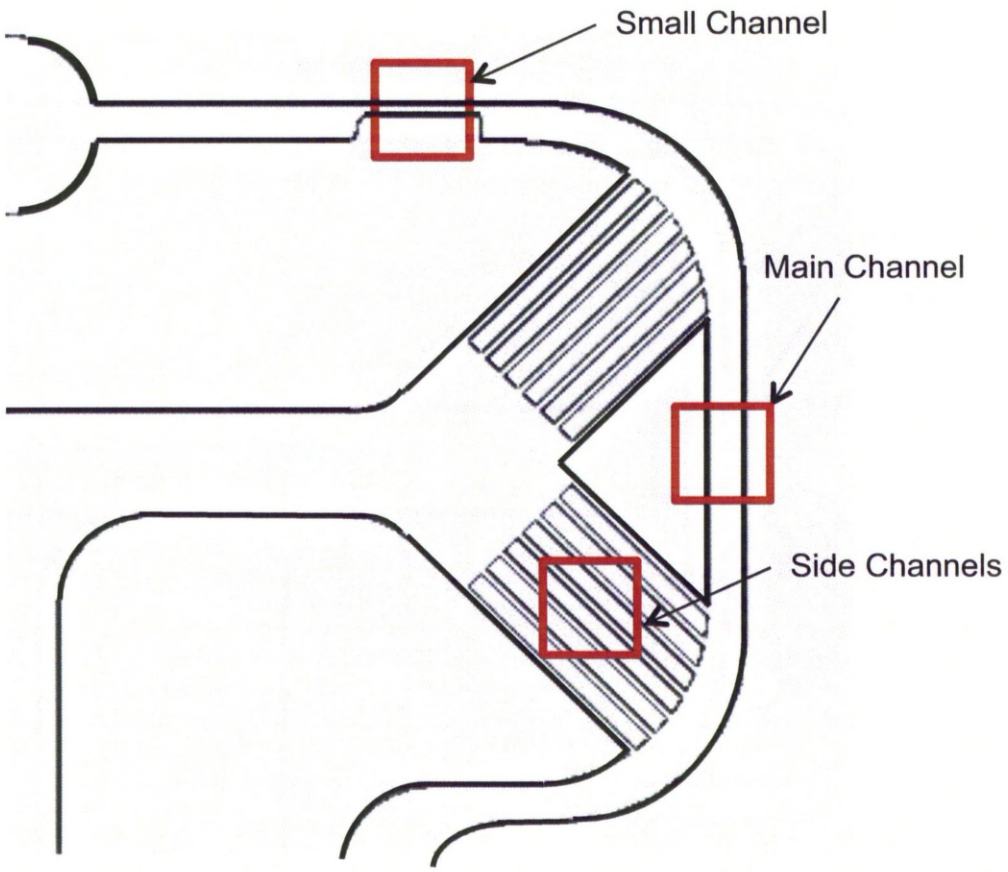

Figure 35: Nomenclature for Micro Channels Manufactured in Preliminary Samples [243].

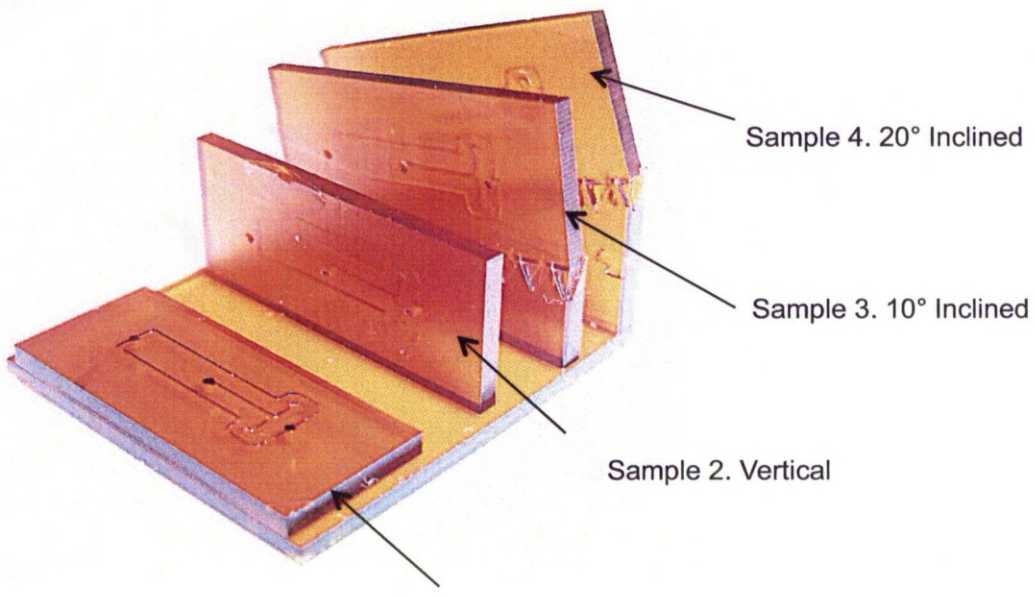

Figure 36: Nomenclature for Preliminary Micro Fluidic Devices Manufactured at Varying Orientation [243].

The channel dimensions of the as-built samples were measured using the Wyko NT3300 white light interferometer and optical microscopy at the University of Cambridge [237]. The optical micrograph in Figure 37 shows that the DLP methodology is suitable for manufacturing microfluidic channels. The boundaries of the main channels were sharp and clear. However, the edges of side channels and smaller channels were uneven having a serrated appearance. This effect becomes more prominent in sample 2, sample 3 and sample 4.

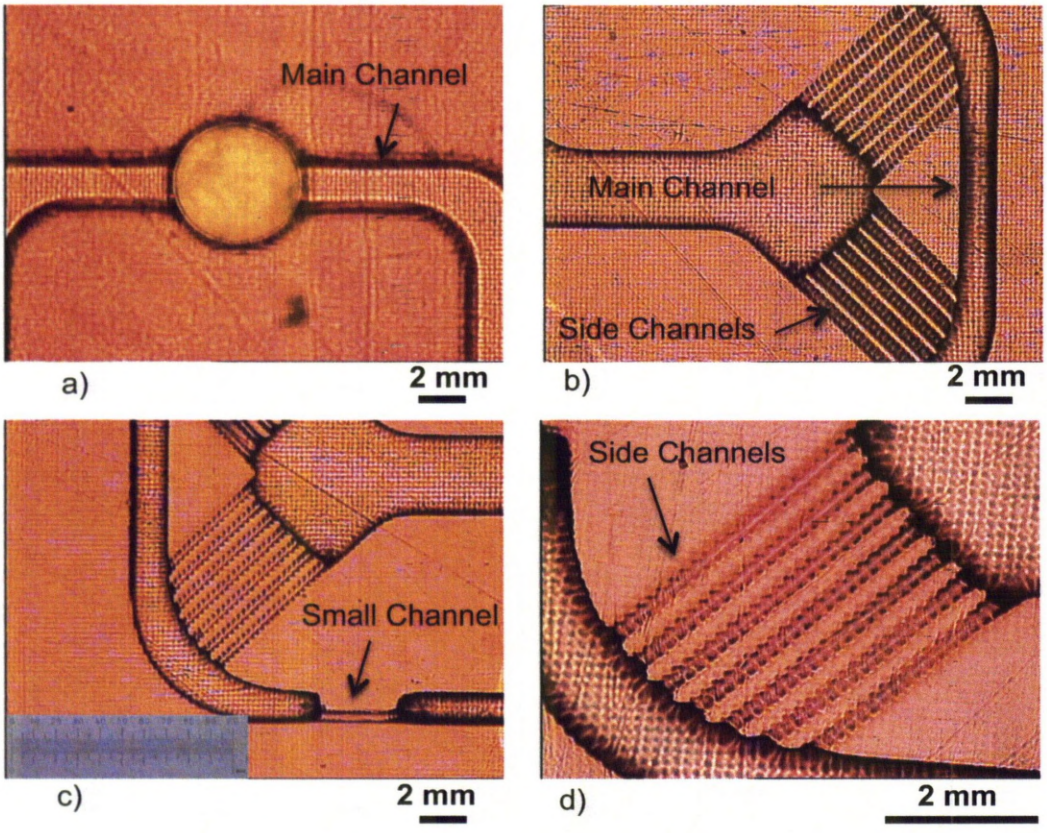

Figure 37: Optical Micrographs of a) the Main Channel, b) Main Channel and Side Channel, c) Small Channel and d) Magnified View of Side Channels [243].

4.1.2 Interferometry of Micro Channels

It was also observed that the width of the micro channel was larger than specified. Table 6 shows a comparison between specified and as built dimensions. The cross sectional profiles for most of the channel were either "U" or "V" shaped. Shown in Figure 38.

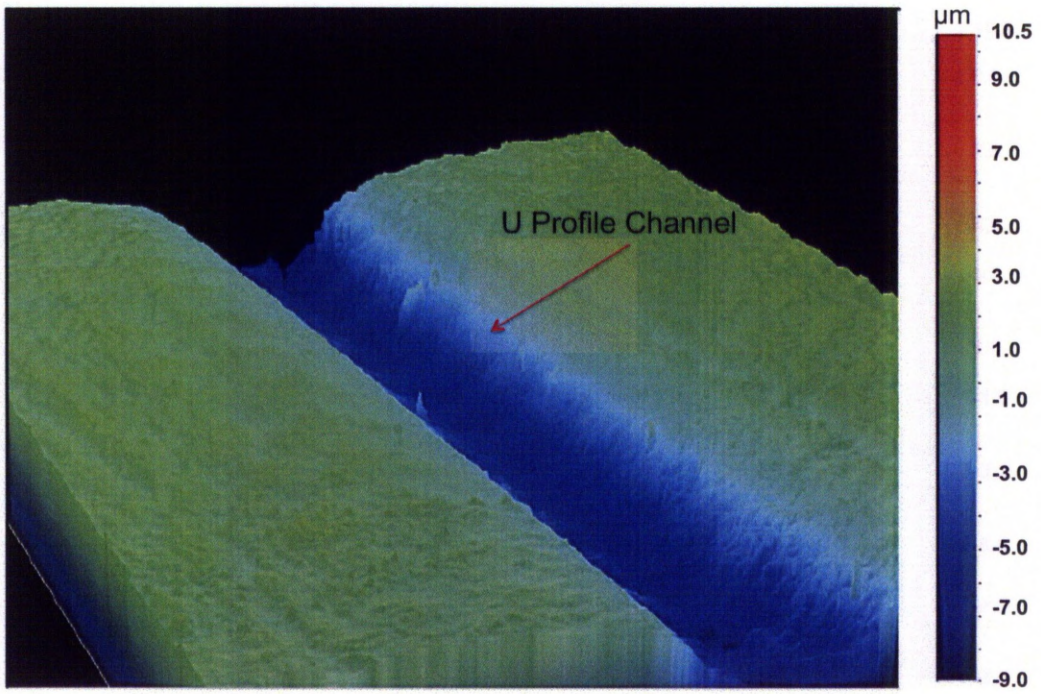

Figure 38: Surface Profile of Sample 1 Showing Noticeable U-Shaped Small Channel Profile [243].

The result shows that the width of the main micro channels was larger than intended as shown in Table 6. The discrepancy was found to be as high as 50%. The dimensions for the small and side channels were however difficult to quantify due to the surface roughness caused by the serrated edges. Micro channels with 20 µm and 25 µm widths on inspection were found to be almost blocked with partially curved resin. The surface roughness, analysed by the white light interferometry, shows an increase with an increasing inclination for the manufactured micro channels. Table 7 summarises these results.

Table 6 and Table 7 indicate that measurement of some of the features was not possible. The apparent surface roughness could be the result of stair stepping effect that was prominent in main channels. The roughness measured for main channel and side channel was similar for sample 4, irrespective to the size of the channels. Horizontal manufacturing was the preferred direction as it gives the lowest surface roughness.

Table 6: Comparison of Required and Measured Dimensions of the Micro Channels

Samples	Channel	Width, (μm)	Depth, (μm)
As Designed	Small	25	100
	Main	100	100
	Side	20	100
Sample 1 - Horizontal	Small	67	8.8
	Main	157	93
	Side	Not measured	5
Sample 2 - Vertical	Small	80	21
	Main	Not measured	Not measured
	Side	Not measured	Not measured
Sample 3 - 10° Inclination	Small	90	24
	Main	Not measured	34
	Side	Not measured	Not measured
Sample 4 - 20° Inclination	Small	88	24
	Main	125	29
	Side	Not measured	12

Table 7: Surface Roughness Measured for The Micro Channels.

Sample	Small Channel	Main Channel	Side Channel
	Average Roughness R_a, (nm)		
Sample 1 - horizontal	170	450	Not measured
Sample 2 - Vertical	320	Not measured	Not measured
Sample 3 - 10° Inclination	480	700	Not measured
Sample 4 - 20° Inclination	570	480	Not measured

Interferometer measurements for the small channel of sample 1 are shown in Figure 38. A noticeable U-shaped profile is apparent for the small channels and the surface roughness of 1 μm is observed on the flat surface. However, Wyko

micrographs (Figure 39) observed for the main channel shows an inability to measure the surface of the steep sides because the method is essentially line of sight.

Samples 2 and 4, in Figure 40 and 41 respectively, show an asymmetric cross-section, with one edge of the channel having a greater slope than the other. The stair stepping effect is evident in the micrograph for sample 2 and 4 (Figure 40-41).

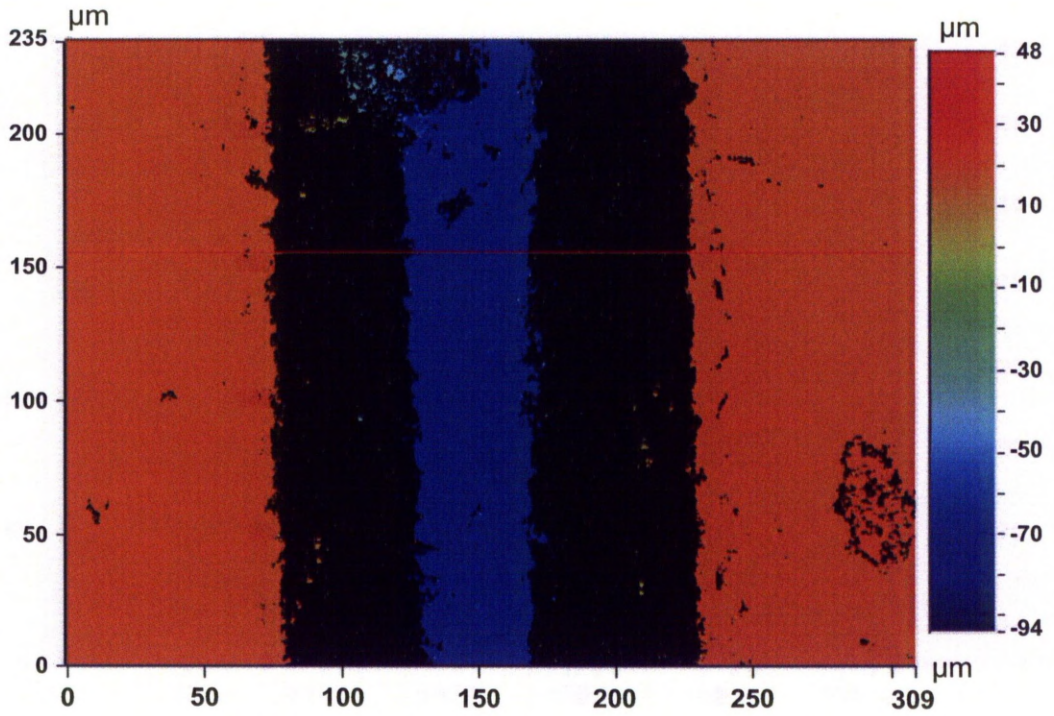

Figure 39: Surface Profile of Main Channel of Sample 1 Showing Black Region of Lost Data Due To Slope [243].

4.1.3 Discussion

The conclusions from the analysis of the micro fluidic devices manufactured in four different orientations, is that the horizontal manufacture is the preferred orientation. Although the accuracy of some features on sample 1 was poor, notably the depth of the channels, the symmetry of the channel cross-section was superior.

The micrographs shown in Figure 40 and Figure 41 shows polymer structure extending from the channel surface. As the channels in both the Figures were

fabricated vertically, these extended surfaces were formed due to over curing of the layers above the geometry, partially curing the layer below, leaving some semi-cured resin behind after cleaning. The stair stepping effect occurring in the sample 2 and 4 evident in Figure 40 and 41, also show poor surface resolution and part quality in vertical direction. Further, the layers manufactured in the vertical build were insufficiently supported and fails due to lack of strength to retain its shape, results in formation of curved profile as evident from Figure 40.

In order to increase the resolution of the machine, the optics was modified. This was achieved by the use of an optical lens with a focal length of 85 mm resulting in a resolution of 20 µm. However, the build envelope also reduces significantly as shown in Table 1. This configuration offers the best resolution for manufacturing of builds with fine details and small feature sizes. Similarly, using thinner layer thickness for manufacturing will reduce the stair stepping and hence reduces surface roughness of the manufactured components.

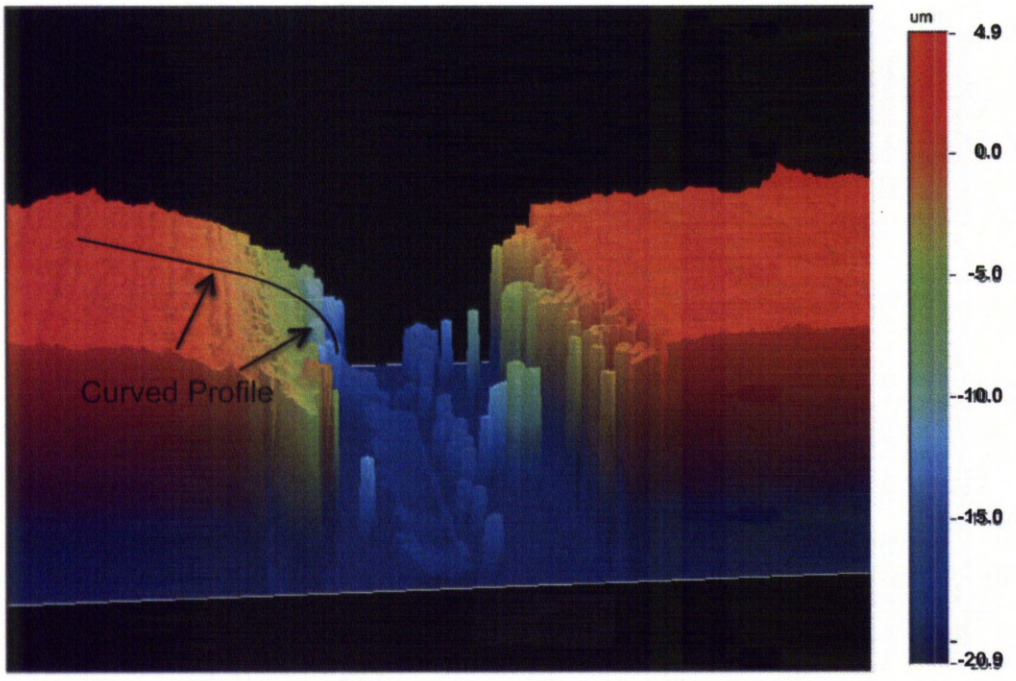

Figure 40: Surface Profile Observed for Small Channel of Sample 2 [243].

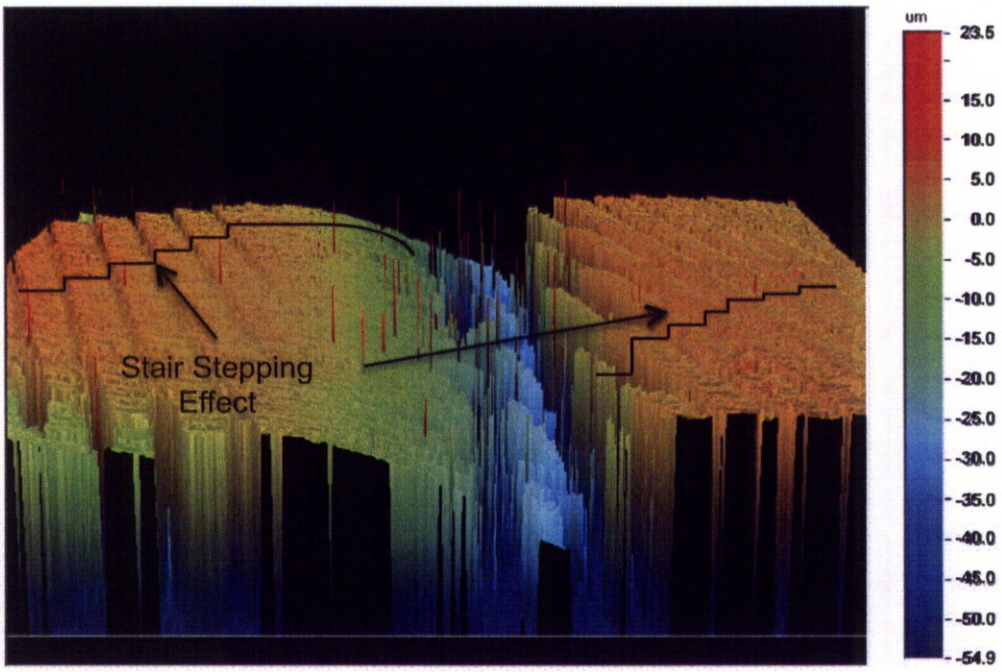

Figure 41: Surface Profile Observed for Main Channel of Sample 4 [243].

4.2 Development of Micro Reactors

In the present work, a mixer reactor was developed as a bioreactor for the seeding and growth of cells. A detailed discussion on the design and assembly of polymer micro reactors along with the experimental set used for bioreactor application is presented. This follows by the results validation the use of micro reactor for cell growth application.

4.2.1 Design of Polymer Micro Reactors

The mixer reactor was designed with micro channels, which were open at the top and bottom faces. Both the plates of the micro reactor were then fixed to a glass slide by spin-coating a layer of epoxy adhesive onto the slide ensuring a uniform thin adhesive layer over the glass surface to avoid blocking the reactor channels with excessive adhesive. The top plate of the reactor has a separate channel similar to the bottom plate and was designed in such a way that it closely fits onto the bottom plate that locating on the protruding connection boss. The reactor consists of two inlet connecting ports and one outlet port, shown in Figure 42. Both the

inlet channels form a "T" joint, which facilitates the mixing of fluids before entering the main channel. The inlet and outlet port on the bottom plate enters the system via a rectangular extension, which acts as a connection boss for the inlet ducts; and also as a locating lug for the top plate of the reactor. Inlet and outlet ports for both channel parts were designed to accept pieces of 1/16" PEEK connector tubing.

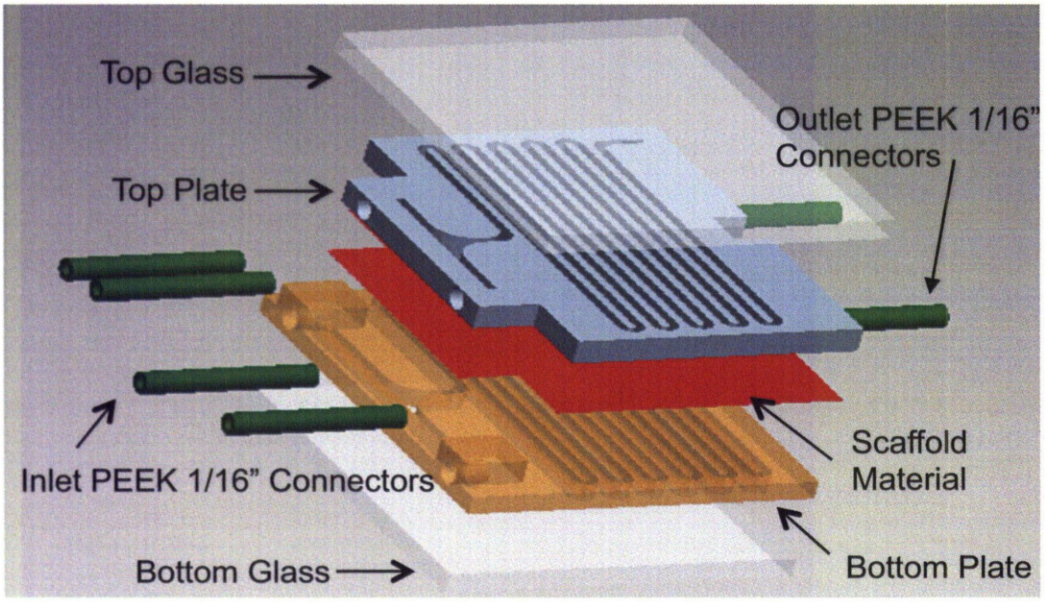

Figure 42: Exploited View of the Polymer Micro Reactor Assembly.

The polymer micro reactor was manufactured using the DLP system fitted with an 85 mm lens from the standard R5 polymer resin at 25 µm layer thickness. The reactors were manufactured in horizontal direction outlined in Section 3.1.1 to ensure sufficiently accurate feature resolution. The manufacturing time for each plate of the micro reactor was 3 hours. Following the description given in Section 3.1.1 completed the post-manufacture cleaning and curing of the micro reactors. Figure 43 shows the completed assembly of micro reactor used for bioreactor application.

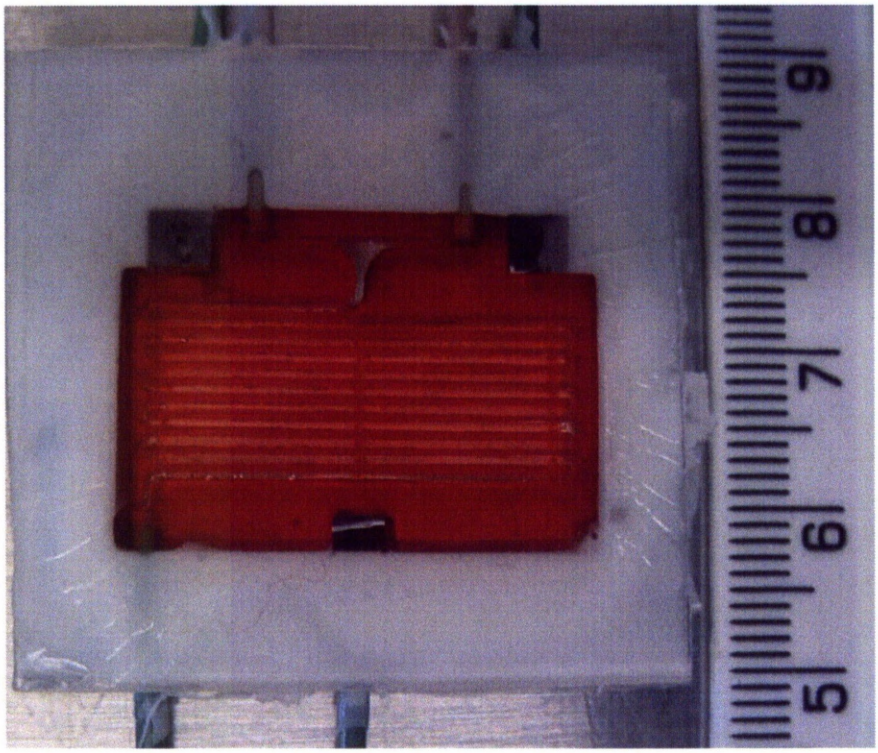

Figure 43: A View of Glass Lined Polymer Micro Reactor Connected to Inlet and Outlet Ports.

4.2.2 Experimental Arrangements

The polymer micro reactor was tested at the University of Bath [244]. The device was connected to an automated perfusing circuit via which the reagent chemicals were continuously supplied to the cells growing on the scaffold. The typical chemical constituents used for the process are listed in Table 8.

The complete process arrangement is shown Figure 44. The micro reactors and PDMS were sterilised by passing 70% ethanol and washed with sterile phosphate buffer saline (PBS). A poly di-methyl siloxane (PDMS) membrane of 20 mm x 22 mm in size was sterilised *in situ*, whilst placed between the both the plates of the reactor. A PDMS film of 120 µm thickness was placed between the reactor plates as a growth surface during the process. Autoclaved tubing was used to connect the reactor to the vessel and pump, which is schematically shown in Figure 45. The chemicals were circulated through the top and bottom plate of the micro reactor by a computer controlled system.

Table 8: List of Chemicals Supplied for Growth of Cells in Tissue Culture

Name	Use
DMEM	A mixture of chemicals used to maintain cells in tissue culture
PBS	To maintain ionic concentration of the medium
Trypsin	Widely used for dissociation of tissues usually combined with EDTA
EDTA	Helps in removing the cell from the growth surface
PDMS	Membrane used as cell growth surface

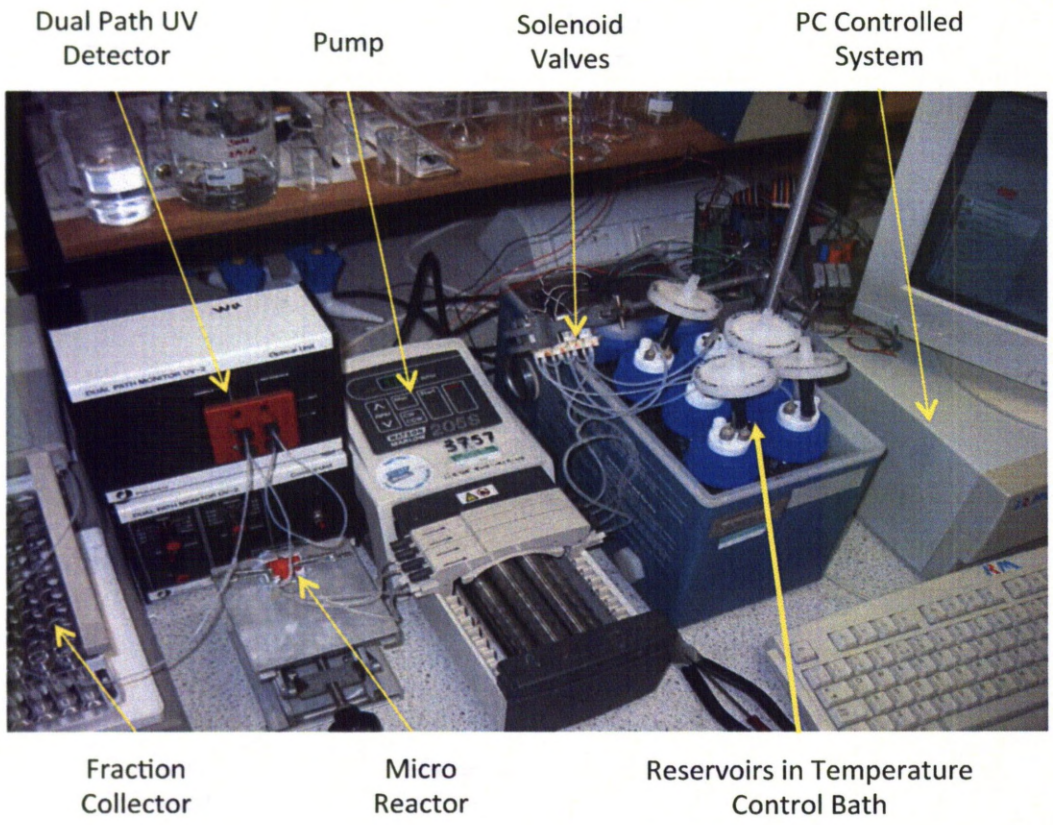

Figure 44: Experimental Setup of Polymer Micro Reactor [244].

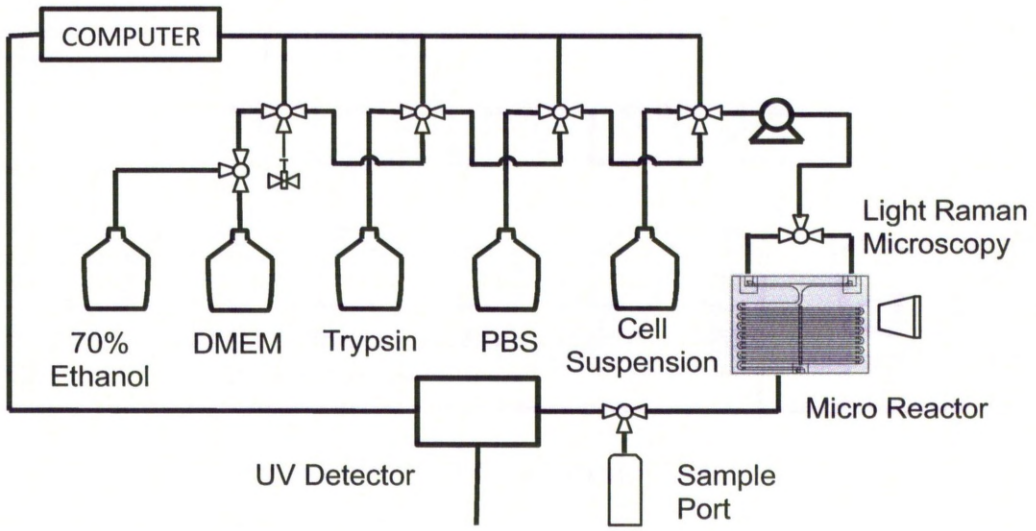

Figure 45: Schematic Process Layout for Micro Fluidic Polymer Reactor [244].

Once the polymer micro reactor is connected to the reservoirs, it can be used to provide specific functions, such as sterilisation, delivering cell media, cleaning and enzyme isolation. The reaction progress in the micro reactors was analysed using dual path UV detector located before the fraction collector where samples were collected at various set times throughout the experiments. Dimensional details of the micro reactor are shown in Figure 46.

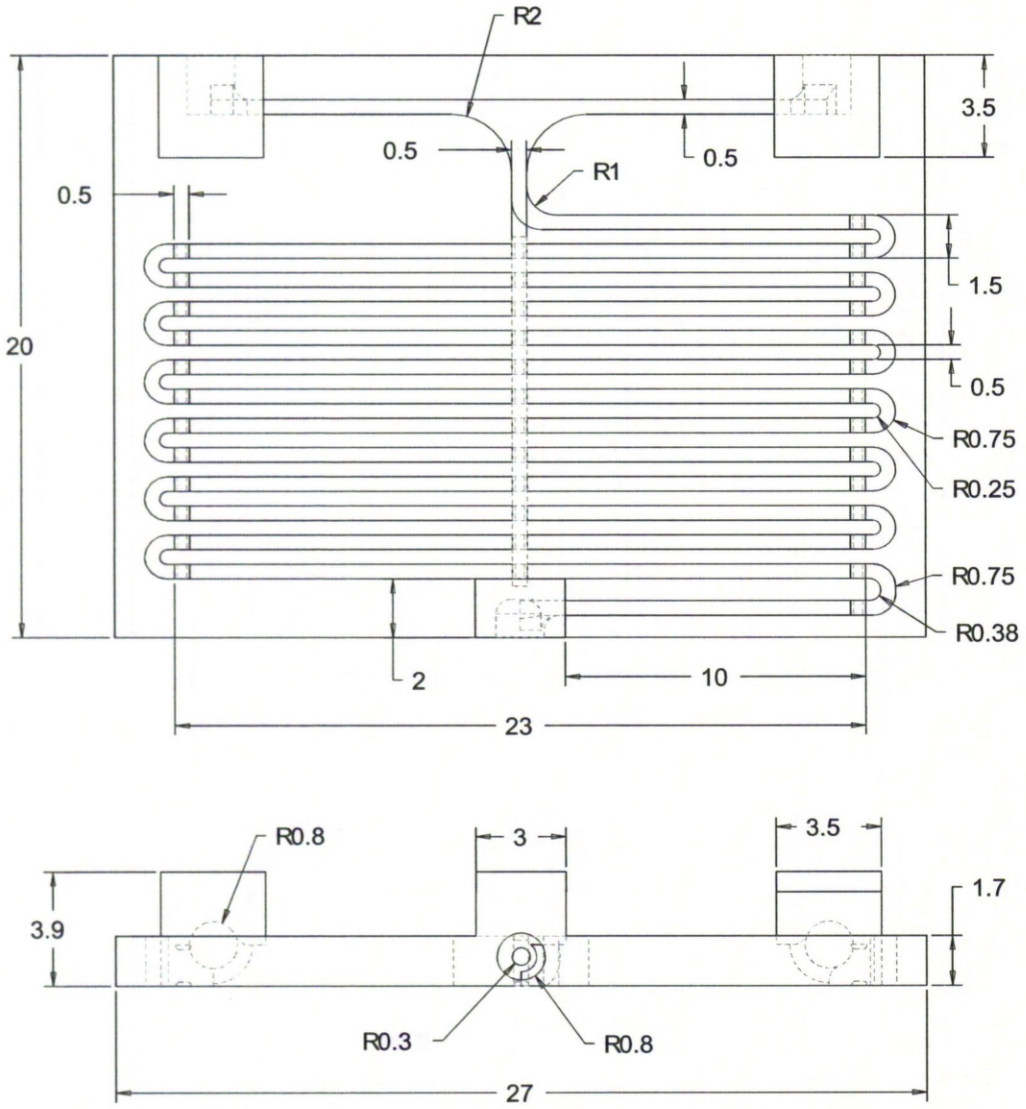

Figure 46: Dimensional Details of Micro Reactor.

The cells were initially seeded at 4.8 x 10^6 in 5 ml of medium, by perfusing at 0.025 ml/min and left to attach overnight under incubation conditions. They were then directly seeded in to the micro reactor from a suspension of diluted cell growth medium using a sterile hypodermic syringe and left to attach overnight before perfusion of growth nutrients. Cells were left to attach for nearly 10 hours before perfusing medium at 0.025 ml/min. Under incubation at 37 °C and 5% CO_2, cells were seeded in the micro reactor by switching a 3 way valve to add cell suspension to the reactor. Subsequently, the valve was closed and perfusion medium was circulated thought the reactor.

4.2.3 Results

Below are the images of different regions on the micro reactors in Figure 47 showing distribution of MG-63 mammalian cells attached within the micro reactor. Figure 47a shows cells at a junction where the 2 inlet ports meet, Figure 47b a view of first turn in the channel, Figure 47c is a view of channels and Figure 47d is the view of channel after flow at 0.025 ml/min.

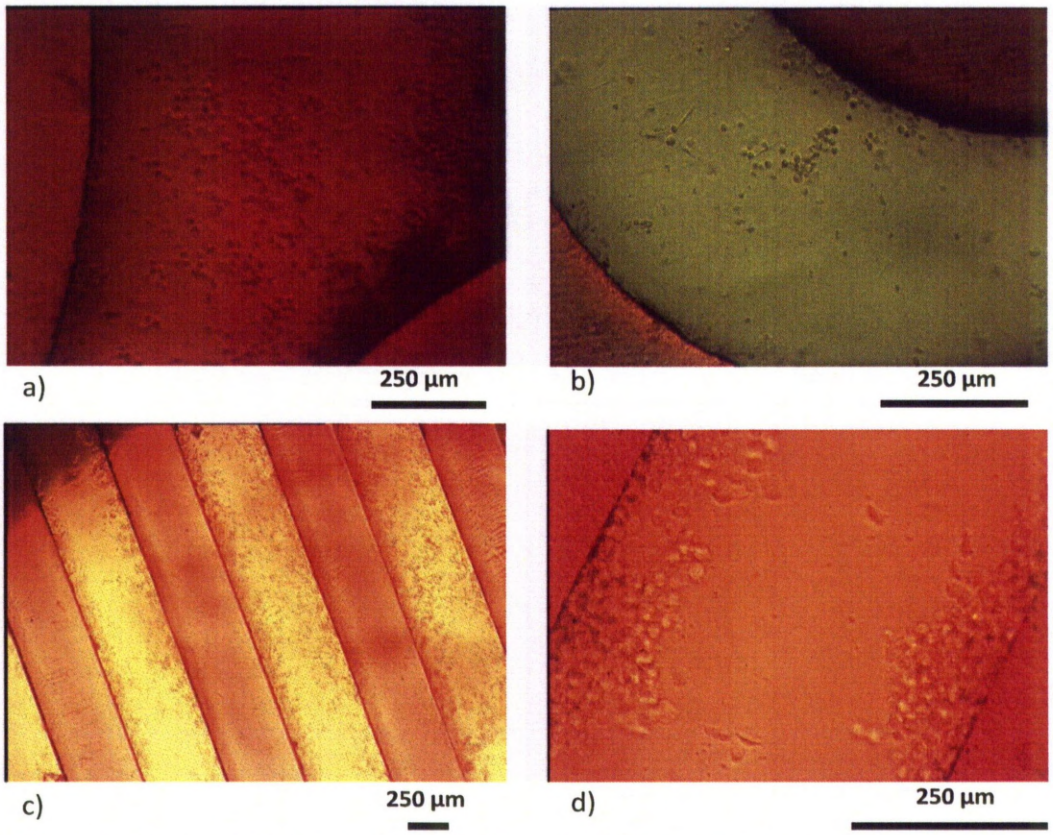

Figure 47: Images Showing Cell Growth Channels of the Micro Reactor a) at the Junction, b) at First Turn, c) Main Channels and d) Magnified View at Single Channel [244].

Molecular weight of the diluted cell growth medium in the reactor was recorded using high performance liquid chromatography (HPLC) with a UV (280 nm) detector is shown in Figure 48. These observations were each recorded for 20 minutes at various time points as the cells grew in the reactors. As expected, the cells attached to the surface of the PDMS membrane in a reasonable large number with a density of 450 x 10^3 /ml.

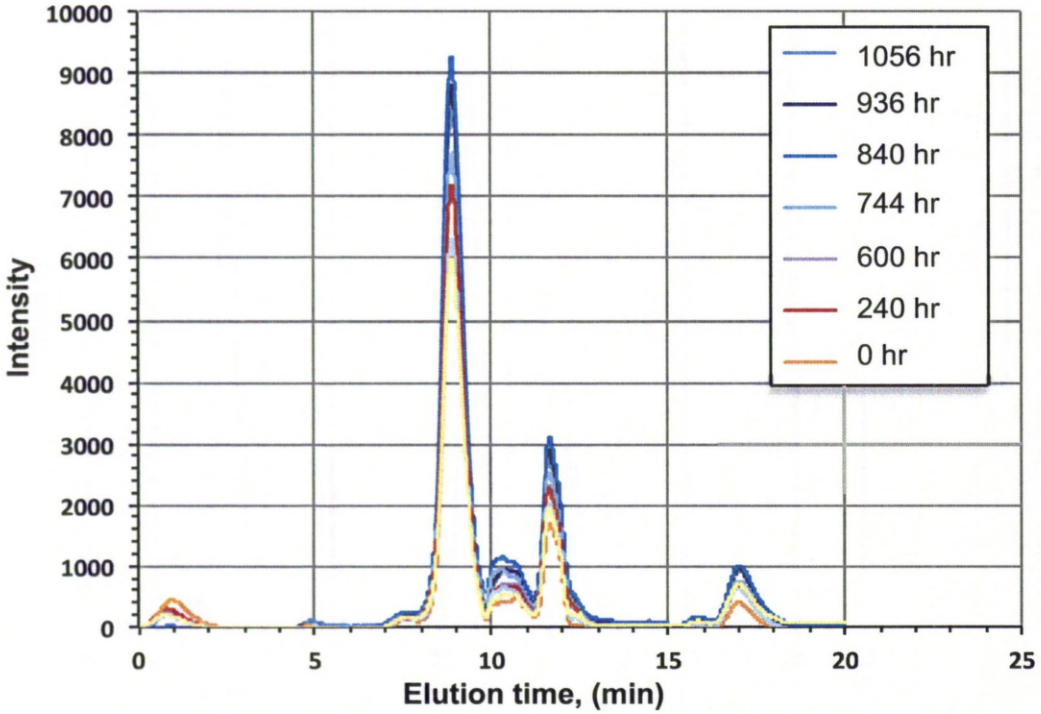

Figure 48: HPLC Molecular Weight Profile of Diluted Cell Growth Medium From the Reservoir [244].

Scanning Electron Microscopy of the cells attached to a PLGA membrane at various locations are shown in Figure 49 confirms the growth of cells in the micro channels and attached to the membrane located between the plated of the micro reactor. Figure 49a shows a conglomeration of cells, Figure 49b is an imprint of the micro fluidic channels on membrane, and cells attached to the surface of the membrane are shown in Figure 49c & d.

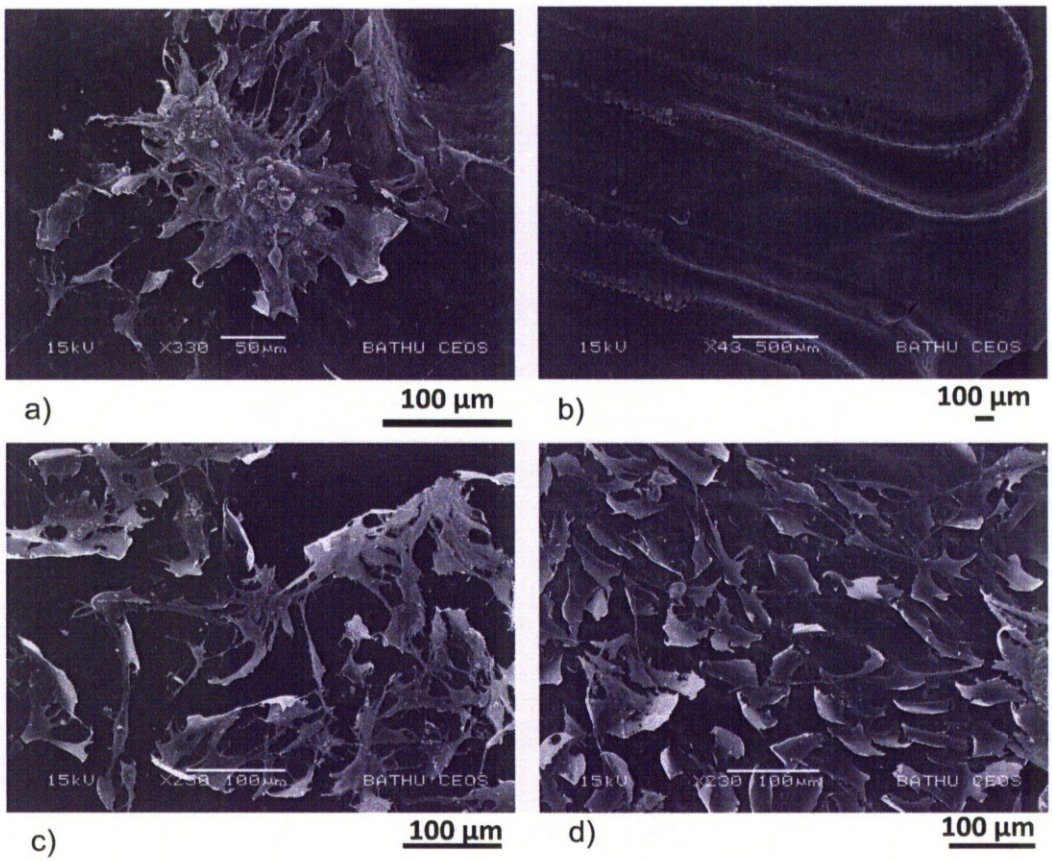

Figure 49: SEM Images of MG63 Mammalian Cells Growth Showing a) Conglomeration of cells, b) Impression of Channels on the Membrane Surface, c) and d) Cells Attached on the Membrane Surface [244].

4.3 Improving Surface Roughness by Adaptive Slicing

The influence of surface roughness of smaller width channels on fluid behaviour is well documented in the literature [166-180]. Improving surface roughness has been shown to improve fluid flow behaviour in the micro channels. From the observation made on the development of the preliminary micro fluidic devices, stair stepping on polymer parts manufactured by the DLP system causes surface roughness. However, it may also be due to the escape of volatile materials, while curing from the polymer component. Manufacturing the part in thin layers will reduce stair stepping effect, therefore, reducing the surface roughness.

Using this approach to reduce the surface roughness and to enhance the performance of the micro reactors was not possible with the standard Perfactory

software. An adaptive slicing algorithm (ASA) was used to reduce the stair stepping with the aim of delivering a real time variation in layer deposition. The methodology of adaptive slicing was discussed in Section 3.5.2.

4.3.1 Experimental Specimen Preparation

In order to set the build parameters for the various layer thicknesses using ASA, a pragmatic approach was taken. For comparison of the PF slicer and ASA a series of experiments were carried out. Cubes of 10 mm width were fabricated with different layer thickness (15 µm, 20 µm, 25 µm, 50 µm and 100 µm) both with and without ERM. Average surface roughness "R_a" values were measured on faces perpendicular to the build direction.

A series of specimens of size 24 mm x 6 mm x 8 mm, were also constructed which contained a number of channels of square and circular cross section, varying in square side length / diameter from 0.1 mm to 1.8 mm is shown in Figure 50. The channel sizes and shapes were representative of typical micro reactor channels and were built to investigate shape integrity, accuracy and surface roughness. To optimise the build time, the layer thickness of the specimen was set at 100 µm and the layer thickness was then reduced to values of 15 µm and 20 µm in regions in the vicinity of the channels. Building the test specimens in this way may reduced the time of build by several hours. The manufacture time for specimen containing a combination of 100 µm and 20 µm layers thickness was reduced from 8 hours to 7 hours for a the block.

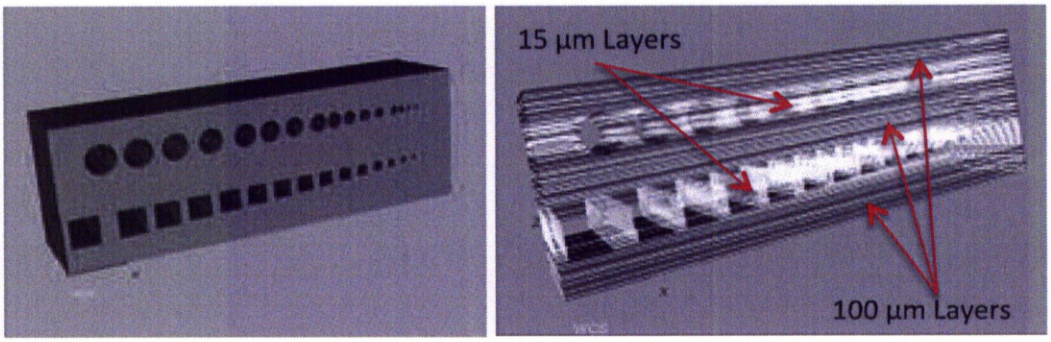

a) b)

Figure 50: (a) Square / Circle Channel Block and (b) Sliced Square / Circle Channel Block Showing Variable Layer Thickness.

4.3.2 Results

The surface roughness measured for these specimens is given in Figure 51. It was clear that the surfaces manufactured in ERM mode showed improved surface roughness manufactured with thinner layer thicknesses.

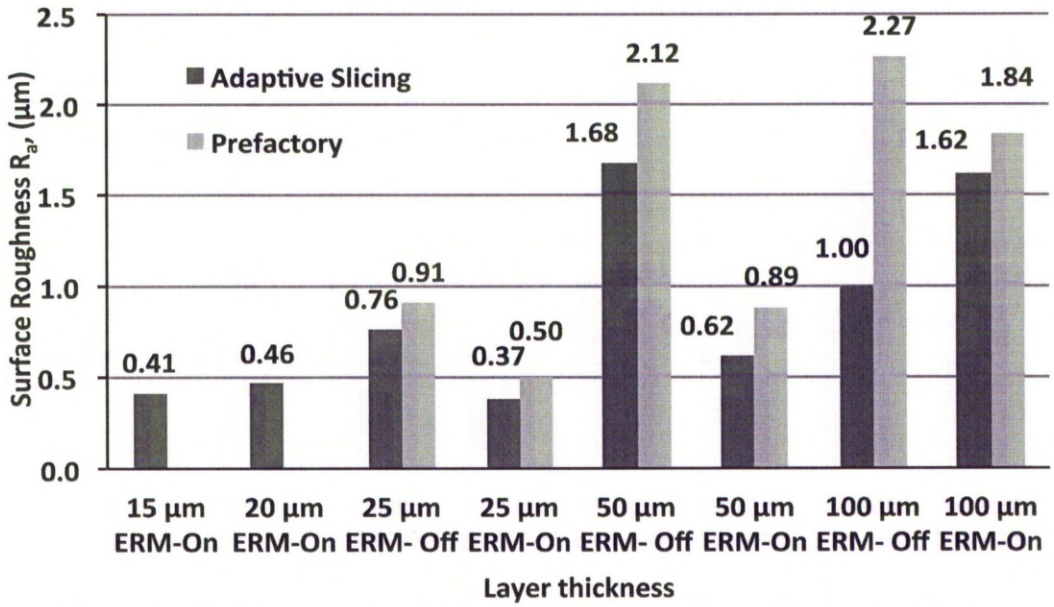

Figure 51: Root Mean Squared (R_a) Surface Roughness Values for Vertical Walls.

There were however some notable observations such as the surface roughness of vertical walls in parts produced using ASA were less dependent on ERM being active. This is especially noticeable at a 100 µm layer thickness where turning ERM off, gave a considerably better surface finish. Furthermore, for every cube built,

the surface roughness was smoother in ASA test samples than equivalent PF slicer specimens. This may be due to the absence of grey-scale border around image masks created using the PF-Slicer suggesting that the reduced exposure intensity per unit time at part edges, gives rise to less pronounced voxels at these locations. The grey - scale border increases the surface roughness in vertical walls, resulting in the greater discrepancy in surface roughness between the ERM and the slicing techniques at larger values of layer thickness. The micro shift in light intensity between consecutive layers, when the ERM is active, may also exacerbate the problem.

Typical micrographs showing the effect of ERM are shown in the Figure 52. The micrograph shown in Figure 52 compares the surface profile of the specimens prepared by using the PF slicer and ASA software. The specimens manufactured by PF slicer using 100 μm layer shows higher degree of variation with many notch's being formed the layers as compared to ASA software which has significantly less. The specimen manufactured in 50 μm and 25 μm using PF slicer shows higher surface strain caused by over curing of polymer. The surface profile for 50 μm and 25 μm specimens manufactured using ASA software showed improved surfaces. Similar observations were measured for the specimens manufactured in 20 μm and 15 μm layers. In both the cases, the surface profile was relatively uniform with no signs of surface strain by excessive curing.

Figure 52 verifies that the surface roughness of specimens manufactured with ERM – on and ERM – off, for 100 μm and 50 μm layer thickness were largely due to the notches formed between the layers, resulting in a surface roughness (R_a) varying from 2.27 – 1.00 μm and 2.12 – 0.62 μm, respectively. Specimens with 25 μm layer thickness however shows the surface roughness is not resulting from notches between the layers but the surface strain, thereby reducing the roughness in the range 0.91 – 0.37 μm. Reducing the layer thickness further reduces the surface roughness, which is apparent from the micrographs of the 20 μm and the 15 μm specimens.

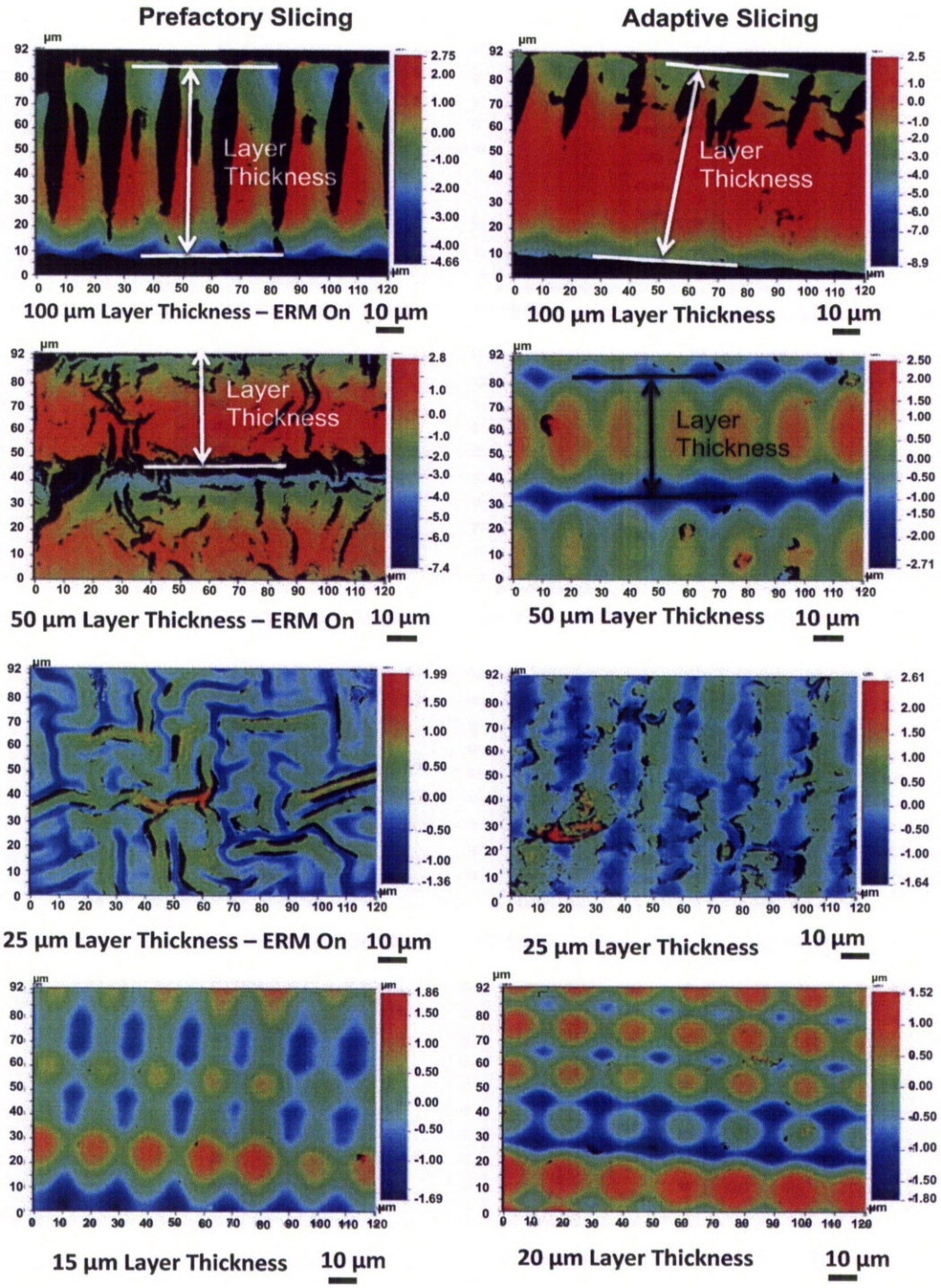

Figure 52: WYCO Images showing Surface Roughness Measured for Specimen with Various Layer Thickness

4.3.3 *Discussion*

The observation shown above also suggests that reducing the layer thickness below 20 µm does not improve surface roughness. On the contrary, the surface roughness deteriorates further possibly because the calculated values of exposure time were interpolated from only three data points, which is likely to give inaccurate results. This may also explain some surface discontinuities observed on part surfaces that are caused by shrinkage stresses from an overexposure of thin layers.

Micrographs of typical examples of square and circular channels are shown in Figure 53. The square cross-section channels exhibited improved shape when built with image masks generated using the ASA. In general, the square channels displayed a uniform cross-section throughout their vertical height.

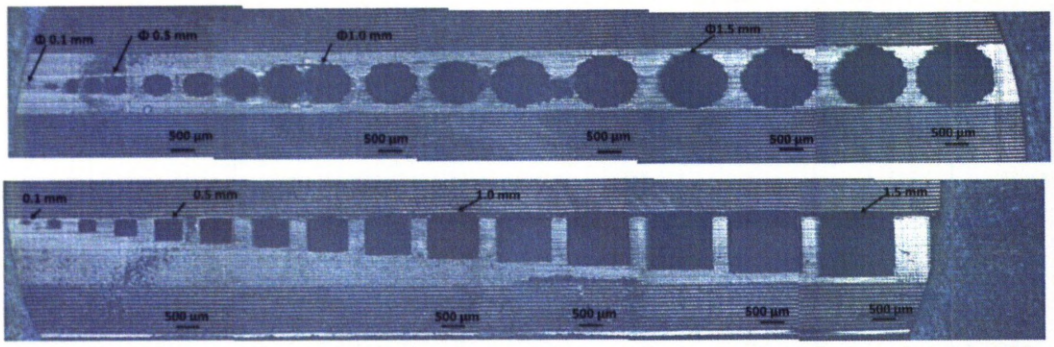

Figure 53: Micrographs Showing Circular and Square Channels Manufactured Using ASA.

The square channels were successfully manufactured using job file prepared by ASA. On the contrary, the profile of circular channels was irregular and distorted showing the stair stepping effect, which is apparent from Figure 54, where the circular channel was manufactured in 15 µm layers. This is probably attributable to the missing grey scale border in the PF slicer image masks. As the reduced exposure intensity per unit time at part edges acted to smooth (or the more likely to "blur") the stair step effect associated with an inclined or circular geometries since the voxels become less pronounced. The shift in the projected image by one pixel in an active ERM aids smoothening of inclined or circular geometries.

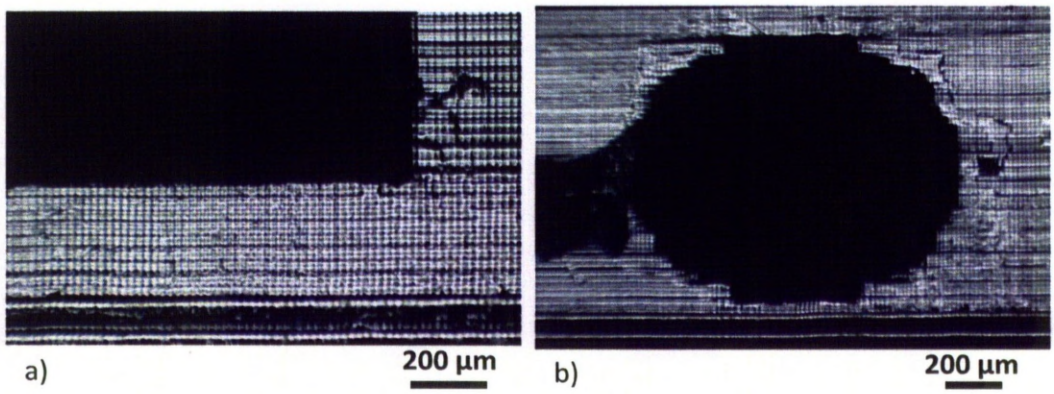

Figure 54: Micrographs of Channel Manufactured in 15 µm Layers Using ASA with a) Square Geometry, b) Circular Geometry.

4.4 Conclusion

The preliminary development of micro fluidic devices using the DLP system addressed the improvements necessary to enable the manufacture of micro channels. The lens with 60 mm focal length was replaced with 85 mm focal length lens to increase the resolution of the system to 20 µm.

Micro reactors manufactured using the DLP system have been used in a bioreactor application. Successful growth of MG63 mammalian cells was observed in the micro reactor manufactured. The current specification of the DLP system limits manufacturability and application for micro fluidic device due to the limitation on layer deposition thickness. A bespoken adaptive slicing algorithm (ASA) was prepared to address these limitations and to explore the possibility of improving surface roughness and component resolution.

Surface roughness and irregularity experienced using the Perfactory software suite were tackled by offering deposition of layers outside the standard range. Surface roughness was found to improve significantly at thinner layer thicknesses. Although the ASA has been successfully demonstrated to improve the surface roughness of parts, it failed to minimise the stair step observed in the circular channels. ASA is therefore still far from being a complete solution and it requires further work to achieve improved performance.

Improvements in surface roughness were found for thinner layer deposition thickness, but reducing layer deposition to less than 20 μm did not improve roughness further. It can therefore be concluded that the limiting threshold layer thickness for the DLP based AM technique is 20 μm, based on the data presented in this research.

Manufacturing of micro reactors by DLP at the improved resolution and hence feature size was successfully obtained using the DLP system. This was shown to be effective in a purpose-designed micro fluidic system, for the seeding and growth of cells on a scaffold. It can therefore be concluded that DLP is a sensible approach for the chemical reactor if several additional features can be made available.

CHAPTER 5

5.0 Additive Manufacturing of Functional Polymers

Functional composites are conventionally manufactured in a mould by pressing at high temperature. This chapter investigates the development of functionally active ceramic – polymer composite using the digital light processing (DLP) based AM technique described earlier in Section 3.1.1, which operates at standard temperature and pressure (STP). Material was manufactured at a range of loadings and fabricated by conventional route at STP. This identified the maximum powder loading achievable by the DLP system. Once the maximum loading by the conventional method was identified, ceramic composites were fabricated using DLP.

Specimens for both, polymer alone and polymer – ceramic powder mixture (R5 - $BaTiO_3$) were manufactured and analysed for the influence of the build orientation on the mechanical properties. A series of experiments was also performed to measure the electrical properties of the composite specimens developed by DLP. The specimens were measured for their piezoelectric and ferroelectric behaviour, at various temperatures, electric fields and frequencies. The piezoelectric properties such as piezoelectric coefficient (d_{33}), capacitance (C) and dielectric loss (tan δ) were recorded by applying a direct current (DC) electric field. The ferroelectric behaviour was measured by applying an alternating current (AC) electric field. The observations for piezoelectric and ferroelectric behaviour were compared with the literature survey to identify their usability for functionally active devices. Mechanical and electrical behaviour of the functional specimens by DLP will aid for the development of functional devices using this novel approach.

5.1 Moulding for the Manufacture of Functional Polymers

In theory, packing density of up to 0.9 volume fraction is achievable as discussed in Section 2.2.2. In practice however, ceramic – polymer composites fabricated by moulding at high pressure sintering have particles randomly arranged in the

polymer matrix. The maximum density of 0.6 has been successfully reported in the literature [54]. In the absence of high pressure sintering, fabrication of composite material with the density of 0.6 may not be achieved. This section, therefore, investigated maximum loading of the particles that can be manufactured at STP.

5.1.1 Experimental Methods

In order that a clear comparison could be made between the AM route and more conventional methodologies, moulding was used to manufacture ceramic – polymer composite specimens with an aim of identifying the maximum load of $BaTiO_3$ that could be achieved at STP. A series of specimens were fabricated by mixing varying loads of $BaTiO_3$ ceramic with the liquid photopolymer R5 and curing in a mould of 20 mm x 20 mm x 1 mm. The moulds were placed in a vacuum chamber. A vacuum was then gradually reduced to 13.33 MPa and held for 3 minutes. The vacuum was then rapidly released to the atmospheric pressure effectively removing air from the liquid mixture. This process was repeated 5 times and the specimens were cured under ambient lighting condition for 14 days. The specimens at a maximum load of 49 vol% (83 wt%) were successfully produced. Following this successful, two series of specimens were produced with 49 vol% (83 wt%), 45 vol% (80 vol%) and 35 vol% (73 wt%) in order to make a comparison.

5.1.2 Results

Microscopy was performed on the cured specimens as shown in Figure 55 – 57. Due to vacuum degassing of the specimens, regions of porosity were observed on the surface of the 49 vol% and 45 vol% specimens. These areas were formed during degassing the specimens, as a result of viscosity of the material. However, the 35 vol% specimen shows much less porosity as the polymer was able to fill the voids left by the trapped air more easily at these lower loadings. The colour of the high-density specimens was uniform throughout; however the 35 vol% example shows regions of colour change indicating that only photopolymer, not photopolymer and powder was filling the voids created during the degassing, leading to non-uniformity of the ceramic distribution in the low density specimens.

These regions are indicated as "low density regions" in optical micrographs on the specimen surface.

Observations also indicate the formation of cracks in the material showing the brittle nature of the high-density specimens. These were absent in the 35 vol% specimens. This crack formation was due to shrinking of the photopolymer during curing.

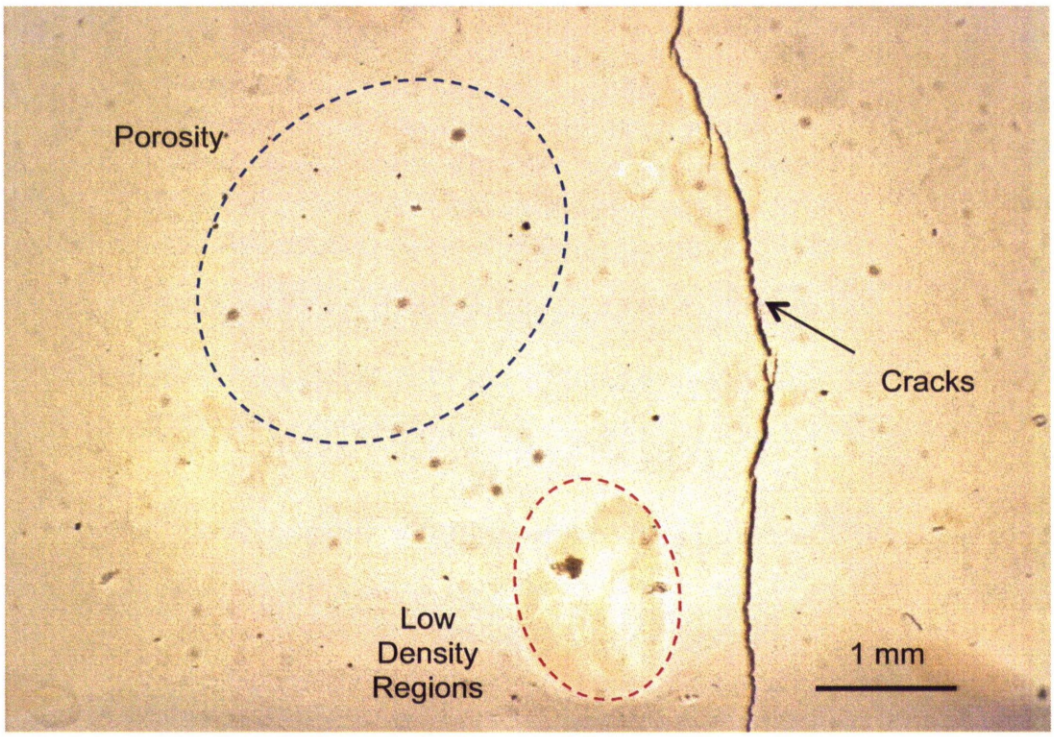

Figure 55: Micrograph of 49 vol% $BaTiO_3$ – Polymer Composite.

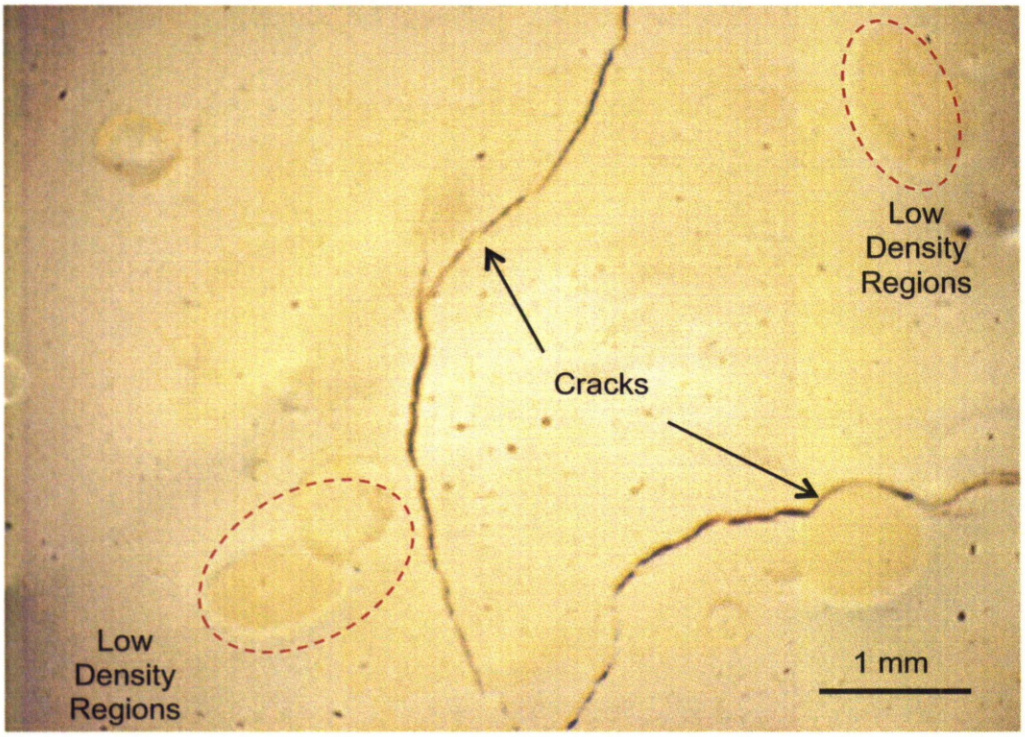

Figure 56: Micrograph of 45 vol% $BaTiO_3$ – Polymer Composite.

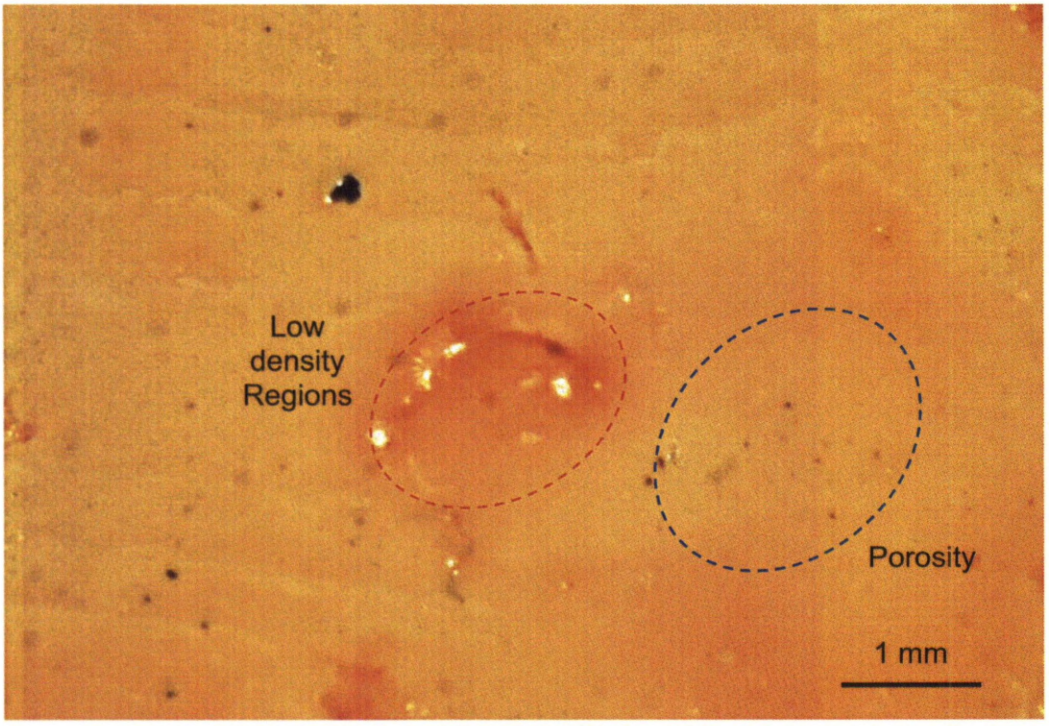

Figure 57: Micrograph of 35 vol% $BaTiO_3$ – Polymer Composite.

As indicated in Figure 57, partial curing was apparent in the 35 vol% specimens as the polymer require an exposure to a specific wavelength to reach green strength.

The partial curing of polymer in specimens with 49 vol% and 45 vol% particle content, however, were not prominent due to higher loading of ceramic content. In order to ensure that these specimens were fully cured, they were further exposed to UV light for 45 hours ensuring complete curing. The optical microscopy images of these specimens are show in Figure 58 – 60. Exposing the high-density specimens to UV, results in a uniform colouration of the specimens. This indicates complete curing of the polymer across the specimen thickness. The 35 vol% specimens, however, showed a high degree of irregularity at the surface due to shrinking of the polymer with a small number of distinct voids with a black appearance were observed at various locations. The thickness of 35 vol% specimens has also reduced from 1 mm to 0.8 mm. The specimen surfaces at all the loading levels were shown to have fewer porous regions.

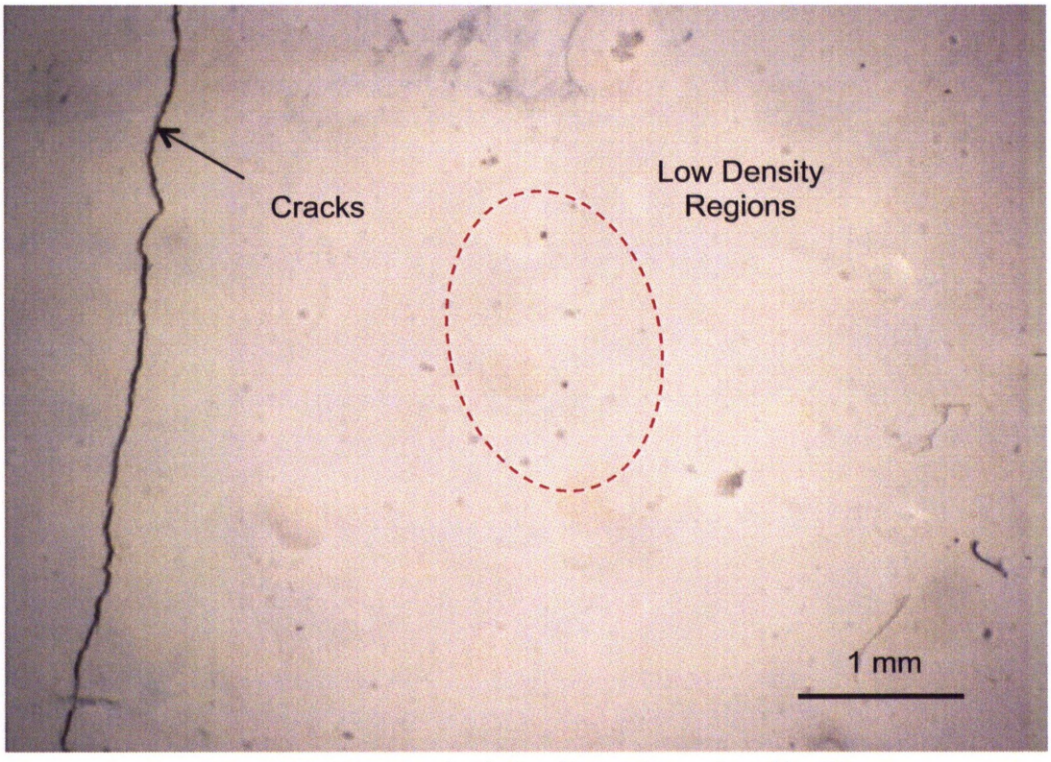

Figure 58: Micrograph of 49 vol% Specimen Cured by UV.

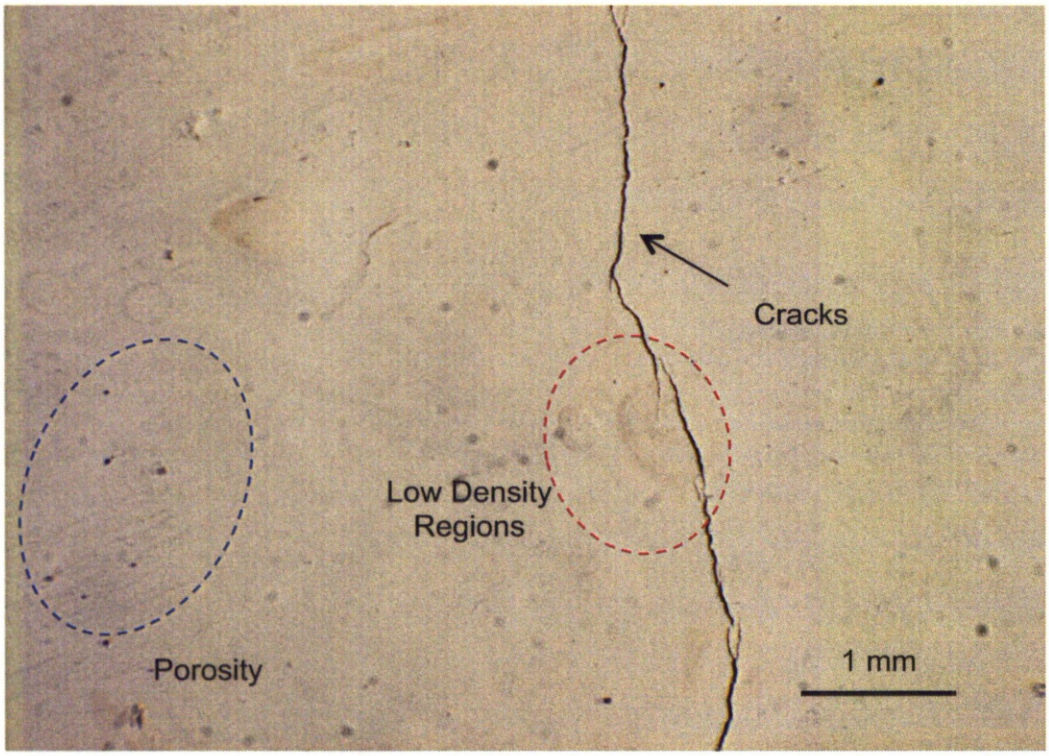

Figure 59: Micrograph of 45 vol% Specimen Cured by UV.

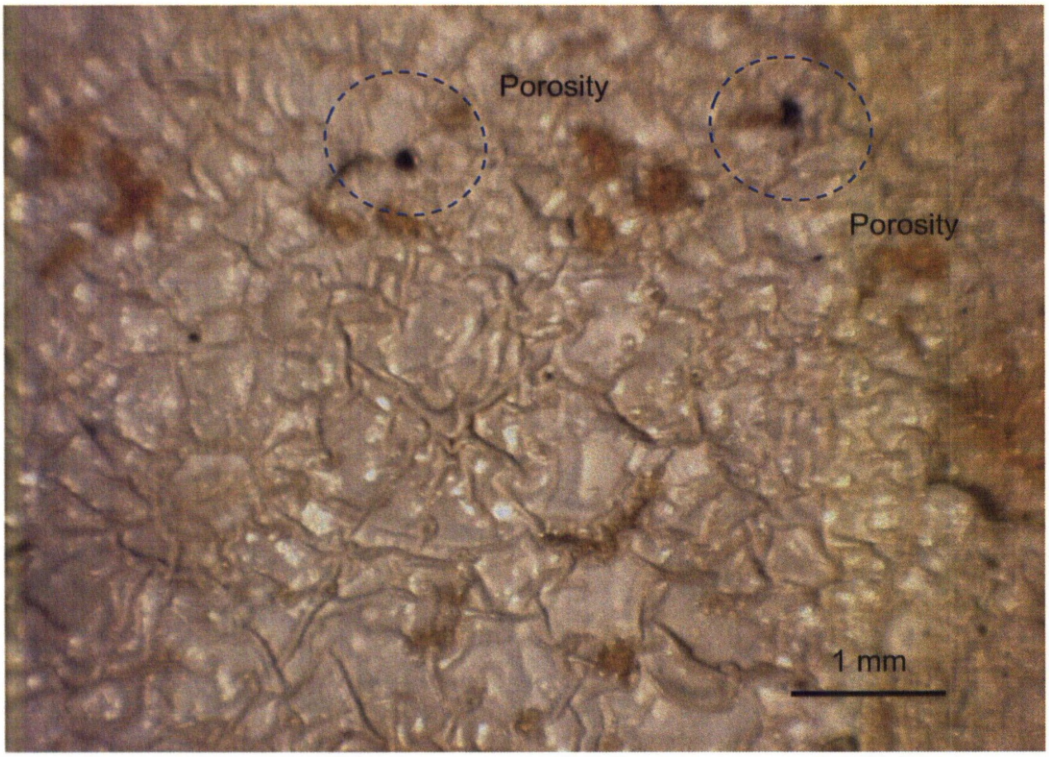

Figure 60: Micrograph of 35 vol% Specimen Cured by UV.

In terms of mechanical properties, the composite at 49 vol% and 45 vol% particle were brittle and difficult to remove from the mould. The specimens from 35 vol% composite were flexible and easily retrieved. Observing all the specimens under an optical microscopy showed that polymer and ceramic particles were bonded together, with very few regions of air entrapment. In particular, the high-density specimens, it was noted that as the flowability of the polymer was significantly reduced, this led to difficulty in filling the mould completely while simultaneously avoiding the entrapment of air. This exercise did however illustrate the challenges, including some of the defects that may occur in the composite parts manufactured by the DLP system.

The functional activation of 49 vol% and 45 vol% specimens require poling. However, their brittle nature meant that they could not be poled. All the unpoled specimens were however carefully measured for piezoelectric coefficient d_{33}. These specimens failed to show any piezoelectric coefficient in unpoled condition confirming their electrical inactivity. A capacitance of 3.0 pF was observed for all the unpoled specimens. A dielectric loss ranging between 0.21 – 0.26 was also recorded.

The specimens containing 35 vol% ceramic loading were poled at 5 kV (6 MV/m) electric field at a poling temperature of 70 °C following the protocol discussed in Section 3.3. Poling at higher electric field could not be completed due to electric field discharge across the specimens. A piezoelectric coefficient of 4 pC/N was recorded at a dielectric loss of 0.25. The high dielectric loss for these specimens is an indication of low permittivity of polymer. Similar investigation for the manufacture of piezoelectric ceramic - polymer composites by the DLP system were undertaken, further discussed in Section 5.2.

5.1.3 Discussion

The ceramic – polymer composite specimens that were manufactured by moulding at STP condition confirmed that the maximum density of 49 vol% was achievable. These specimens, however, showed reduced mechanical strength, typically

observed in composites with high loading of particles. The manufacture of the specimens by moulding acrylic photopolymer and $BaTiO_3$ were also difficult to retrieve due to their brittle nature.

The 35 vol% composite specimens showed an optimum particle loading and material strength, as they were retrieved from the mould. These specimens, however, failed to completely cure at room condition and were exposed to UV to ensure complete curing.

Functional activation of 35 vol% specimens showed promise for the development of functional composites by DLP. The piezoelectric coefficient of 4 pC/N was measured at 6MV/m electric field and 70 °C poling temperature, applying higher electric field and poling temperature could result in high degree of functional activation.

5.2 Additive Manufacturing of Polymer Composites

Development of a composite material by a conventional route has confirmed the manufacturability of up to 49 vol% particle content in the photopolymer at STP. The experiment identified challenges that may be encountered while developing these materials for DLP. As the composite specimens containing 35 vol% showed an optimum mix of mechanical strength and particle loading as compare to 49 vol% and 45 vol% specimen, 35 vol% forms the targeted loading that could be achieved by DLP.

In order to ensure manufacturability, the development of new build parameters had to be identified. These materials were analysed for the distribution of particles in the photopolymer using microscopy. Parts manufactured on the DLP system were analysed for dimensional accuracy and feature resolution. Finally, the mechanical behaviour of the parts produced was investigated.

5.2.1 *Low Density Functional Composites Manufactured by DLP*

The procedure described in Section 3.1.1 was typically used to manufacture the material studied. The addition of $BaTiO_3$ to the photopolymer changes the properties such as density and viscosity, and requires new build parameters to ensure effective manufacture. The manufacture of composites could also suffer from porosity, as viscosity influences the flow of polymer under capillary action and a high viscosity may result in the non - filling of the build envelope, causing air to be entrapped between the layers. The shrinking of the polymer during curing may also leads to the formation of crack.

The functional material was manufactured by mixing measured quantities of $BaTiO_3$ powder with measured volume of liquid photopolymer, followed by manual stirring. This significantly reduced the flowability and the effective area for the exposure of the liquid polymer; therefore restricting the fabrication of high-density composites. To identify the optimum loading of the powder in the liquid polymer, a series of composites with varying load were manufactured using the DLP system. Initially, 16 g of $BaTiO_3$ was mixed in 50 ml of R5. Composite blocks of 10 mm x 10 mm x 1 mm, later reducing to 0.5 mm were manufactured by DLP. The composite specimens were manufactured with 25 μm layer thickness in the normal way using the DLP system. These were used to assess the stiffness and the survival of the thinner components during removal, cleaning and post process curing.

5.2.2 *Methodology for Development of Low-Density Composites*

During the manufacture of specimens, the loading of powder was increased by 0.5 g after successfully manufacturing the initial specimens. As expected, the DLP system could not fabricate composite materials at the recommended manufacturing parameters for R5, hence new parameters were developed requiring an increase in exposure time for higher particle loading. In order to identify new build parameters to develop composite material by DLP, parameters recommended for 25 μm layer thickness of the standard R5 polymer were considered as reference. The material containing 5.1 vol% was successfully manufactured using

recommended build parameters. For high loading of ceramic particles, exposure time was increased by 500 ms for run, unless the material was successfully manufactured. Table 9 gives the build parameters at various concentrations of $BaTiO_3$. Since all the composite specimens manufactured on the DLP system were thin, the manufacturing parameters of the standard burn-in range were applicable. Figure 61 shows the exposure time used to manufacture the materials described here.

Table 9: Comparison of Build Parameters for the Fabrication of Polymer Components and Particulate Composites

Parameters	Liquid Polymer	Particulate Composites		
Weight % of Powder (%)	0	21.33	22.36	23.37 - 54.26
Volume % of Powder (%)	0	5.1	5.4	5.70 - 19.00
Burn-in Range Separation Distance (mm)	7000	7000	7000	7000
Standard Range Separation Distance (mm)	4500	6000	6000	6000
Burn-in Range Waiting Time After Peeling (ms)	2000	3000	3000	3000
Standard Range Waiting Time After Peeling (ms)	500	1000	1000	1000
Burn-in Range Waiting Time After Levelling (ms)	25000	25000	25000	25000
Standard Range waiting time After Levelling (ms)	1000	2000	2000	2000
Burn-in Range Exposure Time (ms)	6000	8000	8500	10000
Standard Range Exposure Time (ms)	3000	4000	4000	5000

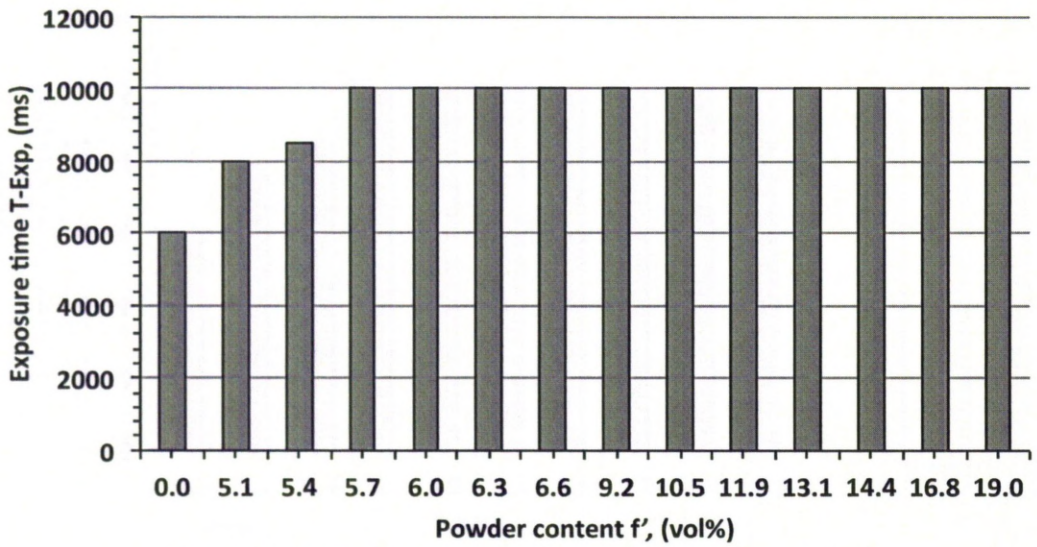

Figure 61: Increasing Exposure Time With Increasing Loading.

Liquid polymer containing higher dosages of powder (> 19 vol% / 54 wt%) showed reduced flowability during the manufacturing process. Although, the DLP system

could cure polymer layers at these loadings, the manufacture of specimens failed due to insufficient structural stiffness and lack of adherence to the build platform, even at increased exposure times.

5.2.3 Microscopy Analysis of Low – Density Composites

The composite specimens were manufactured by mixing the $BaTiO_3$ particles in the photopolymer. It was observed that the powder in the liquid polymer settles during the process and required thorough mixing before starting the manufacturing process. The limiting flowability, insufficient strength of the layer and the deposition of powder bed at the bottom due to absence of mixing during the process have limited the achievable composition to 19 vol%. These limitations were further leading to difficulties with building longer components. Settling of the ceramic powder causes accumulating at the bottom of the build vat where test specimens are manufactured may result in non-uniform distribution of particles through the specimen thickness. The specimens manufactured by the DLP system were analysed for particle distribution at various loads.

The distribution of particles in the composites manufactured by this method was examined using SEM following the procedure described in Section 3.2.2 using JOEL JSM-6610 (Joel (U.K.) Ltd., England). The specimens were prepared by brittle fracturing them by quenching them in liquid nitrogen. The white spots observed in these images are $BaTiO_3$ ceramic aggregates, surrounded by R5 photopolymer (Figure 62 - Figure 65).

Microscopy observation for low loading however showed the particles was spread evening throughout the thickness of the specimen. Each particle was surrounded by cured polymer and the fractured surface was smooth with closely packed particles. The fractured surface for the high loading specimens was not smooth and the crack path diverted along the ceramic particle / polymer interface.

The evident change in crack behaviour is an indication of the changing mechanical properties of the material and control of the mechanical behaviour of ceramic-

polymer composite is crucial for practical use. The micrographs shown in Figure 62 – 65 were recorded using Hitachi S-2460N (Hitachi Ltd. Japan), where as Figure 65 were recorded using JOEL JSM-6610 (Joel (U.K.) Ltd., England).

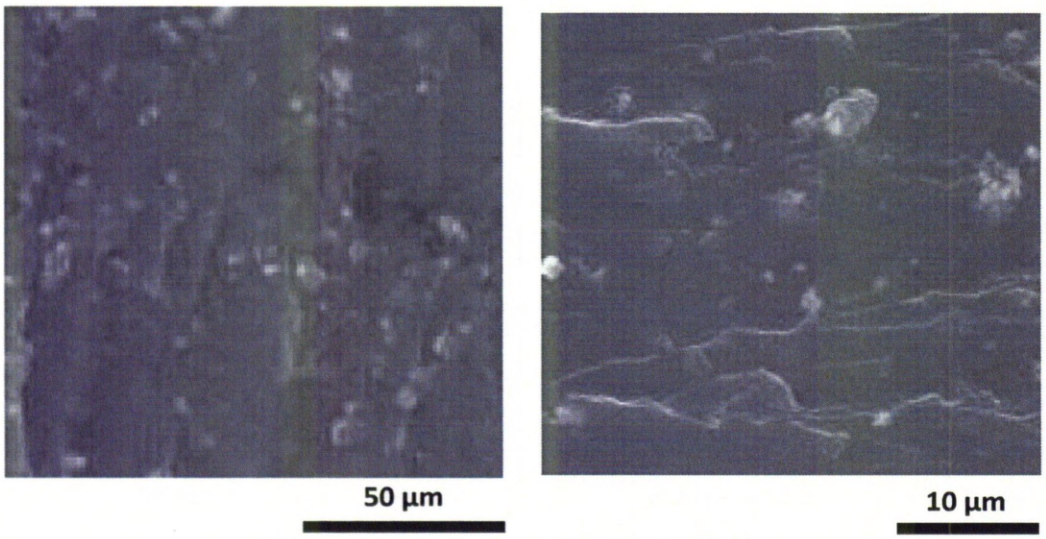

Figure 62: SEM Images of 2 vol% Specimen.

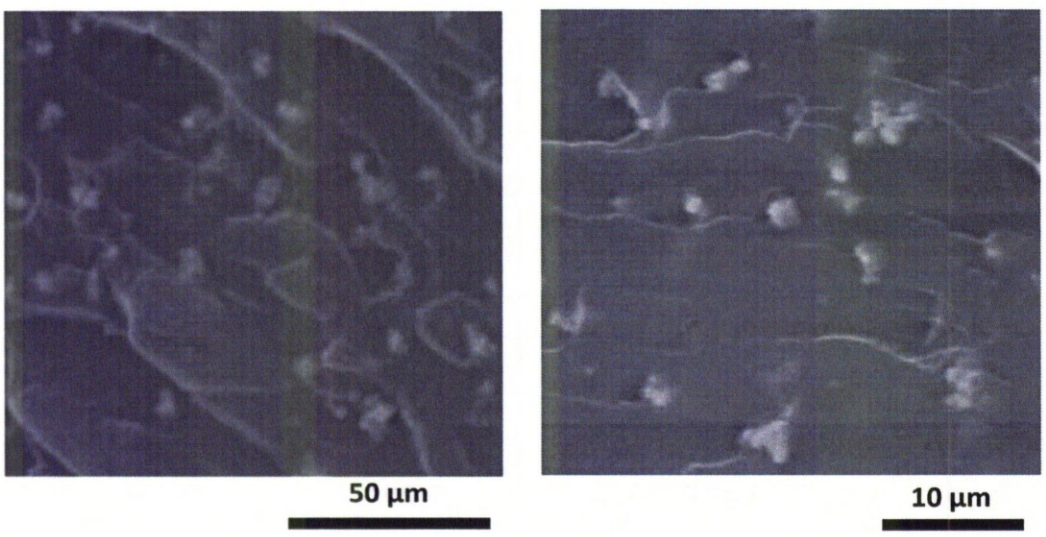

Figure 63: SEM Images of 3 vol% Specimen.

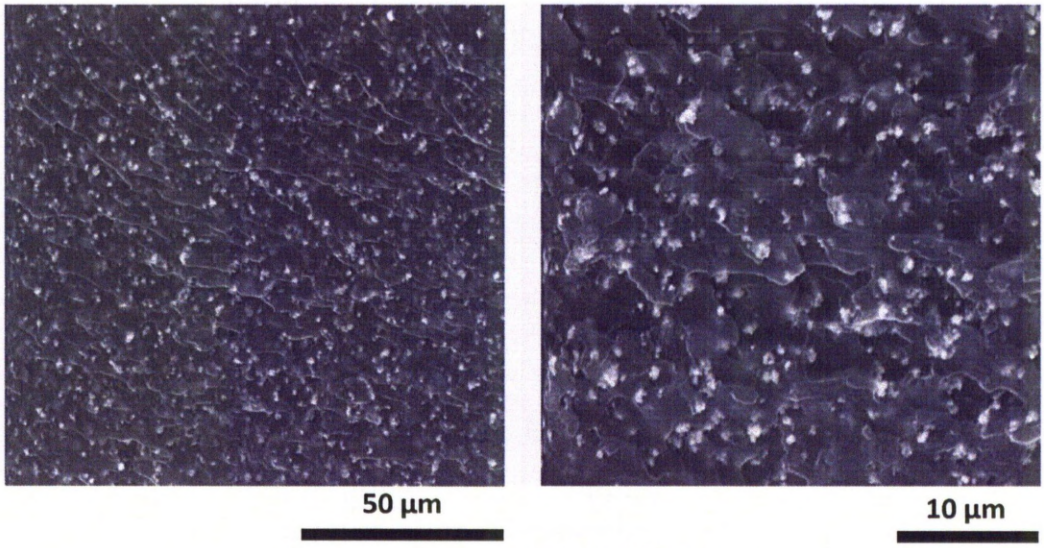

Figure 64: SEM Images of 5 vol% Specimen.

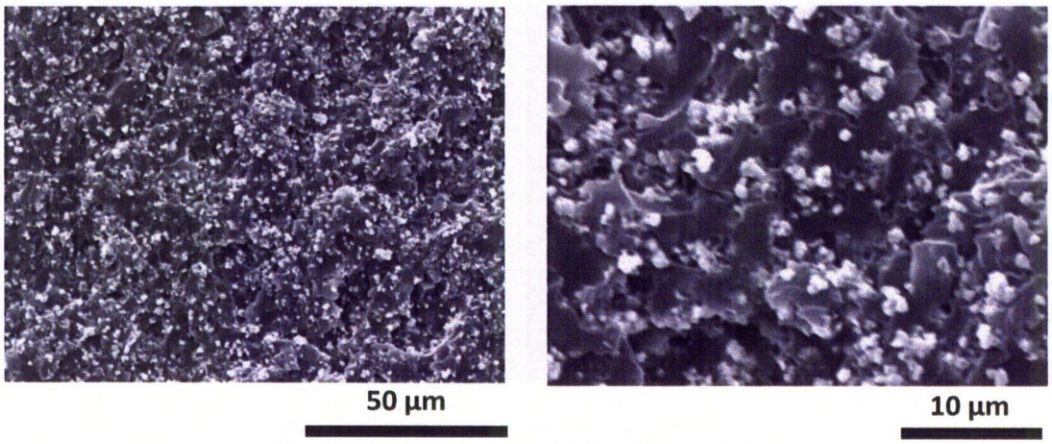

Figure 65: SEM Images of 17 vol% Specimen.

5.2.4 Discussion

In order to develop functional composites by DLP, new parameters were identified ensuring the manufacture of specimens with various loading of $BaTiO_3$ particles. The composite specimens with a maximum of 19 vol% particle loading were successfully manufactured. This was significantly lower that the 35 vol% composition manufactured by moulding, discussed in Section 5.1. This limitation on particle loading was caused by reduced flowability due to the addition of ceramic powder in the photopolymer.

The SEM micrographs observed in Figure 62 - 65 for various loading of composites confirms uniformly distributed particles across the specimen thickness. The fracture surface for the low-density specimens was smooth. The high-density specimens however show diversion of the fracture path along the particle – polymer interface. The apparent change in behaviour due to addition of ceramic particles in the photopolymer indicates the influence on mechanical behaviour of the material developed by DLP.

5.3 Mechanical Properties of DLP Specimens

As discussed in literature, the layer thickness and the orientation of the layer used to manufacture part influence the mechanical properties. An investigation was undertaken to measure the mechanical propertied of the parts developed by DLP.

5.3.1 Experimental methods

Conventionally, tensile testing is performed by preparing standard tensile test specimens, in accordance with a standard specification such as ASTM, BS, ISO etc. In the absence of suitable standards for AM techniques, tensile test specimen geometries were developed from:

- BS EN ISO 527-1: 1996 BS 2782-3: Method 322: 1994,
- BS EN ISO 527-2: 1996 BS 2782-3: Method 322: 1994,
- BS EN ISO 527-3: 1996 BS 2782-3: Method 326 E: 1996

The procedure described in the tensile testing specification is based on applying uniaxial tension to a component of known cross-sectional area and measuring the change in length of the specimen. The tensile stress and the modulus of elasticity are calculated from the given cross section.

Initially, specimens were manufactured according to BS EN ISO 527-2: 1996, test specimen type 5A and 5B. However, due to the limited build envelope of the machine operating in high resolution, the overall dimension of the tensile test

specimen were reduced. The typical dimensions of the specimen are shown in Figure 66.

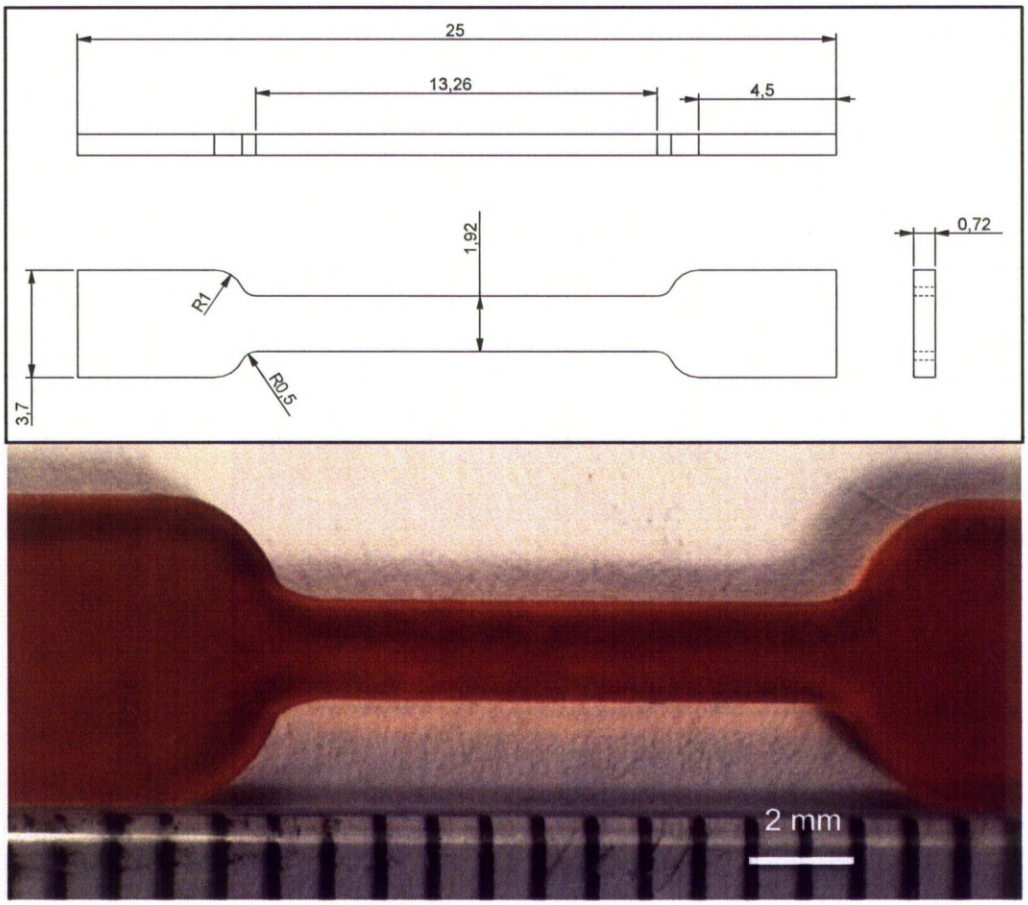

Figure 66: Dimensional Details and Manufactured Primary Tensile Test Specimen (Before Testing) Adopted Form Type 5B, BS EN ISO 527-2:1996

Specimens were manufactured in the XY plane i.e. with the flat surface of gauge length parallel to the surface of the build platform. This build orientation is applicable to chemical reactors as they are generally planar in form. The specimen with gauge thickness parallel to the build platform requires supports necessary for manufacturing (Figure 67a). Removing the support from the specimens results an irregular surface having an extension or an under cut, thus leads to stress concentration and ultimately to crack formation (Figure 67b), and the premature failure of specimens outside the gauge length.

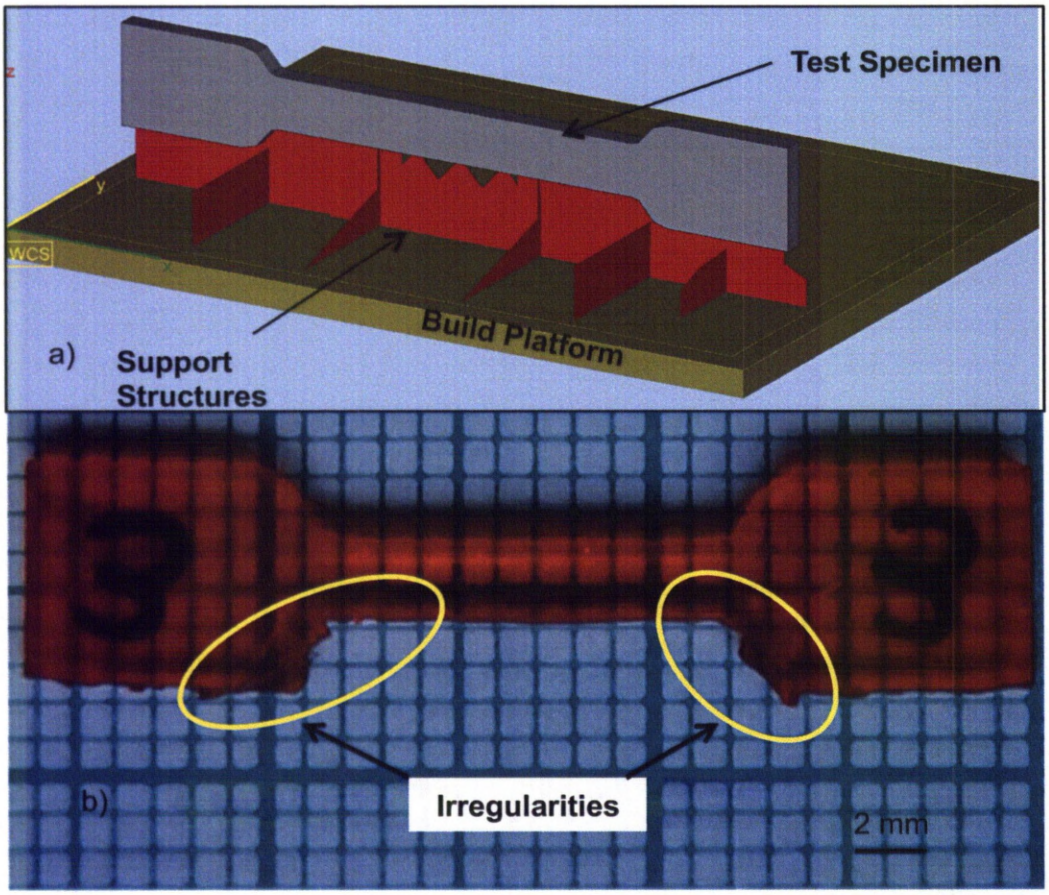

Figure 67: (a) View of Supports Generated for Tensile Specimen and, (b) Irregularities Surface Formed After Removal of Supports

This issue with the removal of supports was overcome by changing the rectangular cross section to a circular cross section in the gauge length. As the circular geometry exhibits similar cross section area in all directions, the influence of layer orientation on failure in the gauge length was minimised. The guideline for the circular cross section tensile test specimen was used from BS 2782-3: method 327 A: 1993.

The specimens that were manufactured based on the guidelines from BS 2782-3: method 327 A: 1993 had longer gauge length than primary test specimen and slag during manufacture in horizontal direction. Initial test results showed that the specimens had a long gauge length to be satisfactorily tested on the Instron 3342 machine. The tensile test specimen was therefore optimised for the build envelope of 20 mm x 27 mm suitable for the testing machine. The dimensional details of the

modified tensile test specimen are show in Figure 68. The modified tensile test specimen consists of a small gauge length extending to a clamping section by a smooth transition. The transition avoided supports in the gauge length and reduced the bending while manufacture, which was observed in specimens with a longer gauge length.

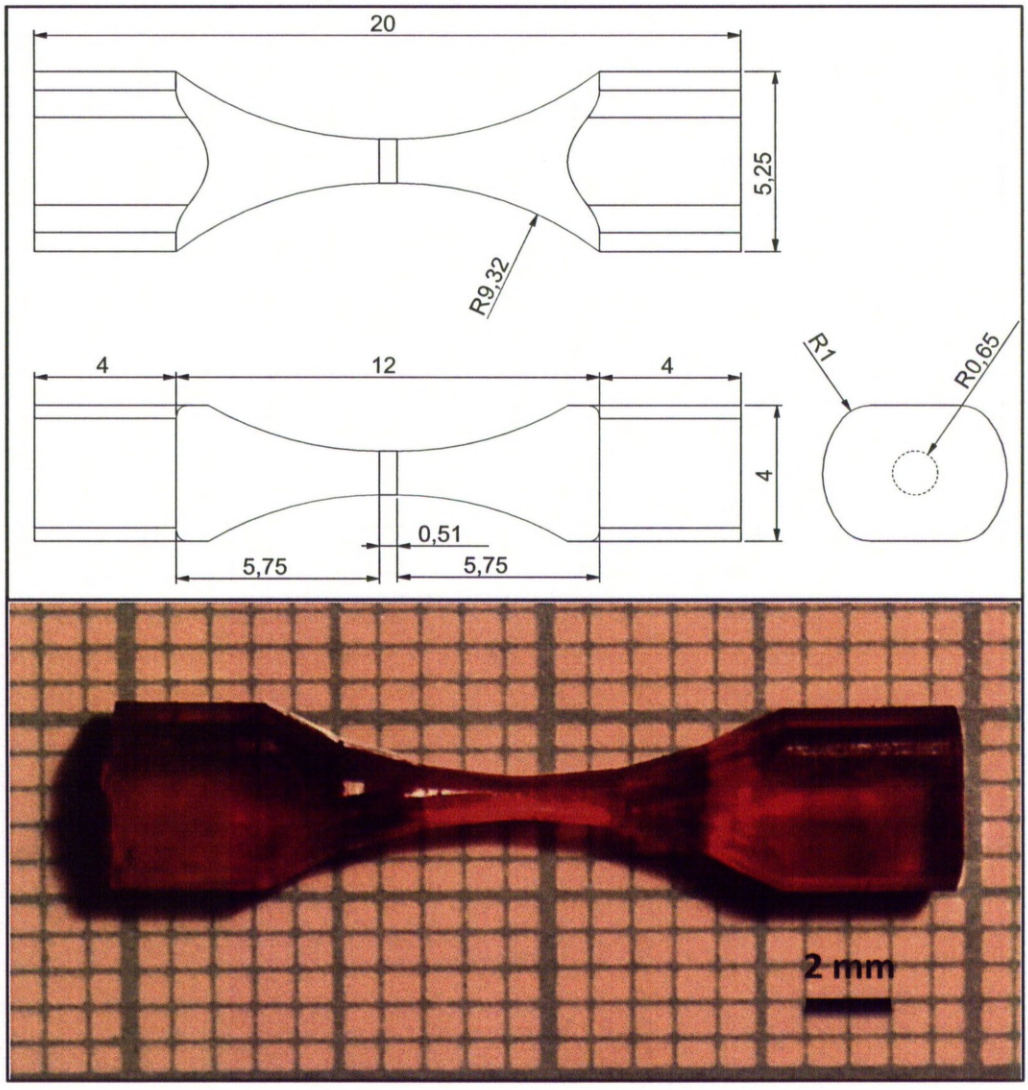

Figure 68: Dimensional Details of Modified Short Gauge Length Tensile Test Specimen.

5.3.2 *Analysis of Tensile Test Specimens*

The observations recorded for tensile testing and fracture analysis for all the test specimens are discussed further.

Mechanical Properties of The Polymer Composites

Although the gauge length of the tensile test specimens was circular in cross section, fabricating them by AM may influence the mechanical properties due to the interfacial bonding between layers. In order to investigate this, test specimens was manufactured in the XY and Z directions as indicated in Figure 69 and Figure 70. The variation in mechanical strength is clearly evident in Figure 71, for the 10 polymer specimens manufactured in XY direction (horizontal) and Z direction (vertical).

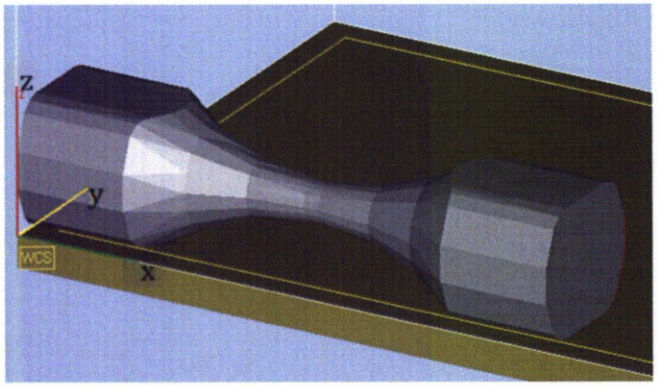

Figure 69: Reference XY Built (Horizontal) for Tensile Test Specimen.

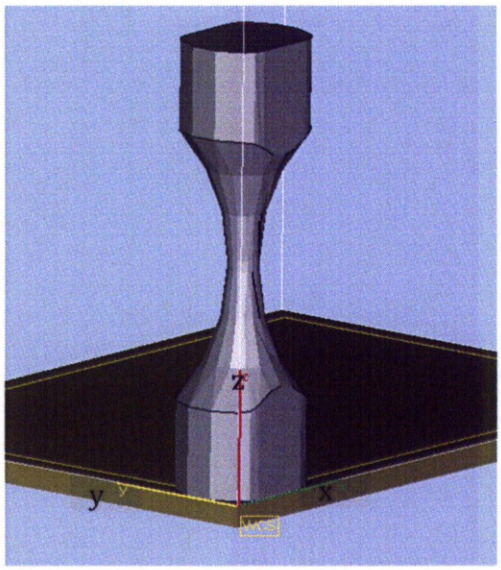

Figure 70: Reference Z Built (Vertical) for Tensile Test specimen.

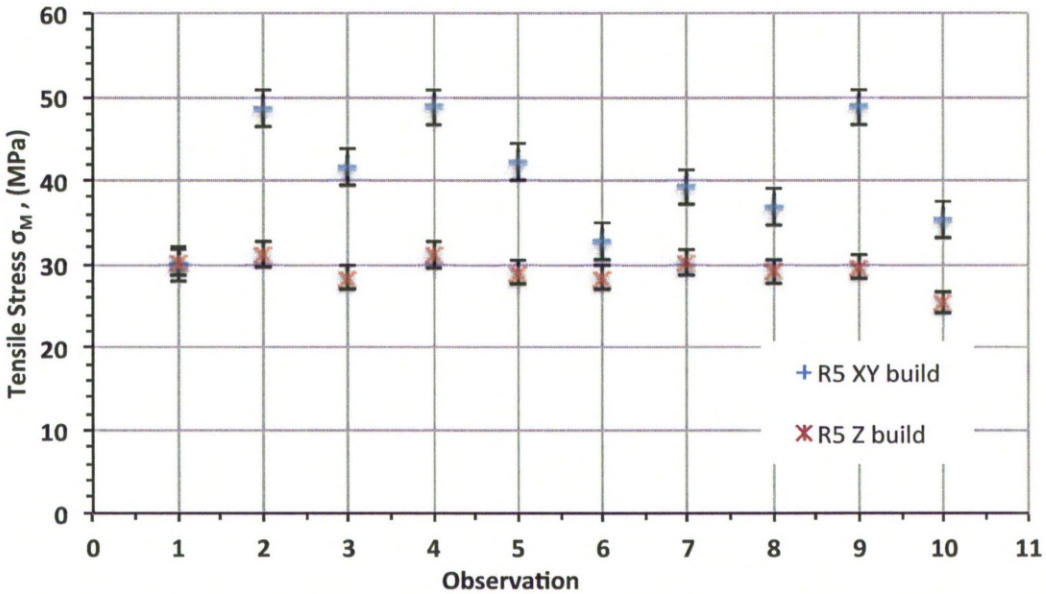

Figure 71: Tensile Stress Observed for the XY and Z Build Specimens.

The tensile strength observed for the XY build (horizontal) was higher than the Z build (vertical) was apparent from Figure 71. The average tensile strength of the XY build specimen was 39 MPa whereas the Z build showed a 25% reduction to 29 MPa. A similar reduction in modulus of elasticity was also observed. The XY build having 1000 MPa where the Z build reduced to 800 MPa, a 20% reduction. The variations in the mechanical properties that occur in the specimens fabricated

in layers are shown in Table 10. Tensile testing was also performed on specimens containing various loading of ceramic powder.

Table 10: Comparison of Literature and Measured Tensile Properties of R5 Photopolymer [245].

Description	Specification	Literature Values	Results
Tensile Stress σ_M, (MPa)	ASTM- D638M	31-39	39 ± 7 (XY Build)
			29.33 ± 1.7 (Z Build)
Modulus of Elasticity Y, (MPa)	ASTM – D638M	1245 – 1510	1000 ± 87 (XY Build)
			800 ± 44 (Z Build)
% Elongation at Break (%)	ASTM – D638M	11 – 25 %	14.2 % ± 2.2% (XY Build)
			19.6 % ± 1.6 % (Z Build)

The optimised tensile test specimen was also used for manufacture of composite specimens containing various loading of $BaTiO_3$ particles. The composite specimens are addressed on the basis of theoretical wt% or vol% shown in Table 11, as these were lighter in weight and could not be measured due to inconsistency in density measured using water displacement method. The mechanical properties of polymer test specimens were compared with two highest ceramic content tensile test specimens. Figure 72 and Figure 73 shows that the addition of ceramic powder reduces the tensile strength σ_M and modulus of elasticity Y when compared with polymer alone.

Table 11: Volume Percentage of Reference Composition.

Specimen set	Composition	Theoretical Volume% of $BaTiO_3$
0	R5	0%
1	46 wt%	14%
2	50 wt%	17%
3	54 wt%	19%

Comparison of results in Figure 73 shows that the addition of ceramic reduces the tensile strength by 21% for 14 vol% and 41% for 17 vol%, respectively. This reduction in strength is caused by reduced interfacial bonding due to inclusion of ceramic particles. This behaviour is typically observed in particulate composites [126].

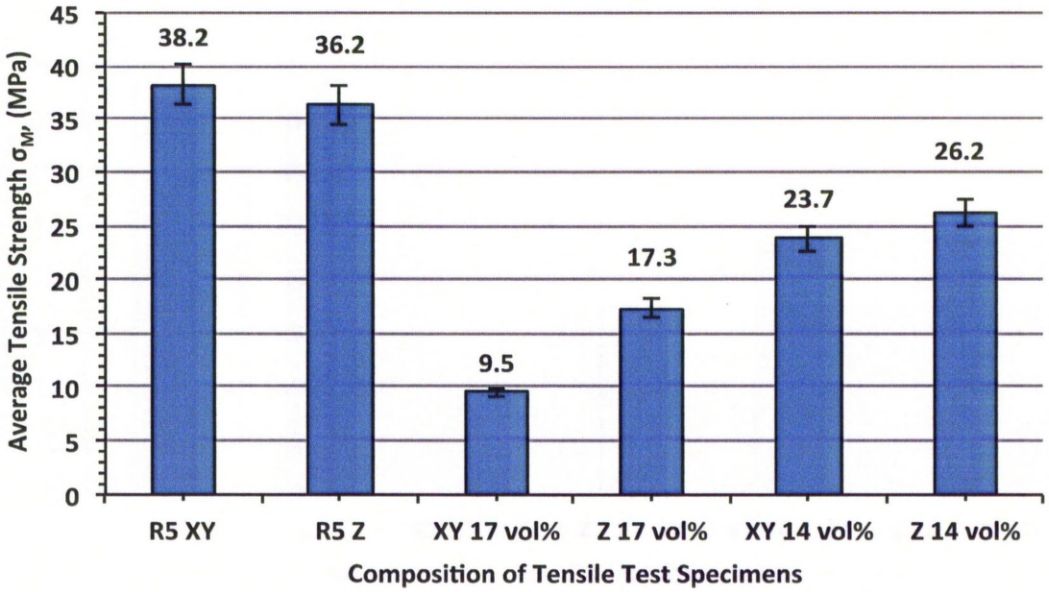

Figure 72: Tensile Stress Observed for Different Loading of $BaTiO_3$.

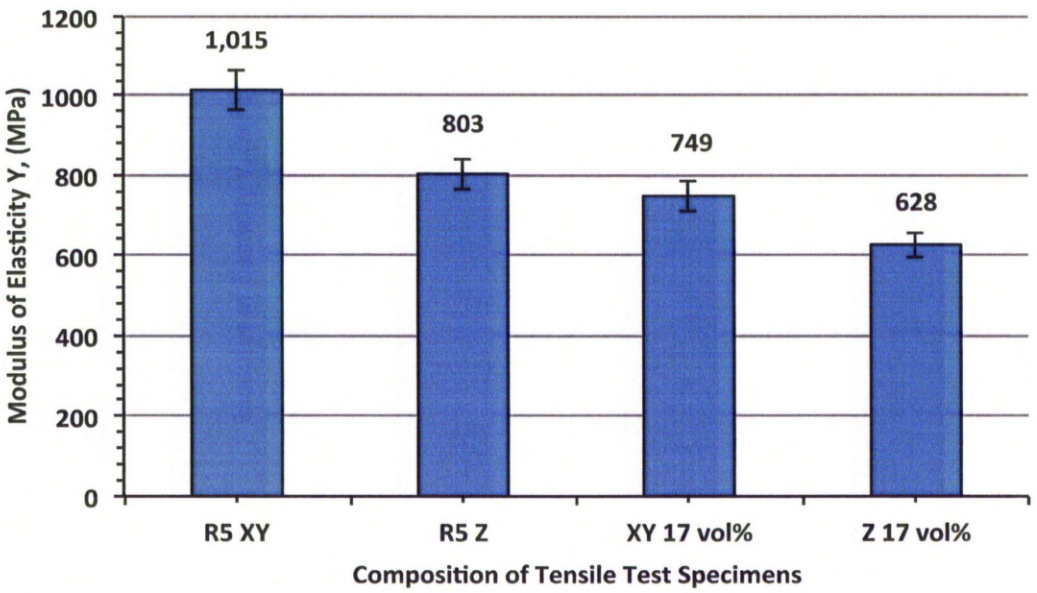

Figure 73: Average Modulus of Elasticity Y Varying With $BaTiO_3$ Content and Built Direction.

Figure 74 shows the typical stress – strain characteristics recorded for the tensile test specimens manufactured in the XY and Z direction. The polymer test specimens built in the Z direction show a greater elongation rate before reaching the yield, followed by a reduced elongation rate beyond yield. The behaviour observed in the polymer test specimens built in XY direction; however, show a uniform elongation until failure. In both cases, the ultimate tensile strength was

close to 30 MPa. On the contrary, the composite specimens built in Z direction had gradual rate of elongation. In the case of composite tensile test specimens, an early failure occurred at tensile strength of 17 MPa in Z built direction and 10 MPa in XY build direction specimens, which is a reduction of 66% in comparison to the polymer specimen (30 MPa).

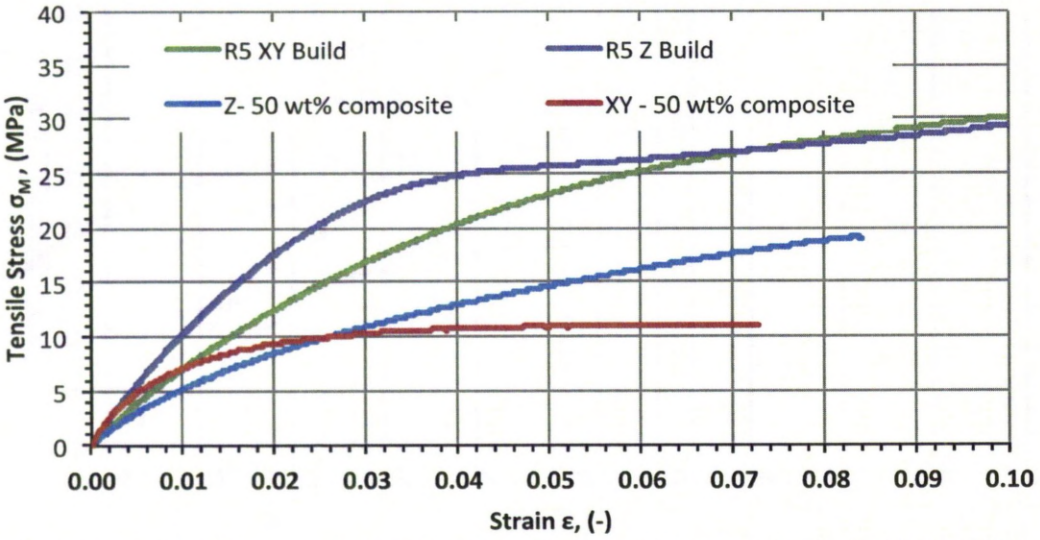

Figure 74: Typical Stress – Strain Behaviour of XY and Z Direction Builds for Various DLP Materials.

In order to understand the behaviour of tensile specimens based on the build orientation, a schematic representation of layer orientation is shown in Figure 75. The test specimens were manufactured in 25 µm layer thickness bounded together as laminate composites, the notches formed between each layer are potential sites for crack initiation when under applied load (Figure 76). Under applied load, each layer will reflect cumulatively the overall stress and strain behaviour of the specimen resulting the elongation resulting in higher elongation in gauge length of 19% for Z direction built specimens. All the layers of the specimens built in XY direction will elongate equally, therefore limiting the elongation to 14% of gauge length (Table 10).

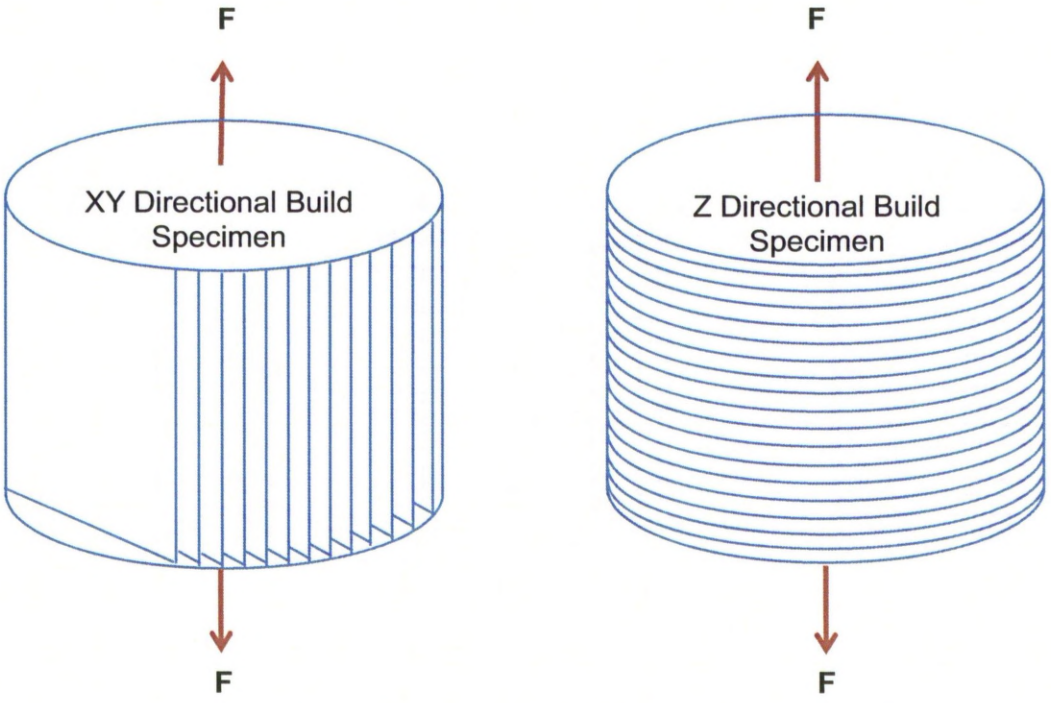

Figure 75: Schematic Representation of Layers in Test Specimens.

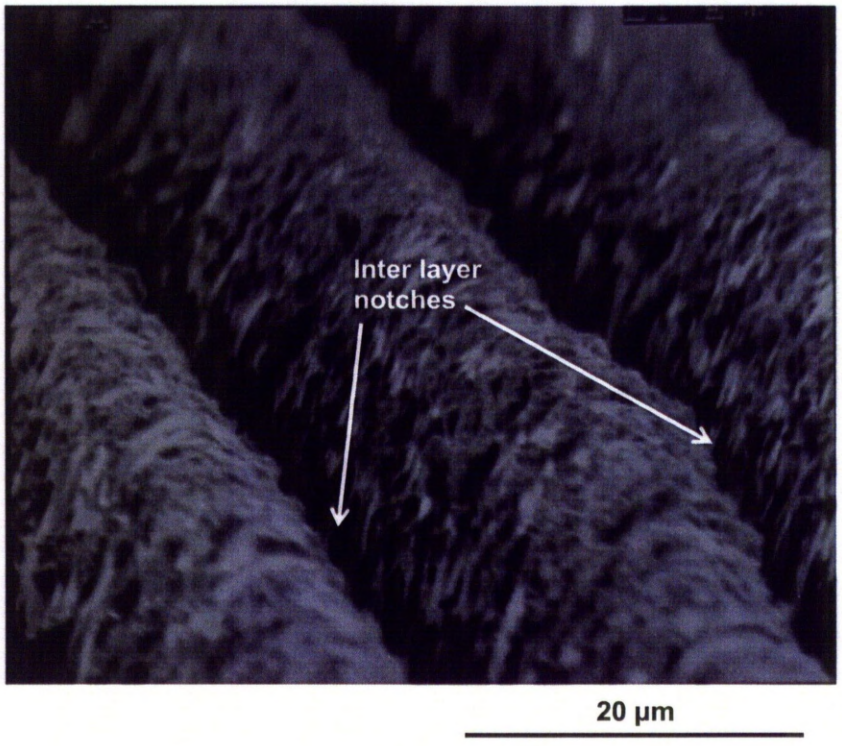

Figure 76: Typical Inter Layer Region Forming Notches

Fracture Analysis of Tensile Test Specimens

The broken surface in the gauge length of tensile test specimens was examined under SEM to observe the fracture behaviour. The interfacial bonding between each layer and the thickness of each layer influenced the elongation measured for the test specimen as previously discussed. The stress within each layer will vary due to the reduced cross sectional area formed by the notch between the layers and a stress concentration will be apparent at the surface, Figure 76 shows the typical morphology of a specimens. These notches form ideal sites for crack initiation. As shown in Figure 77a, the failure of the Z direction test specimen at the notch formed between the layers shows poor interlayer bonding and hence poor cross-linking between the layers [246]. The smooth fracture surface between the layers is typical of a brittle failure occurring in the perfectly cured photopolymers.

In the case of the test specimens built in the XY direction, the fracture surfaces exhibit a region where the crack first accelerates and then decelerates forming a smooth region known as a mirror (Figure 77b). The crack accelerates at a uniform rate through out the gauge cross section for the XY build specimens. This is evidenced by the crack propagation path that is uniform in all directions, as indicated by the river lines, typical of the behaviour.

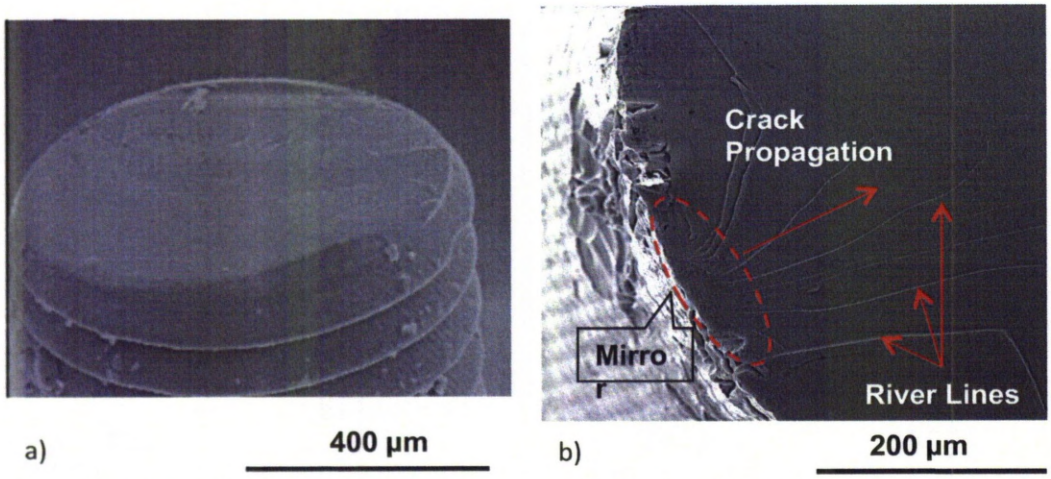

Figure 77: SEM Image of a) Z Direction and, b) XY Direction Build Test Specimen

Comparing the behaviour of composite test specimens with polymer test specimen shows significant deviation from the typical polymeric brittle failure. Figure 78 shows a micrograph of a test specimen build in the Z direction. Here the crack nucleation for tensile test specimen started along the circumference of the gauge length and progressed towards the middle of the specimen. The central region of the specimen eventually brakes by pulling, due to the increased stress in the centre of the specimen (Figure 78a & b). Unlike the polymer specimens, the fractured surface was not smooth but followed the path along the particles (Figure 78c & d). After the crack nucleation, it passes through different layer before failure.

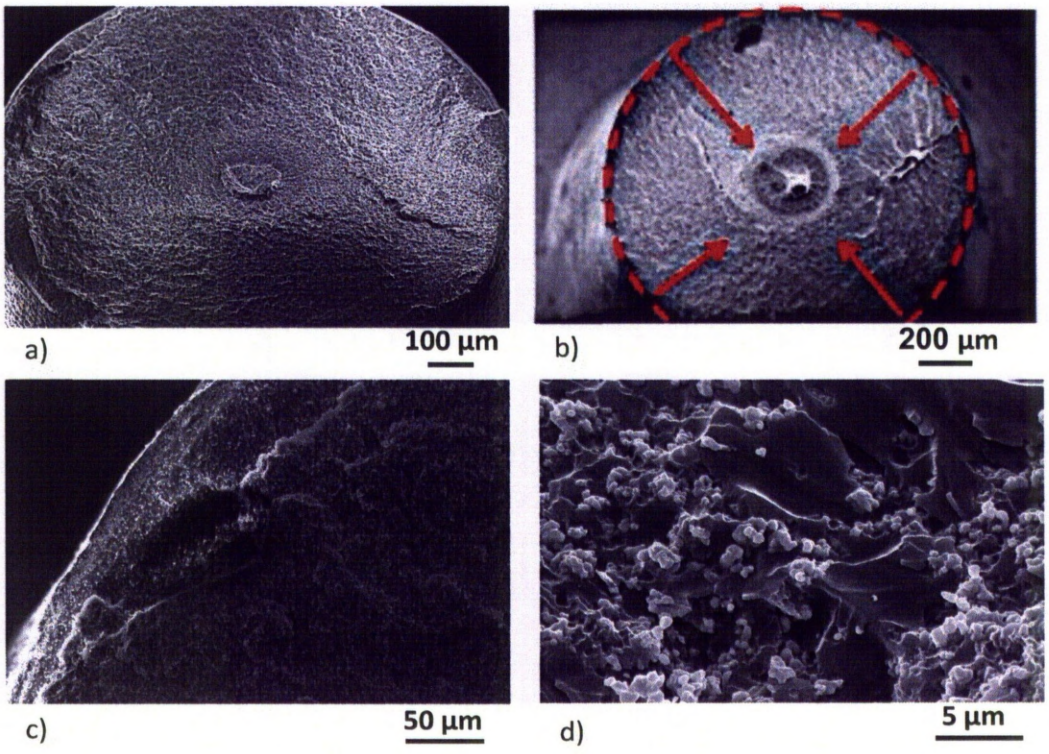

Figure 78: a) Fractured Surface of the Z Build Specimen, b) Crack Propagation in Composite Material Test Specimen Build in Z Direction, c) Crack Initiation at the Notch Between the Layers, d) Fracture Path Diverted at the Polymer - Ceramic Interface.

Figure 79a shows the fractured surface of tensile test specimen manufactured in the XY direction. Crack nucleation is observed in one half of the circular cross section and progresses towards the rest of the area, represented by the arrows. The layers in the specimen undergo shear before failure, resulting in separation of

layers (Figure 79c & d). The week interlayer bonding in specimen is apparent by observing the cracks progressing between each layer in a fractured surface.

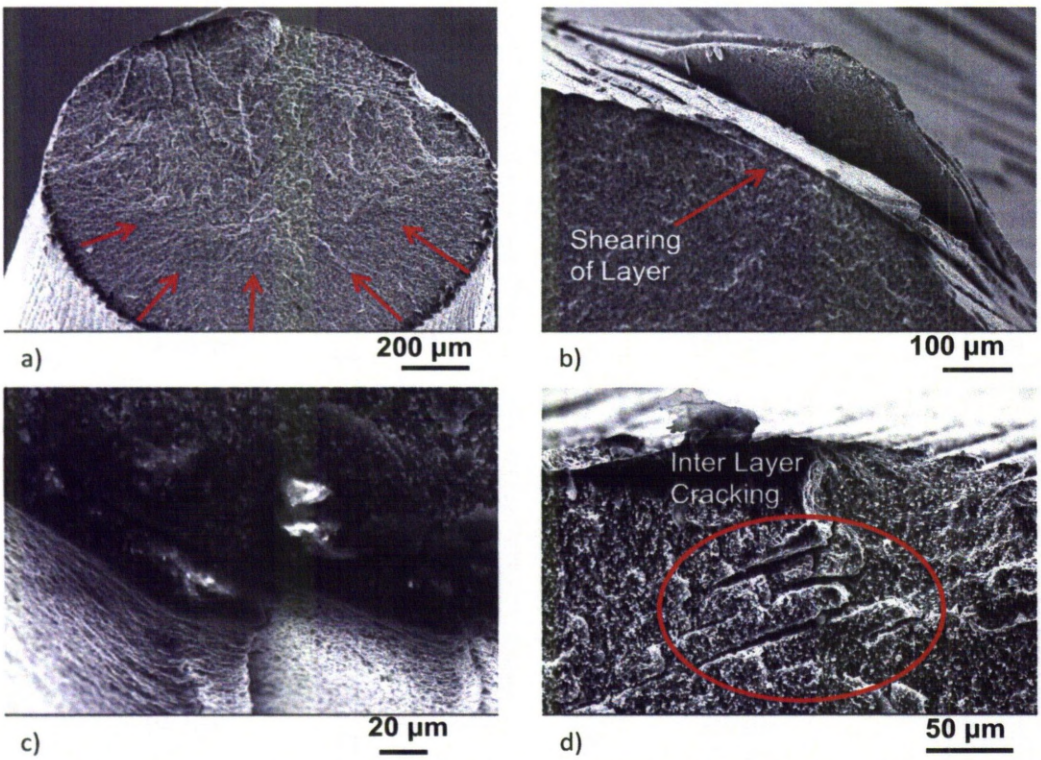

Figure 80: a) Crack Formation and Progression in XY Build Specimen, b) Shearing of Layers at the Periphery Before Failure, c) and d) Magnified View of Shear Between The Layers.

As shown in Figure 80, closely aggregate ceramic particles in the composite material are surrounded by polymer. The crack progresses through the interfacial region and diverts from one ceramic particle to another. The ceramic particles absorb some part of the energy, thus resisting crack propagation.

Initial observation of the fracture surface of the ceramic - polymer composites, gives an impression of brittle failure due to poor interfacial bonding between the photopolymer and $BaTiO_3$ particles providing a low energy path for cracks (Figure 80a – c). Examination of the fractured surface at high resolution however indicates formation of fibrillation of the polymer on the $BaTiO_3$ surface. This fibrillation indicates relatively strong adhesion between the ceramic particles and photopolymer, shown in Figure 80d.

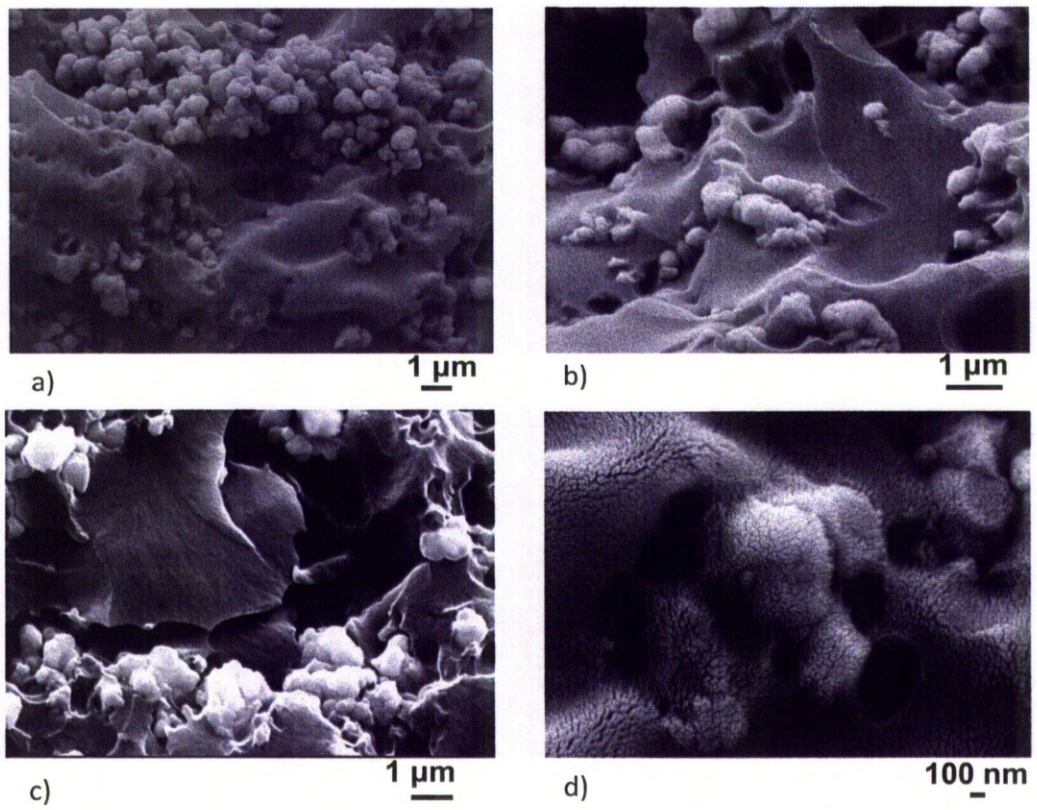

Figure 80: a – c) Typical Fracture Surface of High Loading Particulate Composites Showing Progression of Crack at the Ceramic – Polymer Interface, d) Fibrillation of Polymer Observed at the $BaTiO_3$ Surface.

Fibrillation is usually observed in thermoplastic polymers that have undergone extensive drawing. During fibrillation the material undergoes molecular reorientation in a direction parallel to the applied load. If the force is applied in one direction and all other directions are constrained, the fibril formation is generally separated by voids aligned in the direction parallel to the draw direction. The extent of fibrillation is dependent on the ease of disentanglement of the polymer molecules and the easy sliding between them. Fibrillation is usually formed, just prior to the final fracture. Although, addition of ceramic particles has reduced the mechanical strength in all the specimens manufactured, the path of crack propagation was resisted by the particles, prolonging the failure.

Apart from the effect of build direction on the specimen strength, it was found that discontinuities in the tensile test specimens due to poor inter-layer bonding contributed significantly to the early cracking of the test specimens. The image in

Figure 81 shows this effect in the specimens manufactured in XY and Z direction. These specimens were classed as failures and were discarded.

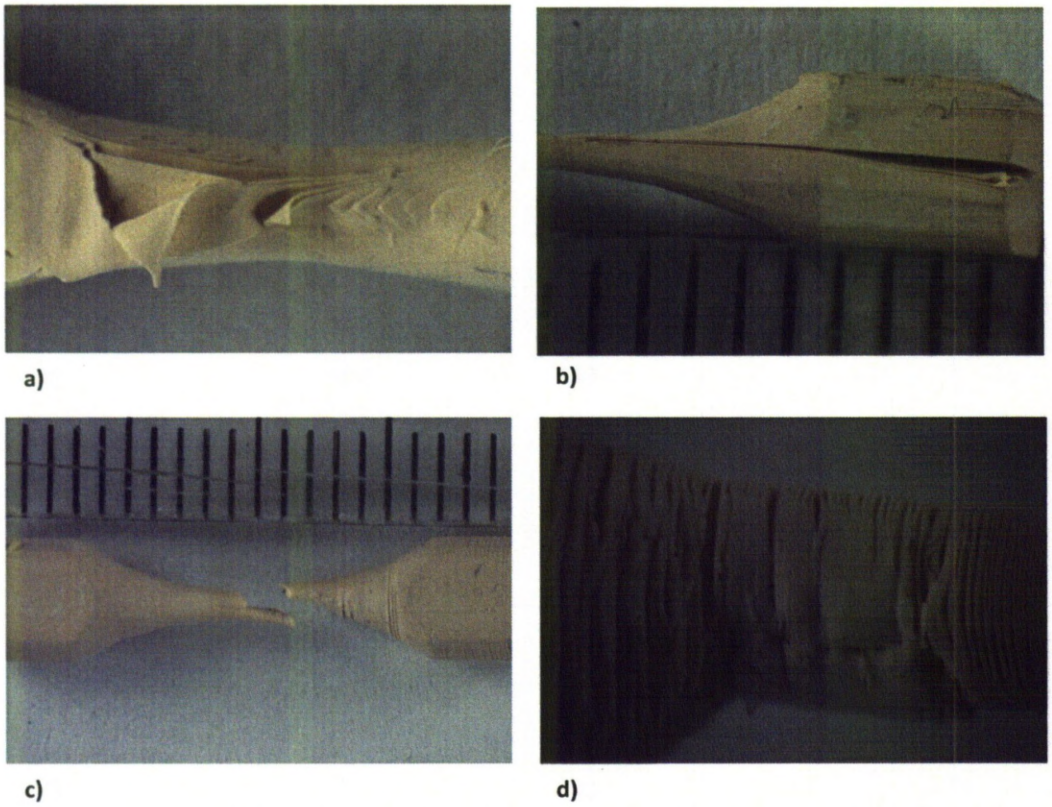

Figure 81: Delamination in Tensile Test Specimens a)&b) in X Build, c)&d) in Z Build.

Theoretically, increasing the exposure for layer deposition should increase the inter-layer cross-linking; strengthening the bonding between the layers, but in practice increasing exposure will cure the polymer layer beyond its green strength, effectively reducing the cross-linking between layers.

5.3.3 Prediction of Mechanical Performance

The upper and lower bound forecast for modulus of elasticity, predicted using the work of Kolarik [123]. The modulus of elasticity is expected to increase with increasing volume fraction of $BaTiO_3$. The upper and lower bound limits for the specimens developed by the DLP system were calculated using Equation 2.36 and Equation 2.45, respectively and plotted in Figure 82. The working area indicated on the graph corresponds to the maximum density of specimens that were successfully

manufactured by DLP. It was apparent from lower bound limit that the addition of $BaTiO_3$ powder will not considerably improve the modulus of elasticity up to 0.8 volume fraction.

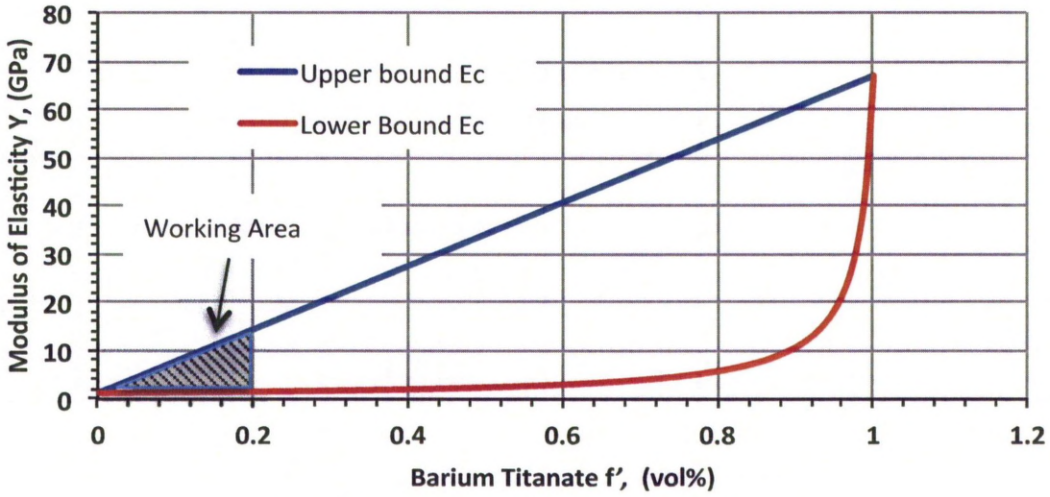

Figure 82: Prediction of Modulus of Elasticity.

The experimental values of modulus of elasticity measured for each specimen, discussed in Section 5.2.3 were plotting against predicted bounding limits. Figure 83 shows that the experimental observation for 19 vol% and 17 vol% were below lower bound limit predicted for the specimens. This difference in theoretical predication and experimental observation is larger than the range of standard error bars plotted for each composite specimen. The experimental observations failed to verify the bounding limits predicted using mathematical model. This could be due to the nature of composite test specimen as they were manufactured in layer showing poor interfacial bonding and stress concentrated regions forming due to notches, hence insufficient strength. In order to suitably adopt the mechanical behaviour based on mathematical models for parts manufactured by AM route, influence of cross-linking, cohesive forces between constituent materials in a composite needs consideration.

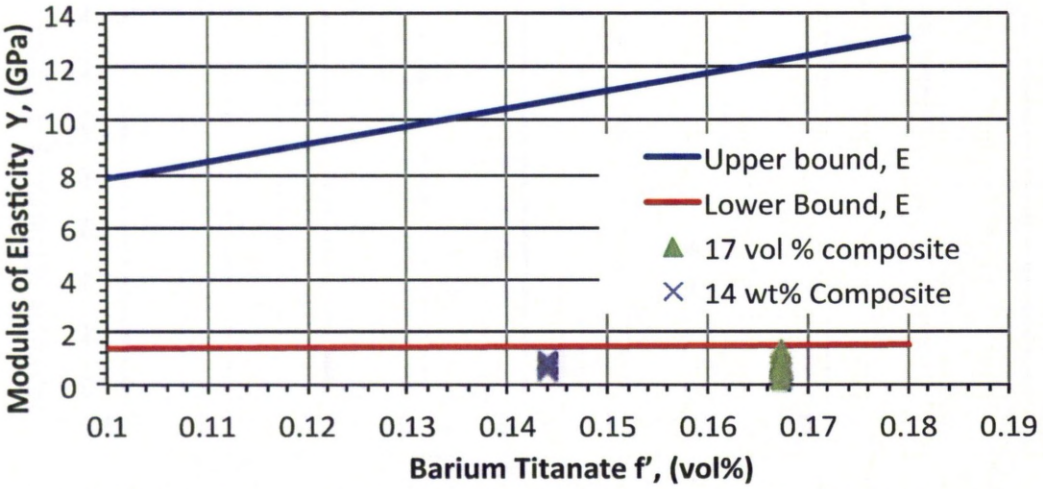

Figure 83: Experimental Observation of Modulus of Elasticity Plotted On Theoretical Forecast.

5.3.4 Discussion

The tensile test specimens for both polymer and R5 – $BaTiO_3$ composite material were analysed for mechanical performance. The design of the tensile test specimen was optimised for the build envelope of the DLP system and other limitations experienced during manufacturing, discussed in Section 5.3.1. Polymer test specimens were built in the XY direction (horizontal) and Z direction (vertical). Testing these specimens confirmed that the mechanical properties were influenced by the build layer orientation. This was apparent from Figure 72, where tensile strength of all the XY built specimens was higher than the Z built specimens.

The mechanical properties of the composite specimens containing various loads of $BaTiO_3$ powder were also analysed. The mechanical properties of the composite test specimens showed, reduction in the tensile strength and modulus of elasticity, behaviour typically observed in particulate composites. The tensile strength of the Z built specimens was 17 MPa compared to the X built specimens at 10 MPa.

The fracture analysis of the test specimens confirms that the notches between the layers were sites of crack initiation. The crack propagation was however varying, influenced by the layer orientation and specimen material. The fracture surface for polymer specimens was smooth with few river lines, where as the composite

specimens showed diverted crack path progressing through the ceramic – polymer interfacial regions. Microscopy observations of the fracture surface in Figure 80 show formation of fibrils at the ceramic – polymer interface, confirming the presence of strong adhesion between the ceramic – polymer interface. The addition of ceramic to the polymer reduced the area between the layers leading to poor cross-linking. The influence of layer orientation and poor cross - linking on mechanical behaviour has resulted in failure to verify the mathematical prediction of mechanical performance.

5.4 Evaluation of Manufacturing Feature Size

The addition of particles to the monomer alters the properties of the photopolymer such as flowability, which influences the resolution of the machine. A set of experiments were undertaken to identify the influence of addition of ceramic powder in the photopolymer on the build resolution of DLP.

5.4.1 Specimen preparation

To investigate the influence of composition on the resolution of the DLP system, walls and slots were manufactured with photopolymer alone and with addition of $BaTiO_3$ were manufactured in 25 μm layer thickness, similar to the polymer and composite specimens discussed in Section 3.1.1 and Section 5.2. The specimen was divided into two regions marked by two rectangular envelopes. The top half of the envelope consists of slots and bottom envelope contains walls. The minimum wall thickness of 0.025 mm located at 0.025 mm from the adjacent wall. The wall thickness is increased in steps of 0.025 mm. The other region contains walls of uniform thickness but with varying separation and a minimum separation distance of 0.025 mm, increasing in step of 0.025 mm. Similar specimens were built from ceramic – polymer composites with ceramic content up to 12 vol% (40 wt%). The dimensional details of the test specimen are shown in Figure 84. In order to ensure that the standard range parameters are used for manufacture of walls and slots, the test specimen were 4 mm in thickness.

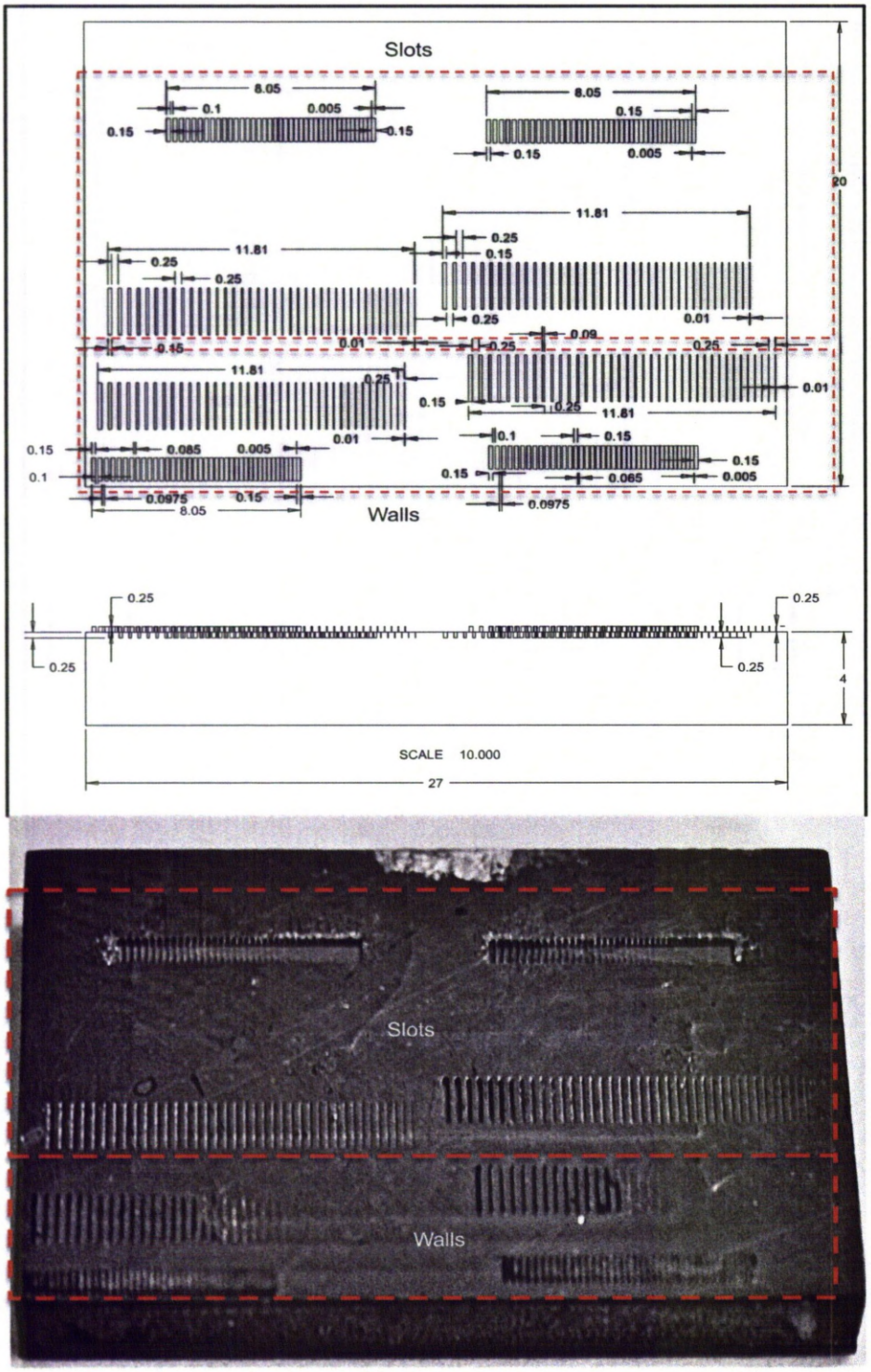

Figure 84: Dimensional Details and Polymer Test Specimen of Walls and Slots for Resolution Testing Specimen.

5.4.2 *Measurement of Build Resolution*

Various test specimens were manufactured to identify minimum feature size that can be successfully manufactured by the DLP system. The polymer test specimen containing wall and slots was manufactured with standard range parameters, as discussed earlier. Figure 85 and Figure 86 shows slots and walls manufactured from photopolymer alone. It was evident that the DLP system could manufacture thin wall. The minimum wall thickness of 0.0525 mm and slot width of 0.075 mm were successfully built. These thicknesses were sufficiently strong to sustain during manufacture. Although, thinner walls were manufactured, they lacked mechanical strength and were not self-sustaining during build. Looking at these results, the minimum feature size for manufacture by DLP is between 0.08 - 0.1 mm to ensure reliable results.

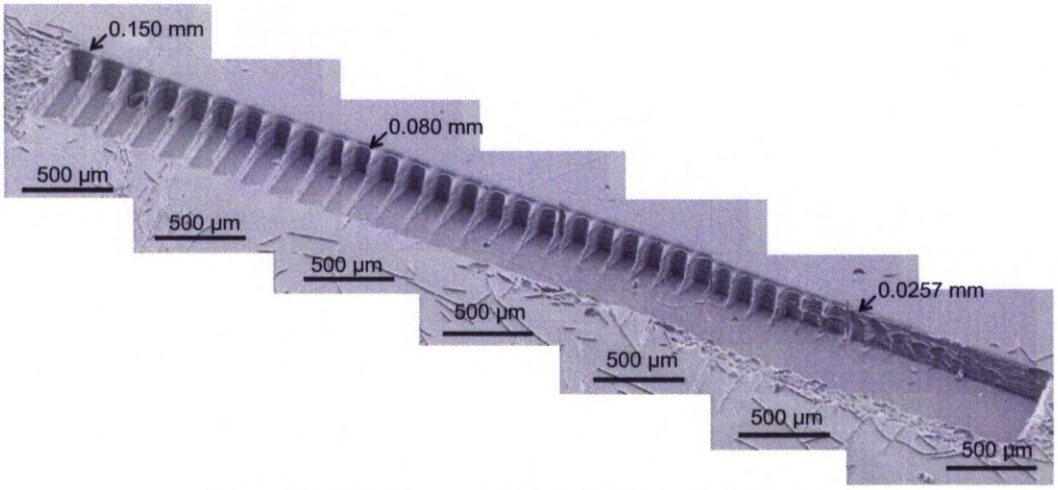

Figure 85: SEM Image of Slots in Polymer Test Specimen

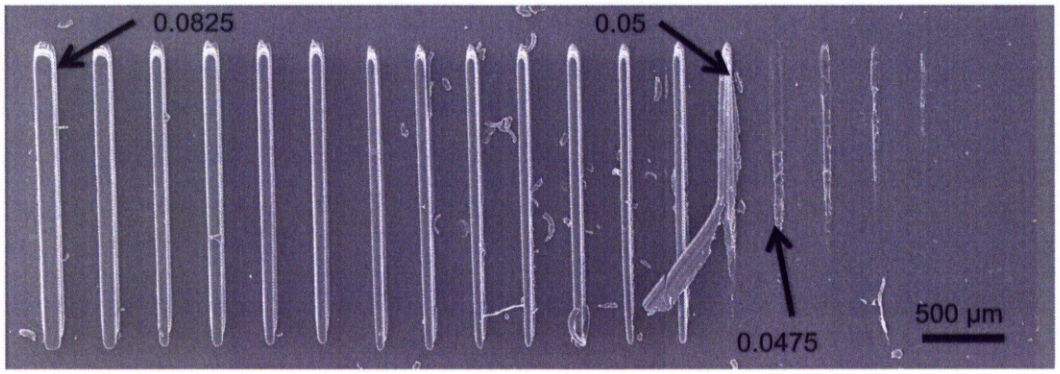

Figure 86: SEM Image of Walls in Polymer Test Specimen.

A similar set of experiments was performed for the $BaTiO_3$ – R5 composite. Figure 87 shows a typical composite test specimen containing walls and slots showing an influence of addition of $BaTiO_3$ on the minimum feature size manufactured by the DLP system. Although, the walls and slots were built by DLP, it was evident that reduced flowability of $BaTiO_3$ – Polymer mix has resulted in curing between the walls and filling the slots. The ability of DLP to build micro features was however inhibited by its inability to remove excess material cured between the features, even for particle load of 6 vol % material.

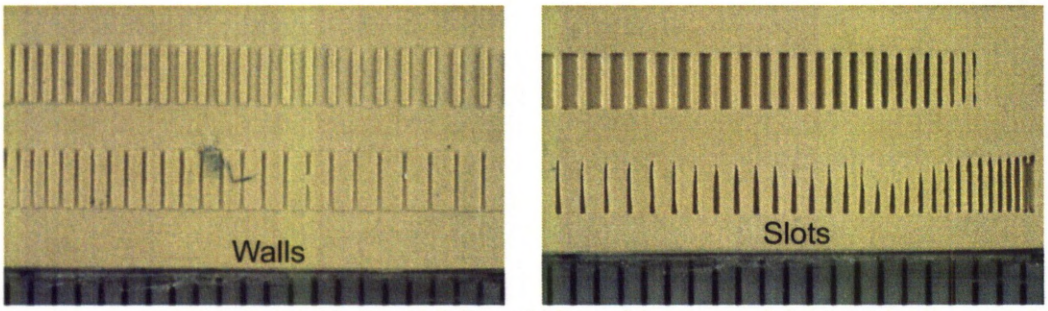

Figure 87: Typical Built of Walls and Slots of Composite Test Specimen.

The microscopy observation shown in Figure 88 presents a comparison between the polymer and ceramic – polymer mix test specimens. The walls of polymer test specimen were clear without any excess polymer cured, shown in Figure 88a & b. The DLP system could successfully build lots having thin walls, but the wall could not sustain during build being too thin evident in Figure 88c & d. The walls and slots manufactured in 12 vol% composite material demonstrates failure to remove the ceramic – polymer mix. In Figure 88e, the walls manufactured at separation distance of 0.025 mm show failure of walls due to poor inter-layer bonding with excess curing of ceramic – polymer material at few locations. The walls manufactured at 0.1 mm distance however were completely filled with cured composite material, shown in Figure 88f.

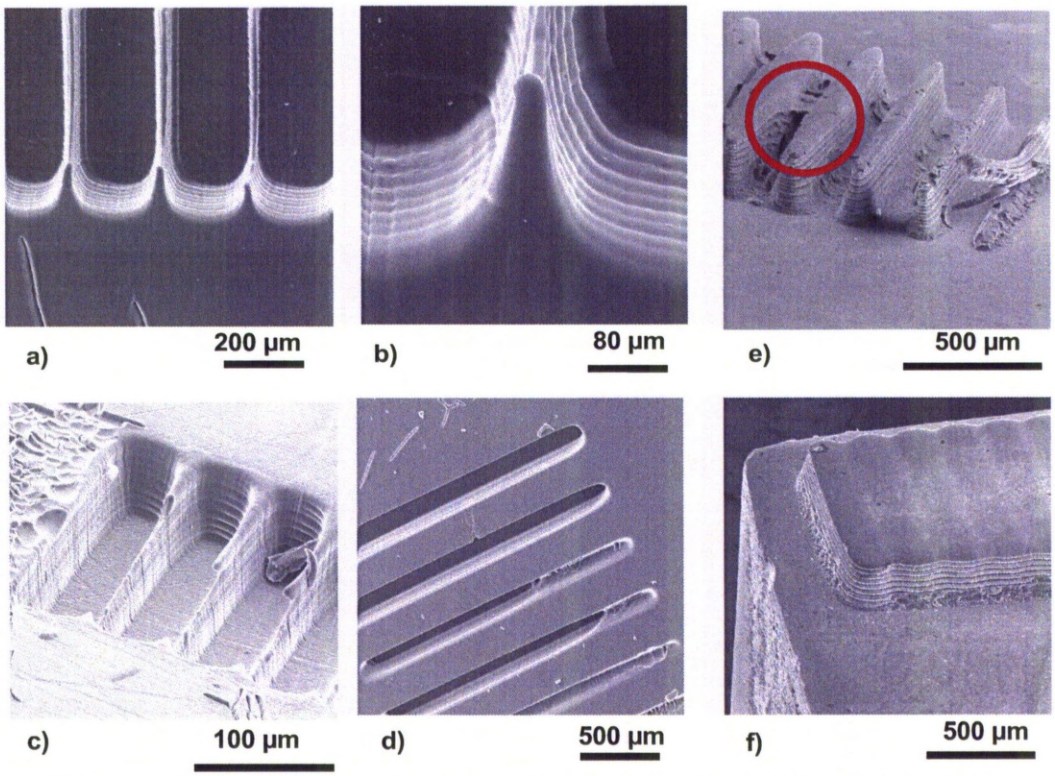

Figure 88: SEM Image of a & b) Polymer Walls, c & d) Polymer Slots, e & f) 12 vol% Composite Walls.

5.4.3 Discussion

The investigation was undertaken to identify the resolution of DLP by manufacturing the test specimens containing walls and slots. The test specimens were manufactured for polymer alone and ceramic – polymer mix containing various loads of $BaTiO_3$ powder. The analysis of these test specimens confirms that the minimum reliable feature size of 0.08 – 1.0 mm can be successfully built in standard R5 polymer. The addition of $BaTiO_3$ powder to photopolymer restricts the manufacture of the minimum feature size. However, this could not be quantified as the potential to manufacture minimum feature size was limited by the inability of the material to flow between the feature and not due to failure of DLP to build thin parts. The microscopy images shown in Figure 88e – f confirm that the small feature sizes may be manufactured if the distance between the features is sufficient for the material to flow. The specimen manufactured with 0.25 mm distance between walls however still showed partial curing between the features.

5.5 Measurement of Electrical and Dielectric Properties

The range of practical applications of piezoelectric materials has expanded greatly in recent years. Although, possessing excellent dielectric properties, piezoelectric ceramics frequently demonstrate poor mechanical strength and often undergo brittle failure, especially in the case of ceramics. Conventional manufacturing routes are based on pressure sintering of ferroelectric materials. Good bonding achieved because of this causes the piezoelectric grains in the body regrow by interdiffusion during the sintering process, leading to a more homogeneous grain size and reduced porosity and hence, good piezoelectric performance.

Unlike most of the AM techniques, the DLP process is relatively new and so far, has a limited selection of photosensitive materials available. Developing ceramic-polymer composites may be highly desirable for electrical and electromechanical applications, as manufacturing via AM may open up the prospect of new design functions.

5.5.1 Prediction of Piezoelectric Coefficient

The relative piezoelectric coefficient for varying ceramic content can be modelled using Equation 6.1 [247]:

$$d_{33} = \frac{vS_{11}^{p} d_{33}^{c}}{S(v)} \qquad (6.1)$$

Where, v is the volume fraction of ceramic, S^{p}_{11} is the compliance of ceramic particles and $S(v)$ is the compliance of composite material given by the formula:

$$S(v) = vS_{11}^{p} + (1 - v)S_{33}^{E} \qquad (6.2)$$

The values of piezoelectric coefficient and compliance used in the theoretical model are given in Table 12:

Table 12: Material Properties of Photopolymer R5 [245] and $BaTiO_3$ Ceramic [31].

Property	Barium Titanate, $BaTiO_3$	Photopolymer, R5
Piezoelectric Coefficient (d_{33})	85.6 pC/N	0 pC/N
Compliance (S_{33},S_{11})	$15.7x10^{-12}$ m^3/N	$662.2x10^{-12}$ m^2/N

The model described has limited accuracy. It depends on uniform temperatures across the composite and presumes strong interfacial bonding between the different phases of the material. This means that any stress in the matrix will be uniformly transferred across all the filler material but it fails to account for the influence of particle size on dielectric properties. The expected behaviour predicted based on Equation 6.1 is shown in Figure 89. It was clear that the increasing the ceramic content up to 20 vol% will result in increased piezoelectric coefficient of 80 pC/N. Further increase in particle loading does not considerable improves the performance.

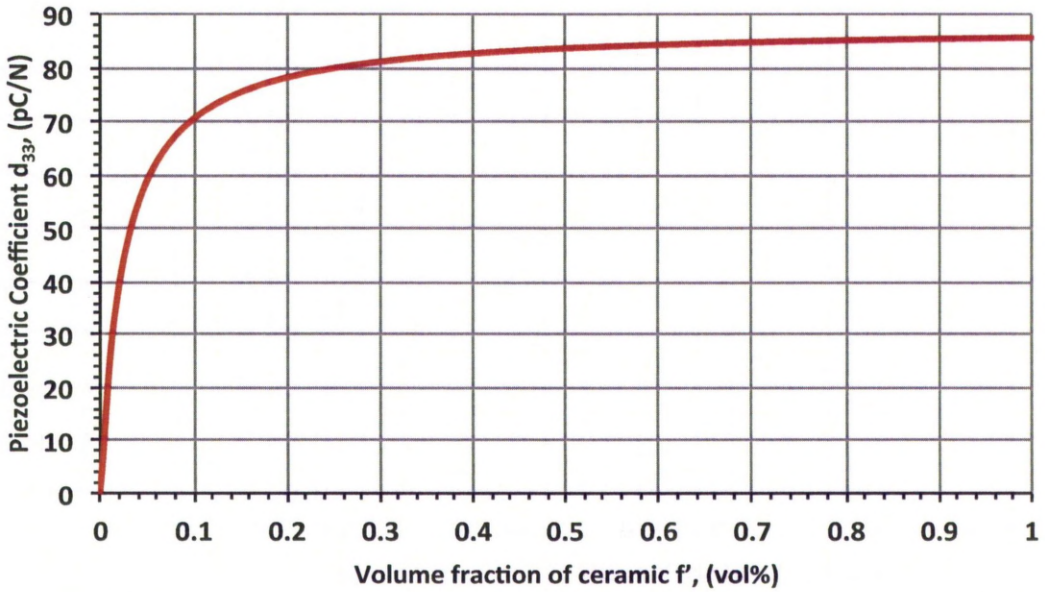

Figure 89: Theoretical Prediction of Piezoelectric Coefficient for Ceramic Composition.

5.5.2 *Preliminary Piezoelectric Analysis of Functional Material*

Various manufacturing processes adopted for the fabrication of piezoelectric ceramic-polymer composites were discussed in Section 2.1.7. Analysis of photopolymer specimens containing $BaTiO_3$ ceramic particles was assessed in terms of their mechanical properties and showed no noticeable improvement in mechanical strength. This was attributed to the delamination of the component layers in the higher wt% specimens causing poor inter-layer bonding. The addition of piezoelectric ceramic particles to the photopolymer may enable micro electrical applications to be served by AM industry.

Method

Thin blocks of size 10 mm x 10 mm x 1 mm consisting up to 5 vol% ceramic particles were manufactured by the DLP system. They were poled by applying voltage field across their surfaces in air. The procedure for poling these composite specimens is described below:

- The specimen is held between the voltage terminals
- The specimen is placed in the furnace
- The voltage is applied across the specimen with the poling voltage kept constant for each run
- The furnace is switched on and heated to a predetermined poling temperature
- Once the furnace reaches the test temperature, the furnace is switched off and cooled to room temperature without removing the voltage field across the piezoelectric specimen
- Once the temperature of furnace reaches room temperature, the voltage field is switched off and the specimen is removed
- Each run is conducted at a constant voltage field and a specific poling temperature

Piezoelectric Behaviour of Preliminary Specimens

The preliminary specimens containing 6 vol% (23 wt%) $BaTiO_3$ particles were polarised in the range of 0 – 2.5 kV and 50 – 90 °C. During polarisation, the poling temperature across the specimen was increased by 10 °C for each measurement without changing the electric voltage for the entire range of poling temperatures. The electric voltage was then increased by 0.5 kV for next set of poling cycles. The specimens made from polymer alone showed no piezoelectric coefficient, confirming an electrically inactive material. However, initial observation of the piezoelectric coefficient d_{33} for the unpoled ceramic -polymer composite specimens confirmed that they were inactive and required poling for functional activation to measure the piezoelectric coefficient d_{33}. The piezoelectric coefficient recorded for the polymer composites is shown in Figure 90. Although, the Curie temperature of $BaTiO_3$ is 120 °C, the poling temperature was restricted to 90 °C as softening of the photopolymer occurs at temperatures between 110 – 120 °C.

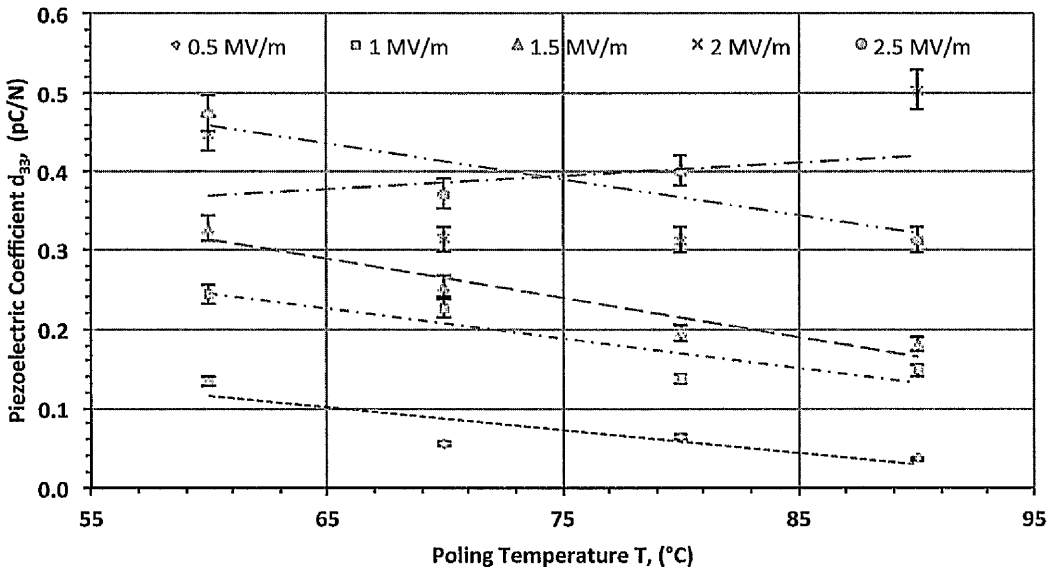

Figure 90: Average Piezoelectric Modulus d_{33} Observed for 6 vol% Preliminary Composite.

The observations recorded for d_{33} shown in Figure 90 are considerably smaller than the piezoelectric constant of $BaTiO_3$ ceramic particles given in literature, typically 85.6 pC/N [31]. However, some piezoelectric effect induced set a baseline for further optimisation work. The piezoelectric coefficient of the composite up to

maximum electric voltage of 2.5 MV/m increased with voltage field. However, increasing the poling temperature measured at a constant voltage field did not show increase in the piezoelectric coefficient d_{33} with increasing poling temperature. The trend lines plotted on the graph shows that the composite containing 6 vol% particles show a reducing piezoelectric coefficient. The variation in the measurements is due to the relatively low weight / volume fraction of piezoelectric ceramic in the composite and the high electrical resistance offered by the photopolymer surrounding the ceramic reducing the available surface charge to the $BaTiO_3$.

5.5.3 Piezoelectric Measurement of High-Density Functional Material

In order to examine the piezoelectric coefficient further, a second set of test specimens were manufactured. The ceramic content was increased to 19 vol% (in comparison to 5 vol%). The thickness of these blocks was reduced to 0.5 mm, resulting in increased electric field from 2.5 MV/m applied in the first sample set to 5.0 MV/m in the second set without practically increasing the electric field across the specimen.

Composites with higher ceramic contents were manufactured at 19 vol% (54 wt%), 17 vol% (50 wt%) and 14 vol% (46 wt%). Two specimens for each composition, from the same batch were poled during the study. They were poled following the procedure described in Section 3.3 and piezoelectric modulus d_{33}, capacitance C and dielectric loss (tan δ) were measured for each sample. 30 measurements were recorded for each poled composite specimen to assess repeatability. Both the specimens were poled initially at lower electric field and lower temperature. They were subsequently poled at a higher poling temperature, only after consistent observations were recorded for both the composite specimens.

Piezoelectric Behaviour of High-Density Specimens

Results from series of experiments are shown in Figure 91. The magnitude of d_{33} was significantly higher (a factor of 10 for 19 vol% specimen) than that achieved in

the preliminary test. The d_{33} observed for both, the preliminary test composite and high-density composites demonstrate the influence of electric field on d_{33}. For high-density composites, the magnitude of d_{33} increases with higher applied electric voltage. Figure 91 shows an agreement with the expected behaviour for 19 vol% and 17 vol% composites. Although consistent increment in the piezoelectric coefficient was not recorded, the trend lines confirm that the higher piezoelectric coefficient was measured at higher electric field for the entire range of poling temperature for 19 vol% and 17 vol% specimens. Similar behaviour was not however observed for 14 vol% specimens. The piezoelectric coefficient compare to 0.5 pC/N poled at 2.5 MV/m for initial test discussed in Section 5.5.1, was considerably higher for 19 vol% specimens at 5.5 pC/N and 14 vol% specimens at 3.8 pC/N poled at electric field of 30 MV/m.

Figure 91 also presents the behaviour of the functionally active composite materials developed by DLP for varying loading of the ceramic content. It was evident that the piezoelectric coefficient measured for 6 vol% specimens shows an unexpected reduction with an increasing poling temperature. The behaviour for 19 vol% specimens however shows an increasing piezoelectric coefficient with an increasing poling temperature. Similar trend lines plotted for specimens with 14 vol% and 17 vol% ceramic content shows an inconsistent behaviour which was a mix behaviour both, the high – density specimens and low – density specimens. It can be therefore presumed that an increase in the ceramic loading beyond 19 vol% will show an increasing piezoelectric coefficient for both, increasing poling temperature and electric field.

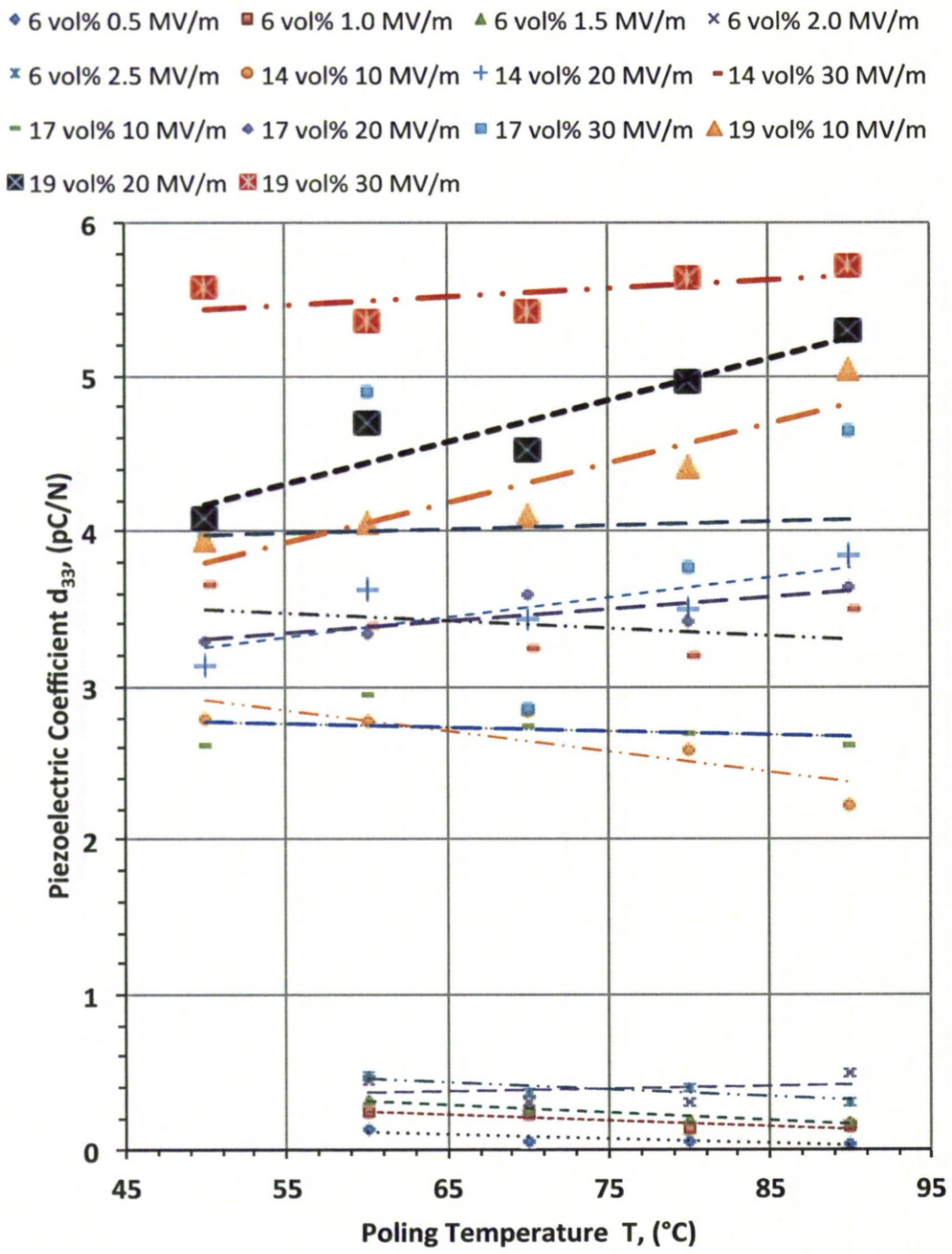

Figure 91: Piezoelectric Coefficient d_{33} Observed for Composite Specimens.

5.5.4 Measurement of Dielectric Loss

The dielectric loss tan δ measured for the ceramic composites are shown in Table 13. It was observed that the dielectric loss for all the specimens are relatively consistent and most of the observations falling within 5% standard deviation.

Overall, the tan δ varied from 0.18 to 0.27. Typically, the dielectric loss tan $\delta < 0.05$ is important for high sensitivity in practical applications [247]. The values of dielectric loss measured during poling of functional composites are similar for the entire range of poling temperatures and applied electric field. The loss function was also independent of volume fraction of ceramic powder in the composite material indicating lower permittivity of the polymer and offers high resistance to electric field across the specimen.

Table 13: Dielectric Loss tan δ Observed for Piezoelectric Composite

Composition		Electric Voltage	Poling Temperature					Average Dielectric Loss
			50 °C	60 °C	70 °C	80 °C	90 °C	
19 vol% (54 wt%)	Specimen 1	5 kV	0.12	0.15	0.19	0.25	0.21	0.19 + 0.05
		10 kV	0.29	0.23	0.28	0.20	0.21	0.24 ± 0.04
		15 kV	0.19	0.22	0.27	0.24	0.23	0.19 ± 0.03
	Specimen 2	5 kV	0.14	0.16	0.19	0.26	0.22	0.19 ± 0.05
		10 kV	0.23	0.22	0.19	0.20	0.19	0.21 ± 0.02
		15 kV	0.19	0.21	0.21	0.21	0.20	0.20 ± 0.01
17 vol% (50 wt%)	Specimen 1	5 kV	0.18	0.21	0.22	0.26	0.23	0.22 ± 0.03
		10 kV	0.22	0.22	0.17	0.22	0.20	0.21 ± 0.02
		15 kV	0.19	0.18	0.24	0.21	0.21	0.21 ± 0.02
	Specimen 2	5 kV	0.18	0.20	0.19	0.22	0.23	0.21 ± 0.02
		10 kV	0.22	0.22	0.19	0.21	0.20	0.21 ± 0.01
		15 kV	0.23	0.24	0.22	0.24	0.20	0.22 ± 0.01
14 vol % (46 wt%)	Specimen 1	5 kV	0.14	0.21	0.26	0.21	0.24	0.21 ± 0.05
		10 kV	0.23	0.19	0.17	0.20	0.20	0.20 ± 0.02
		15 kV	0.22	0.27	0.24	0.25	0.20	0.24 ± 0.03
	Specimen 2	5 kV	0.13	0.13	0.26	0.23	0.24	0.20 ± 0.06
		10 kV	0.23	0.20	0.19	0.23	0.20	0.21 ± 0.02
		15 kV	0.26	0.27	0.20	0.25	0.22	0.24 ± 0.03

5.5.5 Capacitance Characteristics

The high dielectric constant of $BaTiO_3$ makes them suitable material for capacitor-based applications where it is generally bonded to another material [12]. As $BaTiO_3$ is always surrounded by material that it is bonded too, the resultant electronic properties are therefore a complex combination of capacitance and loss occurring at the dielectric material, bonding material, interference, electrodes and connecting leads.

The piezoelectric composites evaluated in these experiments consist of randomly oriented ceramic domains, which cancel each other when unpoled. Poling polymer-ceramic composites reorients these domains in a direction parallel to that of the applied electric field. In this way +ve and –ve polarisations of each domain are aligned creating the piezoelectric effect. The polarisation can be envisaged as charges separated by a distance, filled with a medium between them, hence forming a capacitor.

Electrical poling of ceramics therefore influences the capacitive charge stored in the ceramic polymer. This charge increases with increasing polarisation. Figure 92 - 94 presents the capacitance measured for specimens after poling. These show similar trends to the graphs illustrating the piezoelectric behaviour. The trends in both the piezoelectric coefficient and capacitance showed variability, however the underlying general trend was as expected. The trends did show some unexpected increases at a poling temperature of around 70 °C for all the specimens. The reason for this unusual behaviour is unclear and requires further investigation.

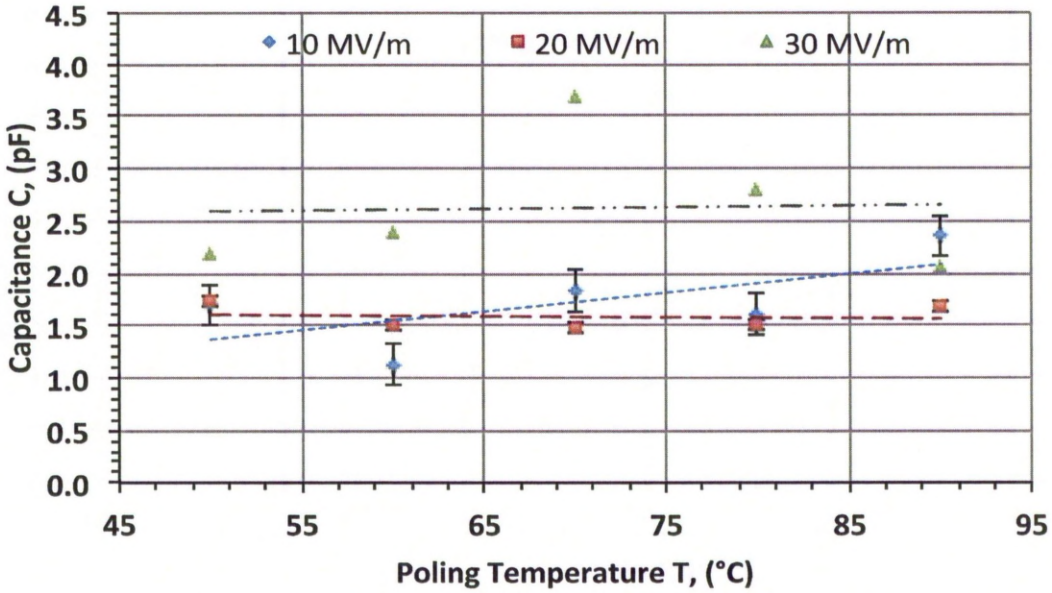

Figure 92: Capacitance Observed for 14 vol% Specimen.

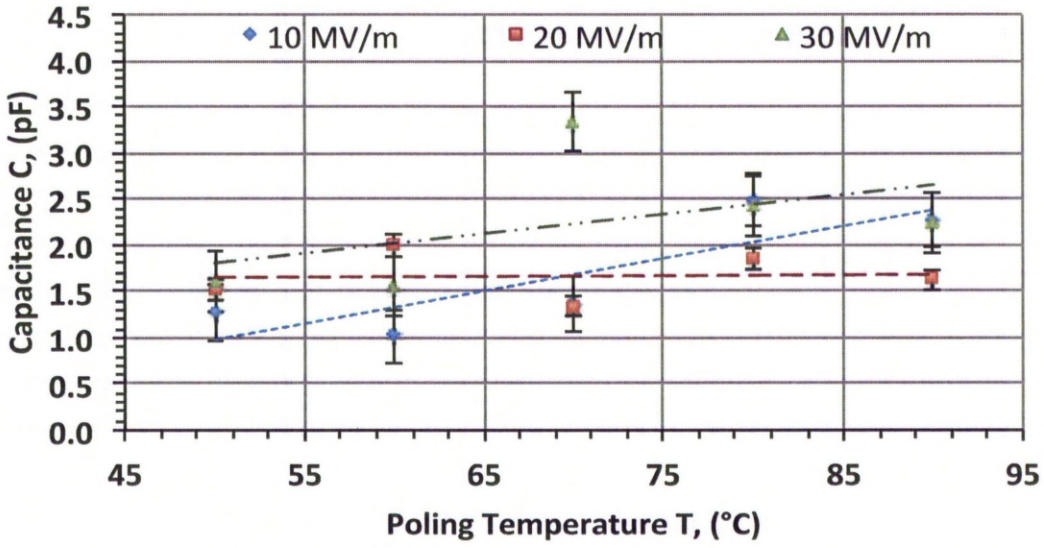

Figure 93: Capacitance Observed for 17 vol% Specimen.

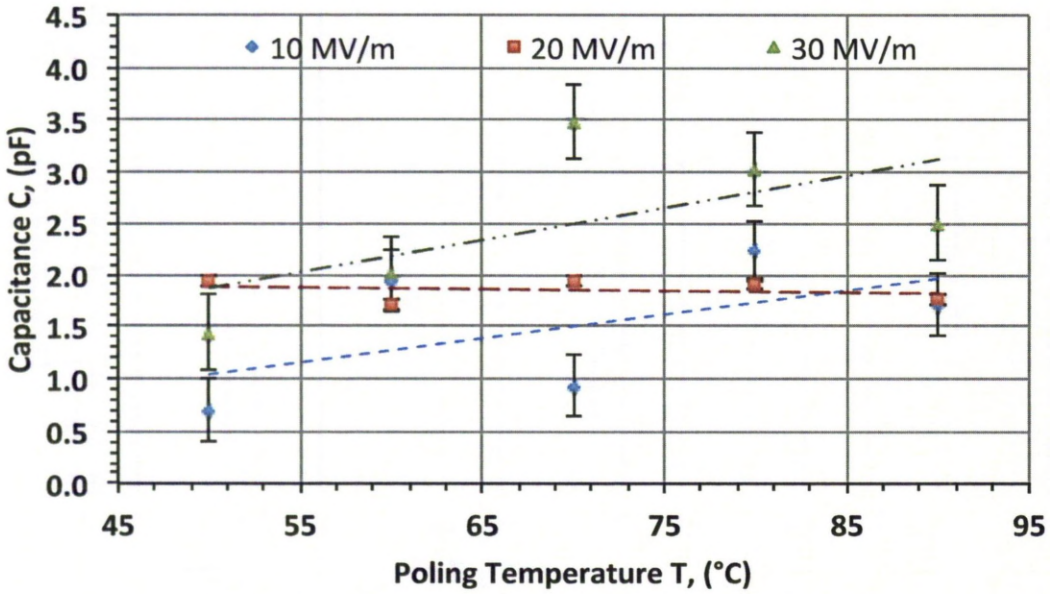

Figure 94: Capacitance Observed for 19 vol% Specimen.

Frequency Dependence of High-Density Functional Materials

The piezoelectric materials used for manufacturing electronic devices operated at high frequency, particularly for making embedded capacitors. The capacitance of functional material containing $BaTiO_3$ was analysed by using a Solartron 1255B Frequency Response Analyzer (AMETEK, Inc., United Kingdom) and a Solartron 1296 dielectric interface (AMETEK, Inc., United Kingdom) for a frequency range from 1 Hz to 1MHz by Dr. Xinming Wan at the Chemistry department of the University of Liverpool. These observations were recorded at various temperatures. The test specimens used for the measurement in this study was similar to the specimens used for measuring piezoelectric properties. They were connected to thin copper wires using conductive silver paint. The specimens were then connected to an electronic circuit and placed in a furnace. The experimental setup was connected to a computer – controlled process and measurements were recorded for the capacitance during the experiment.

The capacitance is influenced by the dielectric constant of a material, surface area holding electrical charge and the distance between the two surfaces. Since the dimension of the test specimen does not change during the experiment, the capacitance will be influenced by the dielectric constant alone. Therefore, change

in dielectric constant due to temperature and frequency across the material will characterise the changes in the capacitance.

The observations measured for the test specimens, in Figure 95 - 97 shows the decreasing capacitance of the functional material with an increase in frequency from 1 Hz to 1 MHz at any constant temperature. Increasing the temperature across all the specimens for any given frequency also validates the theoretical behaviour of increasing dielectric constant measured in terms of capacitance. For all the specimens, the capacitance reduces linearly above 200 Hz. A few peaks in capacitance were, however, observed at frequencies less than 200 Hz. These localised oscillating peaks were prominent at high temperature for all the specimens and increases in magnitude with increased loading of $BaTiO_3$. This unusual localised increase in capacitance or dielectric constant was also observed in the work performed by Kim [248] for $BaTiO_3$ nano composites, although the oscillating peaks were absent. This unusual behaviour may be due to presence of conductive silver particles at the surface of the specimen, charge leakage or due complex dielectric relaxation occurring at low frequency polarisation at resonant frequency. Although the exact reason for dispersion could not be completely verified, further investigation will be needed for understanding the cause.

Application of high frequency across the specimens induces alternating forces in the electric dipoles inducing movement of ions at the atomic level, causing acceleration and deceleration of the atomic masses resulting in oscillation of the material. Since all polarisation mechanisms involve the movement of charges for dipole response, inertia will prevent arbitrarily fast movements. Therefore, at higher frequency, a response from a mechanical system will be difficult as the inertial of the molecules retards their response to the oscillating electric field. This is apparent in the characteristics plotted in Figure 95 - 97. Also, at constant temperature, the relative dielectric constant decreases at higher frequency. The mechanical response of the dielectric material will therefore depend on the frequency of the applied electrical field.

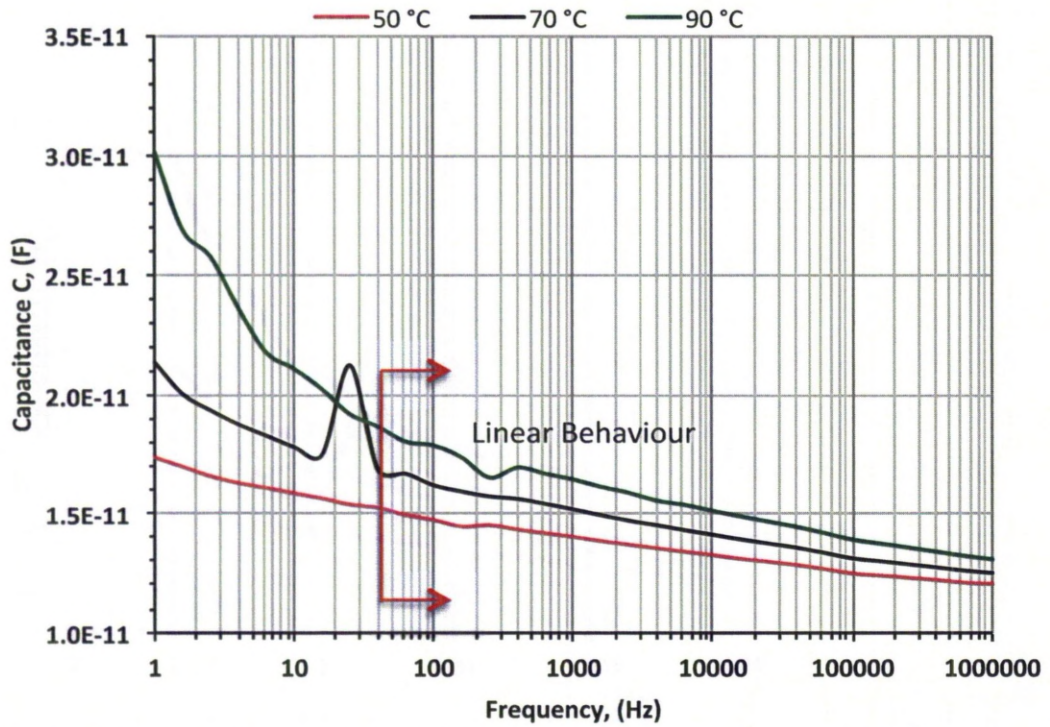

Figure 95: Reducing Capacitance of 14 vol% Specimen Measured at Increasing Frequency.

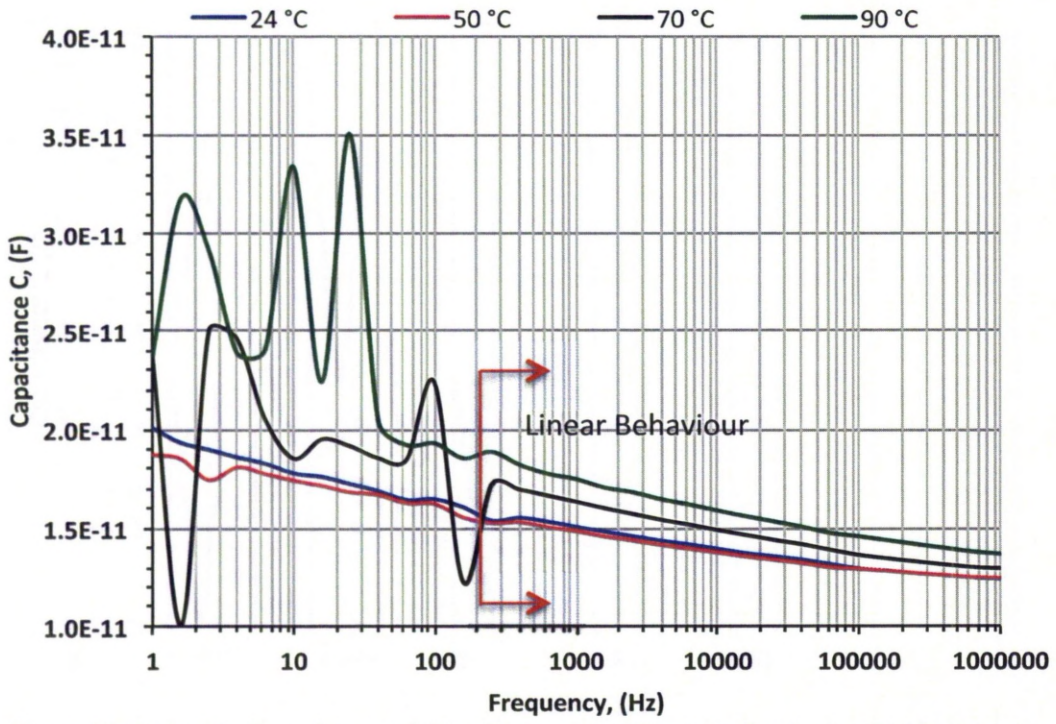

Figure 96: Reducing Capacitance of 17 vol% Specimen Measured at Increasing Frequency.

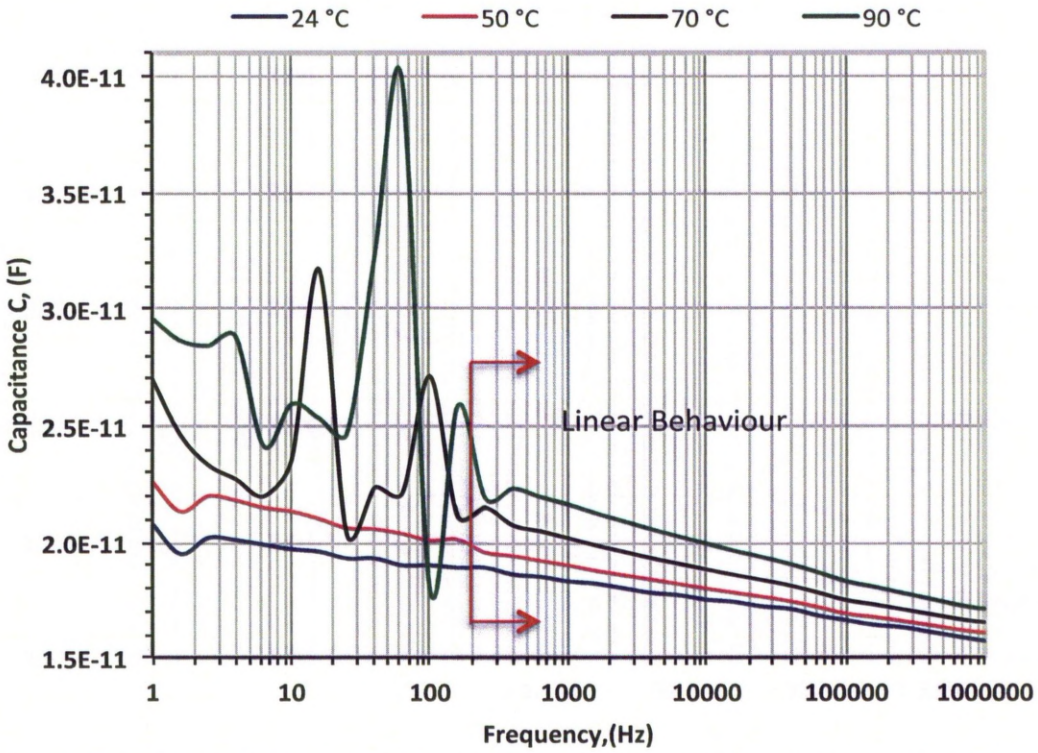

Figure 97: Reducing Capacitance of 19 vol% Specimen Measured at Increasing Frequency.

5.5.6 Ferroelectric Response

AC electric field strength was applied to the material developed here to measure and characterise the ferroelectric behaviour. The ferroelectric hysteresis curves were measured for the functional materials developed by DLP using Radiant Precision high voltage interface (Radiant technologies, United States of America) and TRek 609B high voltage amplifier (Trek, Inc., Japan) by Dr. Xinming Wan at the Chemistry department of the University of Liverpool, are shown in Figure 98 – 100, at various electric fields in the range of 50 kV/cm to 249.97 kV/cm. Due to limitations of the apparatus, the hysteresis behaviour of the piezoelectric composites could not be measured beyond field strength of 249.97 kV/cm. The functional material was shown to however successfully withstand the applied electric field without breakdown across the specimen. For clarity, the ferroelectric response was measured at both lower and higher electric field as shown in Figure 98 – 100.

Increasing the electric field applied across the test specimens induces the ferroelectric effect in the material by aligning the domains, eventually reaching saturated polarisation. The degree of polarisation increases with increasing ferroelectric ceramic content in the test specimen. At saturation, polarisation becomes stagnant and remains unchanged even at a higher electric field. A reverse electric field will be required to reorient all the ferroelectric domains in the opposite direction.

Hysteresis curves measured for test specimens (Figure 98 – 100) show that the remnant polarisation observed for 19 vol% composite is larger and increases noticeably in comparison to the 17 vol% and 14 vol% specimens. Table 14 shows the remnant polarisation and saturation polarisation measured for test specimens. P-E characterisation curve observed for all test specimens show that the increasing electric field rotates the curve in an anti clockwise direction about the origin. The rotation of the curve is an indication of field dependent nature of permittivity. The hysteresis curves for the test specimens show symmetric response with the endpoint below the initial point. The remanent polarisation for both positive and negative sweeps is the same i.e. 0.0417 $\mu C/cm^2$ and (-) 0.0407 $\mu C/cm^2$. The difference in end points of the curve or the barrier height observed in ferroelectric curves could be due to Schottky barrier effects [78-89].

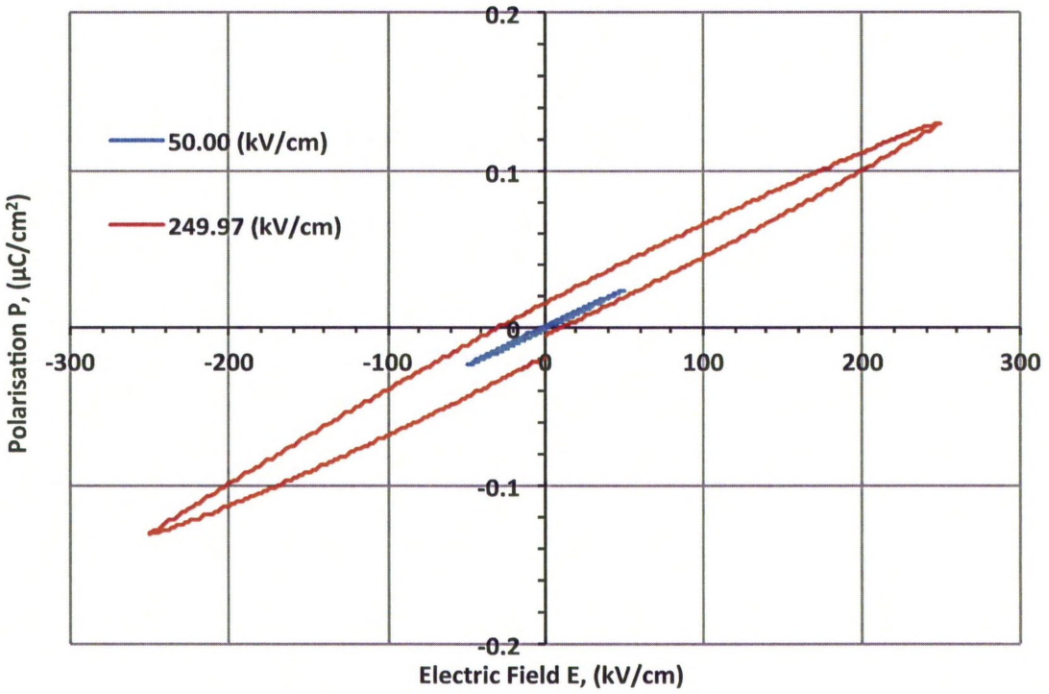

Figure 98: Ferroelectric Analysis for 14 vol% Specimens.

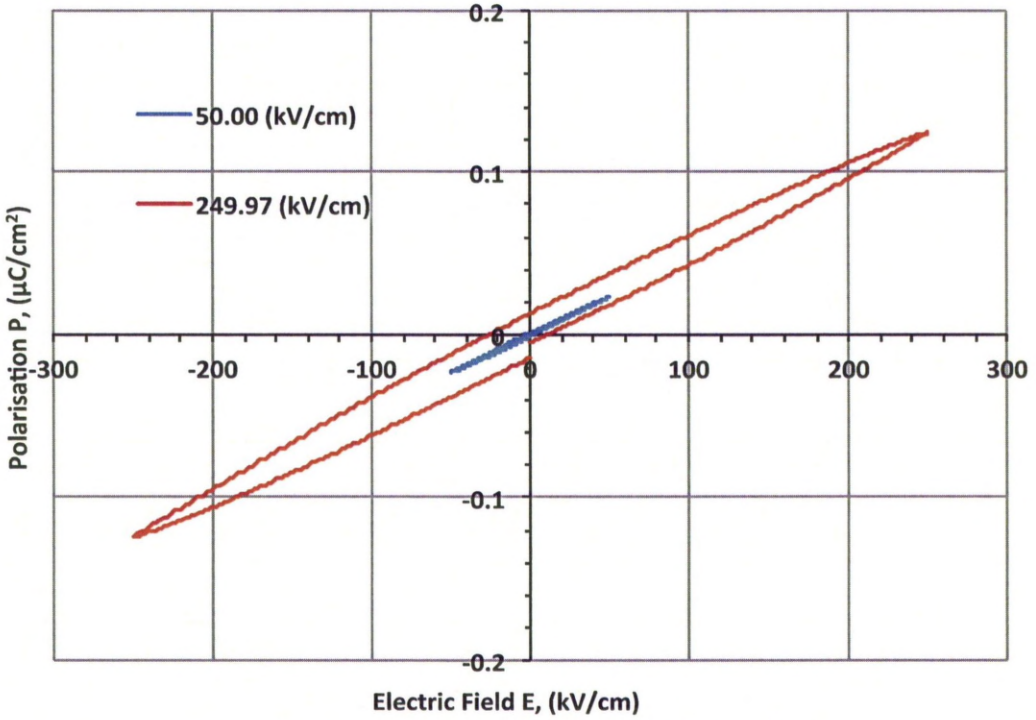

Figure 99: Ferroelectric Analysis for 17 vol% Specimens.

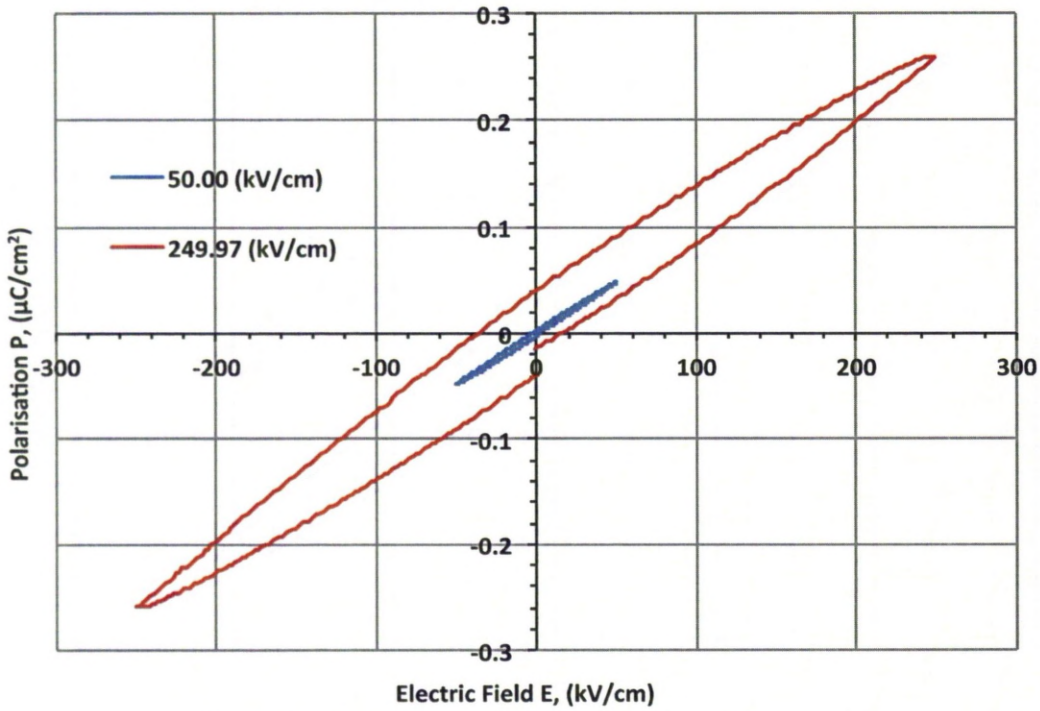

Figure 100: Ferroelectric Analysis for 19 vol% Specimens.

Table 14: Polarisation Measured for Composite Specimens.

Test Specimen	Remnant polarisation, ($\mu C/cm^2$)		Saturation Polarisation, ($\mu C/cm^2$)	
	At 50 kV/cm	At 249.95 kV/cm	At 50 kV/cm	At 249.95 kV/cm
19 vol%	±0.0025	±0.041	±0.0470	±0.359
17 vol%	±0.0010	±0.015	±0.0234	±0.124
14 vol%	±0.0010	±0.015	±0.0240	±0.120

Specimens prepared by Robertson [86] were manufactured by mixing acrylic polymer and barium titanate. Although the specimens for the ferroelectric study were not sintered, the larger particle sizes of 2 μm were considered. The remnant and saturation polarisation observed by Robertson for 35 vol% was 0.04 $\mu C/cm^2$ and 0.12 $\mu C/cm^2$, respectively. Similarly, 15 vol% specimens showed 0.018 $\mu C/cm^2$ and 0.078 $\mu C/cm^2$ of remnant and saturation polarisation. These observations were measured at an electric field of 70 kV/cm. Comparing P-E characterisation with specimens developed by DLP shown in Figure 98 – 100 confirms a significantly smaller remnant and saturation polarisation. The consideration of bigger particles may benefit in the formation of larger grain size, hence higher polarisation.

Conventionally, ferroelectric materials are fabricated at high temperatures and the electrodes are formed at lower temperatures. As a result electrode-ferroelectric interface capacitors are asymmetric which is reflected in the ferroelectric behaviour. Although no electrode was directly deposited on to the composite surfaces, the existence of the barrier at the interface could be due to inadequate contacting of the metal electrode with the composite surface. It is however difficult to know the actual reason for the asymmetry of the curves and this needs further investigation by performing the experiments that measures the cause of the barrier [78-79].

Although an ideal hysteresis ferroelectric behaviour was not obtained for the ceramic – polymer composite material due to limited electric field, an early sign of saturation was observed for the 19 vol% specimens, as show in Figure 101. At an electric field of 249.97 kV/cm, a small part of the curve (indicated by the ellipse) become parallel to the electric field axis indicates saturation. Measuring P-E curve at electric field beyond 249.97 kV/cm may lead to ideal ferroelectric hysteresis curve with larger magnitude of remnant and saturation polarisation.

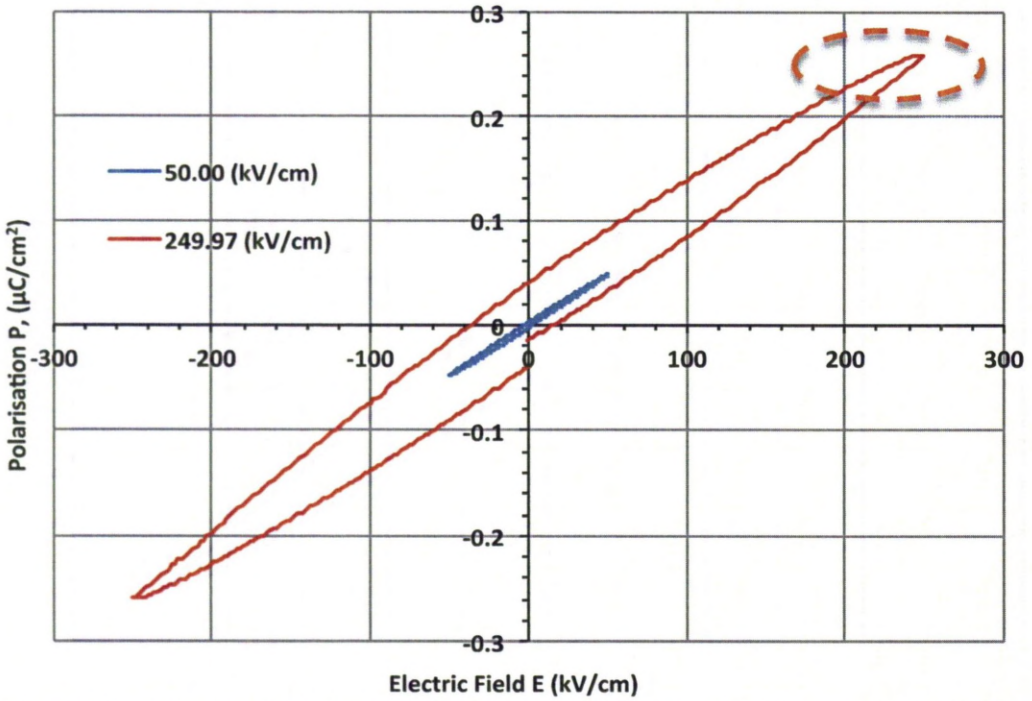

Figure 101: Ferroelectric Hysteresis Curves for 19 vol% Composite Measured at 50 kV/cm & 249.97 kV/cm

5.5.7 Discussion

The preliminary development of functional composites by DLP containing up to 6 vol% showed a piezoelectric coefficient of 0.5 pC/N. Although the functional activation was considerably smaller than the piezoelectric coefficient of $BaTiO_3$ ceramic powder, it formed the base for further optimisation. Further developments of high-density specimens were manufactured by identifying new build parameters, as discussed in Section 5.2.

The maximum particle loading of 19 vol% was manufactured by DLP. The theoretical prediction for 19 vol%, shown in Figure 89 would suggest a piezoelectric coefficient of 78.2 pC/N. However, the d_{33} observed for 19 vol% specimen is significantly lower at 5.7 pC/N. The smaller magnitude and variation in the piezoelectric coefficient observed in the material was attributed to higher resistivity of the surrounding polymer. A noticeable difference in the compliance of polymer and ceramic shows the polymer matrix in the composite undergoes higher stress compared to the ceramic particles. In order to reduce the discrepancy between the

theoretical model and actual observation, it is envisaged that by reducing the difference between the mechanical stiffness of the materials will transfer the applied force from the matrix to the filler material. A possible candidate material would be an epoxy resin, which has considerably higher hardness and stiffness in comparison to the acrylic polymer used here. Unfortunately, the DLP system used in this work is unable to process epoxy materials.

The dielectric loss recorded for all the specimens show relatively consistent tan δ the range of 0.18 – 0.27 varying with in 5% standard deviation. This indicates low permittivity of the polymer material resulting in high dielectric loss. As the Tan $\delta < 0.05$ is acceptable for high sensitivity of functional materials, composite developed by DLP in the current work may fail to be utilised for applications requiring high performance. Similarly, the capacitance measured for high – density specimens was not influenced by ceramic content in the specimens. This has validated the low permittivity and high resistance offered by the polymer.

Frequency dependent behaviour of capacitance measured in the range of 1 Hz – 1 MHz for these specimens were analysed at various temperature. It has shown reduced capacitance at high frequency, particularly beyond 200 Hz where linear behaviour was observed. The capacitance measured at frequency below 200 Hz showed oscillating capacitance. This typical behaviour observed in the specimens was prominent for 19 vol% particle content composites when compared to 17 vol% and 14 vol% specimens, and increases at high temperature.

Ferroelectric behaviour observed for theses specimens in the range of 50 kV/cm - 249.97 kV/cm electric field. The remnant polarisation and saturation polarisation was increasing with high particle content in composite specimens and applied electric field. The observed remnant and saturation polarisation were considerably smaller than the data presented in the literature. It is therefore understood that the currently used standard R5 polymer may not be suitable for development of high performance functional material.

5.6 Conclusion

This chapter focuses on the mechanical and electrical behaviour of the composite parts and the influence of the build orientation on their mechanical strength. It was understood from the literature that the thinner layer thickness would be necessary to achieve higher mechanical strength in the polymer parts. Thinner layer thickness will also be useful for the manufacturing and handling of polymer parts with micro features.

In order to understand mechanical properties of the polymer specimens, tensile test specimens were manufactured by the DLP system using a 25 μm layer thickness. The dimensional details of the test specimen were based on guidelines from standard test specifications normally used in industry and were further optimised for the manufacturing process.

The results obtained from the tensile testing of the optimised specimens manufactured in the XY direction (horizontal) and Z direction (vertical) showed mechanical properties close to the standard values for pure polymer. The tensile strength of these specimens was inside the range of 31 - 39 MPa. Both, the tensile strength and modulus of elasticity influenced by the build layer orientation. In terms of elongation, both the polymer specimen was similar to the literature; although the difference in the XY and Z direction built specimens showed directional influence.

Similar test specimens incorporating ceramic particles in the polymer material were manufactured on the DLP system. The addition of ceramic in the polymer could have to shown an increase in the tensile strength and subsequently the modulus of elasticity. It was discovered however; that manufacturing with the material developed here does not significantly improve the mechanical properties of the parts, which was typically observed for the particulate composites. The tensile strength of the composite specimens was reduced by up to 75% in the XY build direction and 55% in the Z build direction. Due to the limited build envelope, the gauge length of the optimised tensile test specimen was reduced to 0.51 mm and

further optimisation for long gauge length of tensile test specimen and increasing the applied load while testing will increase the accuracy in mechanical properties.

The results obtained from the tensile testing were compared with a mathematical model used for predicting the mechanical properties of the composite material. The forecasted properties of the composites were not validated by the experimental observations. This was primarily due to the inability of these models to account for damages occurring during the AM processes.

The maximum powder loading in the composite that was achieved by DLP was limited to 19 vol%. Further addition of the ceramic powder to the polymer reduced the flowability and consequently prevented manufacture. The higher loading of the ceramic powder in the polymer leads to delamination in the parts caused by poor interlayer bonding.

Addition of ceramic powder to polymer also influences the minimum feature size that can be manufactured by the DLP system. The specimen manufactured from the composite materials was difficult to clean effectively. The minimum feature that can be obtained by DLP was therefore largely dependent on the flowabilty of the material.

Composites manufactured by the DLP based AM technique, were investigated for various functional properties at three ceramic fractions specimens. The piezoelectric modulus d_{33} was measured for each of these. The experimental magnitude of d_{33}, was considerably smaller than that theoretically expected. Specimens containing 19 vol% ceramic were developed by DLP showed maximum d_{33} of 5.5 pC/N, when measured at 30 MV/m electric field and 90 °C poling temperature. This is thought to be partly due to the mechanical properties of the polymeric matrix material. Introducing matrix material (eg. epoxy) having mechanically properties closer to the filler material would have improved the experimental performance. This is not possible unless the range of materials that can be processed by the DLP system expands.

Investigations were also carried out to measure the capacitance of the composites, which shows a trend in agreement with the expected behaviour. The composites were also found to demonstrate a ferroelectric response up to electric fields of 250 kV/cm. The tan δ exhibited by these composite makes them unsuitable for many practical systems, but the properties were measurable and therefore the system may be deployed in the future. Based on the discussion presented in this work, it was understood that the currently used standard R5 polymer is not a suitable candidate for development of high performance functional material. Manufacturing of functionally active particulate composites by AM however shows promise, but further investigation is necessary for achieving improved dielectric properties.

CHAPTER 6.

6.0 Conclusion

This chapter concludes the current investigation and proposes future work. The aim of this research was to manufacture SMART micro reactor by developing functionally active materials via AM technologies. Exploring the ability of SLA techniques to manufacture accurate parts from the functional composite was a novel approach. In order to fulfil this aim, the following objectives were set:

1. To identify the feasibility of envisionTEC AM technique for the development of micro fluidic devices
2. To design micro reactors and employ them to physical systems
3. To identify areas that require improvement for the performance of micro reactors
4. To develop functionally active materials by DLP based SLA
5. To identify electrical and mechanical properties of the functional components built on the system
6. To characterise the performance of polymer based devices
7. Develop methods to integrate functional materials into sensing or actuating within micro reactors

Preliminary work on micro channels fabrication using a 60 mm focal length lens shows serrated edges, partial blocking and dimensional inaccuracy, this was resolved by using a lens of 85 mm focal length, projecting a build envelope of 20 mm x 27 mm at 20 μm resolution. This has enabled the fabrication of parts with significantly improved features. This was particularly beneficial for manufacture of micro channels and smaller parts.

A mixer micro reactor manufactured by the DLP system was successfully utilised for cell culture applications. It demonstrates the conceivability of the DLP system for the manufacture of micro fluidic devices. Although, high resolution and accuracy was achieved, the surface roughness and poor surface finish caused by the stair

stepping could influence the fluid flow behaviour in the micro channels. Manufacturing parts with thinner layers would reduce the surface roughness caused by stair stepping. The minimum layer thickness that the PF slicer could deposit is limited to 25 μm. A software algorithm (ASA) originally designed for rotational printing was then adopted for adaptive slicing of the parts manufactured by the DLP system, where layers less than 25 μm could be successfully deposited.

An investigation to analyse the surface roughness of components manufactured for different layer thickness shows that the thin layer manufacturing could reduce the surface roughness caused by stair stepping. The layer thickness of 20 μm was found to be crucial, since manufacturing in layers smaller than 20 μm does not contribute to improving the surface roughness, but causes an increased surface roughness due to surface strain. The exposure time used for depositing thin layers was however extrapolated from the default parameters. This exposure used to manufacture thin layers may not be suitable as it was interpolated and hence also requires further investigation.

Micro fluidic devices manufactured by the DLP system can be useful for high pressure systems. Therefore, a set of experiments were undertaken to identifying the influence of layer orientation on the mechanical behaviour of the polymer component manufactured by the DLP system. A comparison of the mechanical properties of the polymer specimens manufactured in the XY (horizontal) and Z (vertical) direction reveals that the specimens manufactured in the XY direction have higher tensile strength and modulus of elasticity compared to specimens manufactured in the Z direction. The average tensile strength of all the specimens was in the range mentioned in the literature. The modulus of elasticity however, falls below the theoretical range for polymer material. Therefore, manufacture of micro channels for pressure systems requires consideration of build orientation.

Composites fabricated by conventional routes achieved density up to 49 vol% of ceramic particle at atmospheric pressure and temperature. Composites with 49 vol% and 45 vol% were brittle in nature and were difficult to retrieve. Composites with 35 vol% were flexible, showing optimal loading that may be

obtainable from the DLP system for successful manufacture of functional components.

Addition of ceramic to the photopolymer had influenced the flowability of the polymer, restricting the manufacturability of the high-density components. A preliminary investigation of the manufacture of composites with 5 vol% ceramic powder show a reduced interlayer bonding and an increase in the exposure time required for further development of the high – density specimens, as shown in Figure 61. This has resulted in the manufacture of up to 19 vol% composites by the DLP system. The flowability and poor inter – layer bonding was observed for composites beyond 19 vol%, limiting further manufacture of the high – density composites. The composite density of 19 vol% however, was too low in comparison to the 49 vol% composites fabricated using the conventional route. The defects observed in the composites, manufactured by the conventional route were absent in the specimens manufactured by the DLP system.

The ceramic powder added to the polymer further influences the tensile strength of the specimens, showing the typical behaviour of the particulate composites. Comparing the mechanical properties of the polymer specimens, a fall in the tensile strength and modulus of elasticity was observed for the composite materials. This was similar to the behaviour observed for composites manufactured by the conventional methods.

For functional activation of the ceramic composites, an in-house poling apparatus was designed and fabricated. The poling apparatus was suitable for the voltage up to 30 kV and temperature up to 250 °C. The poling of 35 vol% specimens fabricated by conventional route at an electric field of 5 kV (6 MV/m) and 70 °C poling temperature shows a piezoelectric coefficient d_{33} of 4 pC/N. High-density specimens could not be poled as they were brittle. The composite specimens manufactured by the DLP system were subject to a DC voltage up to 15 KV across their thickness (30 MV/m). The piezoelectric coefficient measured for 19 vol% composite developed by DLP was 5.5 pC/N was too small for MEMS applications, which was measured at 15 kV (30 MV/m) at 90 °C. The dielectric loss recorded for

all the specimens was much higher due to low permittivity of the polymer, reducing their usability as functional devices. Similarly, the ferroelectric properties demonstrated by $BaTiO_3$ composites were not significant for MEMS applications. The DLP system shows promise for the development of the functional composites, but further investigation will be required to increase loading of the ceramic particles, thereby increasing functional response. Limitation of materials that can be manufactured by the DLP system highlights the necessity to expand the material range that can be processed. Also, as all the particles are randomly oriented in the liquid polymer, poling the specimen did not align all the dielectric domains uni-directionally, hence reducing the piezoelectric effect.

The particle distribution in the composites varies with the loading of composites. For all the specimens, the particles start accumulating at the bottom of the build envelope. The ceramic particles could not be successfully suspended in the polymer for manufacturing of ceramic – polymer composites. The suspension of ceramic particles was challenging for the DLP system, as addition of a third material could further influence the minimum feature size that can be fabricated on DLP.

Development of sensing and transducing devices using the polymer and integrating them with micro reactors will be a step forward. Although properties of the polymer materials have improved significantly over the years, there are still great challenges related to usability and functional stability of the material produced. Preliminary investigation for the development of the polymer based cantilever beam for MEMS application is presented in appendix A.

Due to limitations discussed earlier, manufacturing of micro reactors requires development of materials with improved functional response. Addition of impurities into the material utilised for enhancing the dielectric response is well documented in the literature. In the absence of multi – material processing, materials will require separate manufacture and then combined together before using. Substantial modifications will be required to the current AM techniques to achieve multi-material processing along with suitable software for efficient control of the process.

The results presented in this thesis are encouraging. Current work can be considered as a building block for processing the functional materials and identifying areas for further investigation for the manufacture of high permittivity functional materials by DLP.

6.1 Future Work

The current AM technique based on a DLP chip is novel. This work has assessed various aspects of the photopolymer components manufactured by the DLP system, such as the mechanical properties, surface roughness and micro manufacturing of the components.

Fabrication of the polymer micro reactor was successfully employed for cell culture, has a potential for other applications also. The mechanical properties of the polymer materials observed in this research will be useful in the development of micro fluidic devices for high pressure applications.

Addition of $BaTiO_3$ to the photopolymer shows a potential for developing an active particulate composites by direct manufacturing. However, limitations on the loading of particle and therefore dielectric properties of these composites must be overcome by identifying suitable methods to enhance functional response or by using an alternative material possessing a higher dielectric and mechanical properties, also discussed in the literature. In the current composite specimens, piezoelectric domain may be randomly oriented, even after poling. Ensuring all the domains are uni – directionally aligned during the manufacture, can therefore increase the piezoelectric coefficient. This can be achieved by applying electric field across the mix of ceramic – polymer in the vat enabling orientation of particles. Use of large particle sizes for the development of functional material by DLP may improve piezoelectric coefficient, as larger domains will be formed while poling. The piezoelectric coefficient can also be increased by either addition of metal particles, presented in literature. However, as maximum volume fraction was limited to 19 vol%, an addition of metal particles will result in a lower ceramic content, resulting in reduced piezoelectric coefficient. Using larger ceramic

particles with finer metal powder may provide a middle ground for formation of functional composites. An alternative approach presented in the literature considers a coating on ceramic particles with metal for increasing piezoelectric coefficient.

Development of functional polymer can be engaged for MEMS applications. Addition of ceramic powder to achieve higher piezoelectric response results in reduced tensile strength. Therefore, optimisation is required between the volume content of the ceramic particles and the mechanical behaviour of the particulate composites. Further research is also required for identify suitable manufacturing protocols for the development of functional devices. They can then be used to manufacture functional devices from materials showing high permittivity, high piezoelectric and ferroelectric response.

Based on the discussion presented above, future investigation proposed for the development of a functional material using the AM route can be categorised as a long term and short term approach. In the long term, identifying a new build parameters will improve the manufacturability of the part in thin layers. It can also be further extended for the development of composite materials. A similar improvement is required to establish fabrication of multi – material parts by the direct writing method. In order to develop functional material, specifically using DLP based AM technique, it should be able to perform multi – material manufacturing. This requires modification to the system, so that more than one material can be selectively cured in a layer. Currently, 3D printing could successfully deposit multi materials, but are limited to deposition of material in liquid state. The proposed modifications to the current system also require development of software for operational control. Expansion on the material range that can be processed by the DLP system will increase its potential usability.

For the current investigation, focus on the development of functional material requires methods to identify an increase in the functional response, discussed in the background review. This requires further analysis of mechanical and electric properties used for characterising functional devices. Also, applying electric or

magnetic field across the polymer ceramic mix will result in the formation of composites having uni-directionally aligned dielectric domains.

Below are a few proposals that may be used in future for integrating functional devices with micro fluidic devices. Figure 102 is a conceptual ideal showing an application of functional material for micro fluidic devices. The outer surface of the micro channels are either fixed with a functional material fabricated by the DLP system or manufactured as an integral part of the micro channels. They can be sequentially activated resulting in a compression action in different parts of the micro channels to demonstrate peristaltic pumping action. This has a potential use for pumping high viscous fluid through micro fluidic channels or pulsating dosing of fluid in to a stream of another fluid.

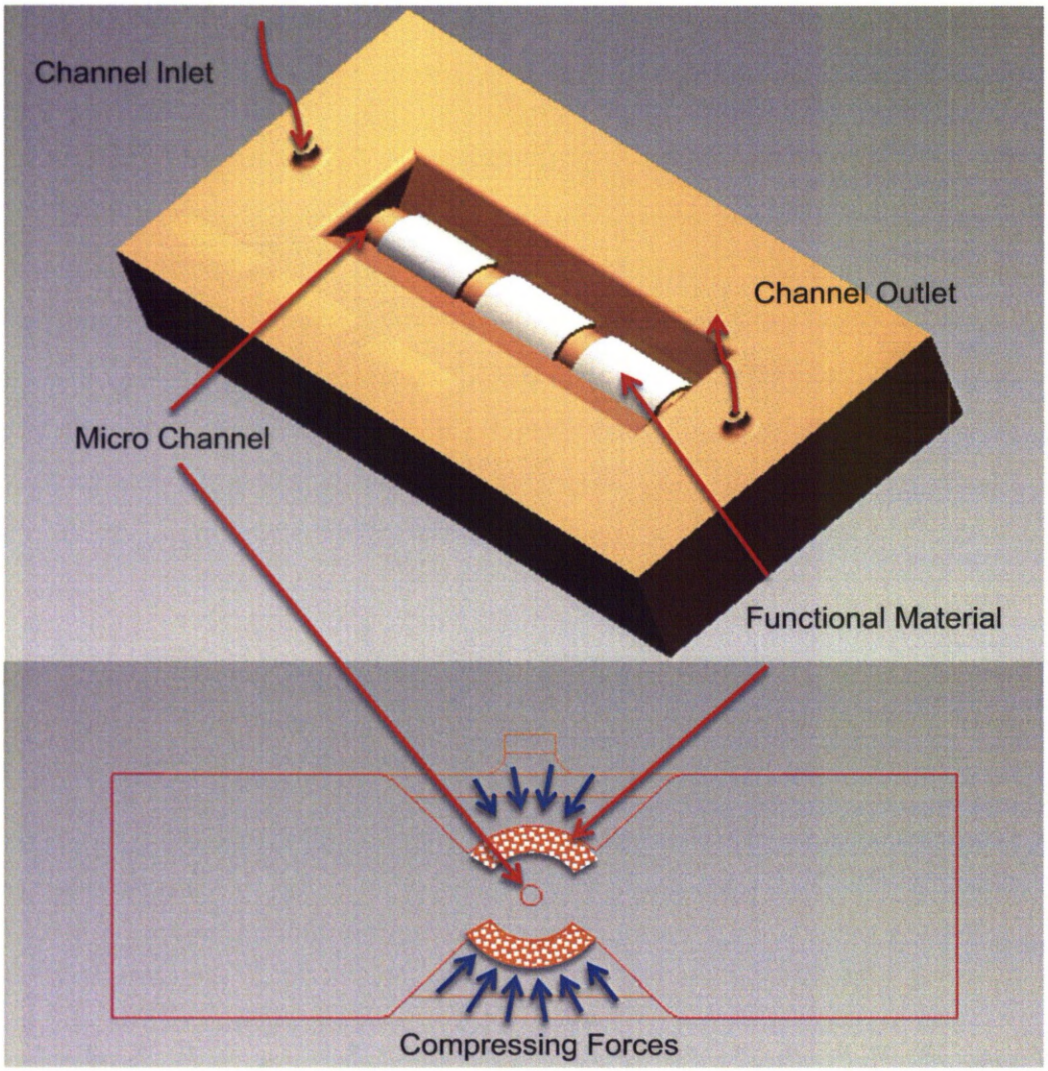

Figure 102: Functionally Active Micro Channel for Pumping.

Similar design for a sensing application (Figure 103) may contain an obround micro channel manufactured from functional material by the DLP system. The pressure exerted by the liquid passing through the micro channel tends to change the shape of an obround micro channel to circular, resulting in generation of potential in the piezoelectric material due to deformation. Measuring the voltage generated while deformation can be calibrated for change in pressure in the micro channel. Voltage generation at two different points in a micro channel can provide differential pressure (pressure drop) in the micro fluidic devices.

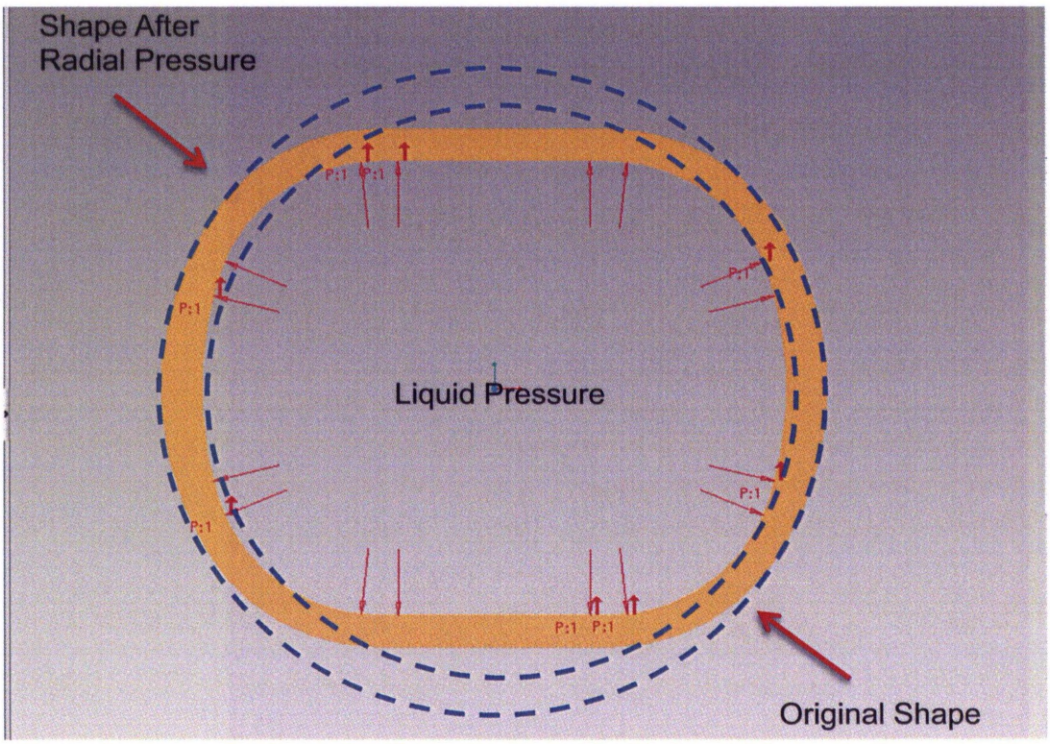

Figure 103: Deforming Channel for Pressure Sensing.

Functional devices manufactured from the functional materials developed by the DLP system can be combined with the micro channels, as shown in Figure 104. The outer part, which is shown yellow in colour represents micro fluidic channel containing a piezoelectric part that may be developed by DLP separately or manufactured with the micro channel, manufactured in a single build. The design of the piezoelectric material is such that it undergoes a high strain when subject to a force, resulting in the generation of a high electric signal from the functional materials. The design of the piezoelectric part will be suitable for pressure or volume flow measurement.

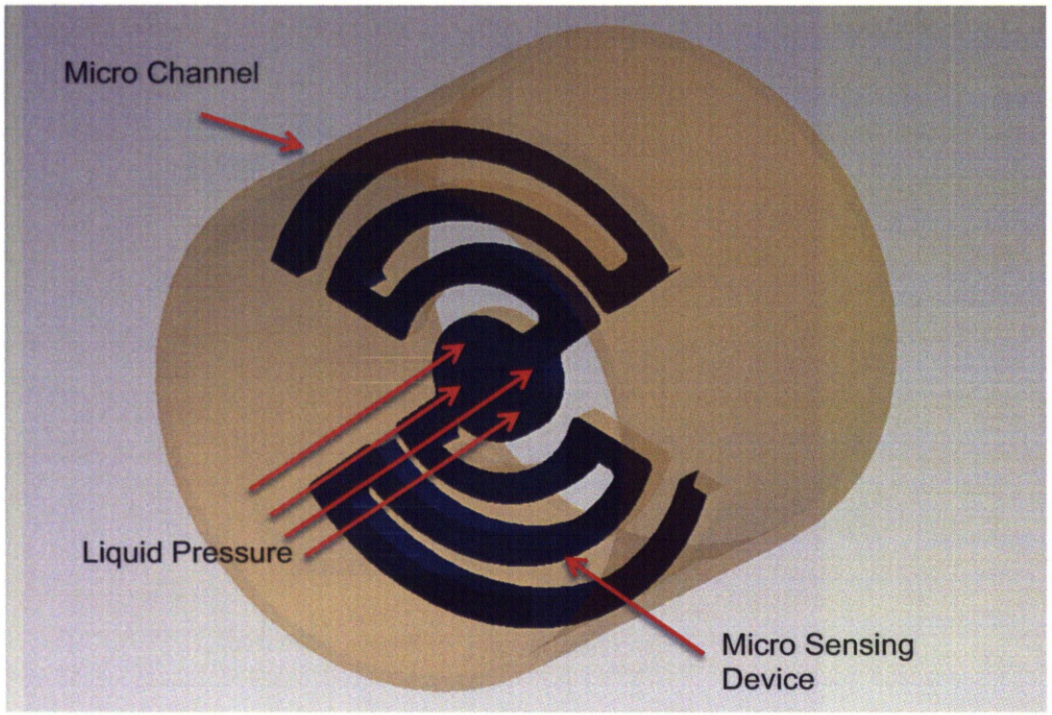

Figure 104: Integrated Sensing Device in Micro Channel for Pressure / Velocity Monitoring.

Manufacturing of polymer smart micro reactor may currently look ambitious, however, better understanding of various aspects discussed in this thesis, along with availability of a wide range of material can bridge the gaps for manufacture of functional devices using DLP system.

REFERENCES:

[1] Butera, F., (2005), "Composites and Smart Materials: a synergic approach for tomorrow's vehicles", [internet]. Available at: http://www.nanotec.it/nanoroadmap_conference/Presentazione_Butera.pdf [Accessed on 3 February 2012].

[2] Anon, Piezo electric gyroscope, Anon. Available at: http://gyroscope.com/d.asp?product= PIEZO [Accessed on 3 February 2012].

[3] Anon, (2011). "Smart Materials and Sensors",[internet]. Available at: "http://www.seminarpaper.com/2011/1 2/smart-materials-and-sensors.html" [accessed on 4 February 2012].

[4] Abgrall, P., Gué, A. M., (2007). "Lab-on-chip Technologies: Making a Microfluidic Network and Coupling it into a Complete Microsystem—a Review." Journal of Micromechanics and Microengineering 17(5): R15.

[5] Mullen, L. , Stamp, R. C., Brooks, W. K., Jones, E., Sutcliffe, C. J., (2008). "Selective Laser Melting: A Unit Cell Approach for the Manufacturing of Porous, Titanium, Bone In-growth Constructs, Suitable for Orthopaedic Applications". Journal of biomedical Materials research PartB: Applied Biomaterials: p 325 - 334.

[6] Chua Chee, K., (1994). "Three - Dimensional Rapid Prototyping Technologies and Key Development Areas." Computing & Control Engineering Journal 5(4): p 200-206.

[7] Salles, A., Gyi, D. E., (2009). " The Specification of Personalised Footwear for Rapid Manufacturing: a Pilot Study". MCPC2009.

[8] Hopkinson, N., Hauge, R.J.M. , Dickens, P.M., (2006). "Rapid Manufacturing: an Industrial Revolution for the Digital Age" 1st ed. England: Wiley & sons Ltd. p 211-219.

[9] Hopkinson, N., Hauge, R.J.M. , Dickens, P.M., (2006). "Rapid Manufacturing: an Industrial Revolution for the Digital Age" 1st ed. England: Wiley & sons Ltd. p 221-232.

[10] s.n., (2007)."RP4Baghdad.org,- Rapid Prototyping for Baghdad". The TCT Magazine Volume 15 / Issue 2, p 8.

[11] Anderson, J. C.,(1963). "Dielectrics". London: Chapman and Hall Ltd.

[12] Hebert, J.M.,(1985). "Ceramic Dielectrics and Capacitors", vol 6. , UK:Gordon and Breach Science Publishers.

[13] Cady, W. G., (1964). Piezoelectricity: "An introduction to the Theory and Application of Electromechanical Phenomena in Crystals- Vol. I", New York, Dover Publications, Inc.

[14] Ballato, A., (1996)." Piezoelectricity: History and New Thrusts". Ultrasonics Symposium.

[15] Bottcher, C. J. F., (1973)."Theory of Electric Polarisation Volume – I", 1st ed. Dielectrics in static field, Elsevier scientific publication company, Amsterdam, p 67.

[16] Taylor, G.W., Gagnepain, J. J., (1985). "Piezoelectricity"Gordon and Breach Science Publishers, New York. USA.

[17] Bottcher, C. J. F., (1973.). "Theory of Electric Polarisation Volume – I", 1st ed. Dielectrics in static field, Elsevier scientific publication company, Amsterdam, p 289.

[18] Leo, D. J., "Engineering Analysis of SMART Material Systems.", 1 ed. 2007: John Wiley & Sons.

[19] Dargaville, T., Celina, M., Elliot, J., Chaplya, P., Jones, G., Mowery, D., Assink, R., Clough, R. , Martin, J., (2005). "Characterization, Performance and Optimization of PVDF as a Piezoelectric Film for Advanced Space Mirror Concepts". Sandia Report SAND2005-6846. p 15. Sandia National Laboratories. [Accessed on 26th January, 2011].

[20] Dargaville, T., Celina. M., Elliot, J., Chaplya, P., Jones, G., Mowery, D., Assink, R., Clough, R. , Martin, J., (2005). "Characterization, Performance and Optimization of PVDF as a Piezoelectric Film for Advanced Space Mirror Concepts". Sandia Report SAND2005-6846. Sandia National Laboratories. [Accessed on 26th January, 2011].

[21] Hundal, J. S., Nath, R., (1999). "Piezoelectricity and Polarization Studies in Unstretched San Copolymer Films." Journal of Materials Science 34(21): p 5397-5401.

[22] Jaffe, B., (1971). "Piezoelectric Ceramics", London, Great Britain: Academic Press.

[23] Dragan, D., (1998). "Ferroelectric, Dielectric and Piezoelectric Properties of Ferroelectric Thin Films and Ceramics." Reports on Progress in Physics 61(9): p 1267.

[24] Hebert, J. M.,(1985). "Ceramic Dielectrics and Capacitors", vol 6, UK:Gordon and Breach Science Publishers.

[25] Bottcher, C. J. F., (1980). "Theory of Electric Polarization Volume – II", 2nd ed. Dielectrics in time-dependent fields, Elsevier scientific publication company, Amsterdam, p 423.

[26] Y. Xu, (1991). "Ferroelectric Materials and their Applications". Amsterdam: North Holland Publishing.

[27] Fattuzzo, E., Merz, W. J., (1967). "Ferroelectricity - Selected topics on in Solid State Physics". Amsterdam: North-Holland publishing company.

[28] Roberts, S., (1947). "Dielectric and Piezoelectric Properties of Barium Titanate." Physical Review 71(12): p 890 895.

[29] Hebert, J. M.,(1985). "Ceramic Dielectrics and Capacitors", vol6. , UK:Gordon and Breach Science Publishers, p 132.

[30] Lazarevic, Z. Z., Vijatovic, M., (2010). "The Characterization of the Barium Titanate Ceramic Powders Prepared by the Pechini Type Reaction Route and Mechanically Assisted Synthesis." Journal of the European Ceramic Society 30(2): p 623-628.

[31] Cheung, M. C., Chan, L. W., (1999). "Characterization of Barium Titanate Ceramic/Ceramic Nanocomposite films Prepared by a Sol - Gel Process." Nanostructured Materials 11(7): p 837-844.

[32] Frey, M. H., Payne, D. A., (1995). "Synthesis and Processing of Barium Titanate Ceramics from Alkoxide Solutions and Monolithic Gels." Chem. Mater., 1995, 7 (1), p 123–129.

[33] Lin, M. H., Lu, H. Y., (2001). "Hexagonal - Phase Retention in Pressureless - Sintered Barium Titanate." Philosophical Magazine a-Physics of Condensed Matter Structure Defects and Mechanical Properties 81(1): p 181-196.

[34] Merz, W. J., (1949). "The Electric and Optical Behavior of $BaTiO_3$ Single-Domain Crystals." Physical Review 76(8): p 1221.

[35] Kwei, G. H., Lawson, A. C., (1993). "Structures of the Ferroelectric Phases of Barium Titanate." The Journal of Physical Chemistry 97(10): p 2368-2377.

[36] Vivekanand, B., Sudhir, C., (2007). "Silicon Dioxide Films by RF Sputtering for Microelectronic and MEMS Applications." Journal of Micromechanics and Microengineering 17(5): p 1066.

[37] Lyahovitskayaa, V., Zona, I., Feldmana, Y., Cohenb, S., Lubomirskya, I., (2004). "Non-crystalline Pyroelectric $BaTiO_3$ Thin Films." Materials Science and Engineering B 109(1-3): p 167-169.

[38] Jaffe, B., (1971), "Piezoelectric Ceramics", Academic Press, London, Great Britain, p 59.

[39] Jaffe, H., Berlincourt, D., (1957). "Effect of Pressure on the Curie Temperature of Polycrystalline Ceramic Barium Titanate." Physical Review 105(1): p 57.

[40] Goswami, A. K. (1969). "Dielectric Properties of Unsintered Barium Titanate." Journal of Applied Physics 40(2): p 619-624.

[41] Zhaoyu, W., Jie, H., Min-Feng, Y., (2007). "Axial Polarization Switching in Ferroelectric $BaTiO_3$ Nanowire." Nanotechnology 18(23): 235203.

[42] Buscaglia,V., Buscaglia, M., Viviani, M., Mitoseriu, L., Nanni, P., Trefiletti, V., Piaggio, P., Gregora, I., Ostapchuk, T., Pokorny, J., (2006). "Grain Size and Grain Boundary - Related Effects on the Properties of Nanocrystalline Barium Titanate Ceramics." Journal of the European Ceramic Society 26(14): p 2889-2898.

[43] Deng, X., Wang, X.,(2007). "Investigation of Ferroelectric Properties on Nanocrystalline Barium Titanate Ceramics." Frontiers of Materials Science in China 1(3): p 319-321.

[44] Hamano, A., Atake, T.,(1988). "Successive Phase Transitions of $BaTiO_3$ Ceramics Synthesized by Powder - Calcination." International Journal of High Technology Ceramics 4(1): p 41-50.

[45] Takashi, Y., Urabe, K., Banno, H., (1993). "$BaTiO_3$ Particel-Size Dependence of Ferroelectricity in BaTiO3/Polymer Composites.", Jpn. J. Appl. Phys. 32: p 4272-4276.

[46] Yoon, D.H., Lee, B. I.,(2002). " $BaTiO_3$ properties and powder characteristics for ceramic capacitors", Journal of Ceramic Processing Research. 3(2), p 41-47.

[47] Kinoshita, K., Yamaji,A., (1976). "Grain-size Effects on Dielectric Properties in Barium Titanate Ceramics." Journal of Applied Physics 47(1): p 371-373.

[48] Lee, M. H., Halliyal, A., (1989). "Poling of Coprecipitated Lead Titanate-Epoxy 0–3 Piezoelectric Composites." Journal of the American Ceramic Society 72(6): p 986-990.

[49] Martirena, H. T., Burfoot, J. C., (1974). "Grain - Size Effects on Properties of Some Ferroelectric Ceramics." Journal of Physics C: Solid State Physics 7(17): p 3182 - 3192.

[50] Agoudjil, B., Ibos, L., (2008). "A comparative Analysis of Dielectric, Rheological and Thermophysical Behaviour of Ethylene Vinyl Acetate/$BaTiO_3$ Composites." Journal of Physics D-Applied Physics 41(5).

[51] Polla, D. L., Francis L. F. (1998). "Processing and Characterization of Piezoelectric Materials and Integration into Microelectromechanical Systems." Annual Review of Materials Science 28(1): p 563-597.

[52] Igreja, R., Wenger, M. P.,(1994). "Pyro- and Piezoelectricity in Sol - Gel Derived Ceramic / Polymer Composites". 8th International Symposium on Electrets.

[53] Cheung, M. C., Chan, H. L. W.,(1999). "Characterization of Barium Titanate Ceramic / Ceramic Nanocomposite Films Prepared by a Sol - Gel Process." Nanostructured Materials 11(7): p 837-844.

[54] Dias, C. J., Igreja, R., (2004). "Recent Advances in Ceramic - Polymer Composite Electrets." Dielectrics and Electrical Insulation, IEEE Transactions on 11(1): p 35-40.

[55] Muralidhar, C., Pillai. P. K. C.,(1987). "Hysteresis Behaviour of Barium Titanate ($BaTiO_3$) / Polyvinylidene Fluoride (PVDF) Composite." Journal of Materials Science Letters 6(3): p 349-350.

[56] Calame, J. P., (2006). "Finite Difference Simulations of Permittivity and Electric Field Statistics in Ceramic - Polymer Composites for Capacitor Applications." Journal of Applied Physics 99(8): 084101-084111.

[57] Pelaiz-Barranco, A., Marin-Franch, P., (2005). "Piezo-, Pyro-, Ferro-, and Dielectric Properties of Ceramic / Polymer Composites Obtained From Two Modifications of Lead Titanate." Journal of Applied Physics 97(3): 034104.

[58] Heywang, W., Lubitz, K.,(2008). "Piezoelectric Composites by Solid Freeform Fabrication: A Nature - Inspired Approach". Piezoelectricity, Springer Berlin Heidelberg. 114: p 377-399.

[59] Newnham, R. E., Skinner, D. P., (1978). "Connectivity and Piezoelectric - Pyroelectric Composites." Materials Research Bulletin 13(5): p 525-536.

[60] Newnham, R. E., Bowen, L. J.,(1980). "Composite Piezoelectric Transducers." Materials & Design 2(2): p 93-106.

[61] Ting, R. Y.,(1985). "Piezoelectric Properties of a Porous PZT Ceramic." Ferroelectrics 65(1): p 11-20.

[62] Dias, C. J., Das-Gupta, D. K.,(1994)." Electroactive Polymer - Ceramic Composites. Properties and Applications of Dielectric Materials", Proceedings of the 4th International Conference on properties and Applications of Dielectric Materials.

[63] Zewdie, H.,Brouers, F.,(1990). "Theory of Ferroelectric Polymer - Ceramic Composites." Journal of Applied Physics 68(2): p 713-718.

[64] Jayasundere, N., Smith, B. V.,(1993). "Dielectric constant for Binary Piezoelectric 0-3 Composites." Journal of Applied Physics 73(5): p 2462-2466.

[65] Sihvola, A.,(2000). "Mixing Rules with Complex Dielectric Coefficients." Subsurface Sensing Technologies and Applications 1(4): p 393-415.

[66] Windlass, H., Raj, P. M.,(2003). "Colloidal Processing of Polymer Ceramic nanocomposite Integral Capacitors." Electronics Packaging Manufacturing, IEEE Transactions on 26(2): p 100-105.

[67] Ramajo, L., Reboredo, M.,(2005). "Dielectric Response and Relaxation Phenomena in Composites of Epoxy Resin with $BaTiO_3$ Particles." Composites Part A: Applied Science and Manufacturing 36(9): p 1267-1274.

[68] Vrejoiu, I., Pedarnig, J. D.,(2002). "Flexible Ceramic – Polymer Composite Films with Temperature - Insensitive and Tunable Dielectric Permittivity." Applied Physics A: Materials Science & Processing 74(3): p 407-409.

[69] Park E. T., Kim, J. J., Lee, H. Y., Lim, S. L., Lee J. C., Chung, Y. K.,(2009). "High - Dielectric Constant Metal - Ceramic - Polymer Composite Material and Method for Producing Embedded Capacitor Using the Same". Patent no: US 7609504 B2, USA.

[70] Jung Min, P., Hee Young, L.,(2008). "Dielectric Properties of Ni - Coated $BaTiO_3$ - PMMA Composite." Ultrasonics, Ferroelectrics and Frequency Control, IEEE Transactions on 55(5): p 1038-1042.

[71] McNeal, M. P., Sei-Joo, J.,(1996). "Particle Size Dependent High Frequency Dielectric Properties of Barium Titanate", Proceedings of the Tenth IEEE International Symposium on applications of ferroelectrics.

[72] En-Bo, W., Guo-Qing, G., Ying-Ming, P., Shin Franklin G.,(2010). "Effective Anisotropic Dielectric Properties of Crystal Composites." Communications in Theoretical Physics 53(2): p 377.

[73] Dulieu-Barton, J. M., Fulton, M. C.,(2000). "Mechanical Properties of a Typical Stereolithography Resin." Strain 36(2): p 81-87.

[74] Popielarz, R., Chiang, C. K.,(2001). "Dielectric Properties of Polymer/Ferroelectric Ceramic Composites from 100 Hz to 10 GHz." Macromolecules 34(17): p 5910-5915.

[75] Kuo, D.-H., Chang, C.-C.,(2001). "Dielectric Behaviours of Multi - Doped $BaTiO_3$ / Epoxy Composites." Journal of the European Ceramic Society 21(9): p 1171-1177.

[76] Pecharromán, C., Esteban-Betegón, F., (2001)."New Percolative $BaTiO_3$ – Ni Composites with a High and Frequency - Independent Dielectric Constant ($\epsilon r \approx 80000$)." Advanced Materials 13(20): p 1541-1544.

[77] Panteny, S., Bowen, C.,(2006). "Characterisation of Barium Titanate - Silver Composites Part II: Electrical Properties." Journal of Materials Science 41(12): p 3845-3851.

[78] Scott, J. F., (2000)."Ferroelectric Memories – Advanced Micoelectric Series." 1st Ed. Springer Publishing Gr. Heidelberg, Germany.

[79] Zheng, L., Lin, C.,(1997)."Leakage Behavior and Distortion of The Hysteresis Loop in Ferroelectric Thin Films." Science in China Series E: Technological Sciences 40(2): p 126-134.

[80] Hebert, J.M.,(1985). "Ceramic Dielectrics and Capacitors", vol 6., UK:Gordon and Breach Science Publishers, p 214.

[81] Turik, A. V., Radchenko, G. S. (2002). "Maxwell - Wagner Relaxation in Piezoactive Media." Journal of Physics D: Applied Physics 35(11): p 1188.

[82] Liu, J., Duan, C.Mie, W. N., Smith, R. W., Hardy, J. R., (2005). "Dielectric Properties and Maxwell-Wagner Relaxation of Compounds $ACu_3Ti_4O_{12}$ ($A = Ca,Bi_{2/3},Y_{2/3},La_{2/3}$))." Journal of Applied Physics 98(9): p 093703-093705.

[83] Apaydin, E., Hansford, D.,(2007). "Integrated RF Circuits Design and Packaging in High Contrast Ceramic - Polymer Composites". Antennas and Propagation Society International Symposium.

[84] Arbatti, M., Shan, X., (2007). "Ceramic - Polymer Composites with High Dielectric Constant." Advanced Materials 19(10): p 1369-1372.

[85] Guo, S. S., Liu, W.,(2005). "Relaxor Ferroelectric Behavior and Structural Evaluation in Electron - Irradiated (Vinylidene Fluoride - Trifluoroethylene) Copolymer Blends." Journal of Materials Science 40(5): p 1177-1181.

[86] Robertson, J. , Varlow, B. R. (2004). "A Comparison Between the Dynamic and Static AC Conductivity Characteristics of Barium Titanate Filled Acrylic Resin". ICSD 2004. Proceedings of the International Conference on Solid Dielectrics.

[87] Wang, Z. H., Mao, J. M.,(2007). "Piezoelectric Thick films and their Application in MEMS." Journal of the European Ceramic Society 27(13-15): p 3759-3764.

[88] Bos, B., Gorter,H.,(2004). "Solid Freeform Fabrication of Piezoelectric Actuators by a Micro-Casting Method." Journal of Electroceramics 13(1):p 409-412.

[89] Smit, M.C., Ferreira, J.A., Van Wyk, J.D., (1992). "Application of Transmission Line Principles to high Frequency Power Converters." Power Electronics Specialists Conference, 1992. PESC '92, 23rd Ann. IEEE. p 1423 – 1430.

[90] Corasaniti, V. F., Arnera, P.L., (2009)."Hybrid Active Filter for Reactive and Harmonics Compensation in a Distribution Network". IEEE transactions on industrial electronics, vol. 56, no. 3, p 670 – 677.

[91] Moon, S.K., Choi, H. D., Lee, A. K., Cho, K. Y., Yoon, H.G., Suh, K.S., (2000). "Dielectric Properties of Epoxy - Dielectrics - Carbon Black Composite for Phantom Materials at Radio Frequencies." Volume 77, Issue 6, p 1294–1302.

[92] Park S. E., Shrout, T. R. (1997). "Characteristics of Relaxor - Based Piezoelectric Single Crystals for Ultrasonic Transducers." J. Appl. Phys. 82, p 1804.

[93] Shung, K. K., Cannata, J. M., Zhou, Q. F. (2007). "Piezoelectric Materials for High Frequency medical Imaging, J Electroceram 19: p 139–145

[94] Sharma, H.B., Mansingh, A., (1997). "Enhanced Electrical Properties of ferroelectric Pb($Zr_{0.5}$, $Ti_{0.5}$)O_3 Thin Films Grown with Low - Energy Oxygen Ion Assistance." Ferroelectric Lett, 22, p 75.

[95] Tu, Y.L., Milne, S.J., (1996). "Processing and Characterization of Pb(Zr, Ti)O_3 films, up to 10 μm Thick, Produced from a Diol Sol - Gel Route." J. Mater. Res., Vol 11 , p 2556.

[96] Byer, R. L., Roundy, C. B.,(1972). "Pyroelectric coefficient direct measurement technique and application to a nsec response time detector." Ferroelectrics 3(1): p 333-338.

[97] Gimenes, R., Zaghete, M. A.,(2004). "Composites PVDF-TrFE/BT used as Bioactive Membranes for Enhancing Bone Regeneration". Smart Structures and Materials: Electroactive Polymer Actuators and Devices. Y. BarCohen. 5385: p 539-547.

[98] Bandyopadhyay, A., Panda R.K., McNulty, T.F., Mohammadi, F., Danforth S.C., Safari, A.,(1998) "Piezoelectric Ceramics and Composites via Rapid Prototyping Techniques", Rapid Prototyping Journal, Vol. 4 Iss: 1, p 37 - 49.

[99] Anon, National Materials Advisory Board (NAS-NAE), (1994), "Hierarchical Structures in Biology as a Guide for New Materials Technology", Washington DC, National Academic Press.

[100] Hull, D., Clyde, T. W.,(2000). "An introduction to Composite Materials". England: Cambridge Solid State science series.

[101] Kelly, A., Mileiko, S.T.,(1983). "Fabrication of Composites- vol. 4". Elsevier science publishers B. V., Amsterdam, Netherlands.

[102] Leonhardt, G., Kieselstein, E.,(1991). "Interface Problems in Aluminium Matrix Composites Reinforced with Coated Carbon Fibres." Materials Science and Engineering: A 135: p 157-160.

[103] Ma, X., Yu, J., (2005). "Studies on the Properties of Natural Fibers - Reinforced Thermoplastic Starch Composites." Carbohydrate Polymers 62(1): p 19-24.

[104] Lubin, G.,(1982)."Handbook of Composites". Van Nostrand Reinhold, New York.

[105] Jones, R. M.,(1976)."Mechanics of Composite Materials". Ed 2. Brunner-Routledge, London.

[106] Liu, Y. B., Lim, S. C.,(1994). "Recent Development in the Fabrication of Metal Matrix - Particulate Composites Using Powder Metallurgy Techniques." Journal of Materials Science 29(8): p 1999-2007.

[107] Rohatgi, P., Pai, B.,(1979). "Preparation of Cast Aluminium - Silica Particulate Composites." Journal of Materials Science 14(10): p 2277-2283

[108] Landon, G., Lewis, G.,(1977). "The influence of Particle Size on the Tensile Strength of Particulate — Filled Polymers." Journal of Materials Science 12(8): p 1605-1613.

[109] Eshelby, J. D.,(1957). "The Determination of the Elastic Field of an Ellipsoidal Inclusion, and Related Problems." Proceedings of the Royal Society of London. Series A. Mathematical and Physical Sciences 241(1226): p 376-396.

[110] Tanaka, K., Mori, T.,(1972). "Note on volume integrals of the elastic field around an ellipsoidal inclusion." Journal of Elasticity 2(3): p 199-200.

[111] Mori, T., Tanaka, K., (1973). "Average Stress in Matrix and Average Elastic Energy of Materials with Misfitting Inclusions." Acta Metallurgica 21(5): p 571-574.

[112] Hill, R.,(1964). "Theory of Mechanical Properties of Fibre - Strengthened materials: I. Elastic Behaviour." Journal of the Mechanics and Physics of Solids 12(4): p 199-212.

[113] Hill, R.,(1964). "Theory of Mechanical Properties of Fibre - Strengthened Materials: II. Inelastic Behaviour." Journal of the Mechanics and Physics of Solids 12(4): p 213-218.

[114] Hill, R.,(1965). "Theory of Mechanical Properties of Fibre - Strengthened Materials--III. Self - Consistent Model." Journal of the Mechanics and Physics of Solids 13(4): p 189-198.

[115] Hill, R.,(1965). "A Self - Consistent Mechanics of Composite Materials." Journal of the Mechanics and Physics of Solids 13(4): p 213-222.

[116] Hashin, Z., Shtrikman, S., (1961). "Note on a Variational Approach to the Theory of Composite Elastic Materials." Journal of the Franklin Institute 271(4): p 336-341.

[117] Brown, Jr. W. F., (1955) "Solid Mixture Permittivities," J. Chem. Phys., Vol. 23.

[118] Hashin, Z., Shtrikman, S.,(1962). "A Variational Aproach to the Theory of the Elastic Behaviour of Polycrystals." Journal of the Mechanics and Physics of Solids 10(4): p 343-352.

[119] Pal, R., (2009). "Influence of Interfacial Phenomena on the Mechanical Properties of Particulate Composite Membranes." Polymer Composites 30(4): p 451-459.

[120] Vratsanos, L.A., Farris, R.J., (1993). "A Predictive Model for the Mechanical Behavior of Particulate Composites. Part 1: Model Derivation, Part 2: Comparison of Model Predictions to Literature Data". Polymer Eng. and Sci. 33, p 1458–1474

[121] Lori, L., Anderson Vratsanos, R. J. F. (1993). "A Predictive Model for the Mechanical Behavior of Particulate Composites. Part I: Model Derivation." Polymer Engineering & Science 33(22): p 1458-1465.

[122] Lori L. anderson, R. J. F.,(1988). "A Predictive model for the mechanical Behavior of Particulate Composites." Polymer Engineering & Science 28(8): p 522-528.

[123] Jan, K., (1997)."Three - Dimensional Models for Predicting the modulus and Yield Strength of Polymer Blends, Foams, and Particulate Composites." Polymer Composites 18(4): p 433-441.

[124] Green, D. J., P. S. Nicholson, (1979). "Fracture of a Brittle Particulate Composite." Journal of Materials Science 14(6): p 1413-1420.

[125] Ahmed, S., Jones, F. R., (1990). "A review of Particulate Reinforcement Theories for Polymer Composites." Journal of Materials Science 25(12): p 4933-4942.

[126] Johnson, W. W., Dhuru, V. B.,(1993). "Composite Microfiller Content and Its Effect on Fracture Toughness and Diametral Tensile Strength." Dental Materials 9(2): p 95-98.

[127] Penn, R. W., Craig. R. G.,(1987). "Diametral Tensile Strength and Dental Composites." Dental Materials 3(1): p 46-48.

[128] Balla, V. K., Bose, S.,(2008). "Processing of Bulk Alumina Ceramics Using Laser Engineered Net Shaping." International Journal of Applied Ceramic Technology 5(3): p 234-242.

[129] Reyes, D. R., Iossifidis, D.,(2002). "Micro Total Analysis Systems. 1. Introduction, Theory, and Technology." Analytical Chemistry 74(12): p 2623-2636.

[130] Bula, W. P., Verboom, W.,(2007). "Multichannel Quench - Flow Microreactor Chip for Parallel Reaction Monitoring." Lab on a Chip 7(12): p 1717-1722.

[131] Manz, A., Sens actuaturs 1990, B1, p 244-248.

[132] Morita, M., Longmire, M. L., (1988). "Solid - State Voltammetry in a Three - Electrode Electrochemical Cell - on - a - Chip with a Microlithographically Defined Microelectrode." Analytical Chemistry 60(24): p 2770-2775.

[133] McGuire, G. E., (1988). "Semicondictor Materials and Process Technlogy Handbook for VLSI and ULSI". 1st ed. New jersey, U.S.A., Noyes Publications, p 329.

[134] Geschke, O., Klank, H., Telleman, P., (2005). "Microsystem Engineering of Lab-on-a Chip Devices", 1st ed. Denmark:WILEY-VCH Verlag GmBH & Co. KGaA, Weinheim.

[135] Abgrall, P., Gué , A. M., (2007). "Lab - on - Chip Technologies: Making a Microfluidic Network and Coupling it into a Complete Microsystem: a Review." Journal of Micromechanics and Microengineering 17(5): R15.

[136] Roumanie, Pijolat, M., C.,(2006). "Deposition of Pt - Catalyst in a Micro - Channel of a Silicon Reactor: Application to Gas Micro - TAS Working at High Temperature." Sensors and Actuators B: Chemical 118(1,Äì2): 297-304.

[137] Saigusa, H., Suga, Y.,(2006). "Non-Photolithographic Manufacturing Processes for Micro-Channels Functioned by Micro-Contact-Printed SAMs." IEEJ Transactions on Sensors and Micromachines 126(11): 603-606.

[138] Mellors, J. S., Gorbounov, V., (2008). "Fully Integrated Glass Microfluidic Device for Performing High-Efficiency Capillary Electrophoresis and Electrospray Ionization Mass Spectrometry." Analytical Chemistry 80(18): p 6881-6887.

[139] Rötting, O., Röpke, W.,(2002). "Polymer Microfabrication Technologies." Microsystem Technologies 8(1): p 32-36.

[140] McGuire, G. E., (1988). "Semicondictor Materials and Process Technlogy Handbook for VLSI and ULSI". 1st ed. New jersey, U.S.A., Noyes Publications, p 8.

[141] Gad-el-Hak, M.,(2002). "The MEMS Handbook", 6th ed. London: CPC press, p16-1.

[142] McGuire, G. E.,(1988). "Semicondictor Materials and Process Technlogy Handbook for VLSI and ULSI". 1st ed. New jersey, U.S.A., Noyes Publications, p 80.

[143] McGuire, G. E.,(1988). "Semicondictor Materials and Process Technlogy Handbook for VLSI and ULSI". 1st ed. New jersey, U.S.A., Noyes Publications, p 191.

[144] Bunshah, R. F.,(1994). "Material Science and Process Technology series". Noyes Publications, New Jersey, U.S.A [Accessed on 30th June 2011]

[145] Malek, C. K., Saile, V.,(2004). "Applications of LIGA Technology to Precision Manufacturing of High - Aspect - Ratio Micro - Components and -Systems: a Review." Microelectronics Journal 35(2): p 131-143.

[146] Gad-el-Hak, M., (2002). "The MEMS Handbook", 6th ed. London: CPC press.

[147] Becker, H., Manz A. (1998). "Integrated Capillary Electrophoresis for Chemical Analysis." Sensors Update 3(1): p 209-238.

[148] Zhang, X., Stefanick, S.,(2004). "Application of Microreactor Technology in Process Development." Organic Process Research & Development 8(3): p 455-460.

[149] Srinivasan, V., Pamula, V. K., (2004). "An Integrated Digital Microfluidic Lab - on - a - Chip for Clinical Diagnostics on Human Physiological Fluids." Lab on a Chip 4(4): p 310-315.

[150] Becker, H., Heim, U.,(2000). "Hot Embossing as a Method for the Fabrication of Polymer High Aspect Ratio Structures." Sensors and Actuators A: Physical 83(1,Ä¡3): p 130-135.

[151] Becker, H., Locascio, L. E.,(2002). "Polymer Microfluidic Devices." Talanta 56(2): p 267-287.

[152] Fedder, G. K., (2003). "MEMS Fabrication", ITC' 03, 1089-3593/03.

[153] Uriarte, L., Herrero, A., (2006). "Comparison Between Microfabrication Technologies for Metal Tooling." Proceedings of the Institution of Mechanical Engineers, Part C: Journal of Mechanical Engineering Science 220(11): p 1665-1676.

[154] Wong, C. C., Chu, D., (1997)."Rapid Prototyping of a Micro pump for Microelectronic Applications". PBD: May 1997: Medium: P; Size: p 39.

[155] Carrozza, M. C. (1995). "A Piezoelectric - Driven Stereolithography - Fabricated Micropump." Journal of Micromechanics and Microengineering 5(2): p 177.

[156] Cohen, A.L., Frodis, U., Tseng, F., Zhang, G., Mansfield, F., Will, P. M., (1999). "EFAB: Low - Cost, Automated Electrochemical Batch Fabrication of Arbitrary 3-D Microstructures", Micromachining and Microfabrication Process Technology, Symposium on Micromachining and Microfabrication.

[157] Ferrell, N., Woodard J., (2007). "Fabrication of Polymer Microstructures for MEMS: Sacrificial Layer Micromolding and Patterned Substrate Micromolding." Biomedical Microdevices 9(6): p 815-821.

[158] Ko, H. S. (2007). "Novel Fabrication of a Pressure Sensor With Polymer Material and Evaluation of its Performance." Journal of Micromechanics and Microengineering 17(8): p 1640.

[159] Kandlikar, S.G., Grande, W. J. (2003). "Microchannels and Minichannels—History, Terminology, Classification and Current Research Needs," First International Conference on Microchannels and Minichannels.

[160] Kundu, P., Cohen, I., (2001). "Fluid Mechanics", Elsevier Academic Press.

[161] Robert H. Perry, "Perry's Chemical Engineer's Handbook",(McGraw-Hill chemical engineering series, 5th Edition, 1973)

[162] Ikuta, K., Maruo, S., (1999). Micro Concentrator with Opto - Sense Micro Reactor for Biochemical IC Chip Family. 3D Composite Structure and Experimental Verification. Twelfth IEEE International Conference on Micro Electro Mechanical Systems.

[163] Robert H. Perry, "Perry's Chemical Engineer's Handbook",(McGraw-Hill chemical engineering series, 7th Edition, 1973).

[164] Kashid, M. N., Agar, D. W. (2007). "Hydrodynamics of Liquid - Liquid Slug Flow Capillary Microreactor: Flow Regimes, Slug Size and Pressure Drop." Chemical Engineering Journal 131(1-3): p 1-13.

[165] Vican, J., Gajdeczko, B. F. (2002). "Development of a Microreactor as a Thermal Source for Microelectromechanical Systems Power Generation." Proceedings of the Combustion Institute 29(1): p 909-916.

[166] Haelrey, J. C., Huang, Y., Bau, H. H., Zemel, J.N., (1995)."Gas Flow in Micro - Channels," J. Fluid Mech., p 257-274.

[167] Satish, G. K., Derek, S., (2005). "Characterization of Surface Roughness Effects on Pressure Drop in Single - Phase Flow in Minichannels." Physics of Fluids 17(10): 100606.

[168] Steinke, M. E., Kandlikar, S. G., (2006). "Single - Phase Liquid Friction Factors in Microchannels." International Journal of Thermal Sciences 45(11): p 1073-1083.

[169] J. Koo, Kleinstreuer, C., (2003)."Liquid Flow in Microchannels: Experimental Observations and Computational Analyses of Microfluidics Effects". J. Micromech. Microeng., 13 , p. 568–579.

[170] Junemo, K., Clement, K., (2003). "Liquid Flow in Microchannels: Experimental Observations and Computational Analyses of Microfluidics Effects." Journal of Micromechanics and Microengineering 13(5): p 568.

[171] Mohiuddin Mala, G., Li, D. (1999). "Flow Characteristics of Water in Microtubes." International Journal of Heat and Fluid Flow 20(2): p 142-148.

[172] Peng, X. F., Peterson, G. P., (1994). "Heat Transfer Characteristics of Water Flowing Through Microchannels." Experimental Heat Transfer 7(4): p 265 - 283.

[173] Brackbill, T. P., Kandlikar, S. G., (2008). "Effects of Roughness on Turbulent Flow in Microchannels and Minichannels." ASME Conference Proceedings 2008(48345): p 1179-1186.

[174] Shou-Shing, H., (2004). "Liquid Flow in a Micro - Channel." Journal of Micromechanics and Microengineering 14(4): p 436.

[175] Hetsroni, G., Mosyak, A., (2005). "Fluid flow in Micro - Channels." International Journal of Heat and Mass Transfer 48(10): p 1982-1998.

[176] Gan, Y., Xu, J., (2007). "An Experimental Investigation of Flow Characteristics for Laminar Flow in Silicon Microchannels". Challenges of Power Engineering and Environment: p 1011-1015.

[177] Jiang, X. N., Zhou, Z. Y., (1995). "Micro-fluid Flow In Microchannel". Solid-State Sensors and Actuators, Eurosensors IX. Transducers '95. The 8th International Conference on Solid-State Sensors and Actuators.

[178] Erickson, D., (2005). "Towards Numerical Prototyping of Labs - on - Chip: Modeling for Integrated Microfluidic Devices." Microfluidics and Nanofluidics 1(4): p 301-318.

[179] Rebrov, E. V., Ismagilov, R. Z., (2007). "Header Design for Flow Equalization in Microstructured Reactors." Aiche Journal 53(1): p 28-38.

[180] Mies, M. J. M., Rebrov, E. V., (2007). "Experimental Validation of the Performance of a Microreactor for the High-Throughput Screening of Catalytic Coatings." Industrial & Engineering Chemistry Research 46(12): p 3922-3931.

[181] Simpson, P. C., Roach, D., (1998). "High-throughput Genetic Analysis Using Microfabricated 96-Sample Capillary Array Electrophoresis Microplates." Proceedings of the National Academy of Sciences 95(5): p 2256-2261.

[182] Erickson, D., Li, D., (2004). "Integrated Microfluidic Devices." Analytica Chimica Acta 507(1): p 11-26.

[183] Haswell, S. J., Middleton, R. J., (2001). "The Application of Micro Reactors to Synthetic Chemistry." Chemical Communications(5): p 391-398.

[184] Weibel, D. B., Whitesides, G. M., (2006). "Applications of Microfluidics in Chemical Biology." Current Opinion in Chemical Biology 10(6): p 584-591.

[185] Beyssen, D., Brizoual, L. Le., (2006). "Microfluidic Device Based on Surface Acoustic Wave." Sensors and Actuators B: Chemical 118(1-2): p 380-385.

[186] Jensen, K. F., (2001). "Microreaction Engineering - Is Small Better?" Chemical Engineering Science 56(2): p 293-303.

[187] Gardner, J. W., Varadan, V. K., Awadelkarim, O. O., (2005), "Microsensors, MEMS and Smart Devices", John Wiley & Sons Ltd., West Sussex, England.

[188] Liu, C., (2007). "Recent Developments in Polymer MEMS." Advanced Materials 19(22): p 3783-3790.

[189] Sameoto, D., Tsang, S.-H., (2007). "Polymer MEMS Processing for Multi - User Applications." Sensors and Actuators A: Physical 134(2): p 457-464.

[190] Fakhfouri, V., Cantale, N., (2008). "Inkjet Printing of SU-8 for Polymer - Based MEMS a Case Study for Microlenses". Micro Electro Mechanical Systems.

[191] Zengerle, R., Ulrich, J., (1995). "A Bidirectional Silicon Micropump." Sensors and Actuators A: Physical 50(1,Ä¦2): p 81-86.

[192] Vandelli, N., Wroblewski, D., (1998). "Development of a MEMS Microvalve Array for Fluid Flow Control." Microelectromechanical Systems, Journal of 7(4): p 395-403.

[193] Bogue, R., (2007). "MEMS Sensors: Past, Present and Future", Sensor Review, Emerald Grp Pblsh. s.l., s.n.

[194] Tabard-Cossa, V., Godin, M., (2005). "A Differential Microcantilever - Based system for Measuring Surface Stress Changes Induced by Electrochemical Reactions." Sensors and Actuators B: Chemical 107(1): p 233-241.

[195] Drafts, B., (2001). "Acoustic Wave Technology Sensors." Microwave Theory and Techniques, IEEE Transactions on 49(4): p 795-802.

[196] Sarin Kumar, A. K., Paruch, P., (2004). "High - Frequency Surface Acoustic Wave Device Based on Thin - Film Piezoelectric Interdigital Transducers." Applied Physics Letters 85(10): p 1757-1759.

[197] Beeby, S. P., (2006). "Energy Harvesting Vibration Sources for Microsystems Applications." Measurement Science and Technology 17(12): R175.

[198] Tay, F. E. H., (1999). "The Effects of Non - Parallel Plates in a Differential Capacitive Microaccelerometer." Journal of Micromechanics and Microengineering 9(4): p 283.

[199] Lai, Y., Bordatchev, E., (2006). "Metallic Micro Displacement Capacitive Sensor Fabricated by Laser Micromachining Technology." Microsystem Technologies 12(8): p 778-785.

[200] Vlassov, Y. N., Kozlov, A. S., (1993). "Precision SAW Pressure Sensors. Frequency Control Symposium.

[201] Tuncer, E., Sauers, I., (2007). "Electrical Properties of Epoxy Resin Based Nano - Composites." Nanotechnology 18(2).

[202] Brusa, E., Munteanu, M., (2009). "Validation of Compact Models of Microcantilever Actuators for RF - MEMS Design." Analog Integrated Circuits and Signal Processing 59(2): p 191-199.

[203] Schimetta, G., F. Dollinger, (2000). "A Wireless Pressure - Measurement System Using a SAW Hybrid Sensor." Microwave Theory and Techniques, IEEE Transactions on 48(12): p 2730-2735.

[204] He, F., Huang, Q.- A., (2007). "A Silicon Directly Bonded Capacitive Absolute Pressure Sensor." Sensors and Actuators A: Physical 135(2): p 507-514.

[205] Hennemeyer, M., Burghardt, S., Stark, R. W., (2008)."Cantilever Micro - Rheometer for Characterization of sugar solutions." Sensors, 8, p 10-22, s.l., s.n. [Accessed on 1st February, 2011]

[206] Blanther, J.E., "Manufacture of Contour Relief Maps", US Patent #473,901, 1892.

[207] Venuvinod ,P. K., Ma, W., (2004). "Rapid Prototyping - Laser - Based and Other Technologies", 1st ed, Kluwer Academic Publisher.

[208] Beaman, J. J., Barlow, J. W., Bourell, D. L., Crawford, R. H., (1997). "Solid Freeform Fabrication: A New Direction in Manufacturing", AH Dordrecht, Kluwer Academic Publisher.

[209] Swainson, W. K., (1980). "Method, Medium and Apparatus for Producting Three Dimensional Figure Products", US patent no. 4238840. [Accesses on 2nd July 2011].

[210] Bourell D. L., Beaman, J. J., Leu, M. C., Rosen, D. W., (2009). "A Brief History of Additive Manufacturing and 2009 Roadmap for Additive Manufacturing: Looking Back and Looking Ahead", RapidTech 2009: US-TURKEY Workshop on Rapid Technologies. [Accessed on 15th December 2010]

[211] Gebhardt, A., (2003). "Rapid Prototyping", Munich, Hanser Publishers.

[212] Gebhardt, A., (2003). "Rapid Prototyping". Munich: Haser Publishers, p 65.

[213] Jacobs, P. F., (1996)."Stereolithography and other RP&M Technologies - from Rapid Prototyping to Rapid Tooling". New York: ASME Press.

[214] Venuvinod ,P. K., Ma, W., (2004). "Rapid Prototyping - Laser - Based and Other Technologies", 1st ed, Kluwer Academic Publisher, p 261.

[215] Gibson, I., Rosen, D. W., Stucker, B., (2010). "Additive Manufacturing Technologies". Springer Science + business media, p 103.

[216] Gebhardt, A., (2003). "Rapid Prototyping". Munich: Haser Publishers, p 162.

[217] Polyjet technology. http://lab1rp.net/ PolyJetTechnology.html [Accessed on 20th January 2012].

[218] Gibson, I, Rosen. D.W., Stucker, B. (2010). "Additive Manufacturing Technologies". Ist ed. Springer Publication. USA. Table 4.1.

[219] Chua, C. K., Leong, K. F., Lim, C.S., (2010). "Rapid Prototyping Principles and Applications". 3rd ed. World Scientific, Singapore.

[220] Cheah, C. M., Nee A. Y. C., (1997). "Characteristics of Photopolymeric Material used in Rapid Prototypes Part I. Mechanical Properties in the Green State." Journal of Materials Processing Technology 67(1,Äì3): p 41-45.

[221] Salmoria, G. V., Ahrens, C. H., (2005). "Stereolithography somos 7110 resin: Mechanical Behavior and Fractography of Parts Post - Cured by Different Methods." Polymer Testing 24(2): p 157-162.

[222] Hackney, P. M., Arulraj, A. C., Chinnaswamy, G. K., Nair, B. T., (2005). "Investigation into the EnvisionTec PerFactory Rapid Prototyping Process for Production of Accurate and Strong Functional Part", 6th National Conference on Rapid Prototyping, Rapid Tooling and Rapid Manufacturing, Buckinghamshire Chilterns University College, p 26.

[223] Chockalingam, K., Jawahar, N., Chandrasekhar, U., (2006). "Influence of Layer Thickness on Mechanical Properties in Stereolithography", Rapid Prototyping Journal, Vol. 12 Iss: 2, p 106 – 113

[224] Chockalingam, K., N. Jawahar, (2006). "Optimization of Stereolithography Process Parameters for Part Strength using Design of Experiments." The International Journal of Advanced Manufacturing Technology 29(1): p 79-88.

[225] Segal, J. I., Campbell, R.I., (2001). "A Review of Research into the Effects of Rapid Tooling on Part Properties", Rapid Prototyping Journal, Vol. 7 Iss: 2, p 90 - 99.

[226] Ishiyama, C., Higo, Y. (2002). "Effects of Humidity on Young's Modulus in Poly (Methyl Methacrylate)." Journal of Polymer Science, Part B: Polymer Physics 40(5): p 460-465.

[227] Jonathan Colton, B. B. (1999). "Experimental Study of Post - build Cure of Stereolithography Polymers for Injection Molds." Rapid Prototyping Journal 5(2): p 72 - 81.

[228] Schaeffer, P., Bertsch, A., (1997). "Industrial Photochemistry XXIV. Relations Between Light Flux and Polymerized Depth in Laser Stereophotolithography." Journal of Photochemistry and Photobiology A: Chemistry 107(1-3): p 283-290.

[229] Safari, A., Ebrahimi, M., (2002). "Layered Manufacturing for Prototyping of Novel Transducers". Ultrasonics Symposium.

[230] Lewis, J. A., Smay, J. E., (2006). "Direct Ink Writing of Three - Dimensional Ceramic Structures." Journal of the American Ceramic Society 89(12): p 3599-3609.

[231] Cabral , J. T., Hudson, S.D., Harrison, C., Douglas, J. F., (2004). "Frontal Photopolymerization for Microfluidic Applications." Langmuir 2004, 20, p 10020-10029

[232] Provin, C., Monneret, S. (2002). "Complex Ceramic - Polymer Composite Microparts Made by Microstereolithography." Electronics Packaging Manufacturing, IEEE Transactions on 25(1): p 59-63.

[233] Francis, E. H. T., (2001). "A novel Micro - Machining Method for the Fabrication of Thick - Film SU-8 Embedded Micro - Channels." Journal of Micromechanics and Microengineering 11(1): p 27.

[234] Hornbeck, L.J., Nelson, W.E., (1988)."Bistable Deformable Mirror Device," OSA Technical Digest Series Vol. 8, Spatial Light Modulators and Applications, p. 107.

[235] John, H., "Perfactory® - A Rapid Prototyping system on the way to the "Personal Factory" for the end user", s.l., s.n.

[236] Lu, Y., Mapili, G., (2006). "A digital Micro - Mirror Device - Based System for the Microfabrication of Complex, Spatially Patterned Tissue Engineering Scaffolds." Journal of Biomedical Materials Research Part A 77A(2): p 396-405.

[237] Envisiontec Perfactory - User Manual.

[238] Warren, B. E.,(1969)."X-ray diffraction" USA: Addison - Wesle.

[239] Brochure Malvern Information and Specification. [Accessed on 14 July 2011].

[240] Hauser, C., Clare, A.T., Taylor, S., Chalker, P.R., Sutcliffe, C.J., Brkic, B. and France, N.(2008). "Rotational 3D Printing of Sensor Devices using Reactive Ink Chemistries". Proceedings Solid Freeform Fabrication Symposium, Austin, Texas, USA.

[241] Watts, P., Haswell, S. J., (2005). "The Application of Micro Reactors for Organic Synthesis." Chemical Society Reviews 34(3): p 235-246.

[242] Yang, J., Liu, Y., (2002). "High Sensitivity PCR Assay in Plastic Micro Reactors." Lab on a Chip 2(4): p 179-187.

[243] Clare, A.T., Envisiontec Microfluidic Build tests, Liverpool, England (Personal communication)

[244] Acosta, F., Experimental Details, Liverpool, England. [email](personal communication dated 30 June, 2010).

[245] Envisiontec R5 "Material Property Data Sheet", dated July 2005. [Accessed on 5th March, 2011].

[246] Hull, D., (1999). "Fractography: Observing, Measuring and Interpreting Fracture Surface Topography", Ist ed, Cambridge University Press, United Kingdom.

[247] Smith, W. A., A. Shaulov, (1985). "Tailoring the Properties of Composite Piezoelectric Materials for Medical Ultrasonic Transducers". IEEE 1985 Ultrasonics Symposium.

[248] Kim, P., S. C. Jones, (2007). "Phosphonic Acid - Modified Barium Titanate Polymer Nanocomposites with High Permittivity and Dielectric Strength." Advanced Materials 19(7): p 1001-1005.

APPENDIX A

A.1 Polymer Cantilever Beam

An investigation was commenced for understanding the behaviour of polymer based functional devices. A polymer based cantilever beam was manufactured by the DLP system. For development of polymer based functional devices, set of experiment was performed to understand behaviour of polymer cantilever beam. The influence of different curing methods on the beam defection was recorded. Cantilever beam have one end fixed, while the other end is free to deflect. The deflection in the beam can be calculated using Equation 7.1:

$$\delta_{max} = -\frac{F\ell^3}{3YI} \qquad (7.1)$$

Where Y is the Young's modulus, F is the force applied, ℓ is length of the beam and I is the moment of inertia (Figure 105). Once the deflection of the beam is know, the stiffness k can be calculated as:

$$k = \frac{F}{\delta} \text{ or } \frac{3EI}{\ell^3} \qquad (7.2)$$

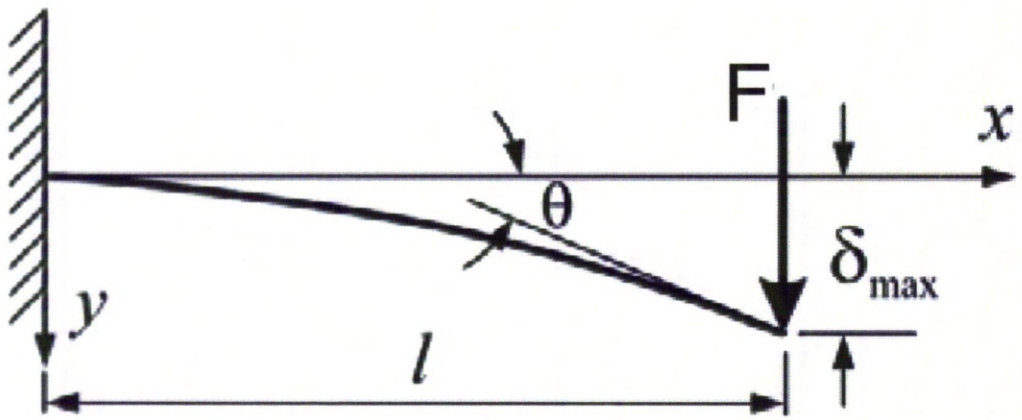

Figure 105: Schematic Representation for Deflection of Cantilever Beam Due To Point Load.

Various micro-cantilever beams were manufactured in standard photopolymer R5. All of the beams were manufactured using layer thickness of 25 µm. The recommended exposure for each 25 µm layer is

3000 ms. However, the current structures were also exposed for 3500 ms and 4000 ms to investigate influence of higher exposure on the sensors. The beams were 1.1 mm in length, 0.4 mm in width and thickness however, varying from 0.2 - 0.5 mm. Optical microscopy of the beams shows that improved feature sizes could be obtained for higher exposures i.e. at 4000 ms as compared to 3500 ms, shown in Figure 106 - 107. The beams manufactured at an exposure of 4000 ms were found to have higher surface roughness, although the dimensions of the structure is relatively uniform along the length of the beam (Figure 108).

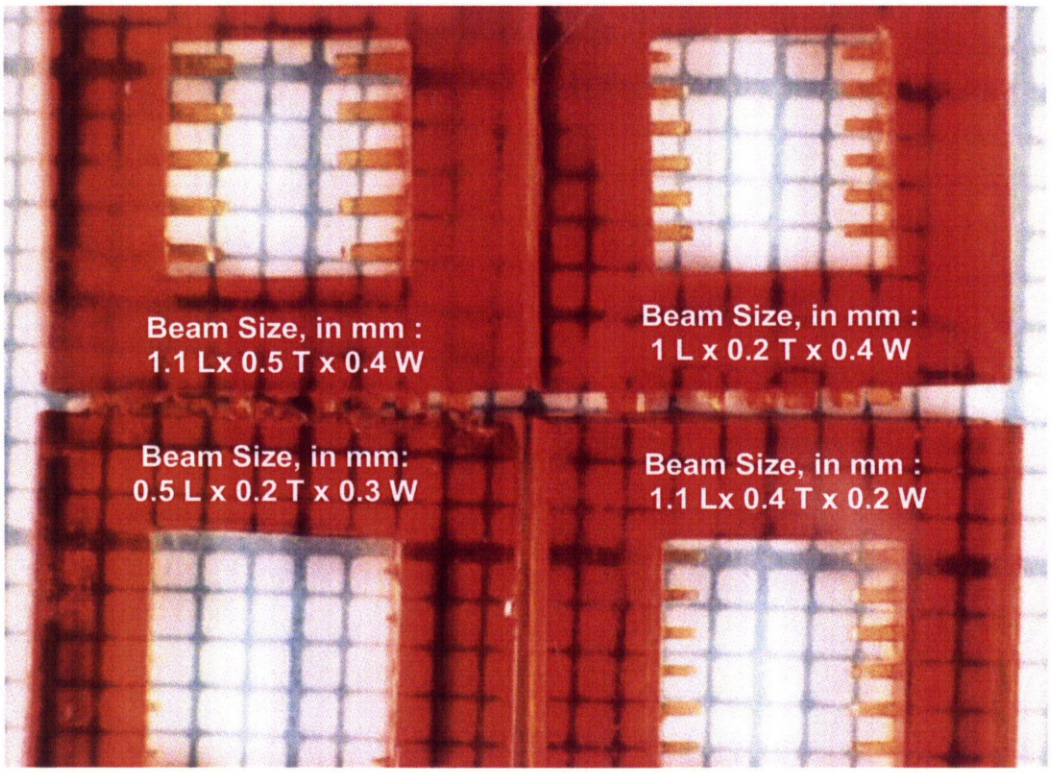

@ 3500 ms Exposure

Figure 106: Micro Cantilever Beams Manufactured at 3500 ms.

Figure 107: Micro Cantilever Beams Manufactured at 4000 ms.

In order to understand and validate the response of polymer beams, longer beams were manufactured at 4000 ms exposure time. These were 8 mm in length, 0.5 mm in width and with a thickness varying from 0.05 - 0.5 mm manufactured by the DLP system in both, horizontal and vertical directions. For longer beams, the surface stress was significant as the beams were arched along their length caused by the residual stress from the material shrinkage. This effect was prominent for thinner vertical builds, as shown in Figure 109. Although, beams with thicknesses up to 0.2 mm were successfully manufactured, they were relatively fragile and cracked while removing them from the build platform. Beam with larger thicknesses were sturdier and exhibited lower curling.

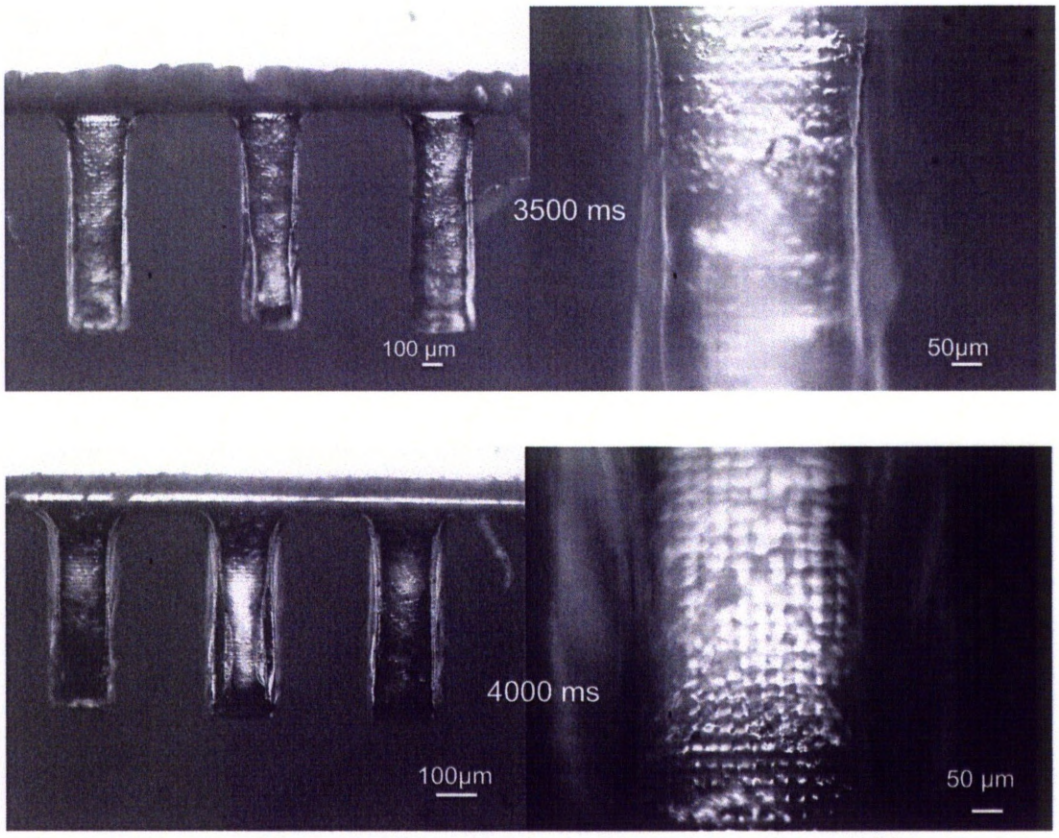

Figure 108: Optical Microscopy of Cantilever Beams Manufactured at 3500 ms (Top) & 4000 ms (Bottom).

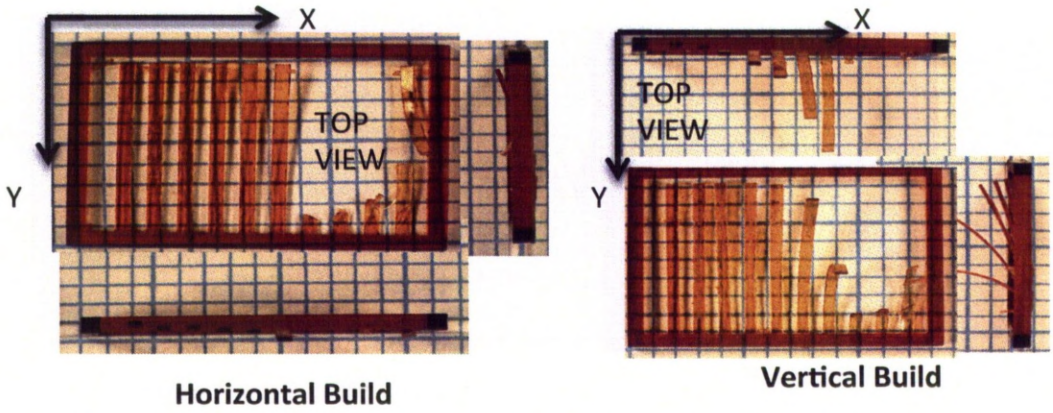

Figure 109: Optical Microscopy of Cantilever Beams Manufactured in Different Orientation.

Based on this study, the beam deflection of 0.3 – 0.4 mm thick cantilevers was assessed under load. Although, the curling effect in the beam could not be completely eliminated, it was however be minimised by pressing them during post-processing. Figure 110 shows the residual curling effect

observed in such beams after curing. Whilst measuring the deflection, each beam was clamped and suspended with a 0.1 g weight at the end of the beam, shown in Figure 111. The beam deflection was recorded by high-speed camera, which was capable of recording 10000 frames per second.

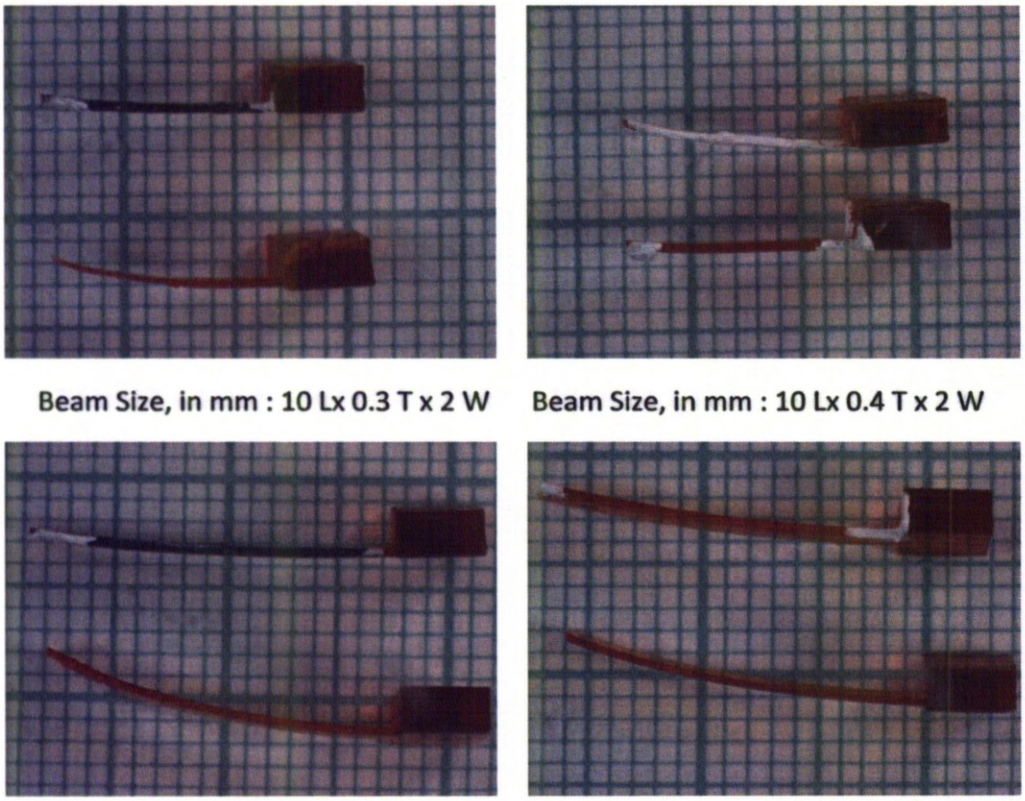

Figure 110: Curling Effect Observed in Cantilever Beams After Curing.

The high-speed camera output was saved as a video clip. The clip was then imported into ProAnalyst software (Xcitex Inc., Unites States of America) to dissect individual frames. The software tool breaks the video clip into sequential picture frames. The picture frames are pixelated and analysis requires two pixels to be selected, representing beam length. One pixel remains fixed, while the displacement of the other in consecutive frames determines the deflection in the beam.

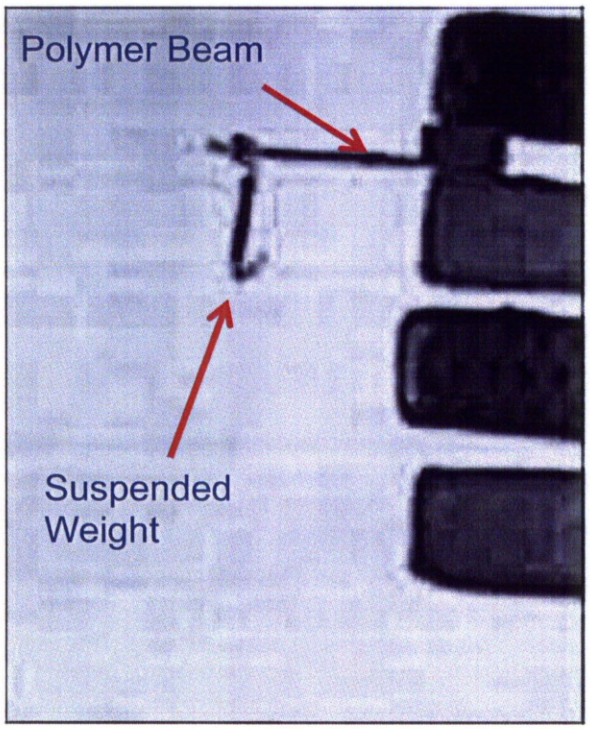

Figure 111: Typical Arrangement for Beam Deflection Analysis.

Based on the measured data, the deflection in the beams was compared with expected theoretical deflection. The Young's modulus of 800 MPa reported in 5.3 for the photopolymer was considered for theoretical calculation of deflection and stiffness. Young's modulus Y and stiffness k were calculated and presented in Table 15 below. It stiffness calculated from the experimental deflection (k2) was 10 times greater than theoretical calculation (k1). This confirms that the beams cured at atmospheric conditions were not perfectly cured. The theoretical Young's modulus (Y1) for the beams was considerably lower than the expected (Y2). The variation in stiffness observed for theoretical and the experimental deflection were noticeably, especially for the 16 mm long beams. The thickness and length of the beam also influences resultant stiffness.

Table 15: Young's Modulus and Stiffness Observed for The Beams, Cured at Atmospheric Conditions.

Specimen	Length, (mm)	Width, (mm)	Thickness, (mm)	Y1	Y2	Y1/Y2	k1	k2	k1/k2
1	10	2	0.3	800	230	3.478	10.935	3.105	3.522
2	10	2	0.4	800	160	5.000	25.920	5.12	5.063
3	14	2	0.3	800	140	5.714	3.985	0.689	5.786
4	16	2	0.4	800	80	10.000	6.328	0.625	10.125

In a separate set of experiment, beams were exposed to UV rays for curing. Similar to the method described earlier, the beams deflection measured by following the protocol is shown in Table 16. Exposing the polymer beam to UV rays has improved the stiffness of the beams. The variation in stiffness calculated from the experimental observation was reduced. This is however, not evident for 16 mm long beam.

Table 16: Young's Modulus and Stiffness Observed for The UV Cured Polymer Beams.

Specimen	Length, (mm)	Width, (mm)	Thickness, (mm)	Y1	Y2	Y1/Y2	K1	K2	K1/k2
1	10	2	0.32	800	120	6.667	13.271	1.966	6.750
2	10	2	0.32	800	90	8.889	13.271	1.475	9.000
3	10	2	0.26	800	130	6.154	7.326	1.176	6.231
4	16	2	0.42	800	240	3.333	7.325	2.171	3.375
5	16	2	0.34	800	180	4.444	3.886	0.864	4.500
6	16	2	0.33	800	170	4.706	3.55	0.746	4.761

Polymer beams were cured as per the recommended procedure by holding the polymer component for 30 min at low temperature of 35 – 45 °C. Experimental observations for deflection and stiffness are reported in Table 17. Magnitude of Young's modulus and stiffness were similar to observations by UV rays curing. The Young's modulus was relatively uniform for all the beams.

Table 17: Young's Modulus and Stiffness Observed for The Polymer Beams Cured by Recommended Procedure.

Specimen	Length, (mm)	Width, (mm)	Thickness, (mm)	Y1	Y2	Y1/Y2	K1	K2	K1/k2
1	10	2	0.38	800	140	5.714	22.233	3.559	6.750
2	10	2	0.38	800	180	4.444	22.233	4.124	9.000
3	10	2	0.38	800	180	4.444	22.233	3.707	6.231
4	16	2	0.38	800	100	8.000	5.426	0.669	3.375
5	16	2	0.38	800	170	4.706	5.426	1.138	4.500
6	16	2	0.38	800	200	4.000	5.426	1.339	4.761

Typical deflection behaviour of beam cured by different methods are shown in Figure 112 shows the influence of curing technique on the deflection of polymer beams. It is clear that the deflection and therefore deflection on the beams cured by UV rays was closer to experimental observation plotted for Young's modulus of 800 MPa. The deflection in the beams curing by heating shows large deflection. This may be due to softening of polymer while curing.

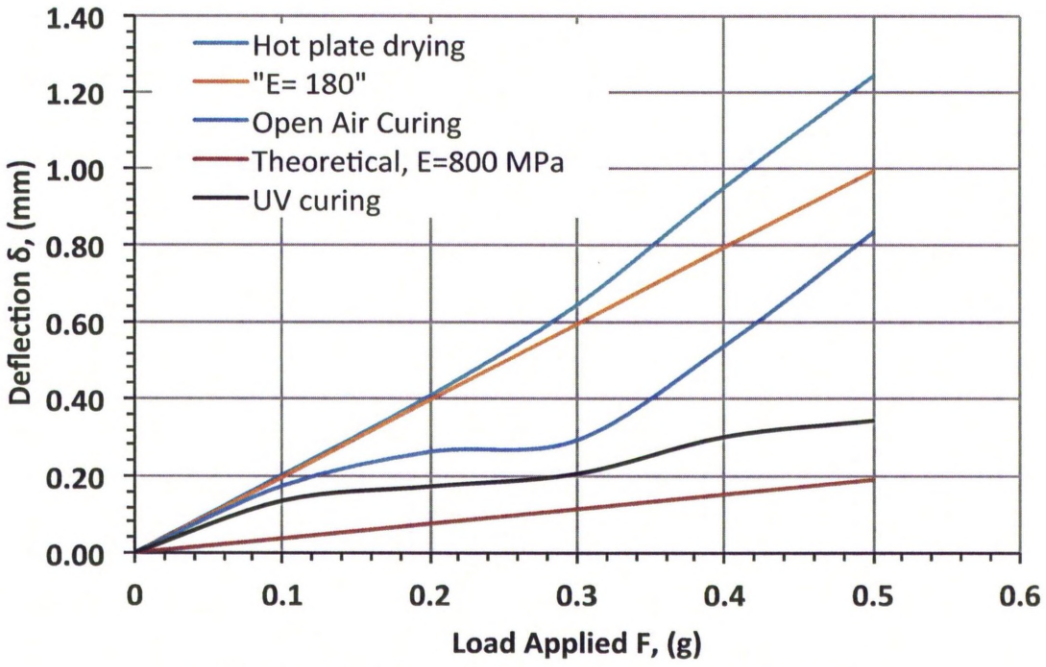

Figure 112: Graph Showing Deflection Observed for Beams.

The outcome of this work highlights the challenges associated with polymer-based devices. It was evident that the methods used for curing influences the mechanical behaviour and hence performance of the devices. Further research is required for methods leading to consistent mechanical behaviour and along with influence of time dependent properties on the performance.